

Nitric Oxide Reactivity and Unusual Redox Properties of Biomimetic Iron-Sulfur Clusters with Alternative Cluster Ligands



Dissertation

zur Erlangung des mathematisch-naturwissenschaftlichen Doktorgrades

„Doctor rerum naturalium“ (Dr. rer. nat.)

im Promotionsprogramm BioMetals

der Georg-August-University School of Science (GAUSS)

vorgelegt von

Christine E. Schiewer

aus Menden

Göttingen 2018

Betreuungsausschuss

Prof. Dr. Franc Meyer

Institut für Anorganische Chemie, Georg-August-Universität Göttingen

Prof. Dr. Kai Tittmann

Zentrum für Molekulare Biowissenschaften, Georg-August-Universität Göttingen

Prof. Dr. Ebbe Nordlander

Chemical Center, Lund University, Sweden

Mitglieder der Prüfungskommission

Referent: **Prof. Dr. Franc Meyer**

Institut für Anorganische Chemie, Georg-August-Universität Göttingen

Korreferent: **Prof. Dr. Kai Tittmann**

Zentrum für Molekulare Biowissenschaften, Georg-August-Universität Göttingen

Weitere Mitglieder der Prüfungskommission:

Prof. Dr. Inke Siewert

Institut für Anorganische Chemie, Georg-August-Universität Göttingen

Jun. Prof. Dr. Selvan Demir

Institut für Anorganische Chemie, Georg-August-Universität Göttingen

Dr. Franziska Thomas

Institut für Organische und Biomolekulare Chemie, Georg-August-Universität Göttingen

Dr. Matthias Otte

Institut für Anorganische Chemie, Georg-August-Universität Göttingen

Table of Contents

1	Introduction	1
1.1	Evolution of life and the discovery of iron-sulfur clusters.....	1
1.2	Natural iron-sulfur clusters	2
1.2.1	Structure	2
1.2.2	Biogenesis	4
1.2.3	Function of iron-sulfur clusters in organisms.....	5
1.3	Synthetic analogues	13
1.4	Iron-sulfur clusters and nitric oxide	16
1.4.1	Nitric oxide as vital messenger molecule and cytotoxic effector	16
1.4.2	Iron-sulfur-nitrosyl complexes	16
1.4.3	Nitrosylation of natural iron-sulfur clusters	18
1.4.4	Nitrosylation of biomimetic iron-sulfur clusters	21
1.5	Summary and conclusion.....	24
2	Nitrosylation of [2Fe–2S] clusters in their diferric, mixed-valent, and protonated state	25
2.1	Introduction and objective	25
2.2	Nitrosylation of diferric homoleptic coordinated [2Fe–2S] clusters.....	27
2.2.1	UV-vis and IR spectroscopy.....	27
2.2.2	NMR spectroscopy.....	29
2.2.3	Crystal structures of 33⁻ and 34⁻	30
2.2.4	EPR and Mössbauer spectroscopy.....	31
2.3	Nitrosylation of mixed-valent [2Fe–2S] clusters	33
2.3.1	Nitrosylation of 29³⁻	33
2.3.2	Nitrosylation of 30³⁻	40
2.4	Nitrosylation of protonated clusters 29H₂ and 30H₂	41
2.4.1	Reaction of 29H₂ with NO	41
2.4.2	Reaction of 30H₂ with NO	42
2.5	Nitrosylation of protonated mixed-valent 29H⁻	43
2.6	Summary and conclusion.....	44
3	Protonation and deprotonation of DNICs	46
3.1	Introduction and objective	47
3.2	Experimental results	47
3.2.1	IR spectroscopy	47
3.2.2	Mössbauer spectroscopy	49
3.2.3	Summary	50
3.3	DFT calculations.....	50
3.3.1	Background	50
3.3.2	Geometry optimization and IR spectra of 33⁻ and 34⁻	50
3.3.3	Mössbauer parameters of 33⁻ and 34⁻ and their protonated forms	52

3.3.4	Investigation of second protonation pathway for 33⁻	53
3.4	Discussion and conclusion	55
4	Cubane-type [4Fe–4S] cluster with one pentacoordinate iron ion	57
4.1	Introduction and objective	57
4.2	Synthesis	59
4.3	Structural characterization of 38²⁻	59
4.3.1	Mössbauer spectroscopy of solid sample and in frozen solution	60
4.3.2	UV-vis spectroscopy	63
4.3.3	NMR spectroscopy	64
4.3.4	Cyclic voltammetry	65
4.4	Conclusion	66
5	Oxidation of 38²⁻ with dioxygen and <i>p</i>-benzoquinone	67
5.1	Introduction and objective	67
5.2	Reaction of 38²⁻ with dioxygen	68
5.3	Equivalents of oxidant	75
5.4	Conclusion	80
6	Protonation of 5,6-Dithia-1,10-phenanthroline, its application as disulfide/dithiol switch, and as ligand for [2Fe–2S] clusters.	83
6.1	Introduction and objective	83
6.2	Synthesis of the ligand	85
6.3	UV-vis titration of 41 with PhCOOH, TFA and TfOH in MeCN	86
6.4	S–S bond cleavage mechanism: the disulfide/dithiol switch	88
6.5	Preliminary application as a chelate ligand for [2Fe–2S] clusters	94
6.6	Conclusion and Outlook	95
7	Experimental Section	97
7.1	Author contributions	97
7.2	Materials and methods	97
7.3	Synthesis	99
7.3.1	Fe–S clusters	99
7.3.2	DNICS	101
7.3.3	3,3'-Disulfur-2,2'-bipyridine	101
7.4	DFT calculations	105
8	Appendix	107
8.1	Benchmark substances for X-ray spectroscopy of iron-sulfur clusters	107
8.2	Supplementary spectra and information	108
9	Literature	119

Abbreviations.....	130
Curriculum Vitae.....	133
Acknowledgements.....	136

1 Introduction

1.1 Evolution of life and the discovery of iron-sulfur clusters

Iron-sulfur clusters are ubiquitous and essential prosthetic groups found in bacteria, plants, animals, and archaea. Their structural versatility allows them to fulfill various tasks in organisms, e.g. electron transfer, substrate binding/activation, and iron or sulfur storage.¹

Evolution

Iron-sulfur clusters are arguably one of the oldest cofactors and they are believed to be of fundamental importance to the evolution of pioneer organisms in volcanic vents. According to the *Iron-Sulfur World* theory,^{2,3} these organisms were composed of an organic superstructure and an inorganic substructure which supported the development of the organic superstructure by chemoautotrophy. Carbon fixation was performed at catalytic active metal centers, in which iron was the most abundant transition metal under the reducing potential of the volcanic exhalation. Dissolved ferrous ions underwent sulfidation in an anaerobic, volcanic environment to produce ferrous sulfide (FeS) which in turn ultimately formed pyrite (FeS₂), the most stable mineral under those conditions. Additionally, pyrite could have provided reducing power to the pioneer organisms.

The *Iron-Sulfur World* theory is promoted by two discoveries. Firstly, it is possible to imitate the reaction *in vitro* by carbon fixation from activated acetic acid on nickel and iron sulfide, (Ni,Fe)S, under primordial conditions.⁴ Secondly, the universal redox carrier in living organisms, nicotinamide adenine dinucleotide (NAD⁺) and nicotinamide dinucleotide phosphate (NADP), are not stable at high temperatures and therefore they had not been available for ancient thermophile organisms. These organisms relied on nonheme iron proteins instead.⁵ Recently published results by Mansy and coworkers describe the synthesis of [2Fe–2S] and [4Fe–4S] clusters through photooxidation of ferrous ions and photolysis of organic thiols.⁶

Discovery and scientific progress

Although iron-sulfur clusters are one of the oldest prosthetic groups and abundant in all life forms, they were discovered only in the second half of the 20th century by EPR spectroscopy.⁷ Beinert and Sands detected the famous hallmark “ $g = 1.94$ signal” in mitochondrial membranes in 1960.⁸ At that time, the source of the signal was unclear and

controversially discussed in the scientific community. Analytical determination revealed that the proteins only constitute of iron, cysteinate and inorganic, “acid-labile” sulfur atoms. Six years later, Gibson *et al.* resolved the dispute by explaining the signal with two iron ions that are antiferromagnetically coupled over a sulfur bridge.⁹ Other spectroscopic methods were used to elucidate the structure and electronic properties of iron sulfur proteins, including magnetic susceptibility, electron-nuclear double-resonance (ENDOR), Mössbauer spectroscopy, and crystal structures from X-ray diffraction.

During the 1970’s, a significant leap in iron-sulfur cluster research was obtained by Holm and coworkers using synthetic analogues.^{10,11} While model clusters share all basic features with protein-bound clusters, they are unfortunately not stable in aqueous solution or aerobic conditions. Nevertheless, synthetic analogues contributed greatly to the elucidation of the electronic structure of their natural counterparts and offer a reasonable approach to the investigation of general properties of iron-sulfur clusters.

1.2 Natural iron-sulfur clusters

1.2.1 Structure

The simplest iron-sulfur center, rubredoxin (**1**, Figure 1.1), consists of only one iron atom that is ligated by four deprotonated cysteine amino acid sidechains from the polypeptide protein backbone in distorted tetrahedral coordination. The name rubredoxin pays tribute to the strong red color due to a ligand to metal charge transfer (LMCT) from the thiolate ligand to the ferric ion. The color bleaches upon reduction to ferrous iron. Rubredoxins are exceptional in the iron-sulfur cluster family because their structural motif excludes “acid-labile”, inorganic sulfides. All clusters of higher nuclearity have bridging sulfides that impact the clusters’ electronic properties greatly. The cluster core of ferredoxins is constituted of either two iron ions and two sulfides, [2Fe–2S] (**2**), or four iron ions and four sulfides, [4Fe–4S] (**4**). These prosthetic groups are dubbed ferredoxins because of the iron content and their predominant role as redox carriers in electron transport chains. [4Fe–4S] clusters have a cube-like structure in which four corners that are opposed to each other are occupied by an iron ion and the others by sulfide. When iron is formally removed from one corner, the also biologically relevant cuboidal-type [3Fe–4S] (**3b**) cluster is formed. Interconversion between a linear and a cuboidal [3Fe–4S] clusters was observed in mitochondrial aconitase when exposed to urea or a pH higher than 9.¹³ [4Fe–4S] clusters can be converted into [2Fe–2S] clusters under physiological conditions.¹⁴ Iron-sulfur

clusters with higher nuclearity are generated through metal substitution in specialized enzymes or merging of simpler iron-sulfur clusters.¹⁵

Iron-sulfur clusters are most commonly ligated by cysteine; other ligands reported include histidine, aspartate, arginine, serine, or the amide groups of peptides.¹⁶ These alternative ligands modify the redox potential (Rieske, **2a**)¹⁷, gate electron transport¹⁸ or couple proton and electron transport (**2a** and **2b**).^{19,20}

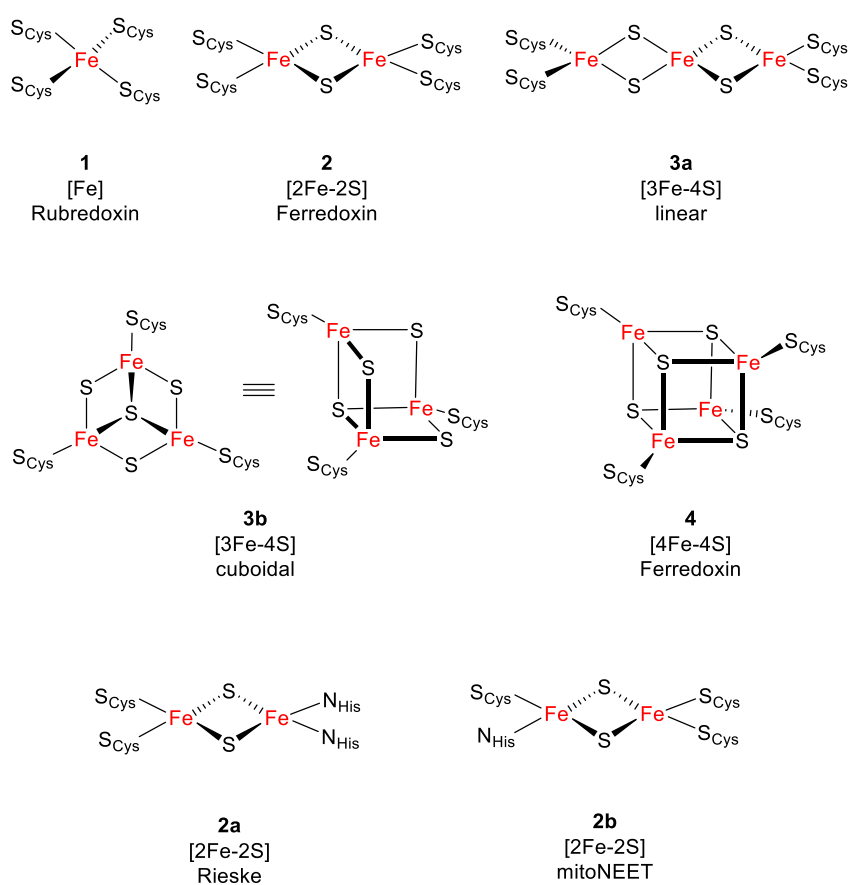


Figure 1.1. Common structural motifs in natural iron-sulfur clusters.

1.2.2 Biogenesis²¹

In 1966, Malkin and Rabinowitz reported that certain apoforms of [2Fe–2S] and [4Fe–4S] proteins can be activated *in vitro* by the simple addition of S^{2-} and $Fe^{2+/3+}$ ions.²² However, biogenesis of FeS proteins is a complex and delicate process in living cells rather than spontaneous self-assembly. Cluster maturation is catalysed by dedicated enzymatic multicomponent systems, namely the NIF (nitrogen fixation), ISC (iron sulfur cluster) and SUF (sulfur assimilation) machineries in prokaryotes.^{23–26} The NIF system deals with maturation of nitrogenase in nitrogen-fixing bacteria and maturation of general Fe–S proteins in some anaerobic organisms lacking nitrogenase. The ISC machinery is found in α -, β - and γ -proteobacteria and in mitochondria. SUF is present in the majority of prokaryotes and in chloroplasts. *E. coli*, as member of the Enterobacteriaceae family, possesses both, the ISC and SUF machinery. ISC operates under normal conditions, while the SUF machinery subs in when the cell is under oxidative stress or suffers from iron starvation. Fe–S cluster biogenesis is more complex in eukaryotes because it combines ISC and CIA (Cytoplasmic Iron-Sulfur Protein Assembly).^{27–29} The CIA machinery is responsible for the assembly of cytosolic and nuclear Fe–S proteins while ISC matures Fe–S clusters in mitochondria. The cytoplasmic CIA depends on the mitochondrial ISC and export machineries.³⁰

The importance of Fe–S clusters to life is stressed by mitosomes which reduced their genome content by evolution as far as possible. They still have the ISC machinery, although they cannot even produce ATP by themselves.³¹ On the other hand, Takahashi and coworkers reported recently of *E. coli* mutants that can survive without Fe–S cluster assembly.³²

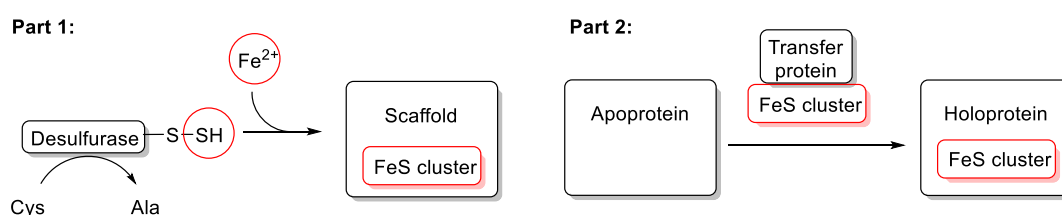


Figure 1.2: Simplified model for the biogenesis of iron-sulfur clusters.

In general, the ISC assembly consists of two parts (Figure 1.2). The first part is the *de novo* synthesis of a Fe–S cluster on a scaffold protein. A desulfurase releases the sulfur from a cysteine as a persulfide/hydrodisulfide which is transferred to the scaffold protein. Electrons are provided via ferredoxin and ferredoxin reductase for the reduction from S^0 in

the cysteine to S^{2-} in the cluster. The iron ions are delivered by specific iron donors. The cluster is bound to the scaffold protein in a labile fashion by conserved cysteine residues as a [2Fe–2S] cluster. The intermediate [2Fe–2S] cluster can be transformed later into [4Fe–4S] clusters or clusters of higher nuclearity by a dedicated set of ISC machinery. In the second part of the cluster assembly, the labile Fe–S cluster is transferred to the target apoprotein by chaperones or transfer proteins. The transfer proteins are essential in living cells to promote an accurate and specific transport to the correct acceptor site. Finally, the holoprotein is assembled into the polypeptide chain.

In 2017, Adams and coworkers published the discovery that the protein IssA stores iron and sulfur as thioferrate (Figure 1.3) in metalloprotein complexes with a diameter of up to 300 nm. It was shown that thioferrate can provide the iron and sulfur units necessary to reconstruct [4Fe–4S] clusters in ferredoxin *in vitro*.³³

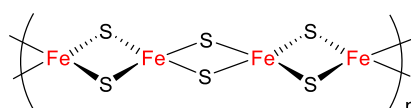


Figure 1.3. Structure of the inorganic polymer thioferrate.

As Fe–S proteins are essential to several processes in cells, shortcomings in the biogenesis thereof are linked to several fatal diseases most of which have an impact on the whole organism. Common features are, firstly, that all diseases are rare with a prominent mitochondrial phenotype because the ISC biogenesis is crucial for mammalian cells to survive. Secondly, tissues demanding high energy are primarily affected, e.g. neurons, muscles, heart tissues. Thirdly, iron dysregulation is always implicated. This means that mitochondrial iron accumulation/deposit is a key feature of these diseases. The best researched disease is Friedreich’s ataxia, but others include microcytic anaemia and erythropoietic protoporphyria.^{34,35}

1.2.3 Function of iron-sulfur clusters in organisms³⁶

Iron-sulfur clusters as electron carriers: unique and tunable redox properties

Generally, metal ions are more versatile than organic redox molecules in regard to redox behavior. The reduction potential is strongly dependent on the coordination sphere around the cluster, but also hydrogen bonding with peptides and water has a strong influence on the reduction potential. This can be seen by the wide range of redox potentials (–700 to 450 mV vs. SHE)¹⁶ covered by iron-sulfur proteins (Figure 1.4).³⁷ Iron-sulfur clusters are

well suitable for biological electron transport because they can delocalize electron density over both iron and sulfur atoms, as the Fe–S bonds are rather covalent.³⁸ The reorganization energy is comparatively small due to metal-ligand covalency and valence delocalization when iron is reduced or oxidized. This allows for a very fast electron transfer. There is a much smaller change in the total electron density on the iron than is indicated by the formal valence difference.³⁸

Examples for iron-sulfur clusters involved in electron transfer are ferredoxins in the respiratory chain in complexes I, II, and III. In these proteins, the clusters form a wire that delivers electrons one at a time between redox couples that are physically separated. Only few unique Fe–S clusters such as the double-cubane [8Fe–7S] cluster of nitrogenase have the potential to act as two electron carrier under physiological conditions.³⁹

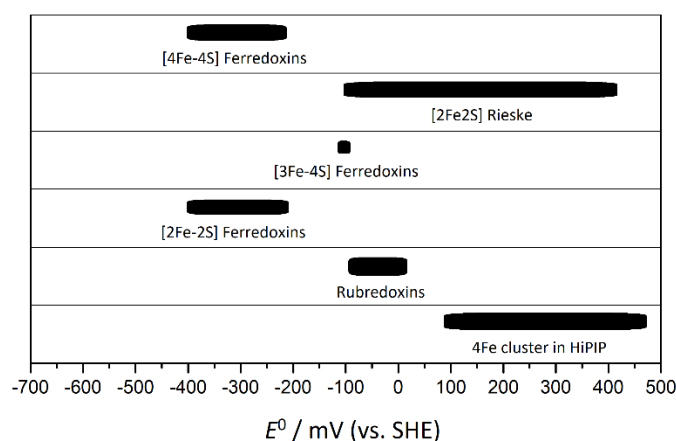


Figure 1.4. Experimental ranges of redox potentials of various iron-sulfur proteins.^{16,37}

The most common metal oxidation levels of iron–sulfur clusters include Fe^{2+} and Fe^{3+} ions as seen in rubredoxin (Figure 1.5, a) or a mixture thereof in clusters with higher nuclearity. The electronic structure and distribution of charge can be determined with EPR, ENDOR, Mössbauer, and MCD spectroscopy. A summary of the most common oxidation states of rubredoxins and ferredoxins is depicted in Figure 1.5.

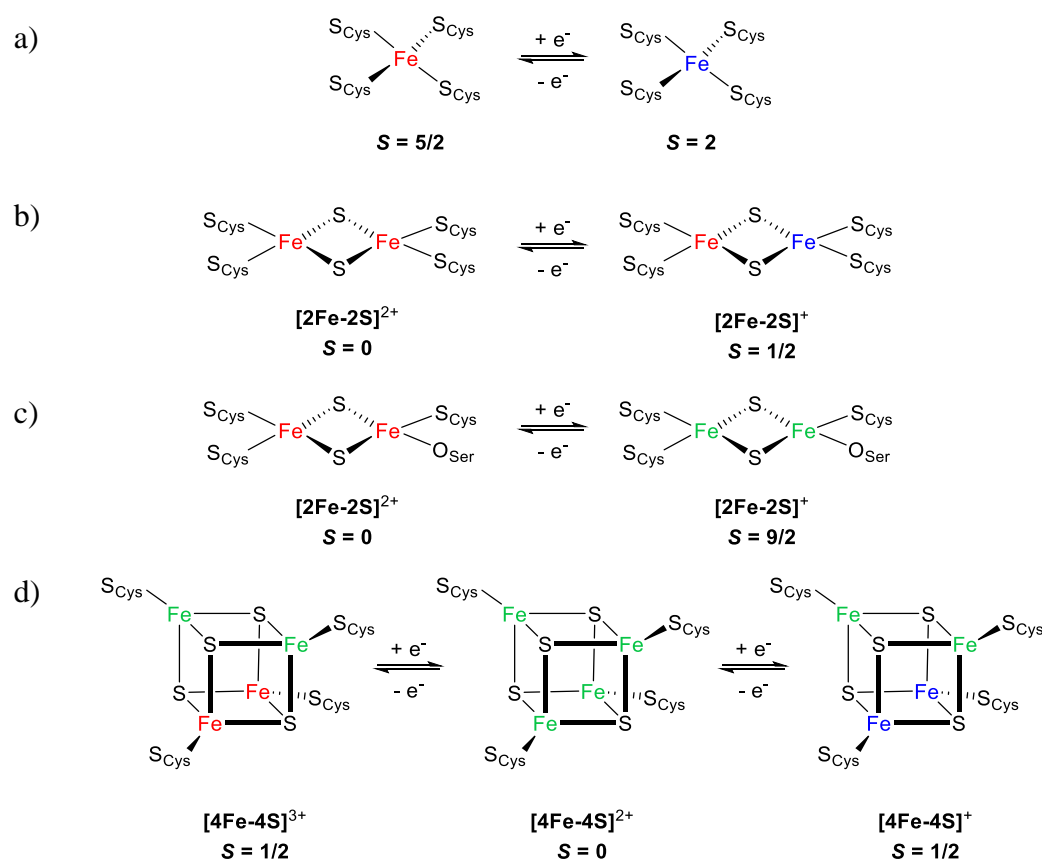


Figure 1.5. Localization and delocalization patterns in common FeS clusters, showing localized Fe^{3+} (red), localized Fe^{2+} (blue) sites and delocalized $\text{Fe}^{2.5+}\text{Fe}^{2.5+}$ pairs (green). Indicated also are the core oxidation state and the spin of the cluster. Figure is adapted from literature.¹

In the case of the diferric $[2\text{Fe-}2\text{S}]$ clusters, two Fe^{3+} ions with a spin of $5/2$ couple antiferromagnetically resulting in an overall spin $S = 0$. When the cluster is reduced the electron can either be localized on one iron ion (Figure 1.5, b) or is delocalized over both iron ions leading to an oxidation state of $+2.5$ each (Figure 1.5, c). The latter was observed in a mutant form of *Clostridium pasteurianum* ferredoxin in which one cysteine residue was exchanged for serine.⁴⁰ The result is a mixed-valence state with parallel spins and $S = 9/2$. Case b can be easily distinguished from c, as it gives a typical EPR signal at $g = 1.94$. The core of $[4\text{Fe-}4\text{S}]$ ferredoxins has a charge of $+2$ in their resting state (Figure 1.5, d middle). They are composed of two mixed-valence pairs antiferromagnetically coupled to each other resulting in $S = 0$. When this cluster is reduced by one electron, two ferrous iron ions couple ferromagnetically to $S = 4$ and a mixed-valence pair couples to $S = 9/2$. The two pairs then again couple antiferromagnetically resulting in overall $S = 1/2$. All-ferrous clusters have been reported, however, they are not naturally occurring.^{12,41,42} $[4\text{Fe-}4\text{S}]^{3+}$ is the resting state of the so called high-potential iron proteins (HiPIPs) with one mixed-valence pair and one pair with two ferric ions.⁴³ The electron can also tunnel to the other

pair.⁴⁴ HiPIPs are small globular proteins with little to no secondary structure.⁴⁵ The [4Fe–4S] cluster is bound to four cysteines like in ferredoxins, however the HiPIP cluster is buried within the protein interior in a hydrophobic cavity while the clusters in ferredoxins are more exposed on the surface. The HiPIP cluster implements the [4Fe–4S]^{3+,2+} transition as a result of its hydrophobic environment and hydrogen-bonding network. HiPIPs act as electron donors on the tetraheme cytochrome in photosynthetic bacteria with their exceptionally high redox potential (+100 to +450 mV *vs.* NHE).⁴⁶

Alternative ligands as histidine have a great impact on the redox potential and chemical properties of Fe–S clusters.^{16,47} Rieske [2Fe–2S] proteins (**2a**, Figure 1.1) are found in respiratory (cytochrome *bc*₁ in mitochondria and bacteria) and photosynthetic (cytochrome *b₆f* in chloroplasts) membrane-associated electron transfer complexes,¹⁷ as well as in some oxygenases.⁴⁸ The [2Fe–2S] cluster is bound by two cysteine and two histidine residues. The difference in the net charges of the ligands causes an upshift of the redox potential (–100 to +490 mV *vs.* NHE) for the [2Fe–2S]^{2+/+} reduction/oxidation. Rieske proteins conduct proton coupled electron transfer as the proton from the N–H group of the imidazole is released easily with *pK_a* values of 7.4 and 9.1 in the oxidized diferric state, and around 12.5 in the reduced mixed valence state.^{49,50} Fe–S clusters of Rieske proteins are close to the protein surface, and express pH- and ionic strength-dependent redox behavior. On the other hand, low-potential Rieske proteins have pH-independent redox potentials of around –150 mV *vs.* NHE.⁵¹

Another example for Fe–S clusters with alternative ligands are CDGSH iron-sulfur domains including mitoNEET, Miner 1, and Miner 2. MitoNEET (**2b**, Figure 1.1) is located in the outer membrane of mitochondria. The homodimer binds one [2Fe–2S] cluster in each subunit. The cluster is coordinated by three cysteine and one histidine residue in the CDGSH motif. They are redox-active, their redox potential is pH-dependent and they undergo electron transfer, potentially proton coupled.^{52–54}

Histidine ligated [4Fe–4S] clusters can be found in the distal clusters of an electron-transfer chain in hydrogenase enzymes.⁵⁵

Sensing and regulation of gene expression^{56–58}

Regulatory enzymes comprise a sensor domain – in this case one or more Fe–S clusters – and a functional domain containing a DNA binding site to promoter regions of genes. After environmental stimuli the structure of the regulatory protein changes and allows for

protein-protein interaction with RNA polymerase (RNAP) or alteration of the DNA architecture which leads to expression of target genes. On the other hand, RNAP can be hindered at recognizing the promoter elements and thus transcription is repressed.

Generally, Fe–S clusters are ideal for sensing environmental signals like gases (O_2 , NO), reactive oxygen species (ROS, including superoxide (O_2^-)) and hydrogen peroxide (H_2O_2) due to their high reactivity towards those species. Signal induced changes of the Fe–S core like oxidation or even disruption propagate a conformational change of the regulatory protein and subsequently mediate transcriptional activation. Some proteins have a specificity for more than one signaling molecule and they can alter gene expression to obtain the correct adaptive response.

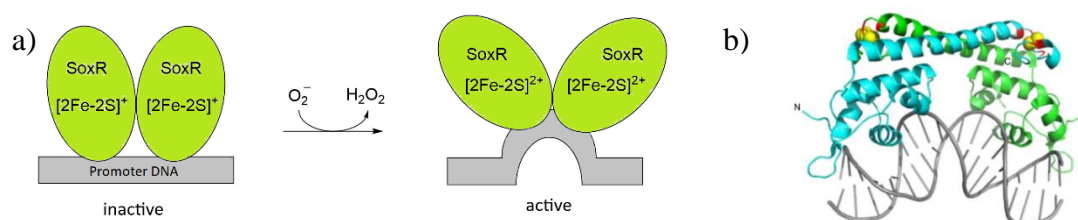


Figure 1.6. a) Cartoon of the mechanism for SoxR transcriptional activation.⁵⁹ b) Crystal structure of oxidized SoxR bound to DNA and induction of sharp DNA bending.⁵⁷

SoxR (superoxide response regulator) is a sensor to oxidative stressors like NO, superoxide (O_2^-), and redox-cycling agents in *E. coli*.⁶⁰ It is constituted of a dimeric transcriptional activator with one [2Fe–2S] cluster in each 17 kDa monomer (Figure 1.6, a). The resting state is the mixed-valent $[2Fe-2S]^+$ which is reversibly oxidized to $[2Fe-2S]^{2+}$. Oxidation reorients the promoter DNA element (Figure 1.6, b) to allow transcription of more than 100 genes in the SoxRS regulon as stress-response against the oxidative stress. Expressed proteins include superoxide dismutase (SOD), oxidized-DNA repair endonucleases and oxidation-resistant enzymes. When oxidative stress abates, reducing systems have SoxR returning in its reduced state.

One of the best studied global regulatory proteins is FNR (fumarate and nitrate reduction) regulator, also known as the “master switch” between aerobic and anaerobic respiration in *E. coli*. The transcription factor triggers the shift from an anaerobic to aerobic metabolism by sensing the level of oxygen in the cell.⁶¹ Only the dimeric [4Fe–4S] protein can bind to DNA. The [4Fe–4S] cluster converts quickly into two [2Fe–2S] clusters in the presence of O_2 and the protein loses its dimerization.⁶² This process can be reversed when anaerobic conditions are reestablished.¹⁴ When it is active it controls 200 genes involved in anaerobic

oxidation of carbon sources and reduction of electron acceptors, e.g. nitrate, fumarate, and DMSO, and represses genes specifically for aerobic metabolism.⁵⁷ FNR also plays a role in sensing NO (see Chapter 1.4.3). However, NO sensing is a secondary function of FNR because fewer proteins are affected than with O₂. Other O₂ sensing regulators include NreB in *Staphylococci*.⁵⁷

It is a challenge to decipher whether reactions of Fe–S clusters with signaling molecules are physiologically relevant or simply adventitious. At times proteins react *in vitro* with signaling molecules although the reaction does not occur in the living organism. Enzymes that react to oxidative stress often also react to nitrosative stress. However, there are also enzymes that are specialized to act on nitrosative stress. NsrR is a wide-spread dedicated NO sensor e.g. in β - and γ -proteobacteria. Upon nitrosylation of the sensing [4Fe–4S] cluster, NsrR loses DNA binding. This process activates genes involved in NO detoxification and damage repair that were repressed before. Expressed genes are *hmp*, encoding a flavohemoglobin, *ytfE*, implicated in Fe–S cluster repair, and, *nrf*, encoding the NrfA periplasmic nitrite reductase.⁶³ Recently, the crystal structure of NsrR from in the dimeric holo form and as apo-DNA complex was reported by Le Brun, Fontecilla-Camps and coworkers.⁶⁴

WhiB-like proteins (Wbl), exclusive to Actinobacteria, fulfill a wide range of functional roles. Among them are cell division, sporulation, nutrient starvation, antibiotic resistance, virulence, and oxidative stress response.⁵⁷ WhiD of *S. coelicolor* and WhiB1, B3, and B4 of *Mycobacterium tuberculosis* contain a NO-sensitive [4Fe–4S] cluster ligated by four cysteine residues. Following cluster nitrosylation or in their apo-protein form, Wbl proteins bind DNA with high affinity. Further information on nitrosylation of Wbl proteins is provided in chapter 1.4.3.⁵⁷

Maintaining homeostasis of iron is essential in cells. Iron serves in cofactors such as heme and Fe–S clusters in most organisms, but an excess of iron under aerobic conditions catalyzes the formation of reactive oxygen species (ROS) that ultimately destroy cellular compounds like proteins, DNA and lipids. IscR (Proteobacteria) and SufR (Cyanobacteria) sense the Fe–S cluster levels as part of control genes in Fe–S biogenesis. IRP (iron regulatory protein) controls and maintains the iron homeostasis in mammals.⁶⁵

Iron-sulfur clusters in enzymes: substrate binding and activation

Fe–S clusters are involved in the activation of small molecules in bacteria and archaea. The enzyme nitrogenase catalyzes the reduction of dinitrogen to ammonia via the catalytically active Fe–Mo subprotein. The Fe–Mo subprotein contains two Fe–S clusters of high nuclearity: the P^N-cluster and the iron molybdenum cofactor (FeMoCo, Figure 1.7). The P^N-cluster mediates intramolecular electron transfer to the FeMoCo where the reduction of dinitrogen takes place. The FeMoCo comprises of a large [MoFe₇S₉-homocitrate] complex with an unusual interstitial carbon atom in the center.^{66,67} Quantum mechanical calculations suggest that the central carbon is bound through six covalent C–Fe bonds and thus is well stabilized.⁶⁸ Some bacteria are able to produce alternative nitrogenases with vanadium or iron ions if molybdenum supply is scarce.⁶⁹ Vanadium nitrogenase is also capable of reducing carbon monoxide and converting it to ethylene, ethane, or propane.⁷⁰

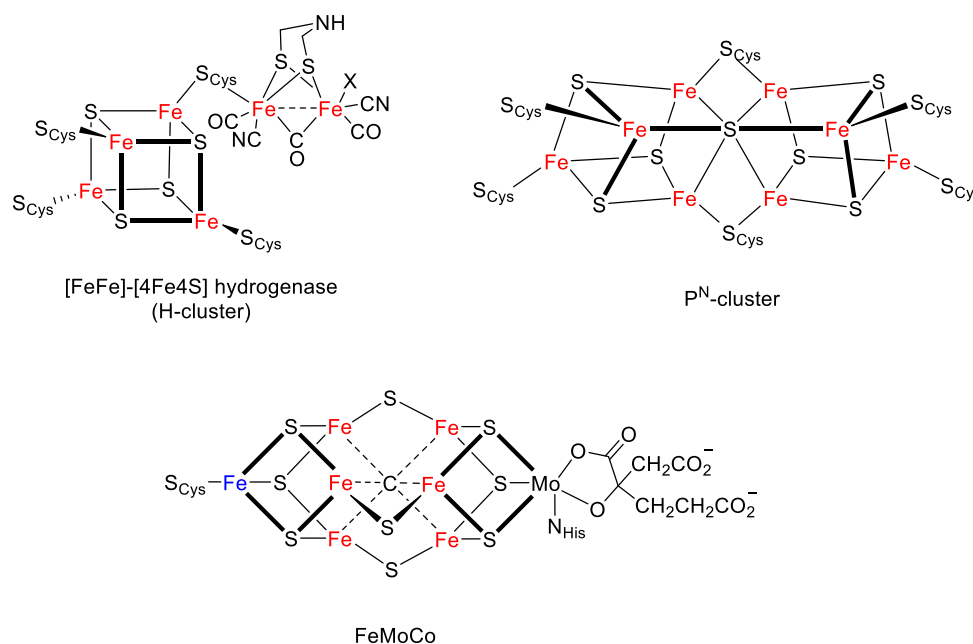


Figure 1.7. Examples for enzymatic active iron-sulfur clusters in hydrogenases and nitrogenase.

Hydrogenases produce or consume hydrogen. In [NiFe] and [FeFe] hydrogenases several [4Fe–4S] clusters fulfill the task of electron mediator or reservoirs (e.g. the H-cluster, Figure 1.7).⁷¹ At the active site cyanide and carbonyl ligands stabilize low oxidation states of the metal ions. Other iron-sulfur cluster containing enzymes are sulfite and nitrite reductases and Ni-Fe CO dehydrogenase (CODH).

Aconitase is an example for non-redox catalysis as no redox chemistry takes place at the Fe–S cluster. It converts citrate to isocitrate in the citric acid cycle of all bacteria and

eukaryotes. In its inactive form, it constitutes of a [3Fe–4S] and in its active form of a [4Fe–4S] cluster in which one iron has no cysteine ligand and thus serves as a Lewis acid to bind the substrate.⁷² During the catalysis the hydroxy group and a proton of adjacent carbon atoms of citrate are removed and reattached in reversed order. ENDOR spectroscopy was used to elucidate the enzyme-substrate complex, which was later confirmed by crystallography (Figure 1.8).⁷³

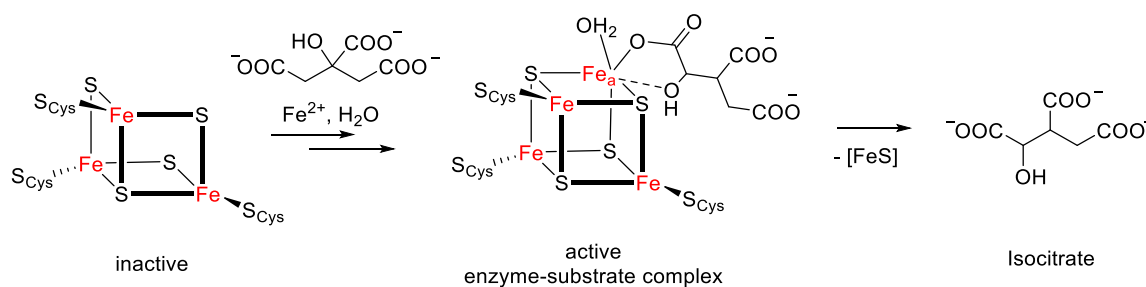


Figure 1.8. Active site of aconitase: reaction of citrate to isocitrate.

The radical-SAM superfamily consists of more than 2800 proteins. These enzymes bind *S*-adenosyl methionine (SAM or AdoMet) in a similar fashion like aconitase via carboxylate and amino groups to a unique iron atom of a [4Fe–4S] cluster that is not ligated by cysteine (Figure 1.9).^{74,75} However, the Fe–S cluster is redox active during catalysis, in contrast to aconitase. A 5'-deoxyadenosyl radical is formed which then abstracts a hydrogen atom from the organic substrate to initiate a radical mechanism used in the biosynthesis of amino acids, nucleotides, co-enzymes and antibiotics.^{76–78}

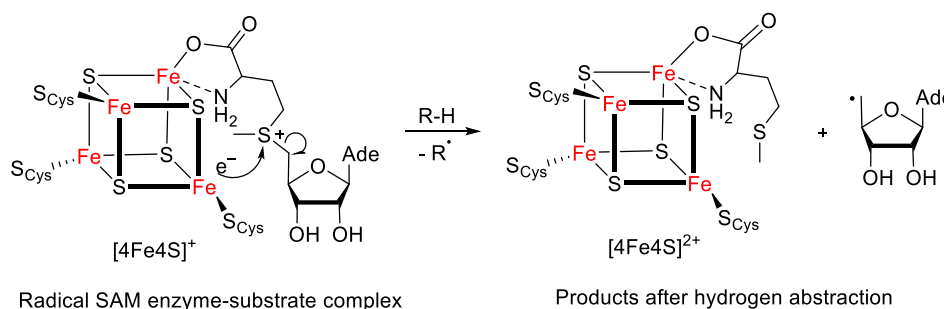


Figure 1.9. Radical mechanism at active site of a SAM enzyme.

As an example, biotin synthase from *E. coli* belongs to the radical SAM family.⁷⁹ It employs two molecules of AdoMet to activate two C–H groups in dethiobiotin. An auxiliary [Fe₂S₂(cys)₃(arg)] cluster⁸⁰ in biotin synthase degrades and provides the bridging sulfur atom for the conversion of dethiobiotin to biotin.⁸¹

Other functions of iron-sulfur clusters

Other functions include Fe or cluster storage in ferredoxins or polyferredoxins, structural stabilization comparable to Zn-finger proteins (Endonuclease III), regulation of enzyme activity (Glutamine PRPP amidotransferase, Ferrochelatase), disulfide reduction (ferredoxin: thioredoxin reductase, hetero-disulfide reductase), and donation of sulfur during the biosynthesis of some S-containing natural products (biotin synthase, [4Fe-4S] cluster of lipoic acid synthase (LIAS)).⁸²

1.3 Synthetic analogues

Biologists have established reliable protocols to extract intact Fe-S clusters from their protein environment through exchange with exogenous thiolate donors since the 1970s.⁸³ At the same time, low-molecular-weight complexes as analogues for biological Fe-S clusters were synthesized by chemists. Generally, the synthetic systems model the natural clusters well in terms of structure and function except for a more negative redox potential.

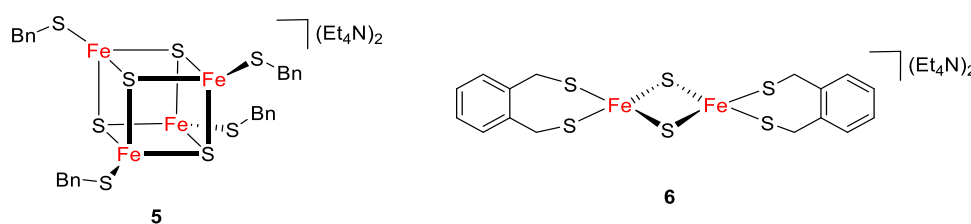


Figure 1.10: First synthetic cubic [4Fe-4S] cluster (**5**) and [2Fe-2S] cluster (**6**).

Holm and coworkers synthesized the first model cluster in 1972.⁸⁴ It was a cubic [4Fe-4S] cluster (**5**) with thio-benzyl ligands mimicking cysteine (Figure 1.10). One year later they published the first synthetic [2Fe-2S] cluster with *o*-xylyldithiolato ligands (**6**).⁸⁵ The clusters can be obtained in self-assembly reactions from ferric iron, thiols, and sulfide. Since then many model complexes for rubredoxins and clusters of higher nuclearity have been reported.^{10,86-88} A selection of synthetic clusters is depicted in Figure 1.11 and Figure 1.12.

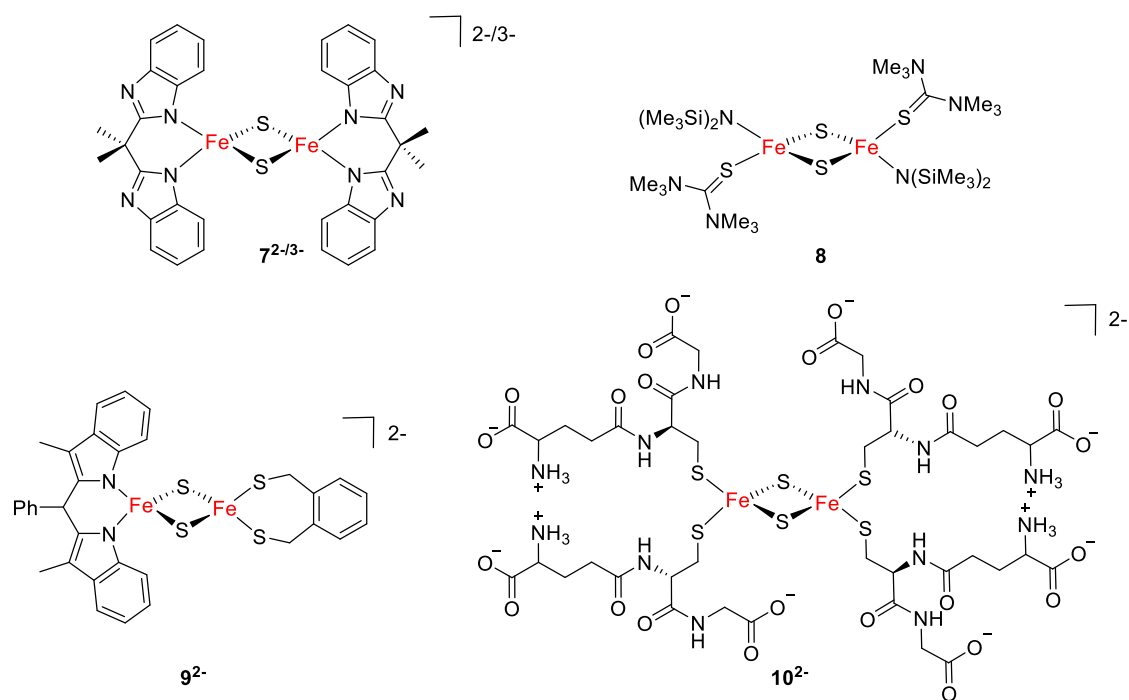


Figure 1.11: Selection of low-molecular-weight [2Fe-2S] clusters: first cluster with N-ligation and first cluster to be isolated in the mixed-valence state (**7^{2-/3-}**),^{89,90} first neutral cluster with N(SiMe₃)₂ as strong π -donor ligands (**8**),⁹¹ first heteroleptic [2Fe-2S] cluster (**9²⁻**),⁹² glutathione-complexed cluster (**10²⁻**).⁹³

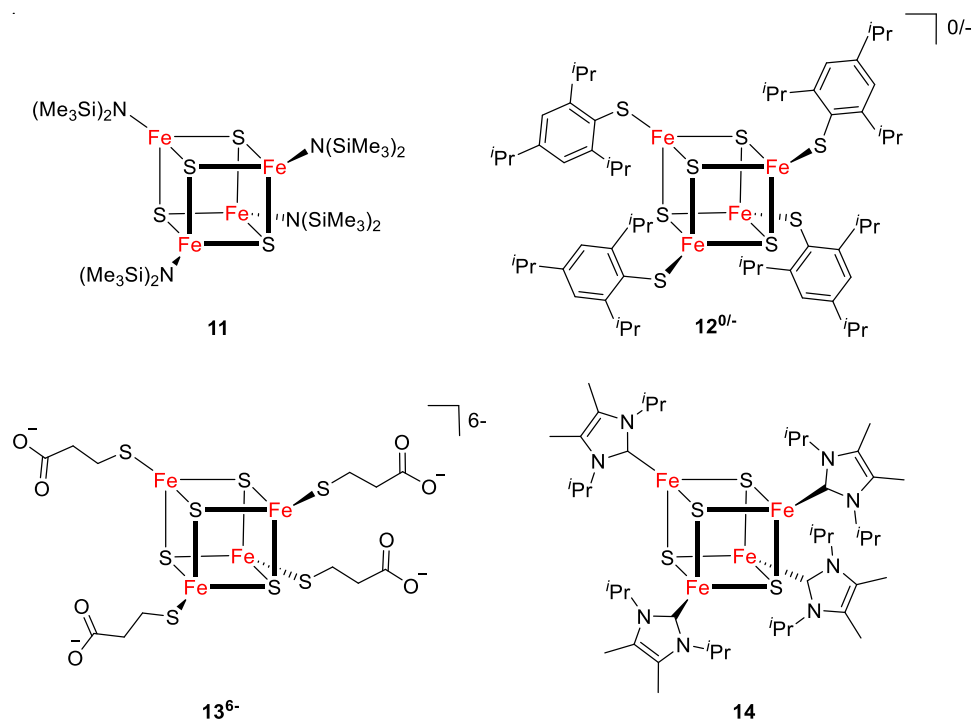


Figure 1.12: Selection of low-molecular-weight [4Fe-4S] clusters: first all ferric [4Fe-4S] cluster (**11**),^{91,94} first HiPIP model with sterically encumbered thiolate ligands (**12^{0/-}**),^{95,96} c) first water soluble [4Fe-4S] cluster (**13⁶⁻**),^{97,98} first all ferrous [4Fe-4S] cluster (**14**).⁹⁹

Tatsumi and coworkers achieved the synthesis of a 3:1 site-differentiated [4Fe–4S] cluster with the help of sterically encumbered thiolate ligands (**15**^{0/-}, Figure 1.13).¹⁰⁰ It mimics the distal [Fe₄S₄(cys)₃(his)] cluster in [FeNi] hydrogenase.

A tridentate cavitand ligand system (**L(SH)**₃ in Figure 1.13) produces a cluster with a single iron site with more labile ligation (**16**²⁻).^{101,102} The apical iron ion can be removed under mild oxidative conditions to obtain a cuboidal [3Fe–4S] cluster. This [3Fe–4S] cluster in turn can be used as starting material for heterometallic [M 3Fe–4S] clusters (M = Mn, Co, Ni, Cu, Zn, Cd, Tl, Mo, V, Re, Ag, W, Nb, Pb, or Cr).^{103,104}

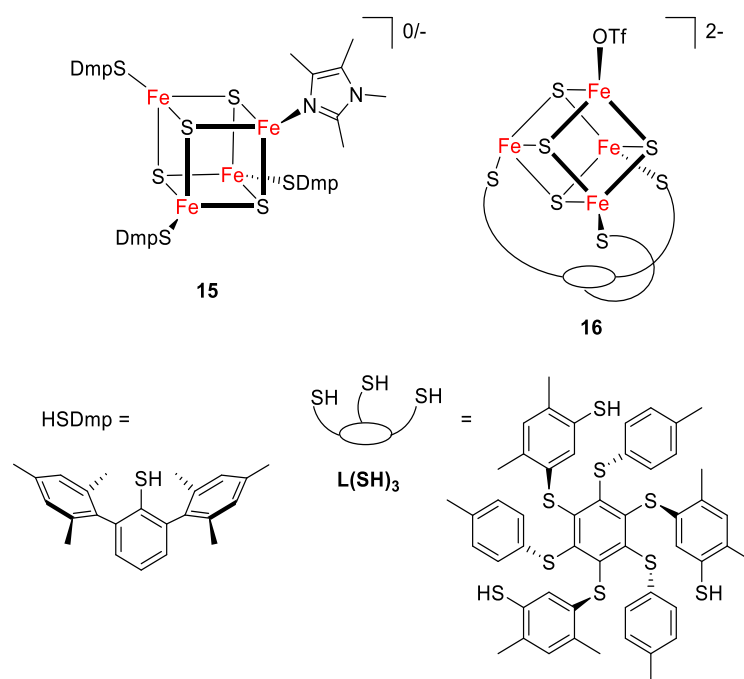


Figure 1.13. Site-differentiated cluster by Tatsumi and coworkers (**15**^{0/-})¹⁰⁰ and by Holm and coworkers (**16**²⁻).¹⁰¹

Today's research does not only focus on mimicking the structure and electro-chemistry of natural Fe–S clusters, but also their enzymatic properties. Special attention is paid to the Fe–S-cluster-containing enzyme nitrogenase because of its ability to activate nitrogen. Holland and coworkers moved away from the idea that it is necessary to copy the whole structure to obtain an active complex. They created the mononuclear iron complex **17**⁻ with a sulfur-rich coordination sphere that binds dinitrogen (Figure 1.14).^{105,106}

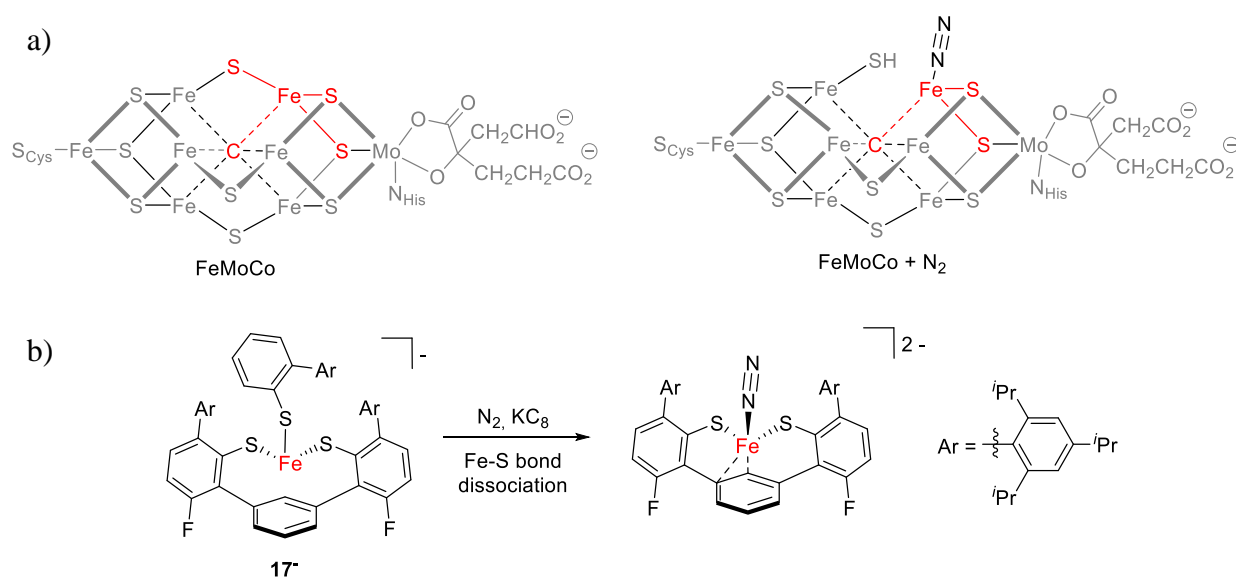


Figure 1.14: a) Possible binding mode of dinitrogen at FeMoCo; b) mononuclear iron-sulfur-carbon cluster **17** as synthetic model system for nitrogenase's active site.¹⁰⁵

1.4 Iron-sulfur clusters and nitric oxide

1.4.1 Nitric oxide as vital messenger molecule and cytotoxic effector

NO plays a role in a wide variety of biological processes.^{107,108} It is formed in cells by members of the NO synthase (NOS) family or by nitrite reductases.^{109,110} The reaction of NO with the heme-iron in guanylyl cyclase has been investigated thoroughly since the 1960s. This reaction starts a cascade which ultimately leads to relaxation of the cardiovascular system.^{111–114} NO also plays an important role in neurotransmission¹¹⁵ and immune regulation.^{116,117} Physiological amounts of NO are neuroprotective, but higher concentrations can be neurotoxic. Nitrosative stress can lead to damage of DNA and amino acids.¹¹⁸ Despite its radical character, the half time life of the NO molecule in the cell can be surprisingly long (0.002–2 s).¹¹⁹

1.4.2 Iron-sulfur-nitrosyl complexes

The primary biological target for NO are metal-containing proteins. In the resulting metal-nitrosyl complexes the NO-ligand is redox non-innocent. Three redox states are biologically relevant: the nitrosonium cation (NO⁺), NO radical (NO[•]), and nitroxyl anion (NO⁻). However, the iron and NO oxidation state is difficult to assign because of a small energy gap between the transition metal 3d and NO π^* -orbitals. Therefore, the electronic structure of iron-nitrosyl complexes is normally described by the Enemark–Feltham notation, in which the iron 3d and NO π^* electrons “x” of the molecule are neither assigned

to the iron ion nor the nitrosyl moieties “n” ($\{\text{Fe}(\text{NO})_n\}^x$).¹²⁰ Transition metal NO^+ adducts have a N–O stretching frequency of $1700\text{--}2000\text{ cm}^{-1}$. When NO behaves formally as NO^- the stretching frequency is $1500\text{--}1700\text{ cm}^{-1}$.¹⁰⁷

The first reported iron-sulfur-nitrosyl clusters were Roussin’s black salt (RBS, **18**) and Roussin’s Red Salt (RRS, **19**) in 1858.¹²¹ RBS and RRS cannot bind to the protein without prior ligand exchange and are therefore biologically irrelevant.¹²²

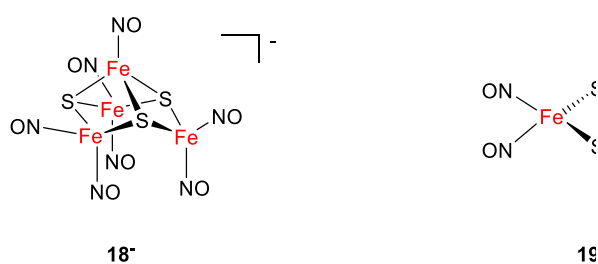


Figure 1.15. First reported iron-sulfur-nitrosyl complexes: Roussin’s Black Salt (RBS, **18**⁻) and Roussin’s Red Salt (RRS, **19**²⁻).

Biologically relevant iron-sulfur-nitrosyl complexes are dinitrosyl-iron complexes (DNIC, **20**⁻) and the esters of Roussin’s salt (RREs, **21**⁻, **22**) or derivatives thereof (**23**⁻, **24**⁻). They are the products of nitrosylation of Fe–S clusters (chapter 1.4.3). EPR spectroscopy is an excellent tool for recognizing DNICs and reduced RREs due to their signature isotropic g -value of 2.03 or 1.99, respectively.¹²³ However, assignment of EPR-silent species is more challenging. IR, Mössbauer, UV/vis, and Raman spectroscopies lack full diagnostic ability to discriminate between the different species. A method that has become more popular in the scientific community in recent years is nuclear resonance vibrational spectroscopy (NRVS).^{124,125} It allows for distinction between different iron-nitrosyl species and has been applied to nitrosylized [4Fe–4S] ferredoxin,¹²⁶ Rieske,¹²⁷ WhiD, and NsrR proteins.¹²⁸ Today NRVS data is available for various iron-sulfur clusters and nitrosyl complexes which allows for comparison of fingerprint regions in order to decipher the product after nitrosylation of an Fe–S cluster.^{128–133}

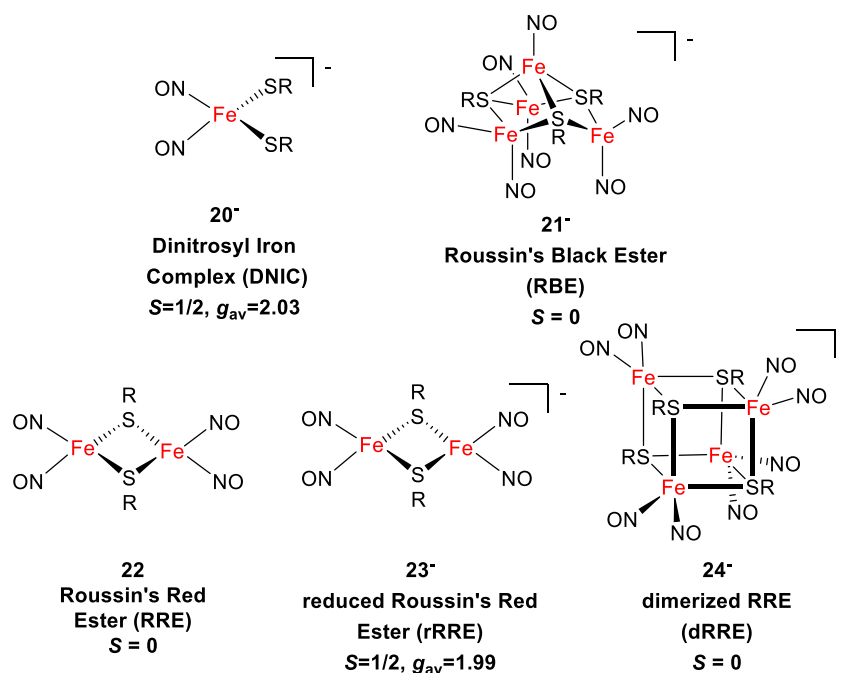


Figure 1.16. Identified reaction products from nitrosylation of Fe–S proteins. The residues (SR) stand for cysteine in proteins and thiolates in model clusters.

Conversion between different iron-sulfur-nitrosyl complexes is possible and depends on the concentration of NO, the redox states of iron and sulfur, and the availability of sulfide and thiol ligands.¹³⁴ For example, S-based oxidation of a DNIC with O₂ results in formation of a RRE.¹³⁵

1.4.3 Nitrosylation of natural iron-sulfur clusters

Nitrosylation of Fe–S proteins usually disrupts the cluster, affects the loss of the enzyme's activity and ultimately has cytotoxic effects.^{119,136} On the other hand, it is possible to reverse the reaction *in vitro* and generate [2Fe–2S] clusters from DNICs via the key intermediate RRE.¹³⁷ Yang *et al.* found that nitrosylation does not necessarily cause cell death as nitrosylated Fe–S enzymes are efficiently repaired in aerobically growing *E. coli* cells by cysteine desulfurase (IscS) in the presence of L-cysteine *in vitro*.^{138,139}

[4Fe–4S], [2Fe–2S] clusters and [2Fe–2S] clusters with alternative ligands yield different products after reaction with NO. The results of prior research are summarized in the following paragraphs.

[4Fe–4S] clusters

Aconitase and IRP1 were the first Fe–S proteins that were reacted with NO *in vitro* in 1997 after cellular studies indicated that Fe–S proteins are targeted by NO.¹⁴⁰ As a result, protein-bound dinitrosyl-iron-dithiolato complexes were identified by EPR spectroscopy by their typical *g*-value of 2.03. In the following years, other [4Fe–4S] proteins were reacted with NO and DNICs were found to be the main product by EPR spectroscopy, e.g. HiPIP proteins¹⁴¹ or regulatory proteins like Fur (ferric uptake regulatory protein)¹⁴² and NorR (NO responsive transcription factor).^{143,144} In 2011 Ding and coworkers published a paper in which they supported the idea that Fe–S proteins are the major source of protein-bound DNICs in *E. coli* cells under nitric oxide stress.¹⁴⁵

New technology such as NRVS and more careful examination of the products after nitrosylation have led to the discovery of EPR-silent reaction products like RRE (**22**), dimerized RRE (**24**⁻), or RBS/RBE (**18**⁻/**21**⁻). Spin-quantification showed that DNICs account only for a fraction of the total iron content.^{140,146,147} Le Brun, Cramer and coworkers found that the main product after nitrosylation of NsrR is a mixture of EPR-silent RRE (**22**) and RBE (**21**⁻) or RBS (**18**⁻). The results are supported by NRVS and DFT calculations. Unfortunately, RBS and RBE are not distinguishable by NRVS and other spectroscopic methods: RBE has the same constitution as RBS except that one to three bridging sulfides are replaced by thiolates from cysteines.^{128,148} FNR and WhiB react with 8 NO molecules yielding octanitrosyl clusters [Fe₄(NO)₈(Cys)₄]⁰ (dimerized RRE).^{147,149,150}

[2Fe–2S] clusters

In general, nitrosylation leads to loss of the enzyme's activity, but nitrosylated SoxR has transcriptional activity similar to that of SoxR after oxidative stress.¹⁵¹ It is important to consider the oxidation state of the [2Fe–2S] cluster in SoxR as the oxidized and the mixed-valence cluster yield different products. When oxidized SoxR is exposed to NO, two DNICs are formed in intact bacteria as well as in the purified enzyme as shown by EPR, dichroic spectral features, and EXAFS.^{59,151,152} Spin quantification with EPR spectroscopy suggests full conversion of the [2Fe–2S] cluster. However, mixed-valence SoxR exposed to NO for 1 min and then frozen at 77 K revealed a mixture of rRRE, RRE, and only a small amount of DNIC as product. In *E. coli* cells rRRE is quickly converted into stable protein-bound DNICs.¹⁵² In summary, rRRE and RRE can be considered intermediates on the reaction pathway to DNICs. It is noteworthy that *E. coli* has a repair system for the nitrosylated

iron-sulfur clusters in SoxR as the DNIC signal disappears after 15 min.^{59,151–153} The [2Fe–2S] cluster of spinach ferredoxin I reacts with NO and traces of O₂ to protein-bound RRE and DNIC, determined by IR spectroscopy.¹⁵⁴

[2Fe–2S] clusters with histidine ligation

A thiolate-bridged dinuclear dinitrosyl iron species (RRE) has been identified as main product of nitrosylation of Rieske-type [2Fe–2S] ferredoxin ToMOC protein beside a cysteine-bound DNIC as minor product.¹²⁷ NRVS spectroscopy indicated that the RRE is the main product of the nitrosylation. Also as indirect proof, the nitrosylation product was reduced with sodium dithionite (Na₂S₂O₄) and an EPR signal typical for a rRRE was detected ($g_{\perp} = 2.008$, $g_{\parallel} = 1.971$).

Recently, Ding and coworkers reported that the reduced CDGSH-type [2Fe–2S] clusters bind one NO molecule without degradation of the cluster (Figure 1.17).¹⁵⁵

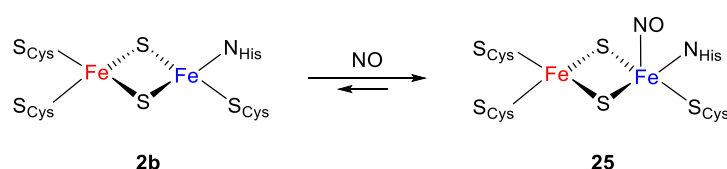


Figure 1.17. Nitrosylation of reduced CDGSH-type [2Fe–2S] cluster.

To conclude, the scientific community assumed that DNICs are the sole product of nitrosylation of Fe–S clusters since 1997 as they are easy to identify by EPR spectroscopy. However, spin quantification did not account for all the starting material. More recent investigations identified intermediates like RRE to play a major role, however the reaction pathway has not been fully elucidated to date. Mononitrosyl [2Fe–2S] clusters like **25** seem to be the exception as no other case is reported so far.

1.4.4 Nitrosylation of biomimetic iron-sulfur clusters

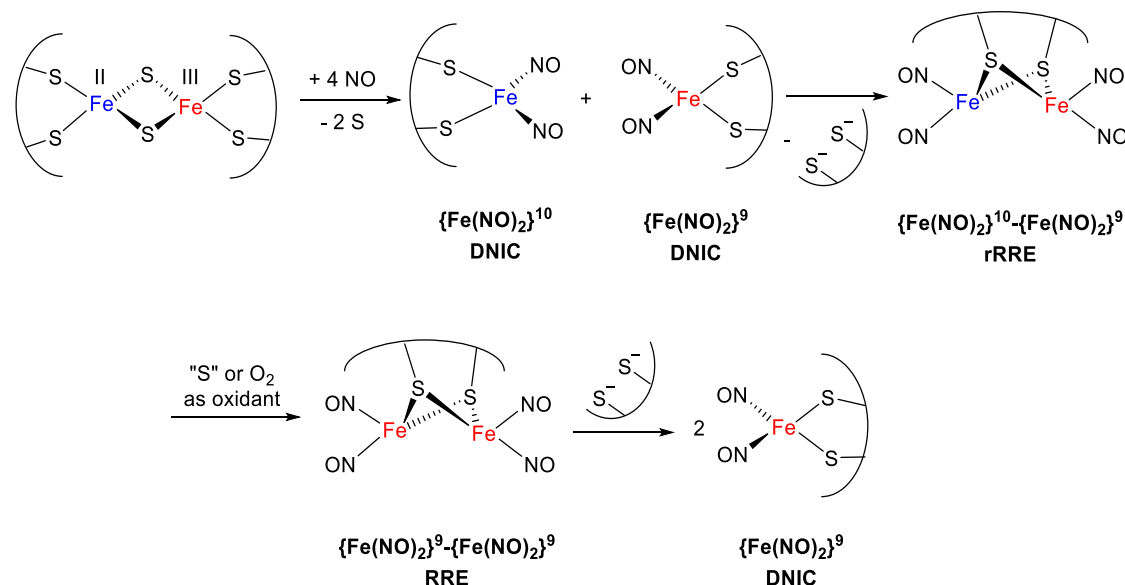
Peptide-based Fe–S clusters

Figure 1.18. Proposed mechanism for nitrosylation of mixed-valent bidentate-peptide bound $[2\text{Fe}-2\text{S}]$ cluster. The sequence of the bidentate-peptide is $(\text{Lys-Cys-(Ala)}_n\text{-Cys-Lys}, n=1-4)$.¹⁵⁶

Liaw and coworkers investigated the reaction pathway of the nitrosylation of Fe–S clusters. They expanded from low-molecular-weight biomimetic chemistry to the synthesis of peptide-based analogues, dubbed “bridged biological assemblies”. They synthesized peptide-bound DNICs and neutral/reduced RREs.¹⁵⁶ The products were water-soluble and characterized mainly by a combination of UV-vis and IR spectroscopy, aside from EPR, CD, ESI-MS and XAS. The peptides were either bidentate ($\text{Lys-Cys-(Ala)}_n\text{-Cys-Lys}, n=1-4$) or monodentate ($\text{Lys-Cys-Ala-Ala-Lys}$) binding via the cysteine residues. As a result, the chelating bidentate-cysteine-bound proteins stabilize the $\{\text{Fe}(\text{NO})_2\}^9$ moiety in DNICs and destabilize the RRE form, i.e. when cysteines are in close proximity on the peptide chain, DNICs are the main product of nitrosylation (Figure 1.18). Whether protein-bound RREs, rRREs or DNICs are formed, appears to rely heavily on the oxidation state of the iron and the chelating effect of the binding protein. The results rationalize why the nitrosylation of the mixed-valent Rieske-type $[2\text{Fe}-2\text{S}]$ cluster of the ToMOC protein¹²⁷ and of the mixed-valent $[2\text{Fe}-2\text{S}]$ cluster of SoxR¹⁵¹ have a different outcome. Based on their research, Liaw and coworkers proposed that the former yields unstable $\{\text{Fe}(\text{NO})_2\}^9$ and $\{\text{Fe}(\text{NO})_2\}^{10}$ monodentate-peptide-containing DNICs after reductive elimination of sulfur (Figure 1.19). The subsequently formed reduced RRE is oxidized to protein-bound RRE as the final product. The reaction mechanism of the latter resembles the one for

nitrosylation of mixed-valent $[2\text{Fe}-2\text{S}]$ clusters with coordination of bidentate-peptides (Figure 1.18). The chelating ligand stabilizes the $\{\text{Fe}(\text{NO})_2\}^9$ DNIC. On the other hand, $[4\text{Fe}-4\text{S}]$ clusters generate RREs regardless of the denticity of the peptide according to Liaw and coworkers. The hypothesis is supported by the reaction of $[4\text{Fe}-4\text{S}]$ regulatory enzymes, WhiD^{149} and Nsr^{150} with NO.

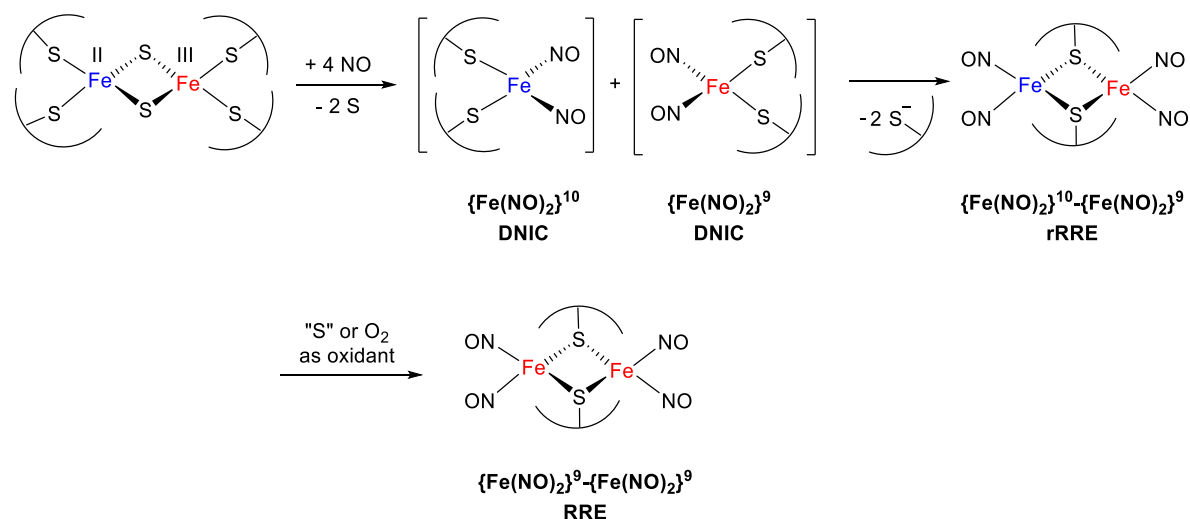


Figure 1.19. Proposed mechanism for nitrosylation of mixed-valent monodentate-peptide coordinated $[2\text{Fe}-2\text{S}]$ cluster.

The sequence of the monodentate-peptide is (Lys-Cys-Ala-Ala-Lys).¹⁵⁶

Interestingly, peptides with the sequence Lys-Cys-Ala-Ala-His-Lys served as monodentate ligands as well, binding only with the cysteine and not with the histidine residue. This supports the theory that the binding affinity for histidine is much lower than for cysteine. Liaw and coworkers investigated the binding affinity by a series of ligand displacement experiments and came to the sequence depicted in Figure 1.20.¹⁵⁷

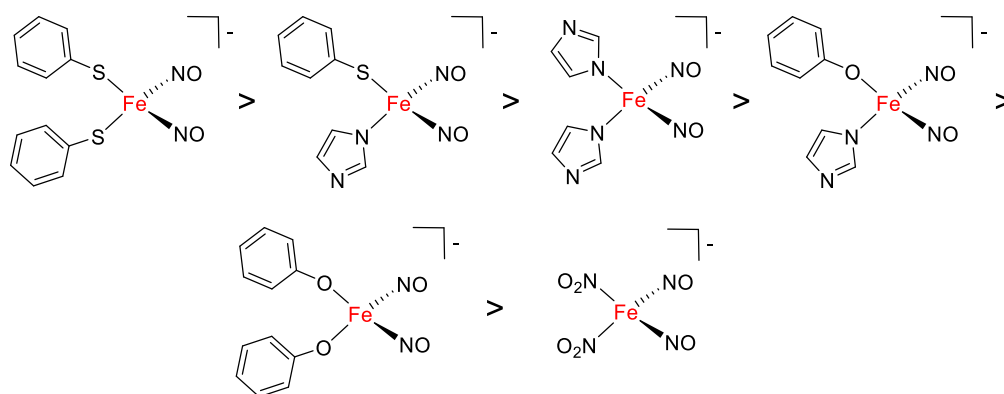
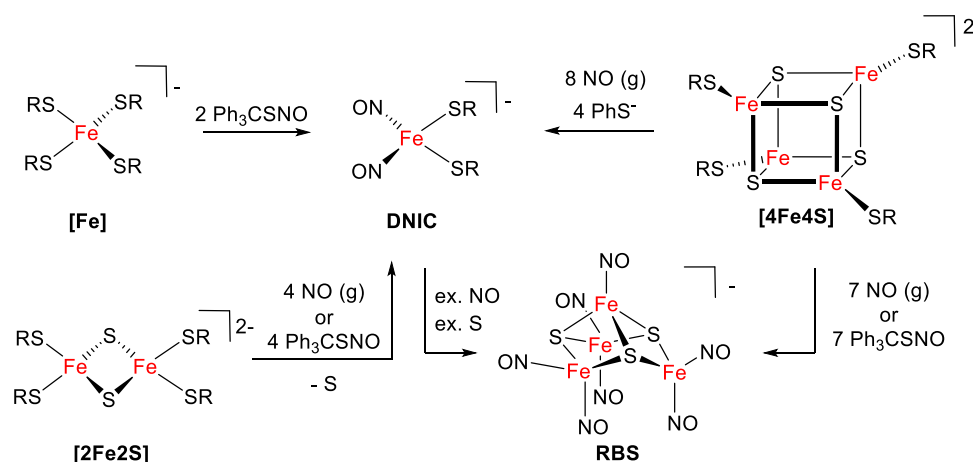


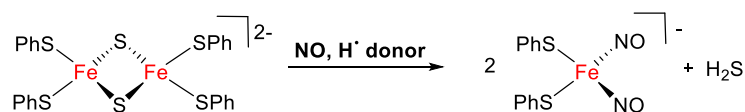
Figure 1.20. Relative binding affinity of nitrite, phenoxide, imidazolite and thiolate towards the $\{\text{Fe}(\text{NO})_2\}^9$ -moiety.¹⁵⁷

Low-molecular-weight Fe–S clusters

Figure 1.21. Nitrosylation of synthetic analogues of rubredoxins, [2Fe–2S] and [4Fe–4S] ferredoxins.¹⁵⁸

Stoichiometric nitrosylation of synthetic rubredoxin and ferredoxin model systems generates DNICs with concomitant reductive elimination of the bridging sulfide ligands as elemental sulfur (Figure 1.21).^{158–160} On the other hand, an excess of NO in the presence of elemental sulfur yields RBS.

When an H-atom donor such as PhSH or ^tBu₃PhOH is present during nitrosylation of the cluster $[Fe_2S_2(SPh)_4]^{2-}$, the products are thiolate-coordinated DNIC and PhSSPh or ^tBu₃PhO•, respectively (Figure 1.22). The bridging sulfide ligands are released as H₂S establishing a link between the two messenger molecules NO and H₂S.¹⁶¹

Figure 1.22. Reaction of [2Fe–2S] cluster with NO and H-atom donor generates DNIC and H₂S.

Nitrosylation of site-differentiated cluster $[Fe_4S_4(LS_3)X]^{15-}$ produces the $S = \frac{1}{2}$ nitrosyl-cluster $[Fe_4S_4(NO)_4]^-$ (**26⁻**) en route to the formation of diamagnetic RBS **18⁻** (Figure 1.23).¹⁶²

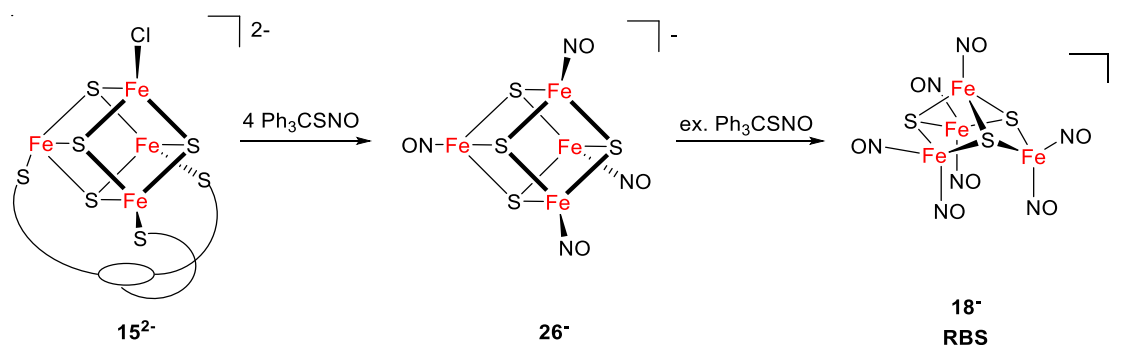


Figure 1.23. Nitrosylation of site differentiated [4Fe-4S] cluster.¹⁶²

1.5 Summary and conclusion

Fe-S clusters are essential in all three kingdoms of life. They are structurally diverse because smaller units can be assembled in a modular fashion to build large multinuclear clusters like in nitrogenases. Chemists have synthesized biomimetic analogues since the 1980s with exceptional contributions by Holm and coworkers. Natural and model clusters have been well investigated with respect to their structural and electronic properties. However, new binding motifs and functions are still discovered today, setting new goals and offering new challenges for the synthesis of appropriate model systems. Some natural Fe-S clusters are essential parts of enzymes with extraordinary capacities, i. a., in the defense against nitric stress.

NO reacts readily with Fe-S clusters to form iron-sulfur-nitrosyl complexes with concomitant degradation of the cluster core. The investigation of Fe-S cluster nitrosylation was conducted with real proteins (Ding, LeBrun, Liaw), peptide-bound (Liaw) and low-molecular-weight models (Lippard, Kim), just to mention a few protagonists in the field. Several iron-sulfur-nitrosyl species have been identified via IR, UV-vis, and NRVS spectroscopy, but the most common reaction products of the nitrosylation of [2Fe-2S] and [4Fe-4S] clusters are dinitrosyl iron species. To date, researchers concentrated on the reactivity of diferric [2Fe-2S] clusters and mostly neglected other physiologically relevant oxidation and protonation states. Investigations in that direction are still necessary to complete the picture.

2 Nitrosylation of [2Fe–2S] clusters in their diferric, mixed-valent, and protonated state

2.1 Introduction and objective

Our group published low-molecular-weight heteroleptic and homoleptic [2Fe–2S] model clusters for Rieske (**9**^{2-/3-}, **27**^{2-/3-}, **29**^{2-/3-})^{92,163–165} and mitoNEET proteins (**28**^{2-/3-} and **30**^{2-/3-}, Figure 2.1).^{166,167} All clusters have been spectroscopically characterized in their diferric (Fe^{III}/Fe^{III}) and mixed-valence (Fe^{III}/Fe^{II}) oxidation states. The proton-responsive nitrogen atoms in the backbone of the benzimidazolato moieties allow for protonation of the clusters **27**²⁻ – **30**²⁻ in contrast to **9**^{2-/3-}. The reactions of the homoleptic clusters **29** and **30** in different oxidation and protonation states with nitric oxide are presented in this chapter.

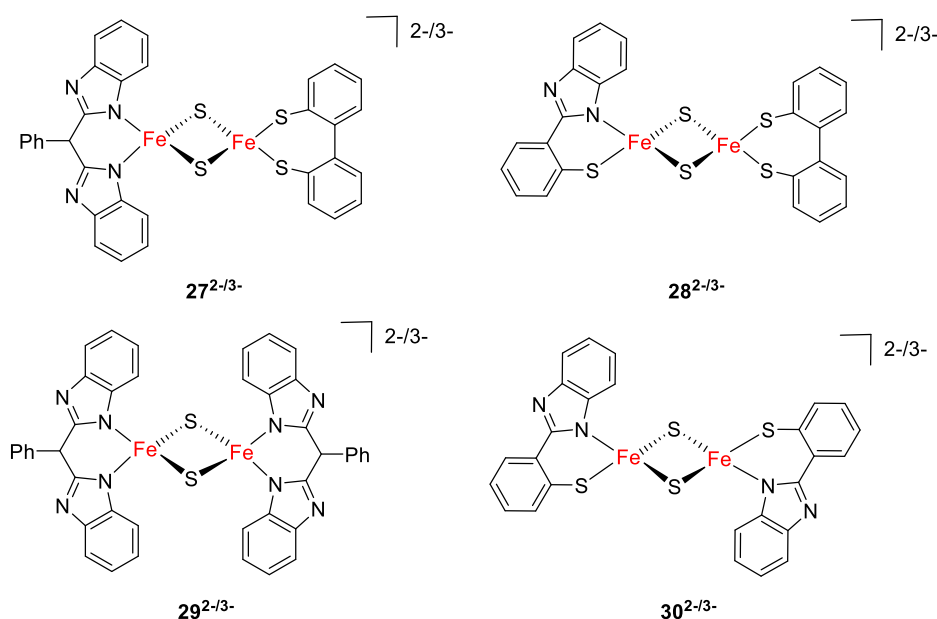


Figure 2.1. Rieske model (**27**^{2-/3-}),¹⁶⁴ mitoNEET model (**28**^{2-/3-}),¹⁶⁶ homoleptic Rieske model (**29**^{2-/3-}),^{163,165} homoleptic mitoNEET model (**30**^{2-/3-}).¹⁶⁷

Lippard and coworkers have reacted Rieske model **9**²⁻ with four equivalents of gaseous NO or Ph₃CSNO (Figure 2.2).¹⁶⁸ The *N,N*-bis(indolate) coordinated DNIC **31**⁻ was characterized by EPR, IR and Mössbauer spectroscopy, but the dithiolate coordinated DNIC **32**⁻ could not be isolated as it reacts further to form RBS. The same reactivity was observed for nitrosylation of the heteroleptic Rieske model **27**²⁻: Only the *N,N*-

2 Nitrosylation of [2Fe–2S] clusters in their diferric, mixed-valent, and protonated state

bis(benzimidazolato) coordinated DNIC was obtained from the reaction mixture.¹⁶⁹ Therefore, it was decided to discard the dithiolate ligands and focus on homoleptic, nitrogen-coordinated [2Fe–2S] clusters and their reactivity towards NO.

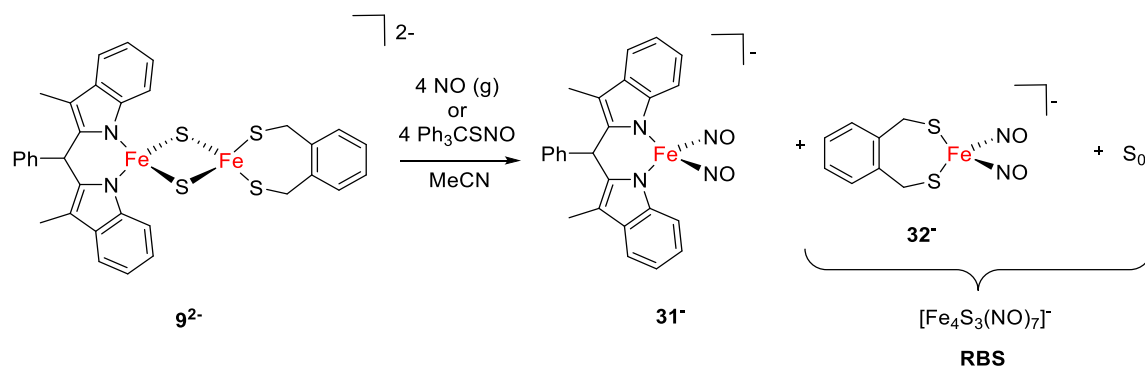
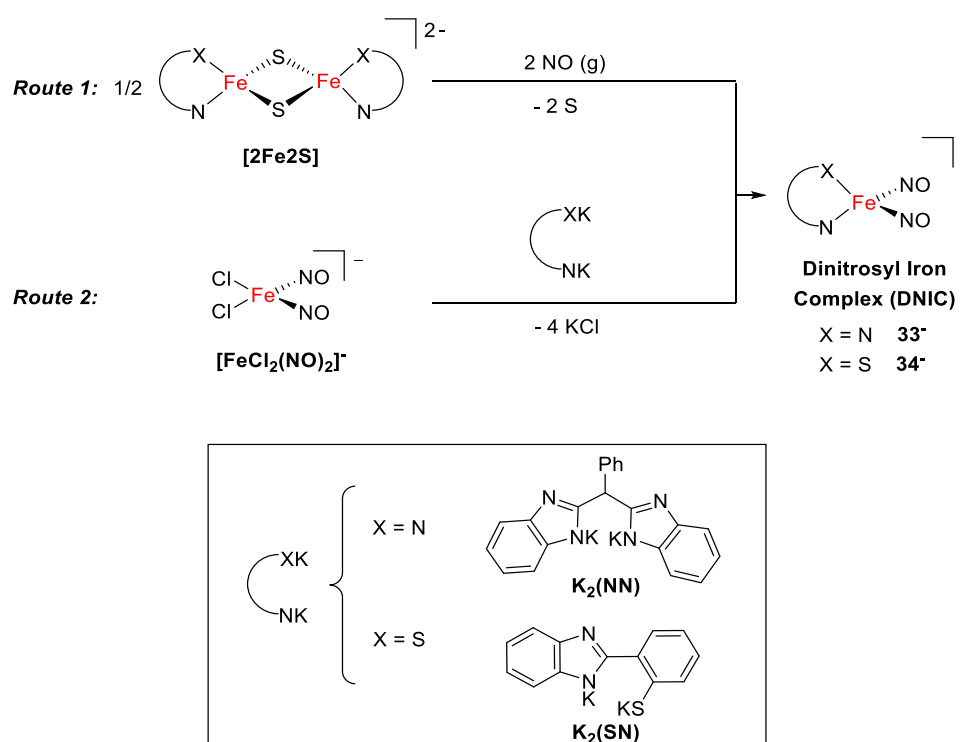


Figure 2.2. Nitrosylation of heteroleptic [2Fe–2S] by Lippard and coworkers.¹⁶⁸

2.2 Nitrosylation of diferric homoleptic coordinated [2Fe–2S] clusters

The DNICs were accessed following one of two synthetic strategies shown below (Figure 2.3). In *route 1* two equivalents of NO per iron ion were added into the headspace of a flask charged with a diferric [2Fe–2S] cluster in MeCN. Precipitated elemental sulfur was separated from the solution by washing with Et₂O. Subsequently, the DNIC was extracted with THF and precipitated from this solution by layering with hexane. *Route 2* started from a previously reported precursor [FeCl₂(NO)₂]⁻.¹⁶⁸ In a ligand exchange reaction with the potassium salt of the ligand K₂(NN) or K₂(SN) the respective DNIC **33**⁻ or **34**⁻ was formed. The latter reaction served to confirm the identity of the products obtained via *Route 1*.

Figure 2.3 Synthesis of DNIC **33**⁻ and **34**⁻ via two routes.

2.2.1 UV-vis and IR spectroscopy

Reaction of **29**²⁻ or **30**²⁻ with NO results in a color change from red to brown or purple to brown, respectively. The nitrosylation was monitored by UV-vis spectroscopy (Figure 2.4, a and c). The intense absorption of the sample bleaches until the sample exhibits a featureless spectrum. In the IR spectra, two new bands at 1780, 1714 cm⁻¹ for the N–O stretching frequencies of **33**⁻ and 1751, 1700 cm⁻¹ for **34**⁻ are detected (Figure 2.4, b and d). Care was taken to employ only four equivalents of NO gas because an excess of gas leads to the formation of Roussin's Black Salt (RBS). RBS is detected in the IR spectrum

if the reaction runs longer than 4 hours. Therefore, the reaction was stopped after 3 hours and residual solvent and NO was removed before work-up.

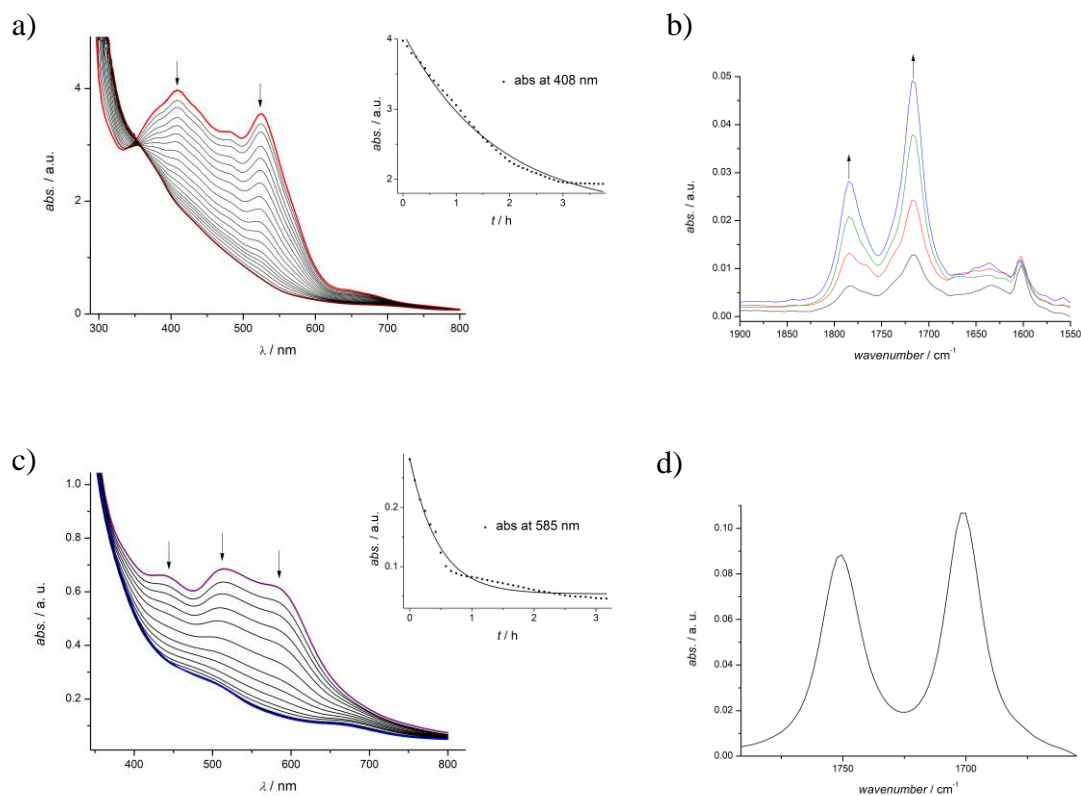


Figure 2.4. a) UV-vis spectra of the nitrosylation of **29**²⁻ taken every 5 min (Σ 180 min). The inserted graph depicts the decrease of the absorbance vs. time at 408 nm (Σ 225 min). An exponential fit gave an observed rate constant k_{obs} of $1.60 \times 10^{-4} \text{ s}^{-1}$ (†). b) Excerpt of the IR spectra from the reaction mixture in MeCN after 15, 30, 60, and 120 min. The arising bands at 1780 and 1714 cm⁻¹ are attributed to formation of **33**⁻. c) UV-vis spectra of the nitrosylation of **30**²⁻ taken every 10 min (Σ 150 min). The inserted graph depicts the decrease of the absorbance at 585 nm vs. time (Σ 223 min). An exponential fit gave an observed rate constant k_{obs} of $6.03 \times 10^{-4} \text{ s}^{-1}$ (†). d) Excerpt of the IR spectrum of the reaction mixture after 3 h in MeCN with bands at 1751 and 1700 cm⁻¹ indicating formation of **34**⁻. (†) The poor fits of the kinetic traces (inserts a and c) indicate a more complicated reaction sequence and rate law.

2.2.2 NMR spectroscopy

The ^1H NMR spectrum of the nitrosylation of 29^{2-} measured hourly for a total of 14 hours shows the decrease of the signals that are attributed to the diferric [2Fe–2S] cluster (Figure 2.5), but no new signals are detected. The signals of the reaction product DNIC 33^- is probably broadened beyond recognition due to its paramagnetic nature.

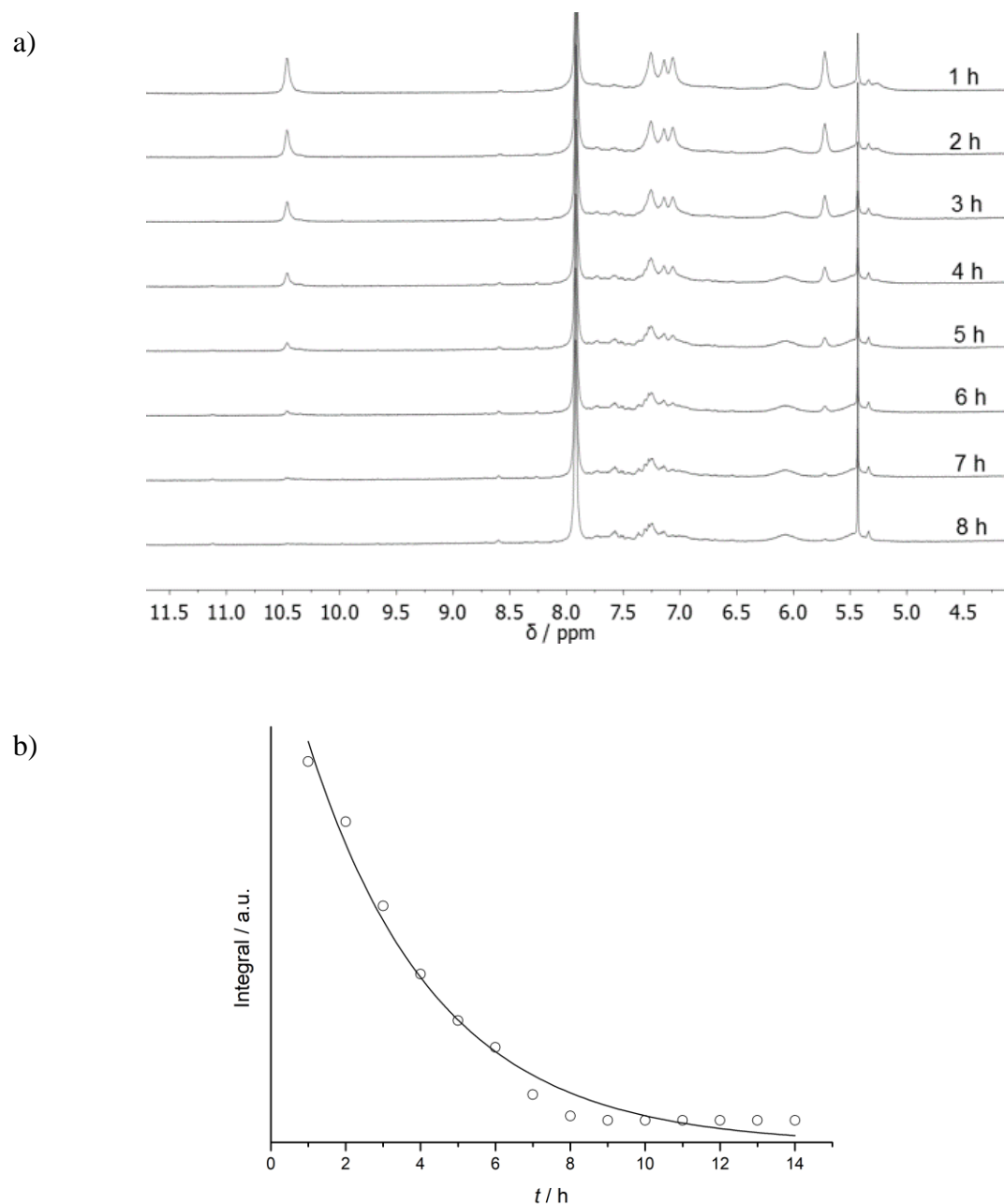


Figure 2.5. a) Hourly measured ^1H NMR spectra of nitrosylation of 29^{2-} in MeCN-d_3 , b) area of the integral at 10.46 ppm vs. time. An exponential fit gave an observed rate constant k_{obs} of $8.15 \times 10^{-5} \text{ s}^{-1}$. The poor fits of the kinetic trace indicate a more complicated reaction sequence and rate law.

2.2.3 Crystal structures of **33**[−] and **34**[−]

Various counter ions (NEt₄⁺, PPh₄⁺, PPN⁺) were tested to optimize the crystallization conditions of the reaction products **33**[−] and **34**[−]. All of them are non-coordinating hence only little effect can be seen on spectroscopic properties of the DNICs. Single crystals suitable for X-ray diffraction were obtained from a DCM solution of (PPN)**33** layered with hexane (Figure 2.6, a) or from diffusion of Et₂O in a MeCN solution of (PPN)**34** (Figure 2.6, b). Both anions crystalized with PPN⁺ as counter ion. Their core geometry is best described as strongly distorted tetrahedral which is induced by the strain of the chelating ligand. Bond distances of Fe–N(O) and N–O are in the usual range for anionic {Fe(NO)₂}⁹ complexes.¹⁷⁰ The nitrosyl moiety binds in a slightly bend fashion with angles ∠Fe–O–N between 157.3 and 171.3° (selected bond dimensions are given in Table 2.1 and Table 2.2).

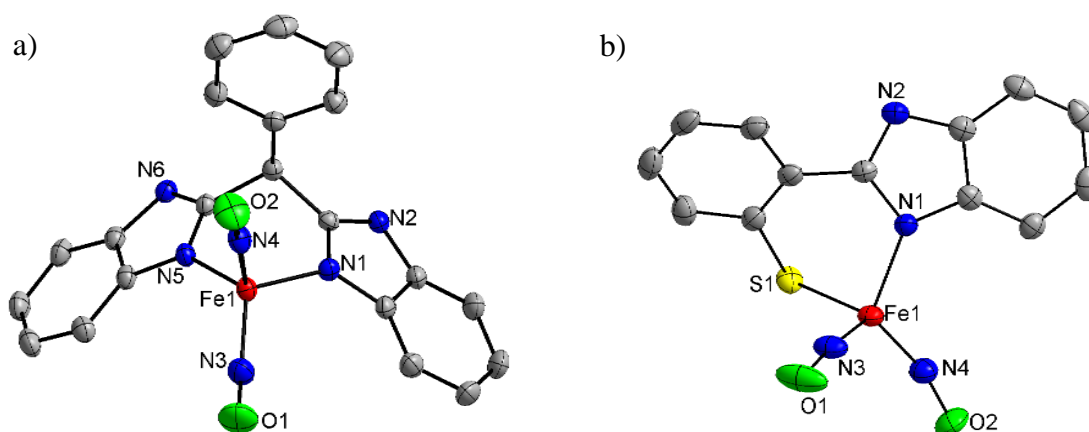


Figure 2.6. Molecular structures of the anion **33**[−] (a) and **34**[−] (b). The counter ions (PPN⁺) and hydrogen atoms are omitted for clarity. The thermal displacement ellipsoids are shown at 50% probability.

Table 2.1. Selected bond lengths (Å) of **33**[−] and **34**[−]:

	33 [−]	34 [−]
Fe(1)–N(4)	1.683(2)	1.681(2)
Fe(1)–N(3)	1.701(3)	1.676(2)
Fe(1)–N(1)	1.979(2)	1.970(2)
Fe(1)–N(5)	1.996(2)	—
Fe(1)–S(1)	—	2.2544(8)
O(1)–N(3)	1.169(6)	1.171(3)
O(2)–N(4)	1.165(9)	1.185(3)

Table 2.2. Selected angles (°) of **33**⁻ and **34**⁻:

N(1)–Fe(1)–N(5)	93.75(9)	—
N(4)–Fe(1)–N(5)	108.80(11)	—
N(4)–Fe(1)–N(3)	111.52(13)	113.70(12)
N(4)–Fe(1)–N(1)	111.77(10)	117.04(10)
N(3)–Fe(1)–N(1)	111.90(11)	111.34(10)
N(3)–Fe(1)–N(5)	117.92(10)	—
N(3)–Fe(1)–S(1)	—	105.36(10)
N(4)–Fe(1)–S(1)	—	112.76(8)
N(1)–Fe(1)–S(1)	—	94.51(6)
O(1)–N(3)–Fe(1)	157.3(3)	169.1(2)
O(2)–N(4)–Fe(1)	171.3(3)	160.5(2)

2.2.4 EPR and Mössbauer spectroscopy

EPR spectroscopy confirms an $S = \frac{1}{2}$ ground state and a rhombic EPR signal points towards a distorted coordination geometry around the metal ion. The EPR spectrum of **33**⁻ recorded at 160.4 K in frozen solution in THF gave an anisotropic g -value of [2.068, 2.039, 2.014] (Figure 2.7, a). The g_{av} of 2.040 compares well to literature.¹⁶⁸ The EPR spectrum of **34**⁻ gave an anisotropic g -value of [2.055, 2.038, 2.015] at 145 K in frozen solution in THF ($g_{av} = 2.034$, Figure 2.7, b). As a conclusion, the **NN** versus **SN** capping ligands have only a minor influence on the electronic state of the iron ion. This statement is supported by Mössbauer spectroscopy as both DNICs give similar parameters. Two doublets were fitted to the experimental data of a solid sample of DNIC **33**⁻ (Figure 2.7, c). The main signal (red) was assigned to **33**⁻ and the minor signal (blue) to an Fe^{II} impurity. The isomer shift and quadrupole splitting of **33**⁻ at 80 K are 0.28 mm s⁻¹ and 0.99 mm s⁻¹, respectively. **34**⁻ shows an isomer shift of 0.18 mm s⁻¹ and a quadrupole splitting of 0.90 mm s⁻¹ in frozen THF solution (Figure 2.7, d). A UV-vis spectrum of crystalline material redissolved in THF displays bands at 430 and 705 nm for **33**⁻ and 470, 545, and 685 for **34**⁻ with low ϵ_{rel} of around 300 M⁻¹cm⁻¹ (Figure 2.7, e and f). ESI-MS and ¹H NMR spectroscopy appear to be unsuitable methods for characterization of **33**⁻ and **34**⁻, efforts to obtain good spectra have been unsuccessful.

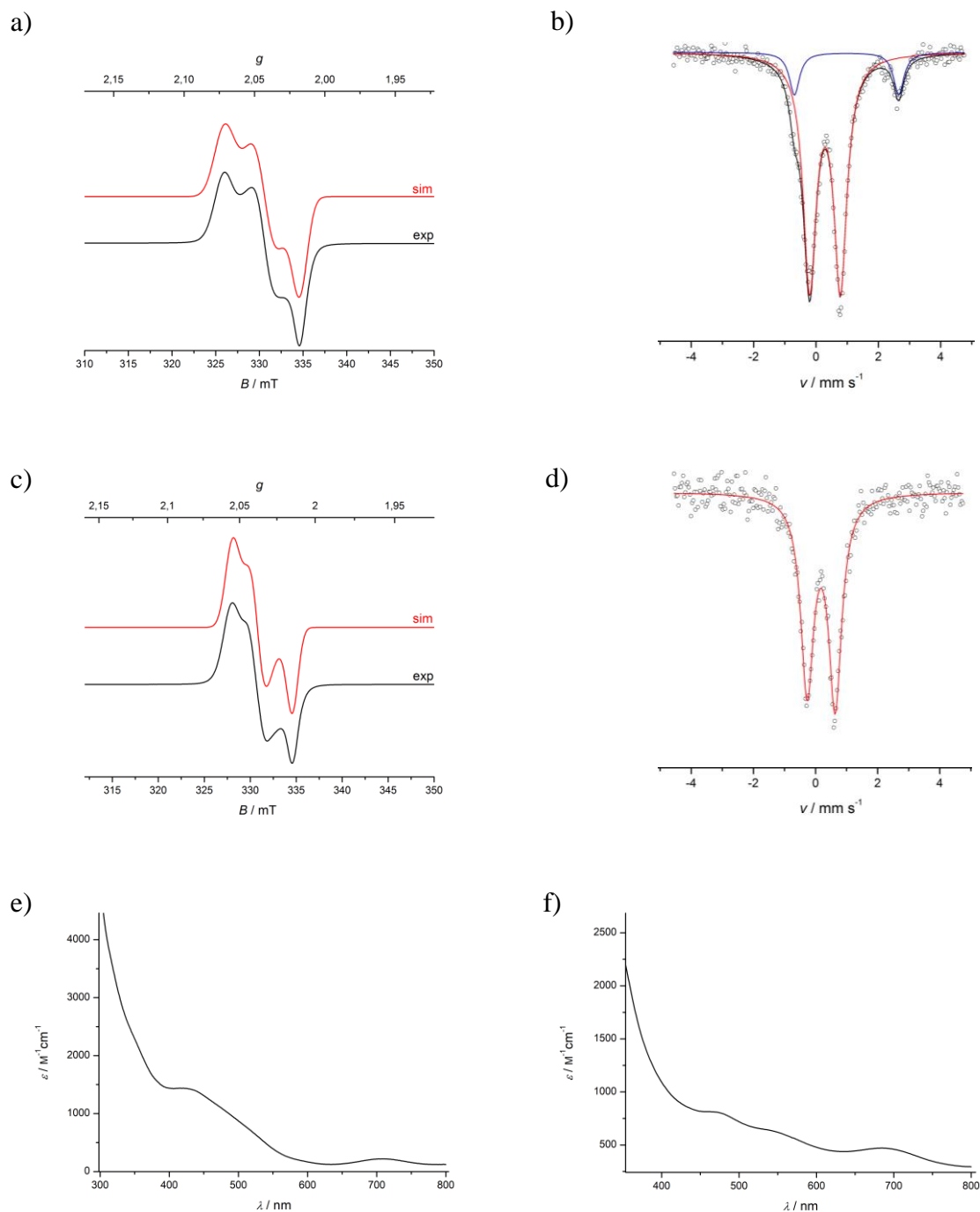


Figure 2.7. a) X-band EPR spectrum of **33**⁻ recorded at 160.4 K in frozen solution (THF, black). The red line is a powder simulation with $g = (2.068, 2.039, 2.014)$. b) Zero-field Mössbauer spectrum of **33**⁻ at 80 K. The solid lines represent the result of a fit with Lorentzian doublets (red for **33**⁻ and blue for an impurity). Summation of the two subspectra affords the black line. c) X-band EPR spectrum of **34**⁻ recorded at 145 K in frozen solution (THF, black). The red line is a powder simulation with $g = (2.055, 2.038, 2.015)$. d) Zero-field Mössbauer spectrum of **34**⁻ in frozen THF solution at 80 K, e) UV-vis spectrum of **33**⁻ in THF at rt, f) UV-vis spectrum of **34**⁻ in THF at rt.

2.3 Nitrosylation of mixed-valent [2Fe–2S] clusters

2.3.1 Nitrosylation of 29^{3-}

2.3.1.1 UV-vis spectroscopy

When a solution of the reduced cluster 29^{3-} in MeCN was exposed to 5 equivalents of NO, three distinct reaction steps can be identified by UV-vis spectroscopy (Figure 2.8). During the first 30 min, the bands at 408 and 528 nm increase and an intermediate 1 is formed (Figure 2.8, a). These two bands are indicative for the diferric cluster 29^{2-} . Intermediate 1 is stable for approximately 30 min. Then the band at 528 nm decreases in intensity while the other maximum shifts from 408 to 419 nm suggesting that a second intermediate is formed (Figure 2.8, b) which ultimately decomposes over several hours (Figure 2.8, c).

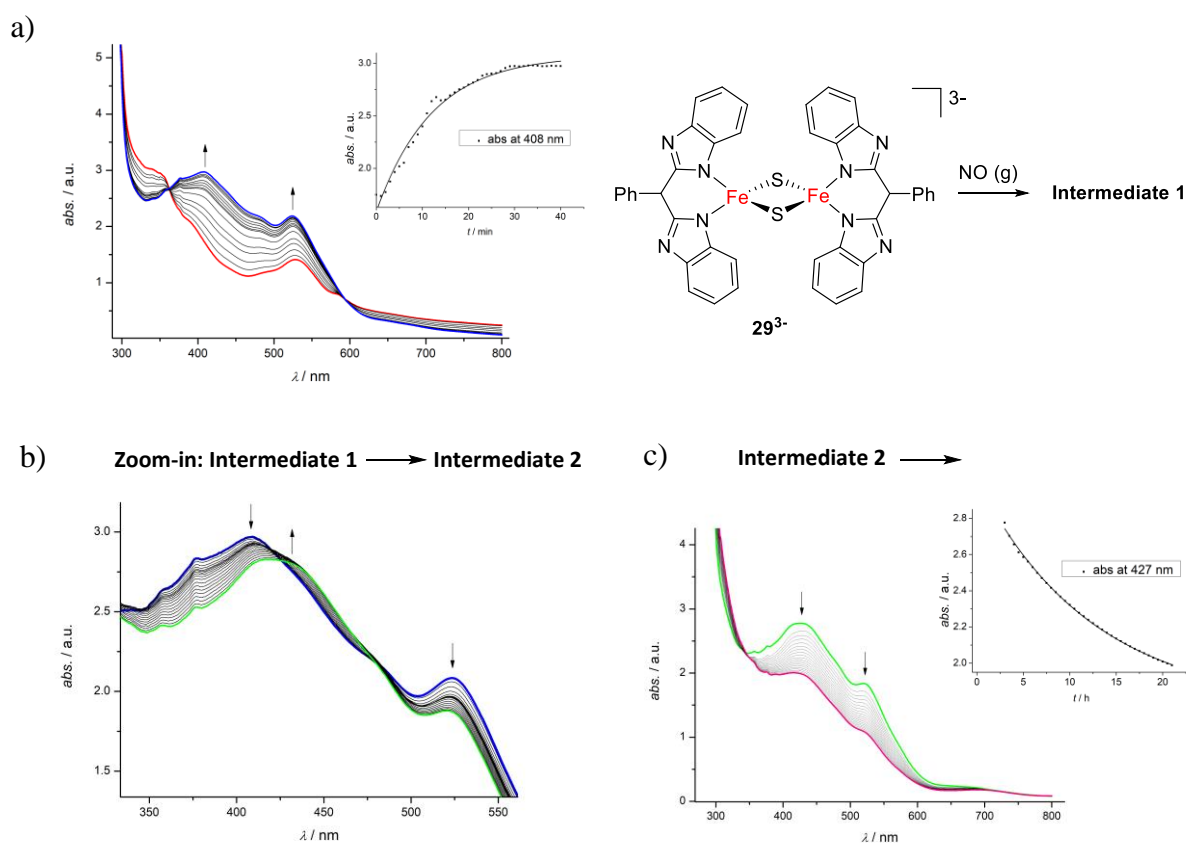


Figure 2.8. a) First step of nitrosylation of 29^{3-} monitored by UV-vis spectroscopy (Σ 40 min). The inserted graph depicts absorbance at 408 nm vs. time. An exponential fit gave a observed rate constant k_{obs} of $1.38 \times 10^{-3} \text{ s}^{-1}$. The poor fit of the kinetic trace indicates a more complicated reaction sequence and rate law. b) Excerpt of UV-vis spectra measured after 50 – 140 min reaction time: Shift of maximum from 408 to 419 nm. c) Degradation of intermediate 2 monitored by UV-vis spectroscopy over the course of 18 h. The inserted graph depicts absorbance at 427 nm vs. time. An exponential fit gave an observed rate constant k_{obs} of $2.24 \times 10^{-5} \text{ s}^{-1}$.

Conducting the reaction at lower temperature ($-30\text{ }^{\circ}\text{C}$) does not affect the reaction pattern monitored by UV-vis spectroscopy or the timescale of the reaction, however, addition of only one equivalent of NO has a strong effect (Figure 2.9). For the first 15 min only a small change of the UV-vis spectrum is detected. Therefore, the first three data points are excluded from the exponential fit in the inserted graph. After this induction period, the reaction to intermediate 1 takes twice as long and the rate constant is almost an order of magnitude smaller (Figure 2.9, a). Under these conditions, intermediate 1 is stable for almost 10 hours before it starts to decay. When the nitrosylation is conducted with 5 equivalents of NO, intermediate 1 is only stable for approximately one hour and transforms into intermediate 2. Formation of intermediate 2 is not detected with only one equivalent of NO. Instead, the overall absorption decreases over several hours (Figure 2.9, b). The absence of any DNIC product is confirmed by IR spectroscopy of the reaction mixture after treatment with one equivalent of NO.

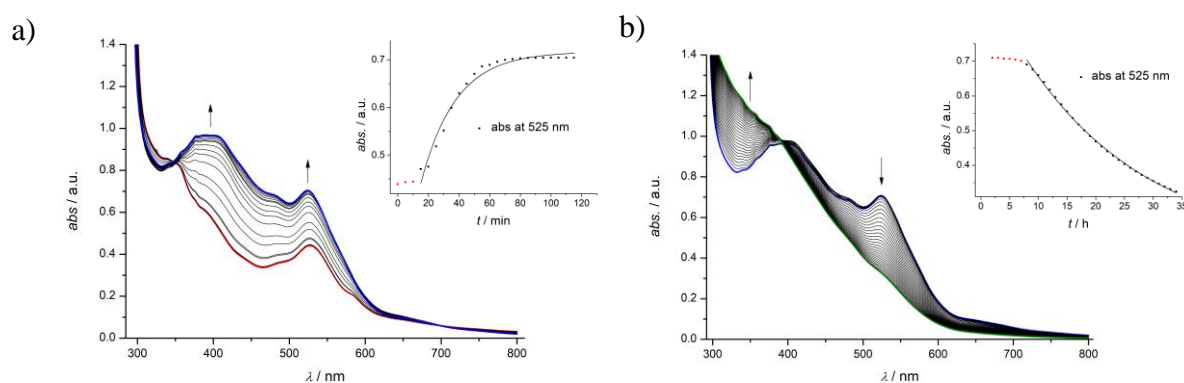


Figure 2.9. UV-vis spectroscopy of nitrosylation with only one equivalent NO. a) First two hours of reaction (24 x 5 min). Insert: exponential fit of the absorption at 525 nm vs. time gives a rate constant k_{obs} of $7.33 \times 10^{-4} \text{ s}^{-1}$ (†). b) 2–34 h after addition of NO (spectrum each hour). Insert: exponential fit of the absorption at 525 nm vs. time gives a rate constant k_{obs} of $1.27 \times 10^{-5} \text{ s}^{-1}$ (†). (†) Data points in red are excluded from the fitting process. The poor fits of the kinetic traces (inserts a and b) indicate a more complicated reaction sequence and rate law.

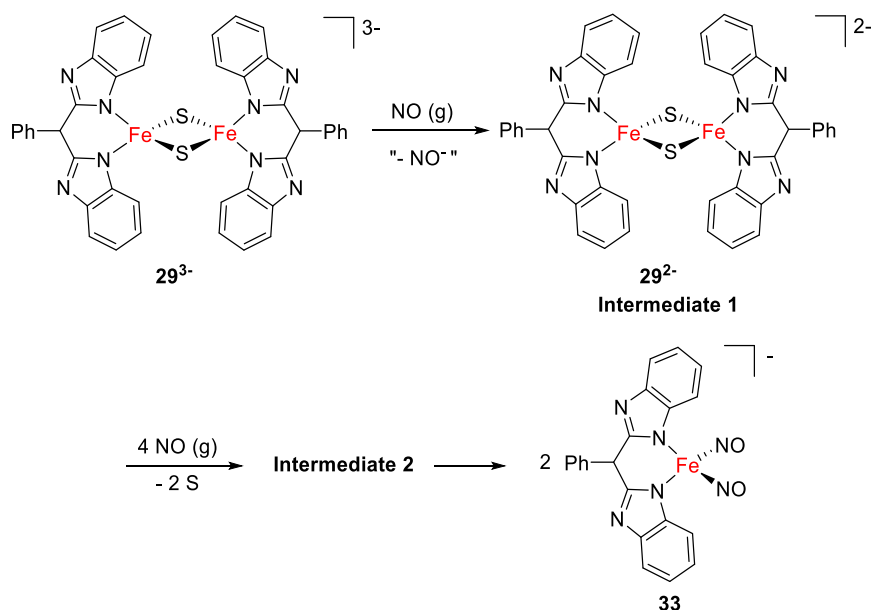


Figure 2.10. Proposed reaction pathway of the nitrosylation of the mixed-valent cluster 29^{3-} .

Taken all the information from the UV-vis measurements into consideration, a reaction pathway with two intermediates is proposed (Figure 2.10). Intermediate 1 can be identified as diferric 29^{2-} from the assignment of the bands in the UV-vis spectrum. It is formed via oxidation of mixed-valence 29^{3-} by one equivalent of NO . The identity of intermediate 2 cannot be deduced from UV-spectroscopy only.

2.3.1.2 IR spectroscopy and ESI-MS of intermediate 1

An IR spectrum was measured of the reaction mixture after 30 min at $-30\text{ }^\circ\text{C}$ and subsequent removal of the solvent (Figure 2.11, a). The spectrum of the redissolved residue in THF confirms that intermediate 1 corresponds to 29^{2-} . Most of the signals can be assigned to diferric 29^{2-} (red) or residual 29^{3-} (orange). Both give similar signals in the IR spectrum. In the region where usually nitrosylized products (green rectangle) resonate, peaks were detected at 1665 and 1683 cm^{-1} with high intensity and 1745 cm^{-1} with low intensity. The signal at 1745 cm^{-1} may belong to some RBS. However, ν_{NO} of DNIC 33^- is not found. On the other hand, DNIC 33^- is clearly the main product in the IR spectrum of the reaction mixture after 3.5 hours (Figure 2.11, b). ESI-MS confirms that the cluster core is still unimpaired after a reaction time of 30 min (Figure 2.12), whereas the signals characteristic for 29^{2-} disappeared in the sample taken after 3.5 hours of reaction time.

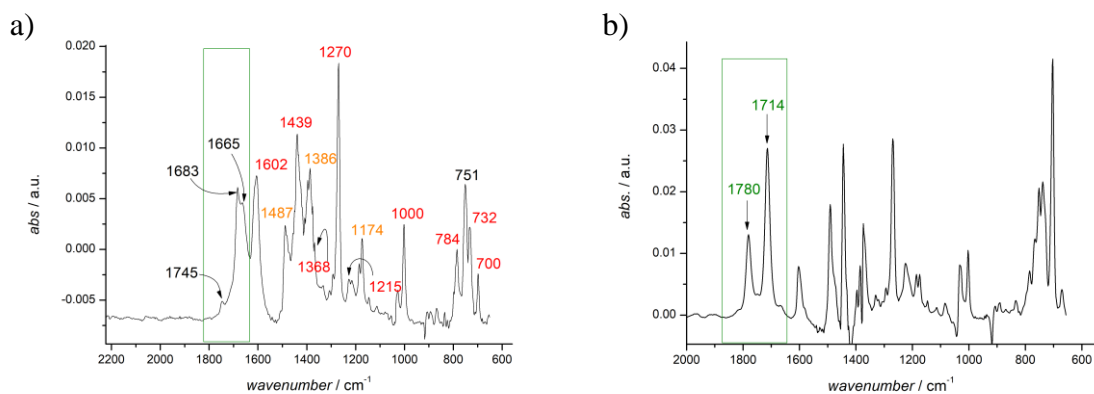


Figure 2.11. IR spectrum of reaction mixture after a) 30 min. and b) 3.5 hrs. The green rectangle encompasses the region where ν_{NO} are usually found. Numbers in green mark NO-stretching frequencies from DNIC **33**⁻ (1780, 1714 cm^{-1}) in MeCN, numbers in red mark diferric **29**²⁻ and in orange **29**³⁻. Numbers in black are not assigned.

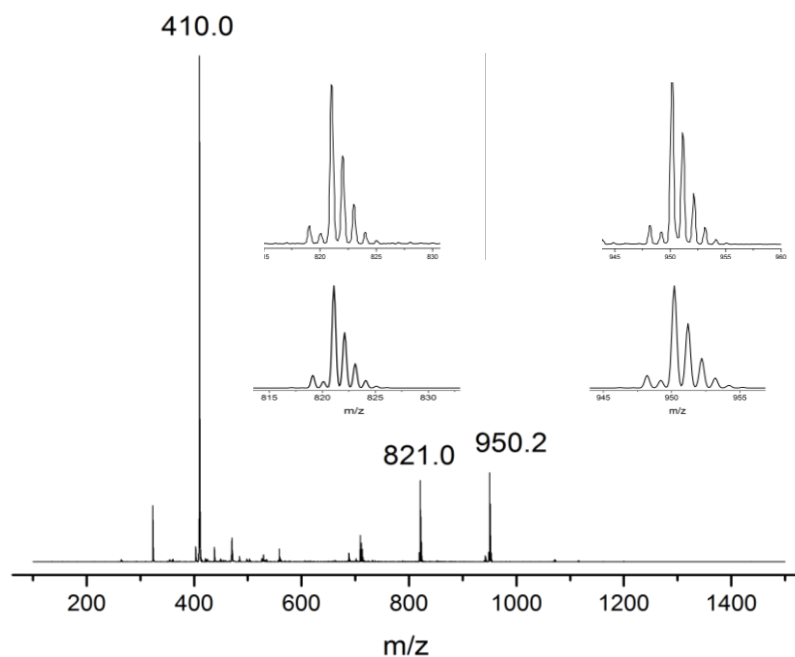


Figure 2.12. ESI(-)MS of intermediate 1 in MeCN. The inserts depict experimental and simulated data of peak $[\text{M}-\text{NEt}_4]^-$ (950.2 m/z) and $[\text{M}-2\text{NEt}_4+\text{H}]^-$ (821.0 m/z). 410 m/z corresponds to $[\text{M}-2\text{NEt}_4]^{2-}$.

2.3.1.3 NMR spectroscopy

A solution of **29**³⁻ in DMF- d_7 was frozen and the inert gasphase was replaced with a mixture of NO and argon that equaled 4 equivalents of NO with respect to **29**³⁻. The solution was thawed and ^1H NMR spectra were recorded over a period of 120 min (10×2 min and 20×5 min). A selection of spectra is depicted in Figure 2.13. The signal intensity for **29**³⁻ decreases within 20 min while a new set of signals characteristic for **29**²⁻ emerges. The

integrals of the peaks at 11.78 (indicative for 29^{3-}) and also 10.46 ppm (indicative for 29^{2-}) were divided by the sum of both integrals in order to obtain their ratio which was plotted against the time (Figure 2.14). The first data points are deduced from the first spectrum taken. As they do not depict a ratio 1:0 (29^{3-} : 29^{2-}) it is obvious that the first few minutes of the reaction were not captured due to the set-up (e.g. time necessary for shimming). The first spectrum is defined as $t = 0$.

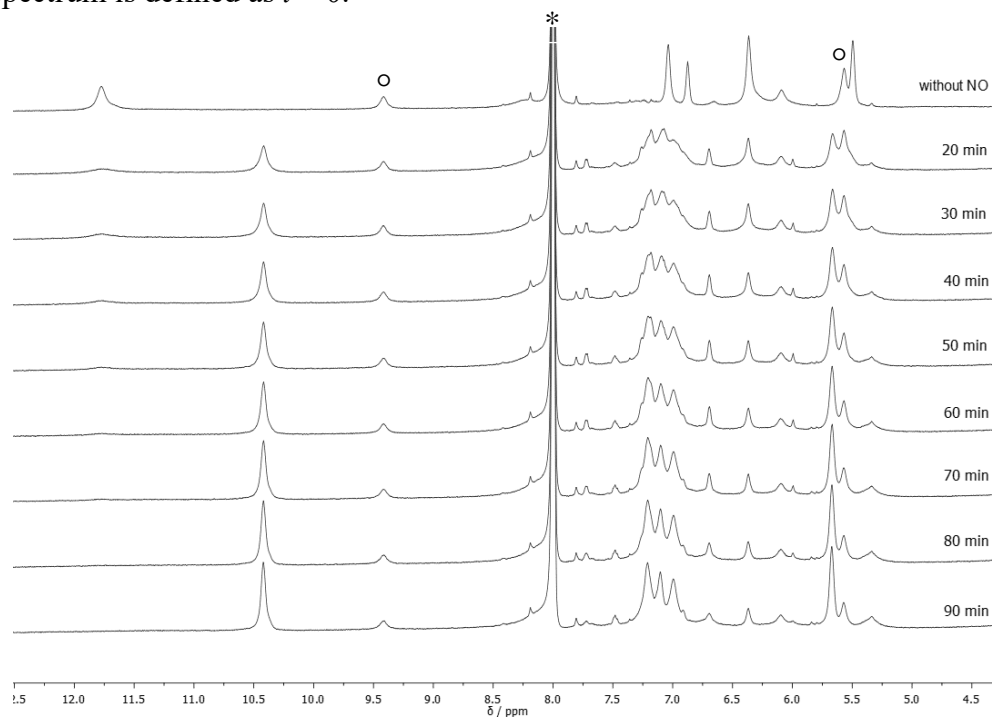


Figure 2.13. Nitrosylation of mixed-valent 29^{3-} monitored by ^1H NMR spectroscopy. Depicted is a selection of spectra within the first 90 min of the reaction. * residual DMF. ° unknown impurity.

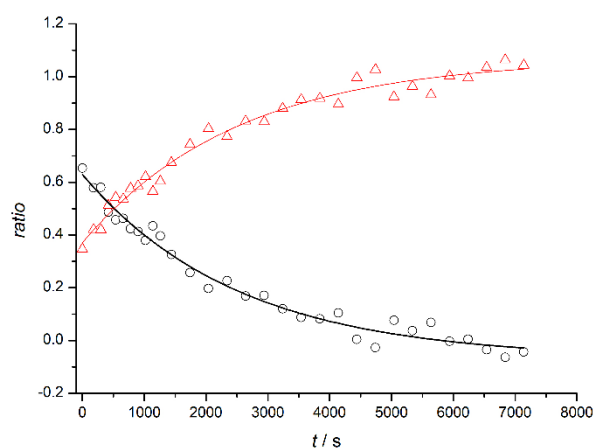


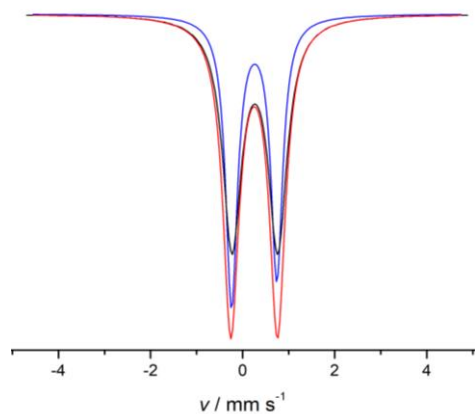
Figure 2.14. Ratio of integral for peak at 11.78 ppm (black circles) and integral for peak at 10.46 ppm (red triangles). An exponential fit gave reaction rate k_{obs} of $3.98 \times 10^{-4} \text{ s}^{-1}$.

The oxidation of $\mathbf{29}^{3-}$ appears to be one magnitude slower in the NMR tube ($k_{\text{obs}} = 3.98 \times 10^{-4} \text{ s}^{-1}$) than in the UV-vis cuvette ($k_{\text{obs}} = 1.38 \times 10^{-3} \text{ s}^{-1}$). The reaction conditions seem to differ greatly in a NMR tube and a UV-vis cuvette. The substrate concentration is significantly higher for NMR spectroscopy than UV-vis spectroscopy. According to this observation, pseudo-first order kinetics are not applicable for this reaction. Another reason for differing k_{obs} could simply be different diffusion coefficient of the gaseous NO dependent on the shape of the glassware.

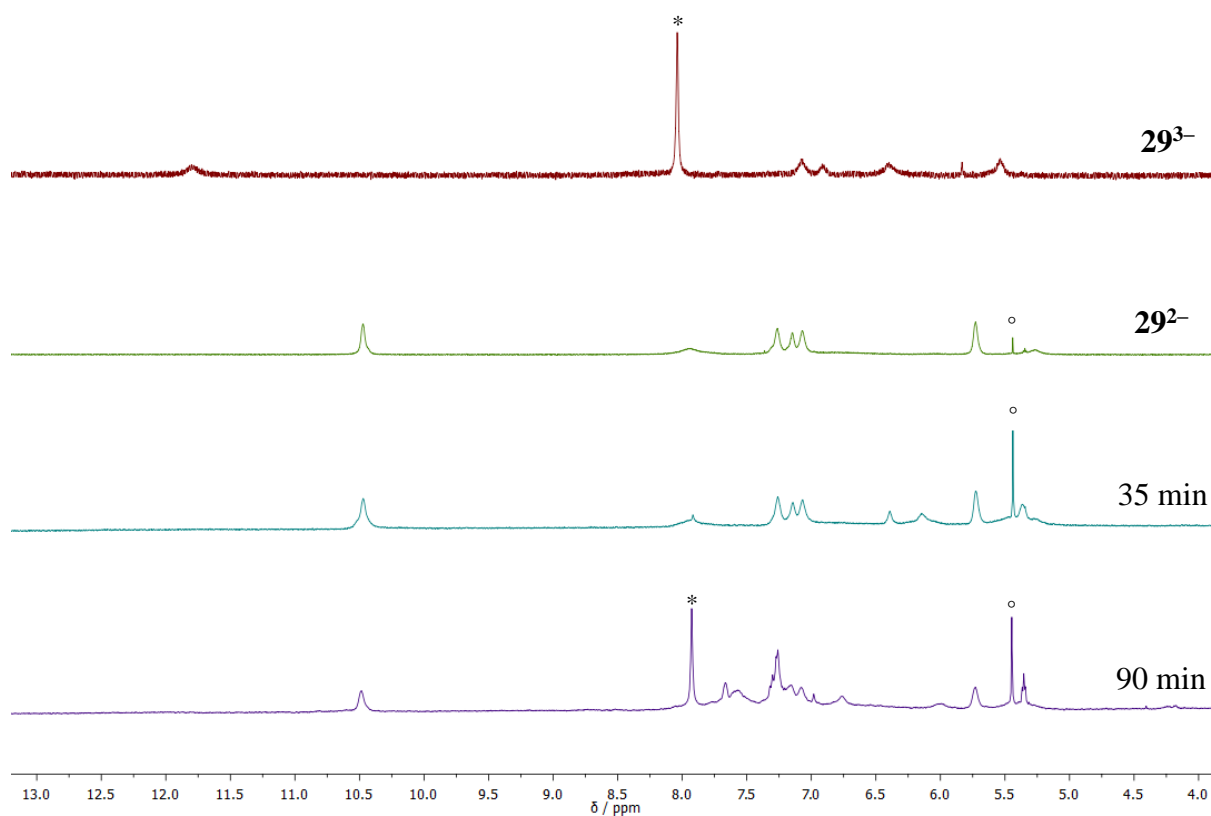
2.3.1.4 Mössbauer spectroscopy of intermediate 1 and 2

Intermediate 1 (int. 1) was isolated by stopping the reaction of $\mathbf{29}^{3-}$ with 5 equivalents of NO after 35 min by removal of solvent and excess NO under reduced pressure. UV-vis spectroscopy confirmed the formation of int.1 ($=\mathbf{29}^{2-}$) (Figure 8.1 in appendix). The Mössbauer spectrum of the obtained solid was measured at 80 K and 6 K (Figure 8.2 in appendix). A more dissolved spectrum at low temperature (6 K) allowed for easier and more precise fitting of the data. The main signal at 6 K has an isomer shift of 0.26 mm s^{-1} and a quadrupole splitting of 1.00 mm s^{-1} indicative of an Fe^{III} species. Other iron-species are detected with a transmission of $<0.5\%$. The experimental parameters of the main signal allow an assignment to either the diferric cluster $\mathbf{29}^{2-}$ or DNIC $\mathbf{33}^-$ (Table 2.3). However, an IR spectrum of the reaction solution does not show the typical nitrosyl bands at 1780 and 1714 cm^{-1} (Figure 2.11), which supports the formation of $\mathbf{29}^{2-}$. Affirmation for $\mathbf{29}^{2-}$ to be the main product is found in the NMR spectrum of the sample after 35 min (Figure 2.16, *cf.* green vs. blue line).

Intermediate 2 was captured with a $33 \text{ \% } ^{57}\text{Fe}$ -enriched sample (Figure 8.3 in appendix). The reaction was stopped after 90 min as the UV-vis spectrum showed full conversion to intermediate 2 (Figure 8.4 in appendix). The Mössbauer spectrum of the frozen solution and a ^1H NMR spectrum of the sample feature the diferric $\mathbf{29}^{2-}$ cluster as main species (Figure 8.3 in the appendix and Figure 2.16 below, violet line). In conclusion, the [2Fe–2S] core remains intact during transformation of intermediate 1 to 2. The difference in the UV-vis spectra between both species must be assigned to a peripheral change on the ligand of the cluster as the Mössbauer parameters of $\mathbf{33}^-$ and $\mathbf{29}^{2-}$ do not differ greatly (Figure 2.15). A pentacoordinated intermediate in which NO binds to the iron ion can be excluded according to Mössbauer spectroscopy.

Table 2.3. Mössbauer parameters of compounds relevant to nitrosylation of 29^{3-} with 5 eq. NO.

	$\delta / \text{mm s}^{-1}$	$\Delta E_Q / \text{mm s}^{-1}$	ref.
29^{3-} (Fe ^{III})	0.47	1.41	165
(Fe ^{II})	0.69	2.90	
29^{2-}	0.25	0.98	165
int. 1	0.26	1.00	
int. 2	0.27	0.99	
33^{-}	0.29	0.99	

Figure 2.15. Overlay of Mössbauer fits of diferric 29^{2-} (80 K, blue) and of the reaction mixture of 29^{3-} with 5 eq. NO after 30 min (**int. 1**, 6 K, red) and 90 min (**int. 2**, 80 K, black).Figure 2.16. ^1H NMR spectrum of mixed-valent 29^{3-} (red in DMF-d_7), diferric 29^{2-} (green in MeCN-d_3), reaction stopped after 35 min by removal of the solvent *in vacuo* (blue in MeCN-d_3), and reaction stopped after 90 min by removal of the solvent *in vacuo* (violet in DMF-d_7). (*) marks the residual DMF solvent peak and (°) marks DCM.

2.3.2 Nitrosylation of 30^{3-}

When a solution of 30^{3-} in MeCN is exposed to 5 equivalents of NO the absorbance in the UV-vis spectra increases until a maximum is reached after 15 min (Figure 2.17, a). The resulting spectrum indicates the formation of diferric 30^{2-} with bands at 434, 512, and 585 nm and a purple colored solution. Then the absorbance decreases over several hours indicating the degradation of the [2Fe–2S] core (Figure 2.17, b). Finally, a brown solution is obtained in which the typical nitrosyl stretching frequencies of 34^- are found in the IR spectrum at 1740 and 1694 cm^{-1} (Figure 2.17, c). These observations support a mechanistic scenario in which 30^{3-} is oxidized to 30^{2-} by a first equivalent of NO and subsequently 34^- is formed (Figure 2.18). The reaction pathway is more straight forward in comparison to nitrosylation of 29^{3-} (Chapter 2.3.1) as only one intermediate is formed, namely diferric cluster 30^{2-} .

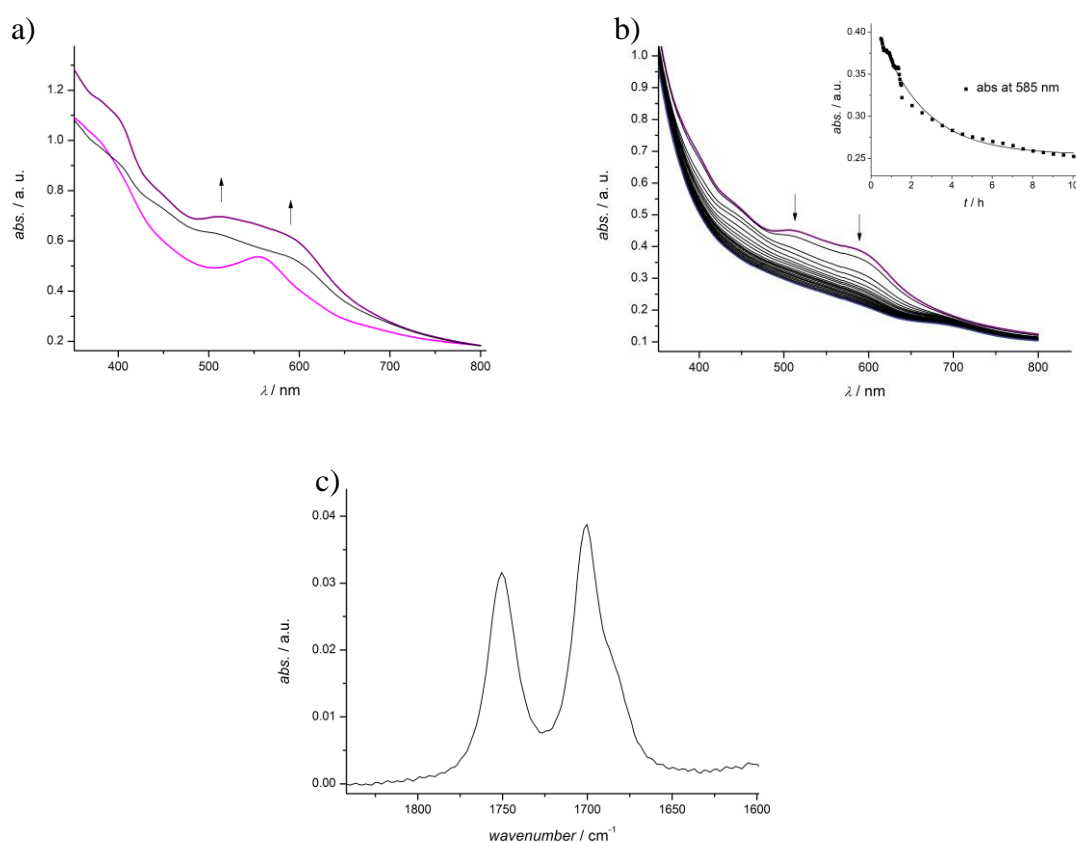


Figure 2.17. UV-vis spectra of nitrosylation of 30^{3-} a) 0–15 min (spectrum taken every 5 min) and b) 30 min–10 h (spectrum taken every 30 min). The inserted graph depicts the absorbance at 585 nm vs. time. An exponential fit gave a rate constant k_{obs} of $1.25 \times 10^{-4} \text{ s}^{-1}$. The poor fit of the kinetic trace indicates a more complicated reaction sequence and rate law. c) Excerpt of the IR spectrum of the reaction mixture after 5 h. The bands can be assigned to DNIC 34^- .

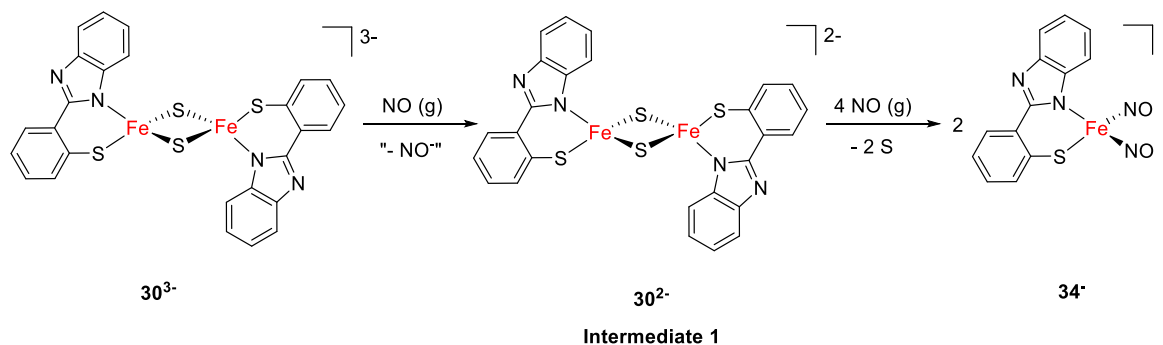


Figure 2.18. Proposed reaction pathway for nitrosylation of mixed-valent cluster 30^{3-} with 5 equivalents of NO.

2.4 Nitrosylation of protonated clusters $29H_2$ and $30H_2$

2.4.1 Reaction of $29H_2$ with NO

Full protonation of the proton responsive ligands from 29^{2-} can be achieved by addition of 7 equivalents of the acid 2,6-dimethylpyridinium tetrafluoroborate (DMPH). The product is a doubly protonated cluster $29H_2$ with concomitant tautomerism of the proton of the methine bridge (Figure 2.19).¹⁶³ Protonation of 29^{2-} is accompanied by rise of a characteristic, prominent band at about 380 nm ($\epsilon = 64000 \text{ M}^{-1}\text{cm}^{-1}$) in the UV-vis spectrum.

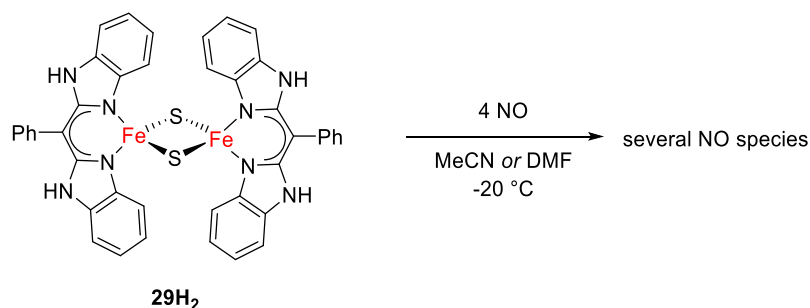


Figure 2.19. Nitrosylation of doubly protonated cluster $29H_2$ produces several species.

When the nitrosylation of $29H_2$ is monitored by UV-vis spectroscopy (Figure 2.20, a), degradation of the [2Fe–2S] core is evident from bleaching of the sample. The reaction proceeds with a rate in the same order of magnitude as observed for nitrosylation of 29^{2-} ($k_{\text{obs}}(29H_2) = 3.98 \times 10^{-4} \text{ s}^{-1}$, $k_{\text{obs}}(29^{2-}) = 1.60 \times 10^{-4} \text{ s}^{-1}$). Several bands are detected in the region for NO species in the IR spectrum of the THF extract, but only RBS can be identified with bands at 1795 (w), 1740 (s), and 1705 (w) (Figure 2.20, b). Bands at 1652 and 1628 cm^{-1} can be assigned to residual DMPH. The presence of unreacted DMPH is not surprising due to the excess needed for full protonation of the cluster. The surplus of acid

possibly prevents the formation of a DNIC-species or accelerates its decomposition, ultimately yielding RBS. Further information on the protonation product of DNIC **33⁻** and its stability are presented in chapter 3.

The characteristic bands for the corresponding base lutidine are not detected (bands at 1593 and 1580 cm^{-1}). Possibly, it was removed with the solvent under reduced pressure prior to the IR measurement.

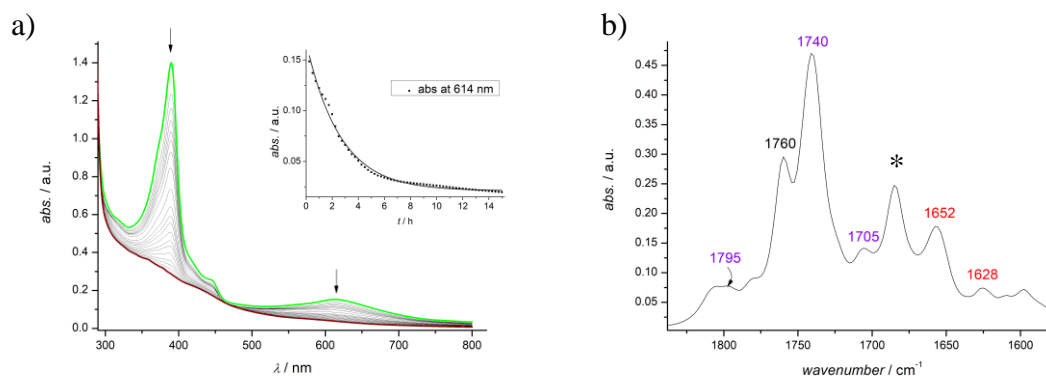


Figure 2.20. a) UV-vis spectra monitoring nitrosylation of protonated cluster **29H₂** (15 min) in DMF at $-20\text{ }^{\circ}\text{C}$. The inserted graph depicts absorbance at 614 nm vs. time (k_{obs} of $3.98 \times 10^{-4}\text{ s}^{-1}$). The poor fit of the kinetic trace indicates a more complicated reaction sequence and rate law. b) IR spectrum of THF extract after a reaction time of 2 h. Bands labeled in purple can be assigned to RBS, bands labeled in red to residual DMPH. (*) marks residual DMF at 1685 cm^{-1} .

2.4.2 Reaction of **30H₂** with NO

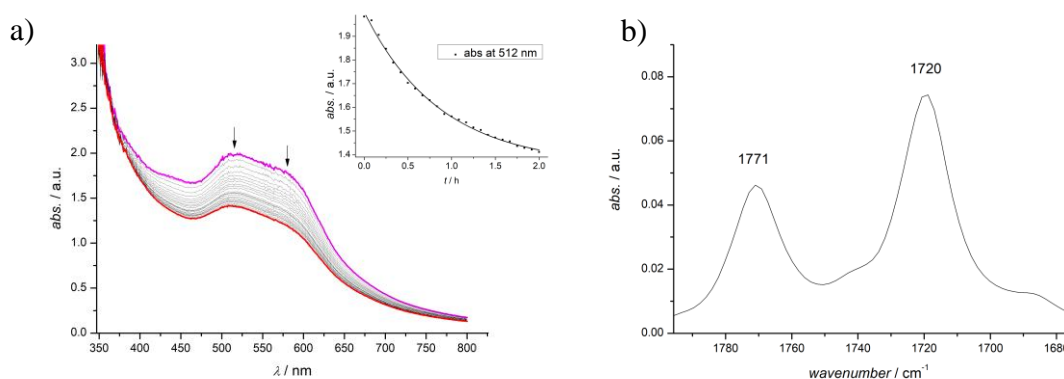


Figure 2.21. a) Nitrosylation of **30H₂** monitored by UV-vis spectroscopy. The inserted graph depicts absorbance at 512 nm vs. time (k_{obs} of $3.21 \times 10^{-4}\text{ s}^{-1}$). The poor fit of the kinetic trace indicates a more complicated reaction sequence and rate law. b) IR spectrum of THF extract from the reaction mixture after 2 h.

Protonation of **30²⁻** takes place readily with only two equivalents of DMPH. The reaction of **30H₂** with 4 equivalents of NO causes the decrease of overall absorbance in the UV-vis

spectra (Figure 2.23, a). The observed rate constant $k_{\text{obs}} = 3.21 \times 10^{-4} \text{ s}^{-1}$ is in the same order of magnitude as for nitrosylation of $\mathbf{30}^{2-}$ ($k_{\text{obs}}(\mathbf{30}^{2-}) = 6.03 \times 10^{-4} \text{ s}^{-1}$). The reaction appears to be more selective than nitrosylation of $\mathbf{29H}_2$ because only two bands, at 1771 and 1720 cm^{-1} , are detected in the typical NO region of the IR spectrum (Figure 2.21, b). These bands are proposed to belong to protonated $\mathbf{34H}$ (Figure 2.22) Further evidence for the proposed molecule is presented in chapter 3.

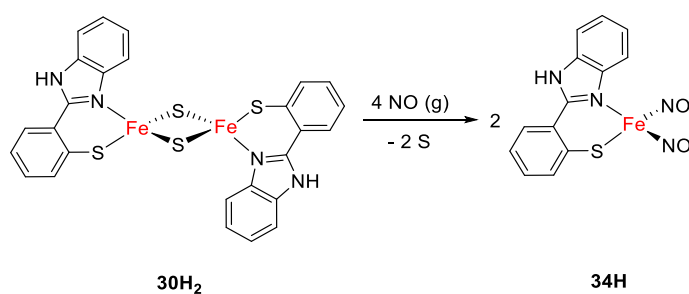


Figure 2.22. Proposed reaction equation for nitrosylation of $\mathbf{30H}_2$.

2.5 Nitrosylation of protonated mixed-valent $\mathbf{29H}^-$

The mixed-valent cluster $\mathbf{29}^{3-}$ was treated with 1 or 2 equivalents of DMPH and 5 equivalents of NO and monitored with UV-vis spectroscopy (Figure 2.23 a and Figure 2.24 a). Decrease of the overall absorbance indicates disassembly of the cluster core. New bands in the IR spectrum indicate the formation of an NO species and residual DMPH (Figure 2.23 b and Figure 2.24 b; DMPH is marked in red). The main band resonates at 1685 cm^{-1} in both cases. Assignment of the signal to a product was impossible so far. No H_2S was detected in the gasphase, probed with MS.

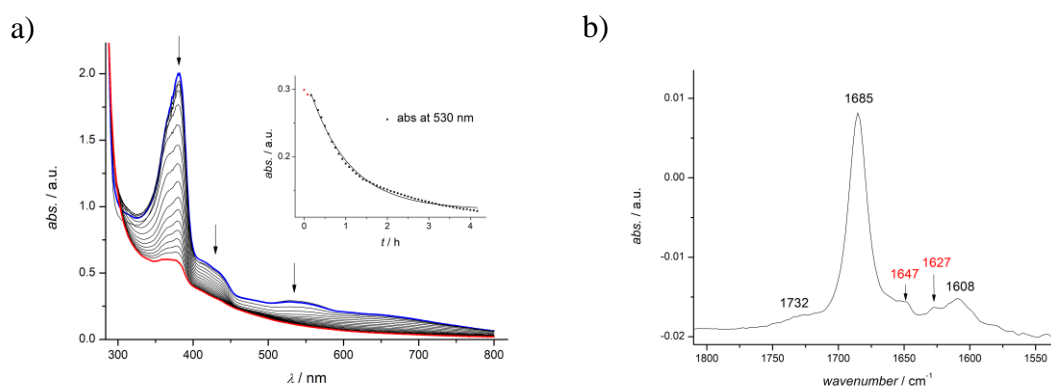


Figure 2.23. a) UV-vis spectra of $\mathbf{29}^{3-}$ after addition of 1 equivalent of DMPH and 5 equivalents of NO at $-30 \text{ }^\circ\text{C}$ in MeCN. Exponential fit of the data in the inserted graph gave a rate constant k_{obs} of $2.8 \times 10^{-4} \text{ s}^{-1}$. The poor fit of the kinetic trace indicates a more complicated reaction sequence and rate law. b) IR spectrum of the THF extract of the reaction mixture. The signals labeled in red can be assigned to DMPH (1650 and 1630 cm^{-1}).

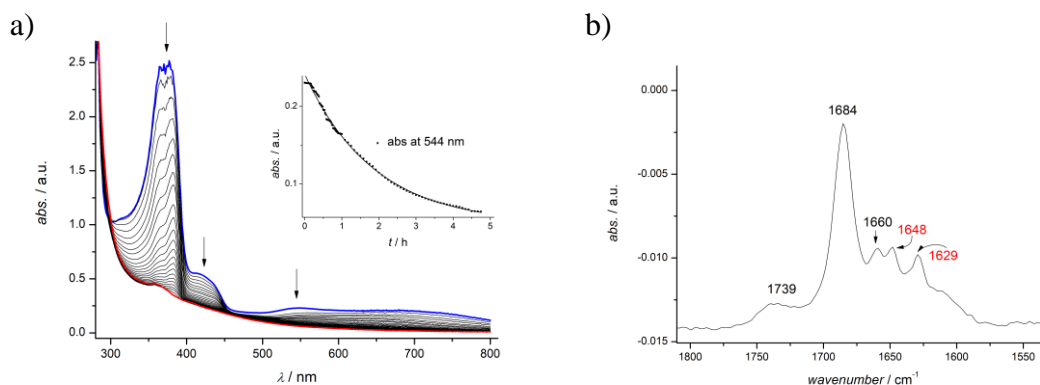


Figure 2.24. a) UV-vis spectra of $\mathbf{29}^{3-}$ after addition of 2 equivalents of DMPH and 5 equivalents of NO at $-30\text{ }^{\circ}\text{C}$ in MeCN. Exponential fit of the data in the insert gave a rate constant k_{obs} of $1.48 \times 10^{-4}\text{ s}^{-1}$. The poor fit of the kinetic trace indicates a more complicated reaction sequence and rate law. b) IR spectrum of the solution after removal of solvent. The signals labeled in red can be assigned to DMPH (1650 and 1630 cm^{-1}).

2.6 Summary and conclusion

DNICs readily form from nitrosylation of diferric [2Fe–2S] clusters ($\mathbf{29}^{2-}$ and $\mathbf{30}^{2-}$) with N,N- ($\mathbf{33}^{-}$) and S,N-chelating ($\mathbf{34}^{-}$) ligands. Both DNICs were fully characterized by UV-vis, IR, EPR, Mössbauer spectroscopy and X-ray crystallography. Liaw and coworkers proposed that chelating systems stabilize DNICs and destabilize RREs (Figure 1.18).¹⁵⁶ They also postulated that thiolate binding is more stable than imidazolate binding (Figure 1.20).¹⁵⁷ The results in this thesis support this proposal and concur with the results from Lippard and coworkers (Figure 2.2).^{158,168}

Extensive literature on nitrosylation of synthetic diferric [2Fe–2S] clusters is available (chapter 1.4.4), however, the reactivity of reduced [2Fe–2S] clusters towards NO is sparsely investigated, although it is the preferred oxidation state under physiological conditions. In this thesis, it was shown that mixed-valent [2Fe–2S] clusters ($\mathbf{29}^{3-}$ and $\mathbf{30}^{3-}$) first undergo oxidation to form intermediate 1 upon nitrosylation. The dubbed intermediate 1 is in fact diferric $\mathbf{29}^{2-}$ and $\mathbf{30}^{2-}$, respectively, supported by UV-vis, IR, NMR, and Mössbauer spectroscopy. Interestingly, in nitrosylation of $\mathbf{29}^{3-}$ a second intermediate is observed in UV-vis spectroscopy. However, no other spectroscopic method could detect a compound different from intermediate 1. In a second step, intermediate 1 or 2 degrade slowly into the two DNICs $\mathbf{33}^{-}$ and $\mathbf{34}^{-}$. These findings are diametric to Liaw's proposed mechanism for the nitrosylation of protein-bound mixed-valent [2Fe–2S] clusters in which rRREs and RREs are the intermediates. According to his hypothesis, the cluster undergoes ligand exchange and then forms a $\{\text{Fe}(\text{NO})_2\}^{10-}$ and a $\{\text{Fe}(\text{NO})_2\}^9$ - DNIC which then reacts

further to rRRE and finally undergoes oxidation. The findings presented in this thesis do not concur. RREs were not detected as intermediates during the nitrosylation of **29**³⁻ and **30**³⁻. However, it was easily possible to identify the oxidized diferric [2Fe–2S] cluster as intermediate due to a relative low reaction rate. Only after oxidation of the clusters further reaction to the respective DNICs take place. The observation of different pathways could be explained by the redox potential: Low-molecular-weight models for Fe–S proteins often have a more negative redox potential than clusters coordinated by proteins. A more negative redox potential facilitates an oxidation as first step of nitrosylation.

Another biologically relevant reaction is the protonation of histidine ligands in Rieske and mitoNEET proteins. The nitrosylation of protonated diferric and mixed-valent model clusters was presented in this chapter. Apparently, the reaction pathways are more complicated in the presence of the acid DMPH. The cluster core of **29H₂** and **30H₂** decomposed as observed by UV-vis spectroscopy. Nitrosylation products of **29H₂** gave a multitude of signals in the ν_{NO} -region of the IR spectrum. In contrast, the nitrosylation product of **30H₂** displays only two signals. The signals are assigned to the symmetric and asymmetric stretching frequency of the protonated DNIC **34H**. Further investigations on this matter are presented in the next chapter.

3 Protonation and deprotonation of DNICs

3.1 Introduction and objective

A library of DNICs with various ligands like chelates, carbenes, and CO have been synthesized to date.^{134,168,171,172} Classical DNICs are isolated as $\{\text{Fe}(\text{NO})_2\}^9$, according to the Enemark-Feltham notation, with a coordination number of four. Nonclassical DNICs have higher coordination numbers of five or six.¹⁷³ The once reduced state, $\{\text{Fe}(\text{NO})_2\}^{10}$, is often accessible; on the contrary, one-electron oxidation of a $\{\text{Fe}(\text{NO})_2\}^9$ DNIC was only achieved by stabilizing the product with a delocalized aminyl radical ligand system.¹⁷⁴ DNICs have been recognized as storage and transport agents of NO.^{175,176} Especially water-soluble DNICs are used as cellular NO donor agents promoting anti-inflammatory as well as anti-cancer activity.^{177,178}

In the following chapter, the reactivity of DNICs **33**⁻ and **34**⁻ towards acid and base is presented. The investigations were done *in vitro* and *in silico*.

3.2 Experimental results

3.2.1 IR spectroscopy

When 2,6-dimethylpyridinium tetrafluoroborate (DMPH) is added to **33**⁻ in MeCN, the IR-signals of the NO-groups shift from 1780 and 1714 cm^{-1} to 1820 and 1743 cm^{-1} and the signals appear broader (Figure 3.1, a). A signal that is attributed to skeletal vibration (1606 cm^{-1}) is split into two signals and shifts to lower wavenumbers (1595 and 1581 cm^{-1} , Appendix Figure 8.6) which proves not only an influence of protonation on the nitrosyl-moieties, but also on the complex's ligand. It is likely that the protonated ligand donates less electron density to the iron ion. Therefore, backbonding from the metal ($\text{Fe}(\text{d}) \rightarrow \text{NO}(\pi^*)$) is reduced and the N–O bond strengthened as higher wavenumbers correspond to a higher bond energy. The intensity of ν_{NO} decreases while ν_{ligand} remains as intense as before. The bands of excess DMPH (1680(w), 1650(s), 1630(s) cm^{-1}) appear in the IR spectrum after the addition of more than one equivalent. Protonation of the precursor $[\text{FeCl}_2(\text{NO})_2]^-$ has no effect on the NO stretches in the IR spectrum confirming that the protonation takes place at the ligand site rather than on the nitrosyl-moieties.

The protonation is reversible when 1,8-diazabicyclo(5.4.0)undec-7-ene (DBU) is added. All IR-bands shift back to the original location after addition of one equivalent of DBU and they do not move further when more DBU is added (Figure 3.1, b).

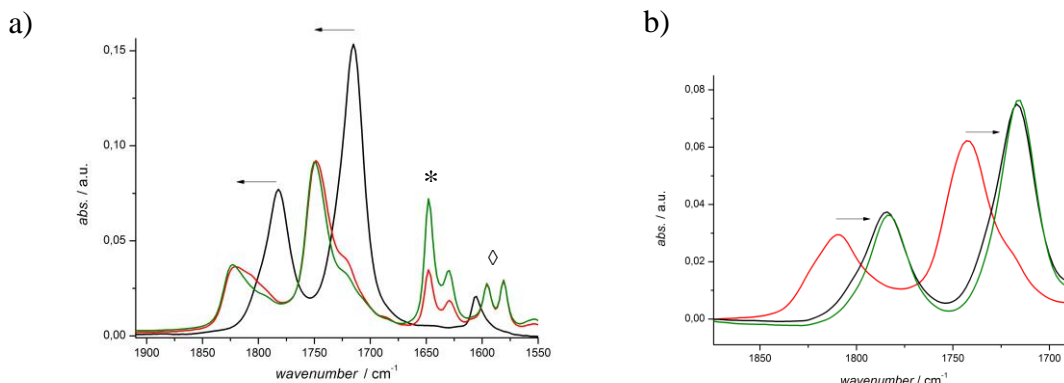


Figure 3.1. a) IR spectra of 33^- (black) after addition of 1.0 (red), and 1.5 eq. DMPH (green). b) IR spectrum of protonated 33 (red), and after addition of 1.0 (black), and 2.0 eq. DBU (green). DMPH (*), skeletal vibration (\diamond).

34^- exhibits similar spectroscopic behavior as 33^- . Upon protonation, the IR bands blue-shift from 1700 and 1751 cm^{-1} to 1722 and 1775 cm^{-1} and back to their original values when DBU is added (Figure 3.2). The process can be repeated several times without loss of intensity of 34^- . Considering this, the protonated species of 34^- appears to be more stable in comparison to 33^- .

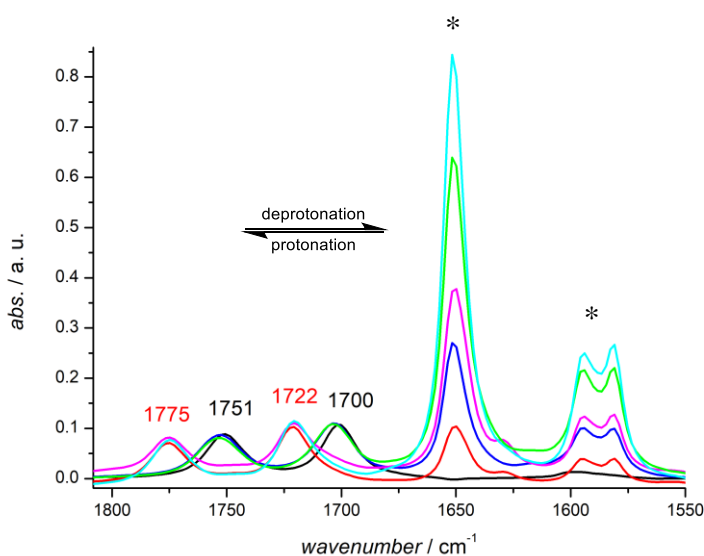


Figure 3.2. IR spectra of reversible protonation of 34^- (black) with DMPH and deprotonation with DBU in MeCN. Spectra are corrected for sample concentration. Bands from DBU are marked with an asterisks (*).

3.2.2 Mössbauer spectroscopy

Addition of DMPH to a solution of **33**⁻ in THF yields two species in the Mössbauer spectrum (Figure 3.3, a). One species has very similar parameters to **33**⁻ (Figure 3.3, b). The other species exhibits a larger isomer shift (1.40 mm s^{-1}) and quadrupole splitting (3.40 mm s^{-1}). These Mössbauer parameters suggest the presence of an Fe^{II} species. The more acid is added the more of species 2 is visible in the spectrum suggesting degradation of the nitrosyl species. The analogous protonation of **34**⁻ forms only one product according to Mössbauer spectroscopy (Figure 3.4, a). The parameters of the product differ only slightly from the parameters of **34**⁻ (Figure 3.4, b).

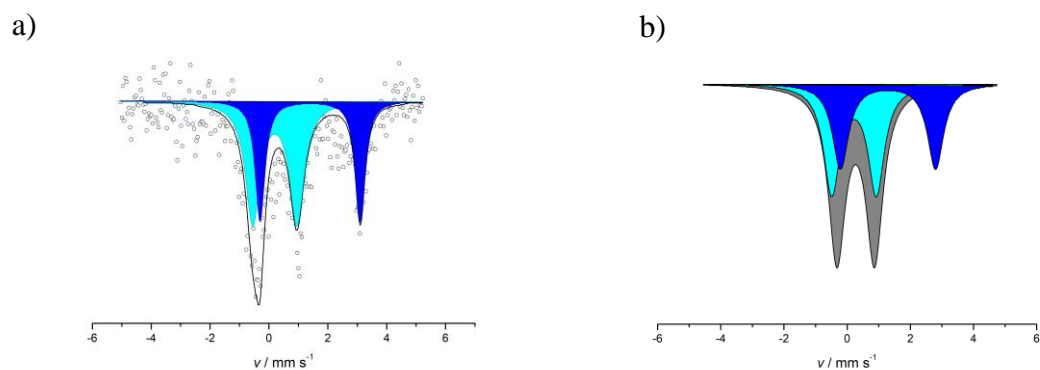


Figure 3.3. a) Zero-field Mössbauer spectrum of **33**⁻ after protonation with DMPH in THF at 80 K. Parameters of species 1 (cyan): $\delta_{\text{IS}} = 0.20 \text{ mm s}^{-1}$, $\Delta E_{\text{Q}} = 1.50 \text{ mm s}^{-1}$, $\text{fwhm} = 0.6 \text{ mm s}^{-1}$, 60%; parameters of species 2 (blue): $\delta_{\text{IS}} = 1.40 \text{ mm s}^{-1}$, $\Delta E_{\text{Q}} = 3.40 \text{ mm s}^{-1}$, $\text{fwhm} = 0.4 \text{ mm s}^{-1}$, 40%. b) Overlay of Mössbauer spectra of **33**⁻ (grey), species 1 (cyan) and species 2 (blue).

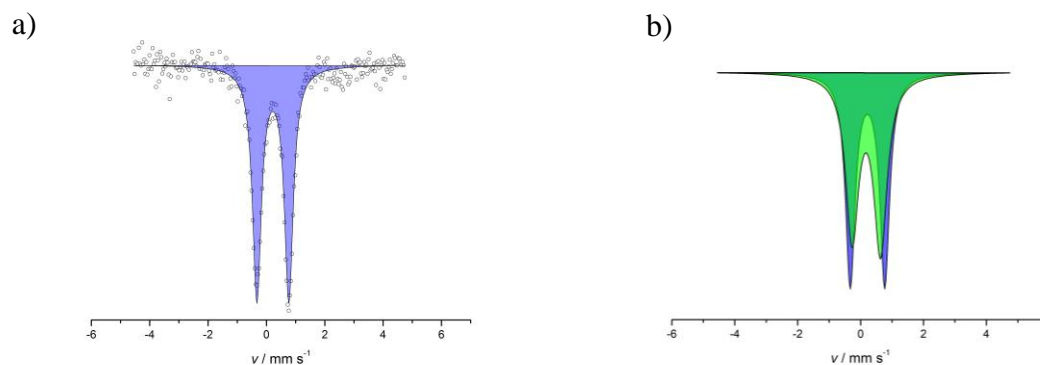


Figure 3.4. a) Zero-field Mössbauer of **34**⁻ after addition of DMPH in THF at 80 K. Parameters of fit (blue): $\delta_{\text{IS}} = 0.22 \text{ mm s}^{-1}$, $\Delta E_{\text{Q}} = 1.09 \text{ mm s}^{-1}$, $\text{fwhm} = 0.37 \text{ mm s}^{-1}$. b) Overlay of Mössbauer spectra of **34**⁻ (green) and protonated **34H** (blue).

3.2.3 Summary

The protonation site of DNICs **33**⁻ and **34**⁻ is most likely at the **NN** and **NS** capping ligand because the NO stretching frequencies ν_{NO} of the chloro-ligated DNIC, $[\text{FeCl}_2(\text{NO})_2]^-$, are not affected by the addition of acid. In contrast, ν_{NO} of DNICs **33**⁻ and **34**⁻ shift to higher wavenumbers after addition of one equivalent of DMPH. The shift can be reversed by addition of one equivalent of DBU.

33⁻ degrades with every cycle of protonation and deprotonation to form a side product, dubbed species 2, that was identified in the Mössbauer spectrum with $\delta = 1.40 \text{ mm s}^{-1}$ and $\Delta E_{\text{Q}} = 3.40 \text{ mm s}^{-1}$. **34**⁻ is more stable in regard to protonation as the cycle of protonation and deprotonation can be repeated several times and no side product is formed according to Mössbauer spectroscopy.

Generally, assignment of oxidation states of $\{\text{Fe}(\text{NO})_x\}$ complexes from Mössbauer parameters is difficult due to the covalent bond between iron and the nitrosyl moieties. The isomer shift is very sensitive to π -back-bonding.^{179–181} DFT calculations were employed to support experimental results.

3.3 DFT calculations

3.3.1 Background

Ye and Neese published a computational study on the electronic structure of DNICs in 2010.¹⁸² They found that the $\{\text{Fe}(\text{NO})_2\}^9$ moiety can be described as a resonance hybrid between $\{\text{Fe}^{\text{II}}(\cdot\text{NO})(\text{NO}^-)\}$ and $\{\text{Fe}^{\text{III}}(\text{NO}^-)_2\}$. The first resonance structure describes a hs-ferrous ion coupled to an overall $(\text{NO})_2^-$ ligand ($S(\text{NO})_2 = 3/2$). In the second resonance structure, a hs-ferric ion couples antiferromagnetically to two NO^- ligands. Both valence structures lead to an overall spin $S = 1/2$. The bonding between the iron ion and the two NO ligands is seen as covalent. Ye and Neese were able to infer IR and Mössbauer parameters in good agreement with experimental data from their calculations.

3.3.2 Geometry optimization and IR spectra of **33**⁻ and **34**⁻

All computation in this thesis were carried out with the ORCA program package.¹⁸³ X-ray data of the anions were employed as starting coordinates for the geometry optimization. Geometry optimizations and frequency calculations were performed with the BP86, TPSS, B3LYP and TPSSh density functionals. The def2-TZVP basis set was applied in combination with the auxiliary basis set def2-TZV/J. The conductor-like screening model

(COSMO) was employed as the experimental parameters of ν_{NO} shift slightly in dependence of the solvent used (Table 3.1). MeCN and THF were modeled in form of an infinite dielectric.

Table 3.1. IR parameter for ν_{NO} [cm^{-1}] of **33**⁻ and **34**⁻ (BP86/def2-tzvp) in a) MeCN and b) THF.

	exp ^{a)}	calc ^{a)}	exp ^{b)}	calc ^{b)}
33 ⁻	1780, 1714	1749, 1673	1773, 1705	1752, 1681
34 ⁻	1751, 1700	1709, 1643	1744, 1694,	1716, 1657

BP86 and TPSS functionals give the best result for IR frequencies of nitrosyl moieties in comparison to the other functionals (Table 3.1 and Table 8.1 in appendix). The calculated values diverge from the experimental ones by a scaling factor of approximately 1.02 (red shifted). The deviation is smaller when THF is used instead of MeCN in the COSMO package. Overall the IR spectrum is well reproduced (Figure 3.5).

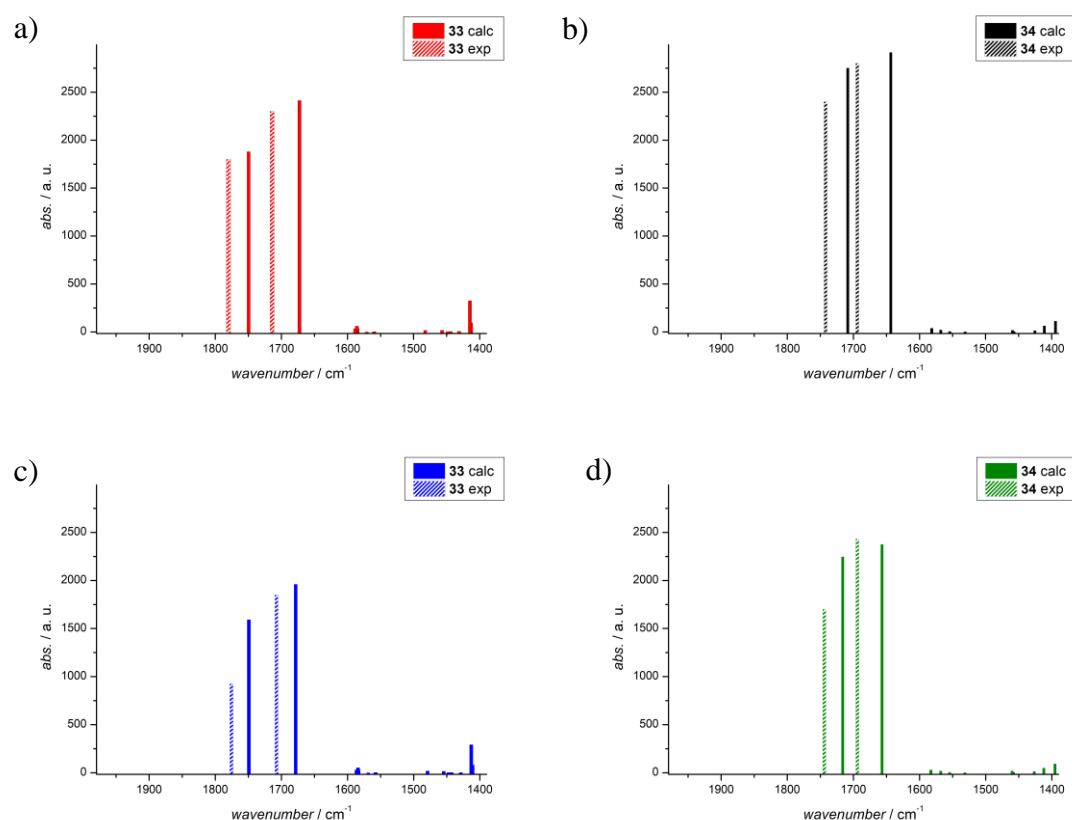


Figure 3.5. Comparison of calculated and experimental data. a) **33**⁻ in MeCN, b) **34**⁻ in MeCN, c) **33**⁻ in THF, d) **34**⁻ in THF.

3.3.3 Mössbauer parameters of $\mathbf{33}^-$ and $\mathbf{34}^-$ and their protonated forms

Geometry optimized anions $\mathbf{33}^-$ and $\mathbf{34}^-$ from chapter 3.3.2 were employed for the calculation of Mössbauer parameters δ_{IS} and ΔE_{Q} . For the protonated species, one H-atom was added to one imidazole-N atom with the program *Chemcraft* and the charge was changed to zero. Optimized structures of $\mathbf{33H}$ and $\mathbf{34H}$ are shown in Figure 3.6. The Mössbauer parameters were computed using the CP(PPP) basis set for Fe and def2-TZVP for the other atoms.^{184–186} Isomer shifts δ_{IS} were calculated from the electron densities at the Fe nucleus ρ_0 . Quadrupole splittings were conveniently stated in the ORCA output file by calculation incorporating the electric field gradient (see chapter 7.4 for more information).

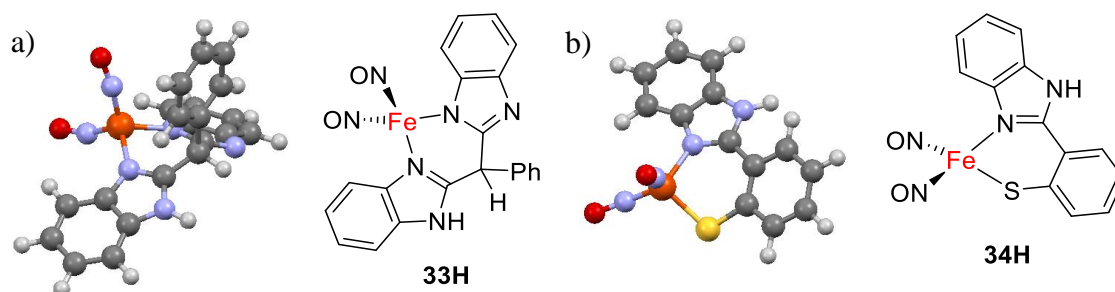


Figure 3.6. Geometry optimized structure of $\mathbf{33H}$ (a), and $\mathbf{34H}$ (b).

The Mössbauer parameters of $\mathbf{33}^-/\mathbf{33H}$ and $\mathbf{34}^-/\mathbf{34H}$ are summarized in Table 3.2. Results for other functionals are presented in the appendix (Table 8.3). The quadrupole splitting especially for $\mathbf{34}^-/\mathbf{34H}$ fits well and for $\mathbf{33}^-/\mathbf{33H}$ adequately. The value becomes larger upon protonation which is in agreement with the experiment. DFT calculation gives an increase of the isomer shift after protonation of DNIC $\mathbf{33}$ and $\mathbf{34}$. Experimentally, this increase is only observed for $\mathbf{34}^-/\mathbf{34H}$. The trend regarding the isomer shift after protonation of $\mathbf{33}$ is not reproduced possibly because the protonation site of $\mathbf{33H}$ is described incorrectly in Figure 3.6.

Table 3.2. Experimental Mössbauer parameters in THF and calculated values (B3LYP/def2-tzvp).

	$\delta_{\text{IS}} / \text{mm s}^{-1}$		$\Delta E_{\text{Q}} / \text{mm s}^{-1}$			$\delta_{\text{IS}} / \text{mm s}^{-1}$		$\Delta E_{\text{Q}} / \text{mm s}^{-1}$	
	exp	calc	exp	calc		exp	calc	exp	calc
$\mathbf{33}^-$	0.28	0.05	0.99	1.07	$\mathbf{34}^-$	0.18	0.00	0.90	0.98
$\mathbf{33H}$	0.20	0.10	1.50	1.33	$\mathbf{34H}$	0.22	0.05	1.09	1.16

3.3.4 Investigation of second protonation pathway for 33^-

The wrong trend in the calculation of the isomer shift of $33^-/33\text{H}$ might be explained by a different pathway for the protonation of 33 in comparison to 34 . In theory, 33^- can be protonated twice while 34^- can be protonated once, assuming that the protonation site is on the imidazole-N of the ligand. However, it is obvious from the experiment that one equivalent DMPH is sufficient for full protonation of 33^- . A rearrangement of the H atom in the backbone of the bis(benzimidazolato) ligand of 33^- can take place as a consequence of the protonation (Figure 3.7, a). The same behavior was reported for the protonation of the bis(benzimidazolato) coordinated $[2\text{Fe}-2\text{S}]$ cluster (compare Figure 2.19).¹⁶³ This protonation goes in hand with an intense absorbance at 380 nm in the UV-vis spectrum ($\epsilon = 64000 \text{ M}^{-1}\text{cm}^{-1}$) and a color change of the solution from red to green. Such an intense band was not seen in the UV-vis spectrum of the protonated DNIC. The solution remained reddish-brown after protonation. Nevertheless, the rearrangement (Figure 3.7, a) was investigated by DFT calculations.

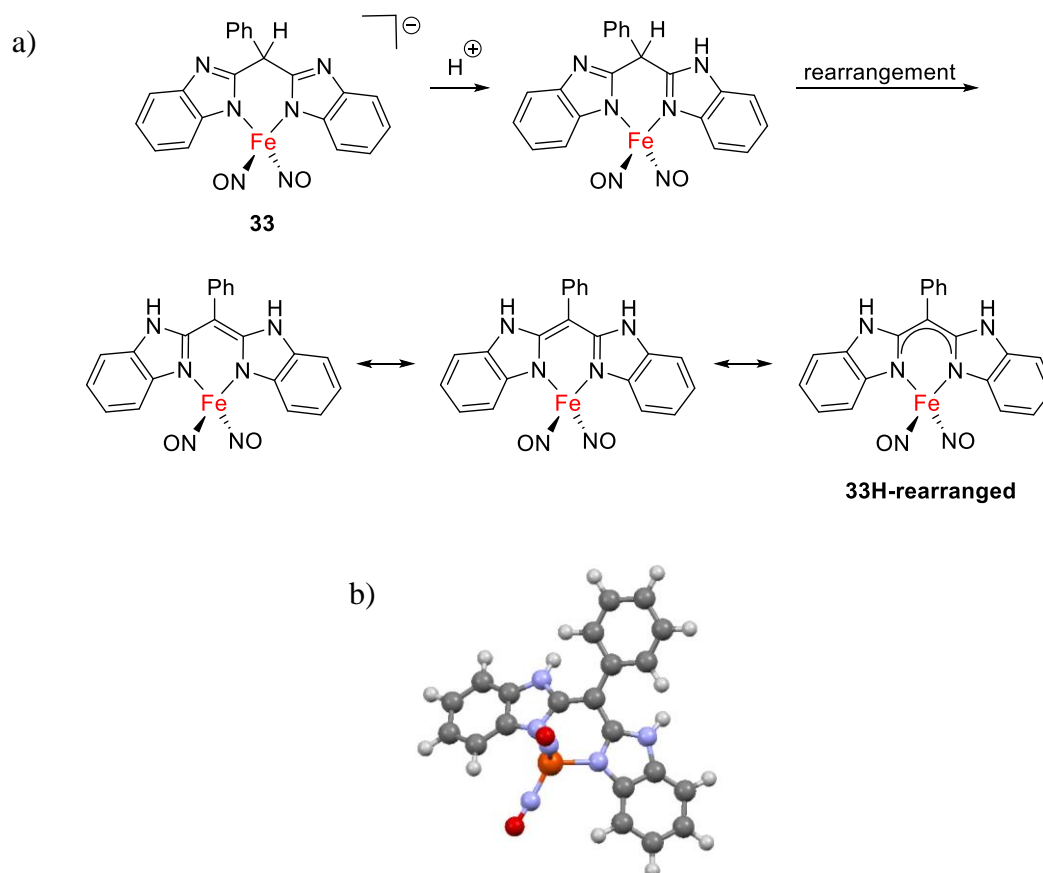


Figure 3.7. a) Proposed mechanism for rearrangement of H atom on bis(imidazolato) ligand of 33 . b) Geometry optimized structure of 33H-rearranged .

A geometry optimization was run on **33H-rearranged** (bp86/def2-tzvp) with a charge of ± 0 and a spin of $S = \frac{1}{2}$. In the optimized structure the carbon atom in the backbone bound to the phenyl group is almost in a planar coordination environment (Figure 3.7, b). The IR data obtained from the optimized structure differ strongly from the experimental data (Table 3.3). A scaling factor of 1.07 would be necessary to arrive at the experimental values. Much better agreement of experimental and simulated data was achieved for the once protonated structures **33H** and **34H**. The scaling factor is the same as for the not-protonated species (1.02). This result in combination with the absence of a characteristic UV-vis band for the rearranged ligand suggest that the molecular structure of **33H** does not feature a rearrangement.

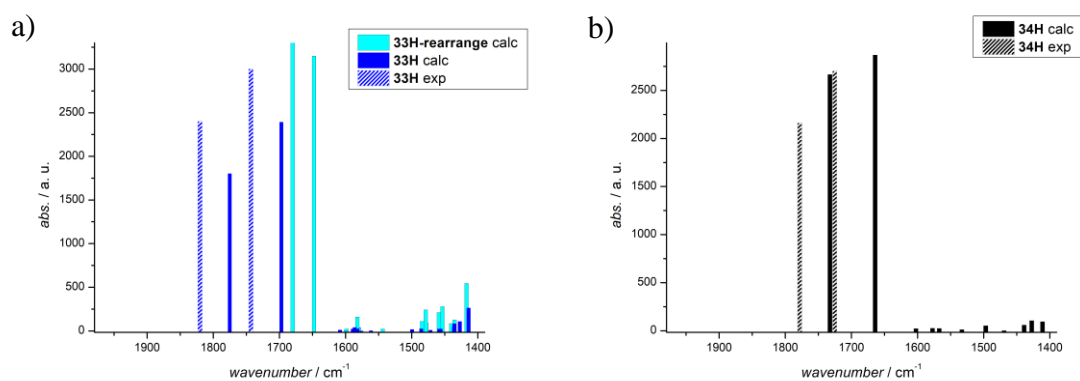


Figure 3.8. Comparison of calculated and experimental data for **33H**, **33H-rearranged** (a) and **34H** (b).

Table 3.3. Experimental and calculated ν_{NO} parameters of protonated species (BP86/def2-tzvp).

	$\nu_{\text{NO}} / \text{cm}^{-1}$	
	calc	exp
33H	1775, 1722	1820, 1743
33H-rearranged	1680, 1648	
34H	1735, 1667	1775, 1722

3.4 Discussion and conclusion

33⁻ and **34⁻** are readily protonated with DMPH and deprotonated with DBU. The protonation/deprotonation is reversible, however, protonation of **33⁻** forms a side product that cannot reenter the de-/protonation cycle. DFT calculations support the idea that the protonation site is on the N-atom of the benzimidazolate ligand. The NO stretching frequencies of **33⁻** and **34⁻** are well reproduced. The observation that ν_{NO} shifts to higher wavenumbers after addition of acid is also confirmed. The deviations of the calculated from the experimental result are between 21 and 57 cm^{-1} . Ye and Neese observed deviations from the experimental values of 61 to 72 cm^{-1} for their system.¹⁸² Therefore, calculated IR spectra are in reasonable agreement with the experimental data.

When the bis(benzimidazolato) coordinated [2Fe–2S] cluster **29²⁻** is protonated, a rearrangement of the methine-H of the ligand takes place (Figure 2.19). This behavior is unlikely for DNIC **33H** as calculations reveal a very different IR spectrum for that species. Single protonation on the N-atom of the aromatic ring, however, leads to reliable results for the IR frequencies that again compare well to experimental values.

Calculations of Mössbauer parameters show that the isomer shift and the quadrupole splitting increase upon protonation of the DNICs. While this holds true for the protonation of **34⁻**, protonation of **33⁻** affects a shift to a smaller value of the isomer shift. No explanation has been found for the divergent behavior thus far. Still, it is possible to derive from calculations that species 2 after protonation of **33⁻** does not seem to be a DNIC that is simply protonated on the ligand because isomer shift and quadrupole splitting significantly differ from the calculated values.

Although protonation of DNIC **33⁻** and **34⁻** was investigated by IR and Mössbauer spectroscopy as well as DFT calculation, the molecular structure of the protonated species remains elusive. Samples of ⁵⁷Fe-enriched **34⁻** and **34H** were prepared for NRVS measurements and sent to the group of Prof. Schünemann at TU Kaiserslautern in order to gain more insight.

4 Cubane-type [4Fe–4S] cluster with one pentacoordinate iron ion

4.1 Introduction and objective

The vast majority of iron ions in Fe–S clusters have a distorted tetrahedral coordination (*cf.* chapter 1.2.1). Five-fold coordination is unusual and results in an activation of the participating iron ion. In nature, several systems make use of this feature. One enzyme discussed in this regard in the scientific community is biotin synthase. Its [2Fe–2S] cluster is ligated by three cysteines and one arginine.¹⁸⁷ Arginine is an exceptional ligand that offers the possibility for mono- and bidentate binding.¹⁸⁸ X-ray crystallography was not able to determine the binding mode of the arginine residue due to low resolution of the crystal structure determination. Five-fold coordination of the iron ion cannot be excluded from the data available.

Synthetic [2Fe–2S] clusters with five-coordinated iron atoms have provided more insight into the matter. On the one hand, an intermediate with a five-coordinated iron ion was postulated by DFT calculation for the slow isomerization of a [2Fe–2S] cluster via a solvent-mediated associative process.¹⁶⁷ On the other hand, models for five-coordinated [2Fe–2S] clusters were synthesized with tridentate capping ligands (**35**²⁻, **36**²⁻, Figure 4.1).^{189,190} With these model structures the effect of pentacoordination was investigated. Secondary bonding was more pronounced for a thioether-S compared to an ether-O in **35**²⁻. In both **35**²⁻ and **36**²⁻ the Fe···Fe distance and Fe–S–Fe angles increase due to the distortion induced by the ligand. The secondary interaction affects a more positive Mössbauer isomer shift for both compounds. An increase of the quadrupole splitting is detected for **35**²⁻ in comparison to related four-coordinate [2Fe–2S] clusters. The quadrupole splitting of **36**²⁻ is unusually small, but relates well to calculated values from DFT studies.

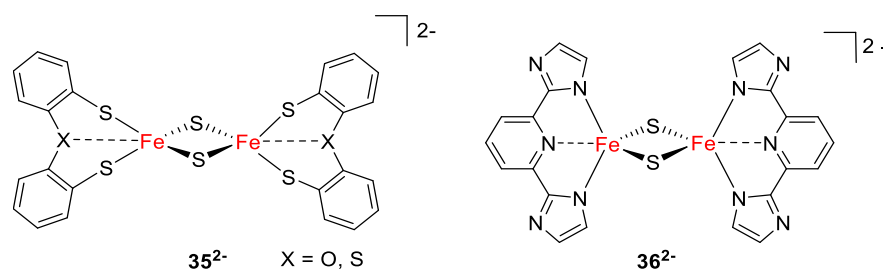


Figure 4.1. Five-coordinated low-molecular weight [2Fe–2S] clusters.^{189,190}

Site-differentiated [4Fe-4S] clusters occur in nature with aconitase as the prototypical example. The enzyme is involved in the catalytic step of transforming citrate into isocitrate (chapter 1.2.3, p. 12). A single iron ion is bound to H₂O/OH⁻ in its resting state and to oxygen atoms of the substrate in its active state.¹⁹¹ Other examples of [4Fe-4S] proteins with one iron site different from the other three include ferredoxin III from *Desulfovibrio africanus*^{192,193} and ferredoxin of *Pyrococcus furiosus*¹⁹⁴. These clusters have one iron ion bound to an aspartic acid instead of a cysteine. Synthetic site-differentiated clusters with various different ligands are presented in chapter 1.3 (p. 15). In 1983 Johnson *et al.* synthesized a series of (Et₄N)₂[Fe₄S₄(SC₆H₄-*o*-X)₄] with X = NH₂, OMe, OH, and SMe to examine the possible formation of five-coordinate Fe sites in cubane-type clusters.¹⁹⁵ The X = OH cluster contains three conventional tetrahedral FeS₄ sites and one distorted trigonal-bipyramidal FeS₄O site (**37**²⁻). The structure was confirmed by X-ray crystallography and Mössbauer spectroscopy. The reduced **37**⁻ and oxidized **37**³⁻ were studied in depth by Le Pape *et al.* with EPR single-crystal and proton ENDOR spectroscopy.^{196,197}

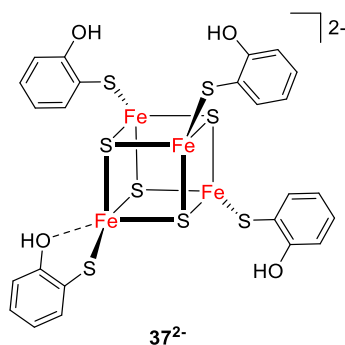


Figure 4.2. Five-coordinated low-molecular-weight [4Fe-4S] cluster.¹⁸³

The objective of this chapter is to carry on investigations of five-coordinated cubane-type [4Fe-4S] clusters. Johnson *et al.* failed in obtaining a crystal structure for (Et₄N)₂[Fe₄S₄(SC₆H₄-*o*-NH₂)₄]. But Mössbauer spectroscopy was used instead to determine the solid state isomer. The spectrum showed only one single quadrupole doublet which indicates that all iron ions are in the same coordination environment. In this chapter the characterization of the cluster in the solid state and in solution is presented.

4.2 Synthesis

A self-assembly approach was followed to synthesize the target molecule **38** effectively and allow for convenient exchange of counter ions. 2-Aminothiophenol was deprotonated with sodium methoxide in methanol. Then iron(III)chloride and lithium sulfide were added. In a self-assembly reaction, a 2-amino-benzenethiol ligated [4Fe–4S] cluster is formed and precipitates upon addition of a halide salt of Et_4N^+ or PhMe_3N^+ (Figure 4.3). The precipitate is filtered from the solution and the product is extracted with MeCN. Crystalline material suitable for crystal structure analysis was obtained by diffusion of diethyl ether in a MeCN solution of the clusters.

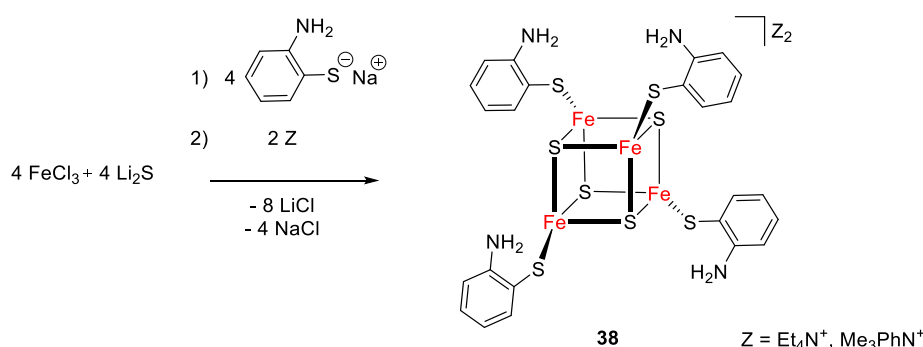


Figure 4.3. Synthesis of [4Fe–4S] cluster **38** with two different counter ions.

4.3 Structural characterization of **38**²⁻

Surprisingly, the crystal structure reveals different ligand binding in dependence on the counter ion (Figure 4.4). All four ligands bind via the thiol group in a monodentate fashion when Et_4N^+ is introduced as counterion, thus the cluster in $(\text{Et}_4\text{N})_2\mathbf{38}$ contains four conventional tetrahedral FeS_4 sites. The cluster crystallizes in the orthorhombic space group $\text{Aba}2$ and no solvent cocrystallizes in the unit cell. The anion $\mathbf{38}^{2-}$ is C_2 symmetric.

The crystallization of two Me_3PhN^+ as counterion induces a change of the coordination number of one iron ion. The ligand at Fe(1) is rotated and forms a chelating ring with the bond distance Fe-S of 2.3318 Å, being only 0.059 Å longer than the mean of the three other terminal Fe-S distances. This bond represents a primary interaction. The distance between the iron ion to the amine group is shorter (2.2770 Å). The symmetry of the molecule is broken due to this constitutional change. The molecule crystallizes in the triclinic space group P-1 with two Me_3PhN^+ and one MeCN molecule.

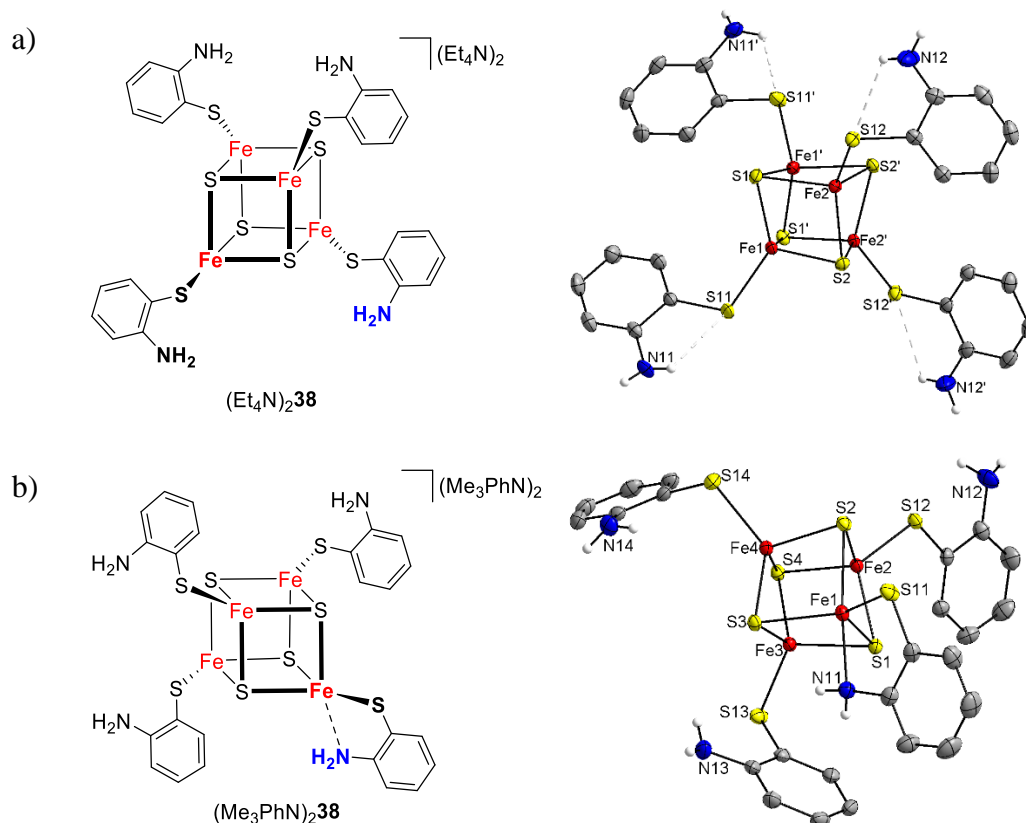


Figure 4.4: Crystal structure and drawing of $(\text{Et}_4\text{N})_2\mathbf{38}$ (a) and $(\text{Me}_3\text{PhN})_2\mathbf{38}$ (b). Thermal displacement ellipsoids are shown at 50% probability, carbon bound hydrogen atoms and counter ions are omitted for more clarity.

Table 4.1: Selected bond length (\AA) and angles ($^\circ$) of $(\text{Et}_4\text{N})_2\mathbf{38}$ and $(\text{Me}_3\text{PhN})_2\mathbf{38}$. $(\text{Et}_4\text{N})_2\mathbf{37}$ is shown for comparison.¹⁹⁵

	$(\text{Et}_4\text{N})_2\mathbf{38}$	$(\text{Me}_3\text{PhN})_2\mathbf{38}$	$(\text{Et}_4\text{N})_2\mathbf{37}^{195}$
Fe(1)⋯S(11)	2.2666(6)	2.3318(4)	2.313
Fe(1)⋯N(11)	5.145 ⁽ⁱ⁾	2.2770(13)	–
Fe⋯O	–	–	2.318
$\text{Fe}_{\text{av}}\cdots\text{S}_{\text{thiolate}}$	–	2.2725	2.278

(i) non-binding

Johnson *et al.* found that the distance $\text{Fe}\cdots\text{OH}_{\text{non-binding}}$ is 4.13–5.57 \AA , evidencing a lack of interaction. For $(\text{Et}_4\text{N})_2\mathbf{38}$ distances $\text{Fe}\cdots\text{NH}_{2,\text{non-binding}}$ were found between 5.026 and 5.145 \AA . The crystal structure of $(\text{Me}_3\text{PhN})_2\mathbf{38}$ exposes very different distances between $\text{Fe}\cdots\text{NH}_{2,\text{non-binding}}$ of 3.941, 4.281, and 5.211 \AA . These findings support that the symmetry of $(\text{Me}_3\text{PhN})_2\mathbf{38}$ is rescinded and that the ligands bind very unsymmetrically.

4.3.1 Mössbauer spectroscopy of solid sample and in frozen solution

$(\text{Et}_4\text{N})_2\mathbf{38}$ exhibits an isomer shift δ_{IS} of 0.43 mm s^{-1} and a quadrupole splitting ΔE_{Q} of 0.88 mm s^{-1} in the zero-field Mössbauer spectrum (Figure 4.5, a). These values are similar

to the values reported by Johnson *et al.* when taking into consideration that they referenced the isomer shift to Fe metal at 4.2 K. The values are typical for $[\text{Fe}_4\text{S}_4(\text{SR})_4]^{2-}$ with R substituents lacking secondary interaction sites. Such clusters exhibit one or two closely overlapping quadrupole doublets with $\delta_{\text{IS}} = 0.32\text{--}0.36 \text{ mm s}^{-1}$.¹⁹⁵ The *o*-NH₂ groups do not appreciably interact with the core.

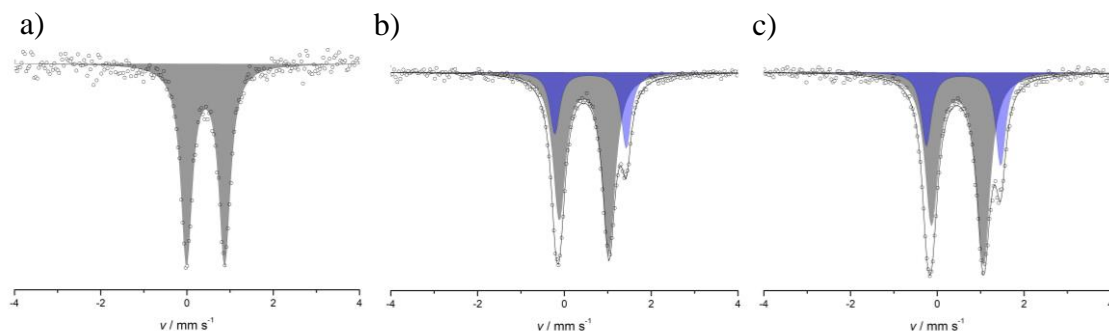


Figure 4.5. Zero-field Mössbauer spectra of $(\text{Et}_4\text{N})_2\mathbf{38}$ at 80 K (a), $(\text{Me}_3\text{PhN})_2\mathbf{38}$ at 80 K (b), $(\text{Me}_3\text{PhN})_2\mathbf{38}$ at 14 K (c).

Table 4.2: Mössbauer parameters of $(\text{Et}_4\text{N})_2\mathbf{38}$, $(\text{Me}_3\text{PhN})_2\mathbf{38}$, and related clusters.

	T / K	$\delta_{\text{IS}} / \text{mm s}^{-1}$	$\Delta E_{\text{Q}} / \text{mm s}^{-1}$	$\Gamma / \text{mm s}^{-1}$	$(I_{\text{R/L}})$	Rel. Int. / %
$(\text{Et}_4\text{N})_2\mathbf{38}$	80	0.43	0.88	0.32	–	100
$(\text{Et}_4\text{N})_2\mathbf{38}^{195}$	4.2–80	0.33 ^{b)}	0.88	0.34	–	100
$(\text{Me}_3\text{PhN})_2\mathbf{38}$	80	0.46	1.14	0.35	0.8	75
		0.60	1.64	0.27	0.8	25
	14	0.47	1.20	0.37	0.8	72
		0.61	1.71	0.28	0.8	28
$(\text{Me}_3\text{PhN})_2\mathbf{38}$ (MeCN)		0.44	1.05	0.40	1.02	100
$(\text{Et}_4\text{N})_2\mathbf{37}^{195}$	80	0.30 ^{b)}	0.76	0.26	–	22
		0.34 ^{b)}	1.23	0.34	–	55
		0.49 ^{b)}	1.82	0.26	–	23
$(\text{Et}_4\text{N})_2\mathbf{37}$ (MeCN) ¹⁹⁵	80	0.32 ^{b)}	1.03	0.43	–	97 ^{a)}

a) Minority spectral component present with intensity of 3 %, b) standard: Fe at 4.2 K.

In the case of $(\text{Me}_3\text{PhN})_2\mathbf{38}$ a shoulder is visible in the Mössbauer spectrum (Figure 4.5, b and c). The experimental data is best fitted with two doublets in a ratio of 3:1. The asymmetry of the doublets was considered with an asymmetry factor ($I_{\text{R/L}}$) of 0.8. A reason

for the asymmetry in Mössbauer spectra can be an anisotropic orientation of crystals in the magnetic field. The asymmetry factor was correlated to be the same in both subspectra. The respective isomer shifts are 0.46 mm s^{-1} (grey) and 0.60 mm/s (blue) and a quadrupole splitting of 1.14 mm s^{-1} (grey) and 1.64 mm s^{-1} (blue). The quadrupole splitting is dependent on the electrical field gradient of the iron core which is indirectly influenced by the coordination sphere and the binding ligands. The fact that two species in a ratio of 3:1 are found confirms the result from the crystal structure that one iron ion is set in a different surrounding than the other three iron ions. The isomer shift of the main signal corresponds well to the isomer shift of $(\text{Et}_4\text{N})_2\mathbf{37}$. The isomer shift of the smaller signal (blue) is higher. Johnson *et al.* attribute the high isomer shift to five-coordinate Fe atoms. The remaining doublets have parameters that are common for conventional $[\text{Fe}_4\text{S}_4(\text{SR}_4)]^{2-}$ clusters with tetrahedral FeS_4 sites. They report an increase by $0.15\text{--}0.20 \text{ mm/s}$ at 4.2 K as a presumed consequence of five-coordination.

The Mössbauer spectrum of $(\text{Et}_4\text{N})_2\mathbf{37}$ has three doublets with the approximate ratio of 1(A):2(B):1(C).¹⁹⁵ Johnson *et al* assign the signals as followed: One iron is in a five-coordinated environment because of the secondary bonding interaction of the hydroxy group. This coordination leads to an unusual large isomer shift $\delta = 0.49 \text{ mm s}^{-1}$ and a large quadrupolar interaction $\Delta E_Q = 1.82 \text{ mm s}^{-1}$ (species C). The other three iron atom have the usual tetrahedral surrounding in the first coordination sphere. However, two iron atoms give the same signal in Mössbauer spectroscopy due to a mirror pseudosymmetry of the whole molecule (species B) while one parameter is slightly lower (species A).

A solution of $(\text{Me}_3\text{PhN})_2\mathbf{38}$ in MeCN was slowly cooled to $-196 \text{ }^\circ\text{C}$ in order to freeze the state in solution and compare it the results from crystalline material. The Mössbauer spectrum of the solution can only be fitted to one doublet with an isomer shift of 0.44 mm s^{-1} and quadrupole splitting of 1.05 mm s^{-1} (Figure 4.6). The signal from the five-coordinated iron atom disappears. The small asymmetry in the signal is fitted with a right/left correlation of 1.02. The quadrupole splitting of the frozen solution is smaller than the quadrupole splitting of the solid sample. Apparently, the inequality of the iron ions is canceled and all of them give the same signal in Mössbauer spectroscopy.

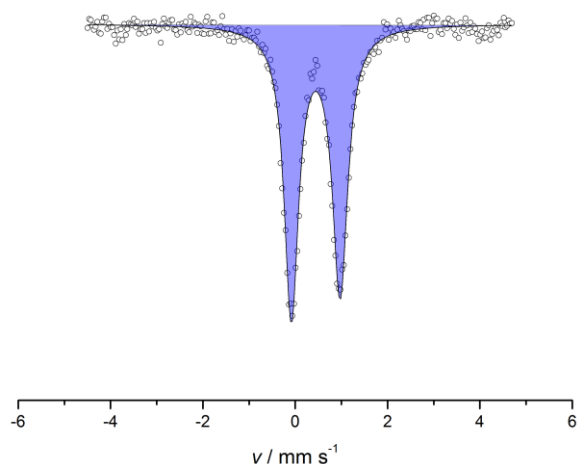


Figure 4.6. $(\text{Me}_3\text{PhN})_2\mathbf{38}$ in frozen solution (MeCN) at 80 K. $\delta = 0.44 \text{ mm s}^{-1}$, $\Delta E_Q = 1.05 \text{ mm s}^{-1}$, $\text{fwhm} = 0.4 \text{ mm s}^{-1}$, asymmetry factor ($I_{R/L}$) = 1.02.

4.3.2 UV-vis spectroscopy

Both complexes $(\text{Me}_3\text{PhN})_2\mathbf{38}$ and $(\text{Et}_4\text{N})_2\mathbf{38}$ have bands at 303, 350(sh) and 484 nm in the UV-vis spectrum in MeCN at room temperature regardless of their different constitution in the solid state. This is in accordance to the results from Mössbauer spectroscopy where there is no difference of the four iron ions in slowly cooled solution (Figure 4.6). It was of interest whether the UV-vis spectrum changes when the freedom of movement was inhibited by lowering the temperature. The solvent was changed to EtCN as its melting point is approx. 50 °C below the melting point of MeCN. Variable temperature UV-vis spectroscopy shows no effect on the bands (Figure 4.7, a). Therefore, there is no hint for constitutional change as the solution cools down. Reflectance spectra of crystalline $(\text{Me}_3\text{PhN})_2\mathbf{38}$ and $(\text{Et}_4\text{N})_2\mathbf{38}$ in the solid state were measured in addition to UV-vis spectra of the solutions (Figure 4.7, b). Overall, both compounds produce similar spectra, however, in the spectrum of $(\text{Me}_3\text{PhN})_2\mathbf{38}$ a band at 450 nm is more pronounced.

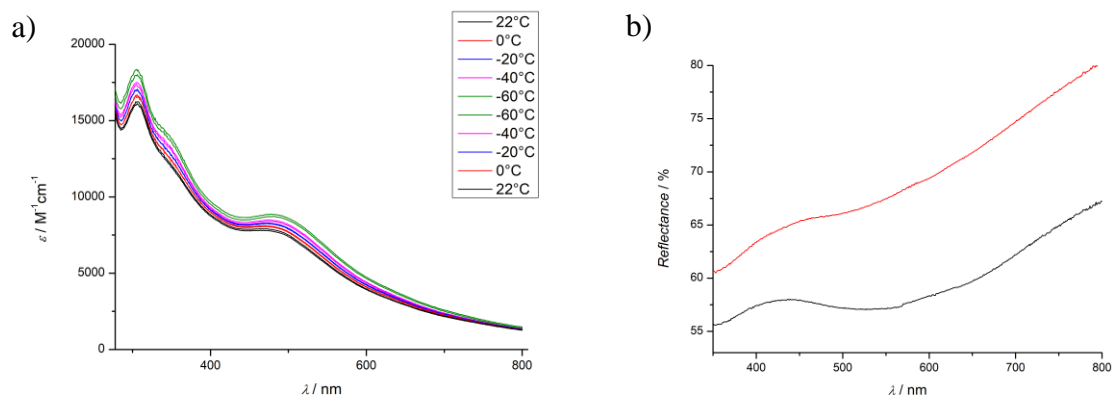


Figure 4.7. a) vt UV-vis spectroscopy of $(\text{Me}_3\text{PhN})_2\mathbf{38}$ in EtCN and b) reflectance spectrum of crystalline $(\text{Me}_3\text{PhN})_2\mathbf{38}$ (black) and $(\text{Et}_4\text{N})_2\mathbf{38}$ (red) in solid state at rt.

4.3.3 NMR spectroscopy

The ^1H NMR spectra of both compounds $(\text{Me}_3\text{PhN})_2\mathbf{38}$ and $(\text{Et}_4\text{N})_2\mathbf{38}$ in acetonitrile at 243–298 K reveal no inequivalence of *o*- $\text{C}_6\text{H}_4\text{NH}_2$ substituents nor any clear evidence of fluxional processes involving NH_2 groups on the NMR time scale (Figure 4.8). Chemical shifts are given in the experimental section (Chapter 8). The signals are well resolved due to the strong antiferromagnetic coupling of two $\{\text{Fe}^{2.5}\text{Fe}^{2.5}\}$ -pairs in the cluster.

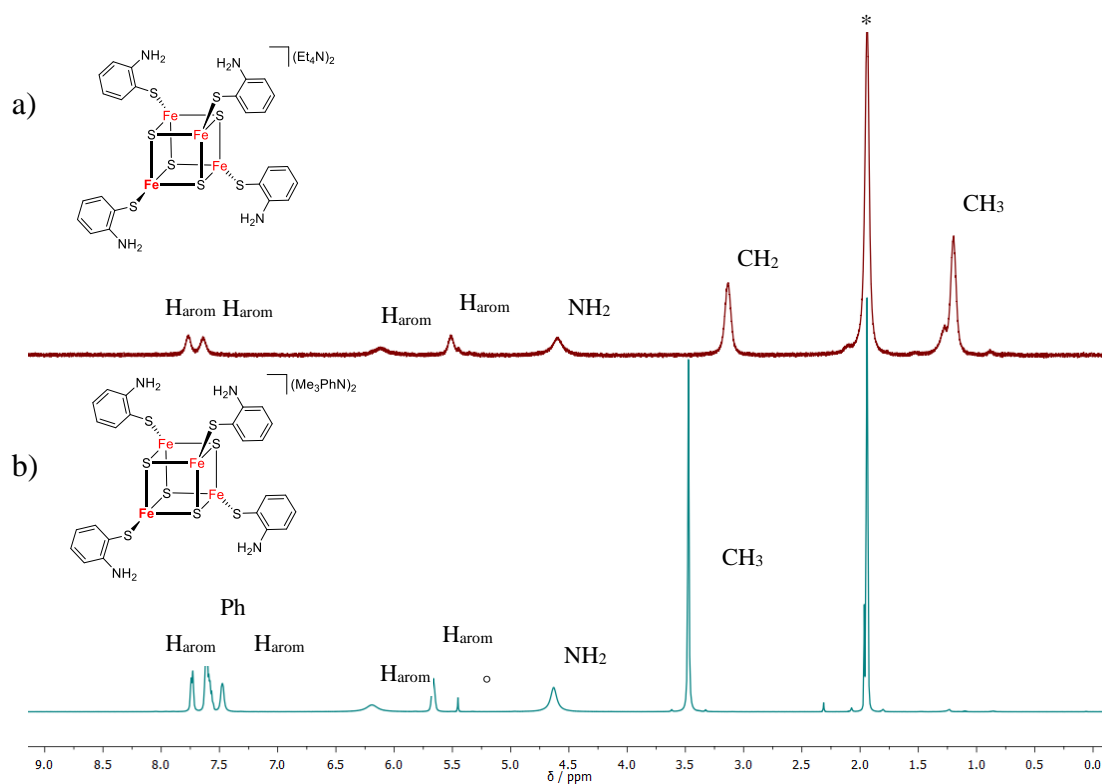


Figure 4.8: ^1H NMR spectrum of a) $(\text{Et}_4\text{N})_2\mathbf{38}$ at 298 K in MeCN-d_3 , b) $(\text{Me}_3\text{PhN})_2\mathbf{37}$ at 243 K in MeCN-d_3 . The asterisk (*) marks residual solvent signal and the circle (°) marks DCM.

4.3.4 Cyclic voltammetry

The cyclic voltammogram of $(\text{Me}_3\text{PhN})_2\mathbf{38}$ in MeCN ($0.1 \text{ M}^{-1} \text{ Bu}_4\text{NPF}_6$) compares well to the values measured in literature for $(\text{Et}_4\text{N})_2\mathbf{38}$ (Table 4.3). The first reduction is reversible with $E_{1/2} = -1.48 \text{ V vs. Fc}^{+/0}$ while the second reduction is irreversible with $E_{\text{pc}} = -2.11 \text{ V vs. Fc}^{+/0}$ at 100 mV/s (Figure 4.9, a). Although oxidative waves are not reported in literature, two irreversible anodic processes were recorded concomitant with precipitation on the working electrode (Figure 4.9, b). It appears that the first oxidation becomes quasi-reversible at higher scan rates while the second moves out of the measured potential.

Table 4.3. Redox properties of $(\text{Et}_4\text{N})_2\mathbf{38}$ and $(\text{Me}_3\text{PhN})_2\mathbf{38}$.

	$E_{1/2} / \text{V}$	$E_{\text{pc}} / \text{V}^{(b)}$	$E_{\text{pa}} / \text{V}^{(b)}$	$E_{\text{pa}} / \text{V}^{(b)}$
$(\text{Et}_4\text{N})_2\mathbf{38}$ in DMF ^(c)	-1.45	-2.07	–	–
$(\text{Me}_3\text{PhN})_2\mathbf{38}$ in MeCN ^(d)	-1.48	-2.11 ^(e)	-0.47 ^(e)	-0.18 ^(e)

(a) All potentials vs. $\text{Fc}^{+/0}$, (b) Irreversible reaction, (c) Johnson *et al.*: glassy carbon, SCE, $(n\text{-Bu}_4\text{N})\text{ClO}_4$, DMF,¹⁹⁵ (d) glassy carbon, Pt-wire, Ag-wire, $(n\text{-Bu}_4\text{N})\text{PF}_6$, MeCN, (e) at a scan rate of 100 mV/s .

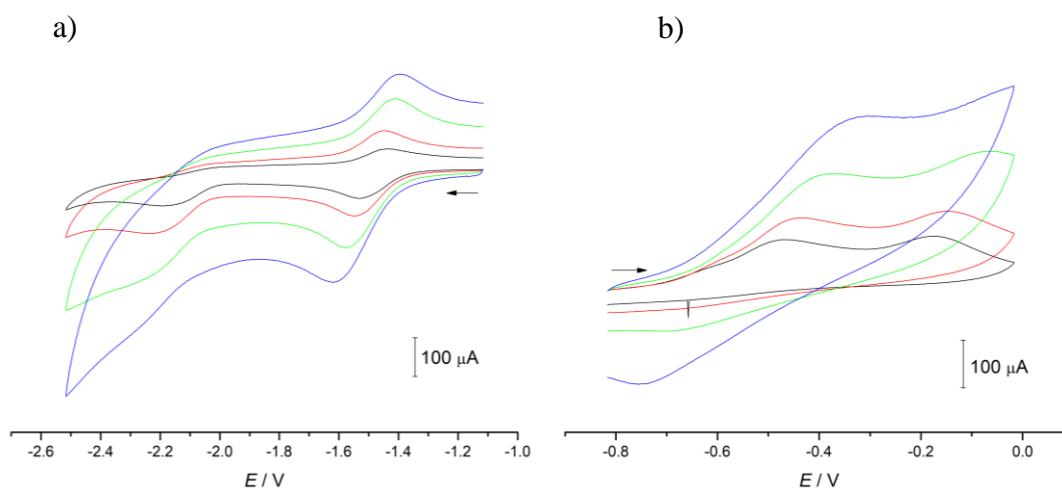


Figure 4.9. Cyclic voltammogram of $(\text{Me}_3\text{PhN})_2\mathbf{38}$ ($c = 1 \text{ mM}$) in MeCN/ $0.1 \text{ M NBu}_4\text{PF}_6$ at rt vs. $\text{Fc}^{0/+}$ at various scan rates ($v = 100, 200, 500, 1000 \text{ mV s}^{-1}$).

4.4 Conclusion

A [4Fe–4S] cluster was synthesized with four 2-aminothiophenolate ligands. Interestingly, the counter ion affects the packing of the molecules in the crystal yielding different structures for the anions of (NEt₄)₂**38** and (Me₃PhN)₂**38**. (NEt₄)₂**38** comprises a symmetric cubane core with four equivalent tetrahedral {FeS₄} sites.¹⁹⁵ The structure of the previously reported compound was now supported by crystallographic data in this work. Me₃PhN⁺ induces a change of one iron site to become pentacoordinate {FeS₄N}. The structural difference is reflected in Mössbauer spectroscopy with two doublets in a ratio of 3:1 for (Me₃PhN)₂**38**. The unique iron ion exhibits a more positive isomer shift and a larger quadrupole splitting than the other three iron ions. The doublets collapse into one single doublet when a frozen solution of (Me₃PhN)₂**38** is measured instead of crystals, suggesting that the site-differentiation is absent in solution. In fact, UV-vis and NMR spectroscopy confirm that the anion **38**²⁻ has the same configuration independent of the presence of (NEt₄)⁺ or (Me₃PhN)⁺ in solution. Finally, cyclic voltammetry was conducted. One reversible and one irreversible reduction was found for (Me₃PhN)₂**38** in accordance to previously reported results for (NEt₄)₂**38**.¹⁹⁵ Two irreversible oxidation waves were detected for (Me₃PhN)₂**38** of which the first appeared to become more reversible at high scan rates. Further investigations on the oxidation of **38**²⁻ are presented in the following chapter.

5 Oxidation of 38^{2-} with dioxygen and *p*-benzoquinone

5.1 Introduction and objective

Low-potential ferredoxins cycle between the resting state $[4\text{Fe-4S}]^{2+}$ and $[4\text{Fe-4S}]^+$ (midpoint potential at -0.4 V vs. SHE) while high-potential iron-sulfur proteins (HiPIPs) are oxidized from $[4\text{Fe-4S}]^{2+}$ to $[4\text{Fe-4S}]^{3+}$ (with midpoint potential of 0.3 V vs. SHE).¹⁰ The protein's structure and environmental influences dictate the potential of the $[4\text{Fe-4S}]$ cluster.¹⁹⁸ Therefore, normally only one, either oxidation or reduction, is observed for one specific $[4\text{Fe-4S}]^{2+}$ cluster in nature. An exception is found in the $[\text{NiFe}]$ hydrogenase of *Aquifex aeolicus* where a $[4\text{Fe-4S}]$ cluster is reported to be stable in all three oxidation states +1, +2, and +3.¹⁹⁹ In its usual enzymatic activity mode, the cluster switches between +1 and +2. The +3 state is a special response to oxidative stress.

In general, the $[4\text{Fe-4S}]^{2+}$ state is diamagnetic with two delocalized $\{\text{Fe}^{2.5+}\text{Fe}^{2.5+}\}$ pairs in the cluster core and the reduced/oxidized +1 and +3 states are paramagnetic (see Introduction 1.2.1). $[4\text{Fe-4S}]^{3+}$ consists of one delocalized mixed-valence pair $\{\text{Fe}^{2.5+}\text{Fe}^{2.5+}\}$ and a ferric $\{\text{Fe}^{3+}\text{Fe}^{3+}\}$ pair.^{200,201} Current research shows that HiPIPs are essential in many processes in the body. For example, the redox reaction between $[4\text{Fe-4S}]^{2+/3+}$ clusters serves as a switch for initiation and termination of human DNA primase²⁰² and as a modulator for the DNA-binding affinity of DNA repair proteins.²⁰³⁻²⁰⁵

Synthetic clusters imitate the natural ferredoxins well with a reversible redox reaction between the oxidation states +1/+2/+3 as $[\text{Fe}_4\text{S}_4(\text{SR})_4]^{3-/2-/1-}$ anion. However, the terminal oxidation to all ferric or reduction to all ferrous $[4\text{Fe-4S}]$ is usually irreversible.¹⁰ Tuning of the potential is possible via the steric demands of the substituent R, e.g., bulky substituents stabilize +3 states. Examples for synthetic $[4\text{Fe-4S}]^{3+}$ clusters were given in the introduction ($[\text{Fe}_4\text{S}_4(\text{N}\{\text{SiMe}_3\}_2)_4]$ (**11**⁻), $[\text{Fe}_4\text{S}_4(\text{STip})_3]$ (**12**⁰), $[\text{Fe}_4\text{S}_4(\text{SDmp})_3(\text{Me}_4\text{Im})]^-$ (**15**⁰), pp. 14). It is noteworthy that the symmetric cubane cluster with terminal amide ligands **11** is the only cluster that was isolated in three oxidation states (+2, +3, +4) as the bulky weak-field terminal amide ligands stabilize the high oxidation states of the core. In addition to the clusters above, results will be compared with the data from the symmetric cluster $[\text{Fe}_4\text{S}_4(\text{SDmp})_4]^-$ (**39**⁻).

In contrast to the isolated $[4\text{Fe-4S}]^{3+}$ clusters mentioned above, Le Pape *et al.* produced paramagnetic compounds from asymmetrical $(\text{Et}_4\text{N})_2$ **37** *in situ* for single-crystal EPR and

Proton-ENDOR measurements.^{196,197} The diamagnetic $[4\text{Fe-4S}]^{2+}$ sample was irradiated with γ -rays which created simultaneously the “oxidized” $[4\text{Fe-4S}]^{3+}$ and the “reduced” $[4\text{Fe-4S}]^+$ species. Both paramagnetic species were trapped at low concentration in a diamagnetic crystalline matrix and then measured.

5.2 Reaction of $\mathbf{38}^{2-}$ with dioxygen

The color of the solution of $\mathbf{38}^{2-}$ changed from brown to blue-violet once oxygen is allowed to diffuse into the solution via a cannula. This color change is monitored by UV-vis spectroscopy (Figure 5.1, a). The reaction is completed after 30 min with isobestic points at 354 and 480 nm. Apparently, the reaction rate is mainly controlled by diffusion. When a flask is opened to air and then stirred well or shaken the color change is immediate. The new compound $\mathbf{38}^{\text{ox}}$ exhibits intense bands at 550 and 305 nm tentatively assigned to ligand-to-metal charge transfer (LMCT). Similar bathochromic shifts of the major bands are reported for the oxidation of $\mathbf{11}^{2-}$ (amide ligand) and $\mathbf{12}^{2-}$ (thiolate ligand) and for HiPIPs in proteins.²⁰⁶ Comparison to other systems (Table 5.1) confirms the general trend, however, reasonable comparison is limited because different solvents are used and, most importantly, the energy of the LMCT severely depends on the ligand.

Although the cluster reacts readily with oxygen from air it is not stable under aerobic conditions for longer times. The characteristic band of $\mathbf{38}^{\text{ox}}$ at 550 nm in MeCN fades significantly when the solution is kept under air over 35 hours (Figure 5.1, b) suggesting the products degeneration.

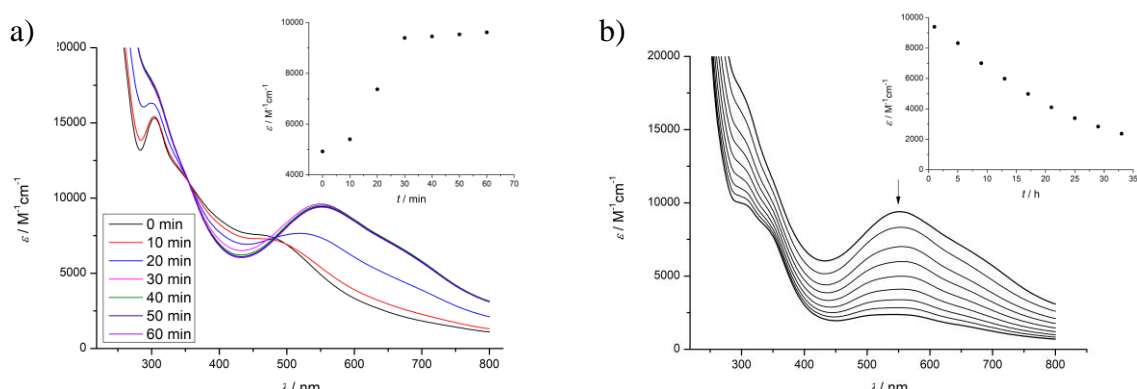
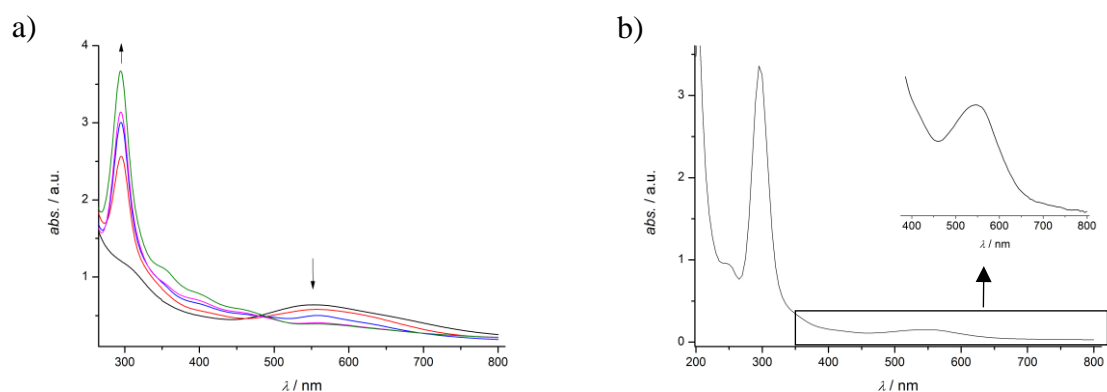


Figure 5.1. Reaction of $(\text{Me}_3\text{PhN})_2\mathbf{38}$ with O_2 in MeCN monitored by UV-vis spectroscopy. a) Reaction to intermediate with strong absorption at 550 nm, b) decay of $\mathbf{38}^{\text{ox}}$ over several hours. Both inserts depict ϵ vs. time at 550 nm.

Table 5.1. Electronic absorption data of clusters in the oxidation states $[4\text{Fe}4\text{S}]^{3+/4+}$. The oxidation state of $\mathbf{38}^{\text{ox}}$ is not assigned.

		solvent	λ [nm] (ϵ [$\text{M}^{-1}\text{cm}^{-1}$])	ref
$\mathbf{38}^{\text{ox}}$		MeCN	302 (sh, 18 300), 550 (18 000), 680 (sh, 9 700).	—
$\mathbf{39}^-$	$[4\text{Fe}4\text{S}]^{3+}$	DCM	236 (sh, 48 000), 276 (sh, 23 700), 328 (13 400), 475 (28 100).	100
$\mathbf{11}^-$	$[4\text{Fe}4\text{S}]^{3+}$	THF	257 (22 900), 404 (17 700), 630 (sh, 2400).	94
$\mathbf{11}^0$	$[4\text{Fe}4\text{S}]^{4+}$	THF	231 (19 900), 268 (21 900), 449 (19 400).	94
$\mathbf{15}^0$	$[4\text{Fe}4\text{S}]^{3+}$	THF	348 (17 000), 446 (14 000).	100

The oxidation product $\mathbf{38}^{\text{ox}}$ is not reactive towards H_2 or TEMPOH. CoCp_2^* and CoCp_2 can be used to reverse the oxidation as monitored by UV-vis spectroscopy (Figure 5.2, a). Subsequent opening of the cuvette to air reorges a band at 550 nm, but it is less intense (Figure 5.2, b).

Figure 5.2. UV-vis spectroscopy of a) titration of $\mathbf{38}^{\text{ox}}$ with CoCp_2^* , b) UV-vis spectrum after opening the vessel to air.

When a solution of $\mathbf{38}^{\text{ox}}$ in MeCN is measured a molecule peak at 843.7 m/z is detected in ESI(-)MS (Figure 5.3). A simulation of $[\mathbf{38} - 4\text{H}]^- (= \text{C}_{24}\text{H}_{20}\text{Fe}_4\text{S}_8\text{N}_4)$ calculates for the experimental value and isotopic pattern of that peak. This means that the $[4\text{Fe}-4\text{S}]$ core persists the oxidation process under the loss of 4 hydrogen atoms. The same peak at 843.7 m/z with the same isotopic pattern is seen in LIFDI-MS spectrum (Figure 8.7 in appendix).

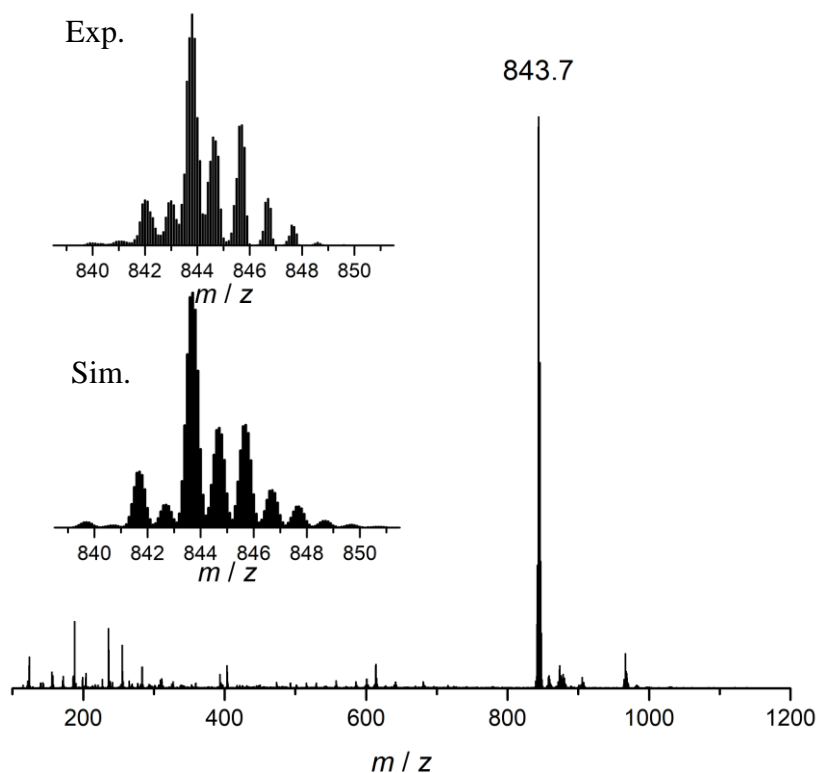


Figure 5.3. m/z range 100-1200 of the ESI(-)MS spectrum of 38^{ox} in MeCN. The insert depicts an excerpt of the spectrum from 1098 to 1113 m/z (top) and the simulated pattern for $[38 - 4 H]^-$ ($= C_{24}H_{20}Fe_4S_8N_4$).

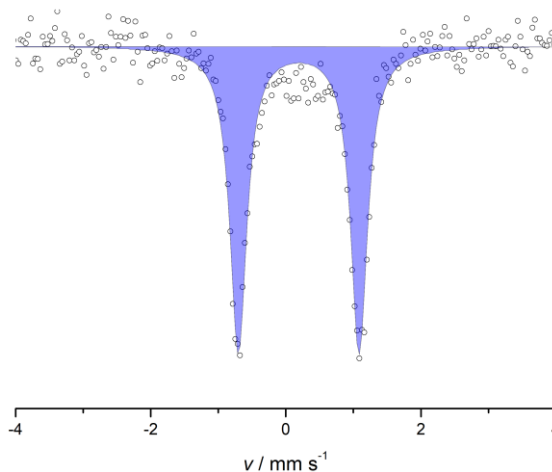


Figure 5.4. 38^{2-} in MeCN after exposure to air for 30 min and then frozen at 80 K.

$$\delta_{IS} = 0.19 \text{ mm s}^{-1}, \Delta E_Q = 1.79 \text{ mm s}^{-1}, \text{fwmh} = 0.3 \text{ mm s}^{-1}.$$

The Mössbauer spectrum of 38^{ox} (Figure 5.4) has only one doublet with a small isomer shift of 0.19 mm s^{-1} and a large quadrupole splitting of 1.79 mm s^{-1} . An isomer shift in that range is indicative for iron(III) ions. A guideline for the assignment of oxidation states to

Fe–S clusters is provided by the formula below for the Mössbauer isomer shift δ_{IS} in dependence on the oxidation number s at 77 K.¹⁰

$$\delta_{\text{IS}}/\text{mm s}^{-1} = 1.43 - 0.40s$$

The formula was inferred from a data set of known $\text{FeS}_n(\text{SR})_{4-n}$ sites ($n = 0, 2, 3$) in synthetic species. It is best applicable to $[\text{Fe}_4\text{S}_4(\text{SR})_4]^{2-,3-}$ clusters, but the nature of the counterion and the lattice can cause small modulations. For the isomer shift of $\mathbf{38}^{\text{ox}}$ (0.19 mm s^{-1}) the oxidation number s amounts to 3.1 which supports the assignments of four iron(III) ions. Rao *et al.* reported that a difference of 0.1 mm s^{-1} is typical for adjoining $[\text{4Fe-4S}]$ oxidation levels.¹⁰ The difference between $\delta_{\text{IS}}(\mathbf{38}^{2-})$ and $\delta_{\text{IS}}(\mathbf{38}^{\text{ox}})$ amounts to 0.24 mm s^{-1} . Therefore, two oxidation steps seem reasonable for $\mathbf{38}^{2-}$ which again supports the oxidation of two formally Fe(II) ions to Fe(III) ions in $\mathbf{38}^{\text{ox}}$.

A large quadrupole splitting implies a large electronic field gradient at the iron nucleus due to valence contributions from 3d-electrons or ligand contributions. As all d-orbitals are singly populated in Fe^{III} -hs complexes, the valence contribution can be largely excluded as reason. Therefore, deviation from total symmetric coordination, as is the case for five-fold coordination, can be one explanation for the larger quadrupole splitting in comparison to the quadrupole splitting of $\mathbf{38}^{2-}$. The small full-width-at-half-maximum (fwhm) of 0.3 mm s^{-1} does not allow for the fitting of several Fe-species. Therefore, all iron ions are probably in the same oxidation state and ligand environment.

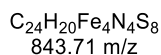
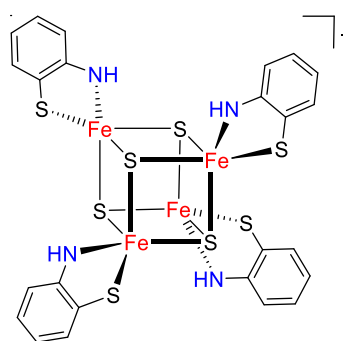


Figure 5.5. Proposed structure of $\mathbf{38}^{\text{ox}}$.

The isomer shift for amide ligated $\mathbf{11}^-$ and thiolate ligated $\mathbf{12}$ is more positive than for $\mathbf{38}^{\text{ox}}$ ($\mathbf{12} > \mathbf{11}^- > \mathbf{38}^{\text{ox}}$, Table 5.2). Unfortunately, no Mössbauer parameters are reported for $[\text{Fe}_4\text{S}_4(\text{SDmp})_4]^-$ or $\mathbf{15}^0$ to compare the data from this thesis to. The quadrupole splitting of

38^{ox} is much larger than that of all the clusters in [Fe₄S₄]³⁺ state, but similar to that of **11** in the [Fe₄S₄]⁴⁺ state.

Table 5.2. Mössbauer parameters for [Fe₄S₄]^{3+/4+} of model compounds and HiPIP protein from *C. vinosum*. α and β refer to the mixed-valence Fe^{2.5}-Fe^{2.5} pair or diferric Fe³⁺-Fe³⁺ pair, respectively. (*C.* = *Chromatium*)

		<i>T</i> / K		δ_{IS} / mm s ⁻¹	ΔE_{QS} / mm s ⁻¹	reference
38 ^{ox}		80		0.19	1.79	this work
11 ⁻	[Fe ₄ S ₄] ³⁺	4.2		0.33	1.35	94
11 ⁰	[Fe ₄ S ₄] ⁴⁺	4.2		0.26	1.67	94
12 ⁰	[Fe ₄ S ₄] ³⁺	4.2	α	0.40	1.05	96
			β	0.34	0.90	
12 ⁰	[Fe ₄ S ₄] ³⁺	100	α	0.39	0.79	96
			β	0.32	0.73	
<i>C. vinosum</i>	[Fe ₄ S ₄] ³⁺	4.2	α	0.40	1.03	207
			β	0.29	0.88	
		77		0.33	0.83	

38²⁻ was dissolved in DCM and exposed to air. Samples for EPR spectroscopy were taken from the reaction mixture after 5, 18, and 30 min, then frozen and measured (Figure 5.6). An isotropic signal with a *g*-value of 2.006 appears and intensifies over time. The EPR spectrum of [Fe₄S₄]³⁺ in proteins and model clusters are normally axial and their *g*_{av}-value is larger than the value for the free electron (*g*_e = 2.0023). In literature values are found between 2.0555–2.0693 (Table 5.3). Papaefthymiou *et al.* observed broad EPR lines for synthetic clusters compared to lines of protein due to considerable *g*-strain.⁹⁶ Nevertheless, model compounds achieve a good agreement with *g*-values for the HiPIP proteins with experimental values between 2.043 and 2.066. Pape *et al.* excluded that the paramagnetic species are free radicals on the ligands or on the counterions, since they would rather exhibit much less anisotropic *g*-tensors and resolved proton hyperfine structure.¹⁹⁶ In the case of **38**^{ox}, a free radical on the ligand cannot be excluded as the isotropic *g*-value is close to *g*_e. On the other hand, a [Fe₄S₄]³⁺ cluster seems not reasonable as the *g*-tensor is not axial and the *g*-value is too small.

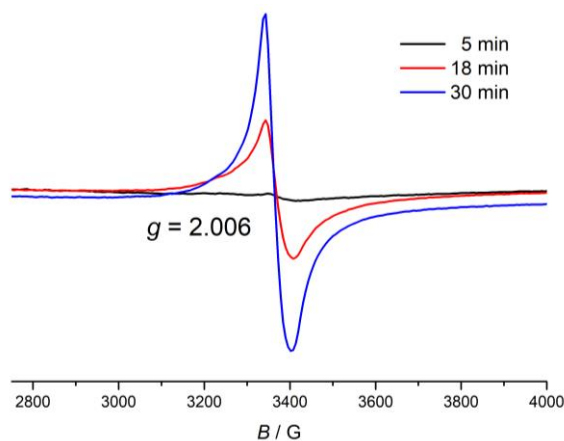


Figure 5.6. EPR spectrum of reaction mixture in frozen solution (DCM) at 159 K after 5, 18 and 30 min.

Table 5.3. Compilation of g_{av} -values for selected HiPIPs (*A.* = *Allochrochromatium*, *H.* = *Halorhodospira*, *R.* = *Rhodopila*, *E.* = *Ectothiorhodospira*, *Ru.* = *Rubrivivax*, *Rh.* = *Rhodocyclus*) and model compounds.

		g_{av} -values	ref
Model clusters:	$[\text{Fe}_4\text{S}_4(\text{SDmp})_4]^-$ (39 ⁻)	2.043	100
	$[\text{Fe}_4\text{S}_4(\text{STip})_4]$ (12 ⁰)	2.066	96
	$[\text{Fe}_4\text{S}_4(\text{SC}_6\text{H}_5\text{-}o\text{-OH})_4]^-$ (37 ⁻) a)	2.048, 2.041, 2.038	196
	$[\text{Fe}_4\text{S}_4(\text{SBn})_4]^-$ a)	2.053, 2.053, 2.054, 2.038, 2.055	208
	$[\text{Fe}_4\text{S}_4(\text{SPh})_4]^-$ a)	2.034	209,210
HiPIPs	<i>A. vinosum</i>	2.0626	211
	<i>H. halophila</i> isoprotein I	2.0693	211
	<i>R. globiformis</i>	2.0640	211
	<i>E. vacuolata</i> isoprotein I	2.0555	211
	<i>E. vacuolata</i> isoprotein II	2.0583	211
	<i>Ru. gelatinosus</i>	2.0579	211
	<i>Rh. tenuis</i>	2.0576	211

a) Data from single-crystal EPR measurements. Site multiplicity, i.e. different location for the mixed-valence pairs, was detected for asymmetric $(\text{Et}_4\text{N})_2\mathbf{37}$ (three centers) and symmetric $(\text{Et}_4\text{N})_2[\text{Fe}_4\text{S}_4(\text{SBn})_4]$ (five centers). In a fully symmetrical cluster each of six possible topologies for the mixed-valence pairs should be equally likely.

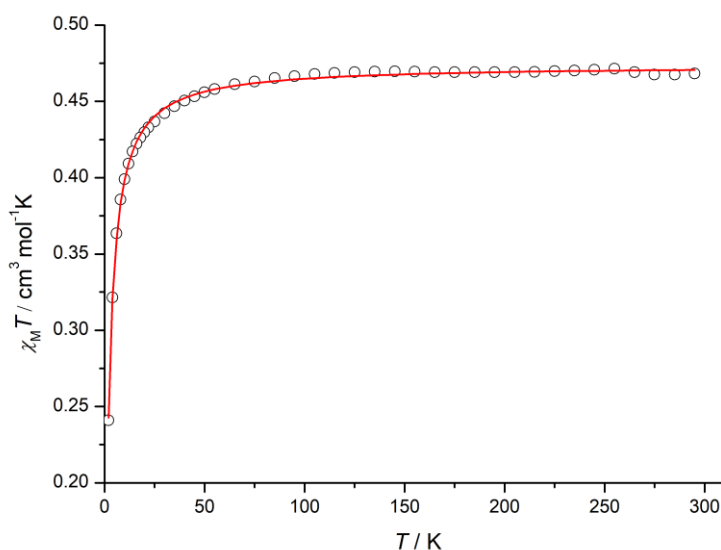


Figure 5.7. Plot of $\chi_M T$ vs. T for $\mathbf{38}^{\text{ox}}$ at applied field $B = 0.5$ T. The red solid line is a fit to the experimental values. Best fit parameters are: $g = 2.247$, Curie-Weiss temperature $\Theta = -1.893$ K, TIP = 1741.4×10^{-6} emu (subtracted).

Magnetic susceptibility measurements (SQUID) of precipitated $\mathbf{38}^{\text{ox}}$ confirm a spin of $1/2$. The g -value is 2.247 and therefore higher than the one determined with EPR spectroscopy. In order to achieve a good fitting of the data, temperature independent paramagnetism (TIP) was subtracted (1741.4×10^{-6} emu) and the Curie-Weiss parameter was set at -1.894 K.

In summary, reversible oxidation of $\mathbf{38}^{2-}$ is possible with dioxygen as monitored by UV-vis spectroscopy. ESI-MS and LIFDI-MS suggest that the cluster is still intact under the loss of four hydrogen atoms. Mössbauer provides evidence that only one iron species is present. The isomer shift is too low for $[\text{Fe}_4\text{S}_4]^{3+}$ suggesting that two oxidation steps took place and both Fe^{II} from the starting $[\text{Fe}_4\text{S}_4]^{2+}$ are oxidized to Fe^{III} . However, this electronic structure would produce an EPR-silent cluster due to antiferromagnetic coupling, as seen in the amide ligated $[\text{Fe}_4\text{S}_4]^{4+}$ cluster **11**. EPR and SQUID of $\mathbf{38}^{\text{ox}}$ measurements suggest a $S = 1/2$ spin system. It is not likely that the unpaired electron is localized on an iron as one would expect a more anisotropic pattern. The quadrupole splitting of $\mathbf{38}^{\text{ox}}$ is almost as large as for **11** in the oxidation state $[\text{Fe}_4\text{S}_4]^{4+}$. Normally, quadrupole splitting is a sign for the symmetry around the iron core. It seems to be asymmetric which could be due to a pentacoordination of the iron ions as depicted in Figure 5.5.

5.3 Equivalents of oxidant

It was not sufficiently possible to determine the oxidation state and charge of 38^{ox} with ESI-MS, Mössbauer and UV-vis spectroscopy. Therefore, a Clark electrode was used to identify the number of equivalents of dioxygen necessary for the oxidation of 38^{2-} to give 38^{ox} .

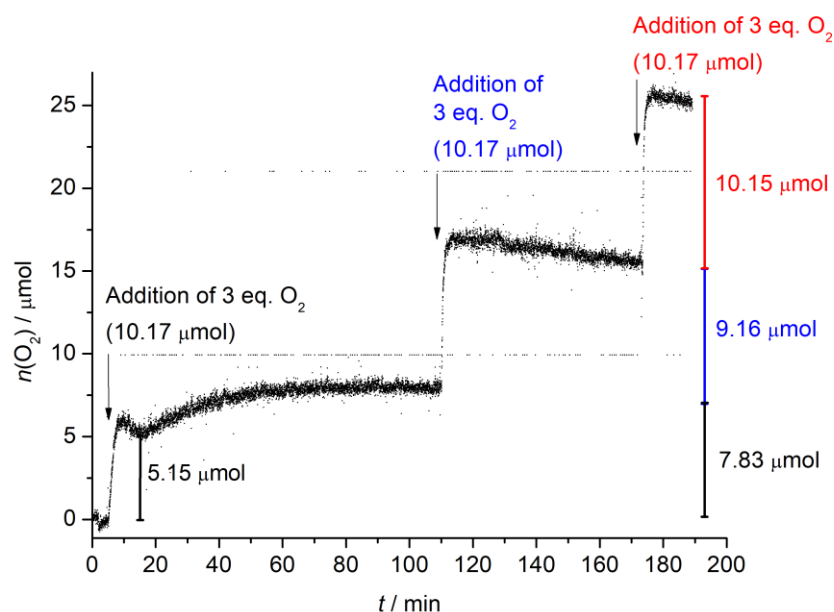
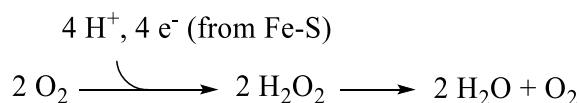


Figure 5.8. Oxygen uptake by 38^{2-} in MeCN.

After the calibration of the electrode in an air tight flask, 3×3 equivalents of dioxygen (10.17 μmol) were added with an air-tight Hamilton syringe into a solution of $(\text{Me}_3\text{PhN})_2\mathbf{38}$ in MeCN (Figure 5.8). The electrode detected a minimum of 5.15 μmol of oxygen in the gas phase above the solution after an induction period of 11 min. After that the level of oxygen rises to 7.83 μmol . At the lowest point 1.5 eq. of oxygen were consumed. Some of the oxygen was not detected probably because it was consumed right away by a fast reaction. The rise of dioxygen amount from 17–110 min could be explained by disproportionation of hydrogenperoxide to water and dioxygen (Scheme 5.1). This pathway would explain why the amount of O_2 first goes down and then rises again.



Scheme 5.1. Possible reaction pathway of oxygen during the oxidation of 38^{2-} .

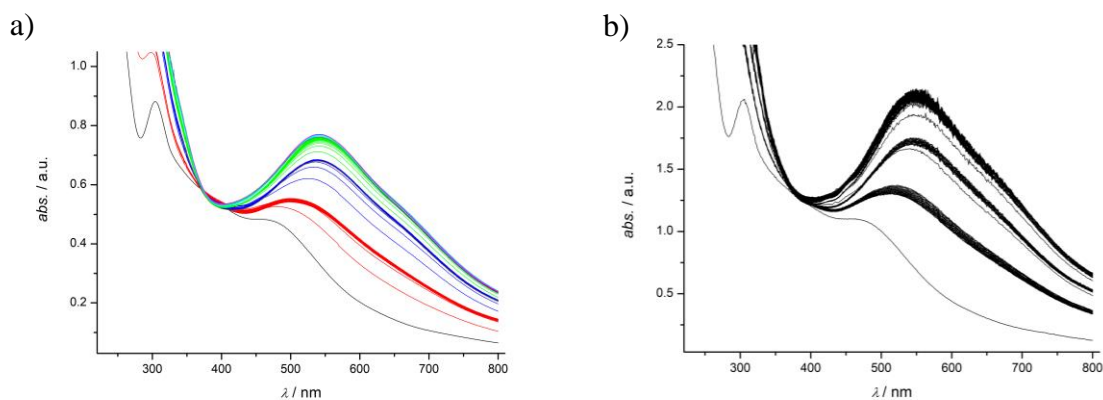
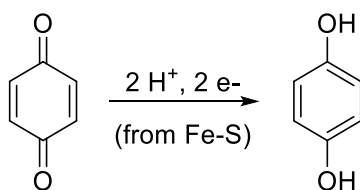


Figure 5.9: Titration of $(\text{Me}_3\text{PhN})_2\mathbf{38}$ with *p*-benzoquinone monitored by UV-vis spectroscopy. a) 1 eq. (red), 2 eq. (blue), 3 eq. (green), 4 eq. (cyan), 5 eq. (magenta). 30 min between each addition. One spectrum was measured every minute. b) Addition of 1–10 eq. while stirring and waiting in between at least 15 min.

As an alternative to dioxygen, other oxidants were tested in order to find the correct number of equivalents necessary for the reaction to take place. TEMPO did not react at all and a combination of DBU and thianthrenium tetrafluoroborate did not lead to reproducible results. DDQ seemed to degrade the complex, but addition of *p*-benzoquinone produced the characteristic band at 550 nm. It takes three equivalents of *p*-benzoquinone to reach full conversion (Figure 5.9). Addition of further equivalents does not affect a rise in absorption of the band 550 nm. According to the reaction in Scheme 5.2 three equivalents of *p*-benzoquinone account for the uptake of 6 protons and 6 electrons.



Scheme 5.2. Reduction of *p*-benzoquinone to hydroquinone.

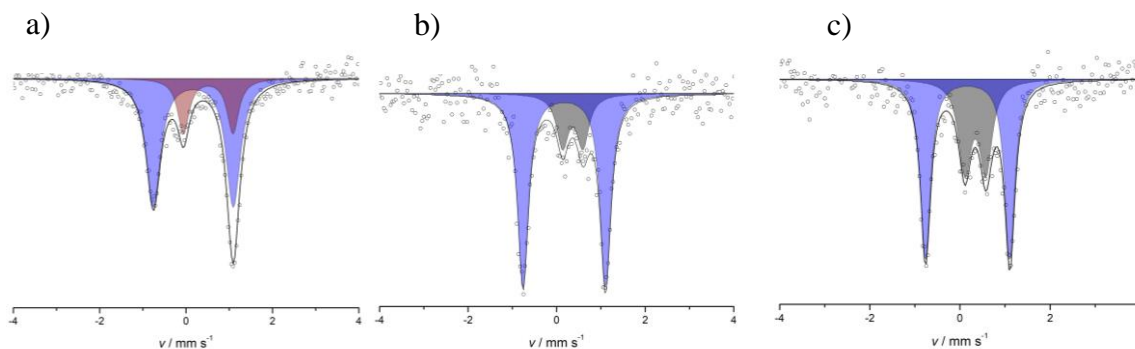


Figure 5.10. Zero-field Mössbauer spectra of $\mathbf{38}^{2-}$ and a) 2 eq. *p*-benzoquinone in THF/MeCN at 80 K, b) 3 eq. *p*-benzoquinone in MeCN at 80 K, c) 5 eq. *p*-benzoquinone in MeCN at 80 K.

Mössbauer spectra were measured of $\mathbf{38}^{2-}$ with 2, 3, and 5 equivalents of *p*-benzoquinone (Figure 5.10, Table 5.4). The blue subspectra have the same parameters as $\mathbf{38}^{2-}$ after the reaction with dioxygen. In the sample with two equivalents of *p*-benzoquinone unreacted starting material is still visible (red subspectrum). Besides $\mathbf{38}^{\text{ox}}$ another Fe containing product can be identified by Mössbauer spectroscopy after addition of 3 and 5 equivalents of *p*-benzoquinone (grey subspectrum). The more *p*-benzoquinone is added, the more side product is formed.

Table 5.4. Mössbauer parameters after addition of 2, 3 or 5 eq. *p*-benzoquinone to $\mathbf{38}^{2-}$ in MeCN at 80 K.

		$\delta_{\text{IS}} / \text{mm s}^{-1}$	$\Delta E_{\text{QS}} / \text{mm s}^{-1}$	ratio / %
$\mathbf{38}^{2-}$ + 2 eq. <i>p</i> -benzoquinone	blue	0.17	1.85	74.30
	red	0.51	1.15	25.70
$\mathbf{38}^{2-}$ + 3 eq. <i>p</i> -benzoquinone	blue	0.17	1.86	77.54
	grey	0.36	0.46	22.54
$\mathbf{38}^{2-}$ + 5 eq. <i>p</i> -benzoquinone	blue	0.17	1.87	62.76
	grey	0.34	0.47	37.24

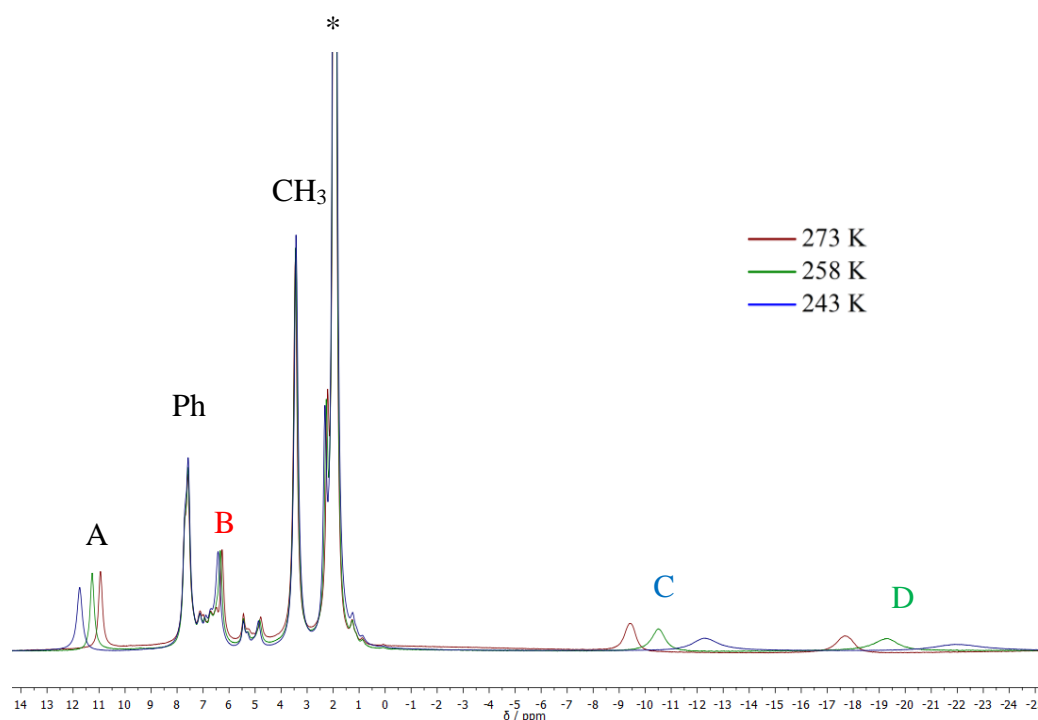
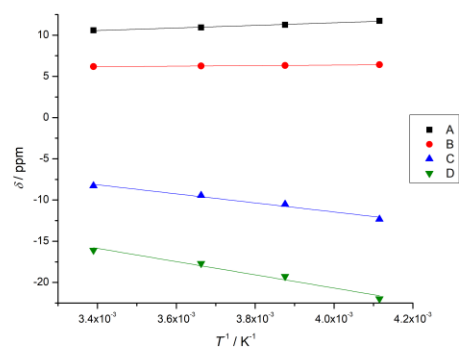


Figure 5.11. ^1H NMR spectrum of oxidation product 38ox . (*) denotes residual solvent. Paramagnetic signals that change their position in dependence on the temperature are marked with the letters A–D.

The NMR spectrum in Figure 5.11 was recorded one hour after the sample was exposed to an excess of O_2 at $-30\text{ }^\circ\text{C}$, $-15\text{ }^\circ\text{C}$ and $0\text{ }^\circ\text{C}$. While signals for diamagnetic species should show no significant shift with temperature, paramagnetic signals can be influenced quite strongly. Taking this in consideration, it is possible to assign the signals in Table 5.5 to a paramagnetic compound that evolved after exposure to O_2 . After the addition of *p*-benzoquinone as oxidant the same signals appear (Figure 5.12) in the proton NMR spectrum. Hydroquinone formation is proven by proton NMR spectroscopy ($\delta = 6.60\text{ ppm}$).

Table 5.5. ^1H NMR shifts of paramagnetic 38^{ox} in MeCN-d_3 .

	T / K	δ / ppm	δ / ppm	δ / ppm	δ / ppm
A	243	11.73	6.41	-12.32	-21.99
B	258	11.26	6.33	-10.50	-19.27
C	273	10.94	6.26	-9.44	-17.69
D	295	10.58	6.18	-8.28	-16.10



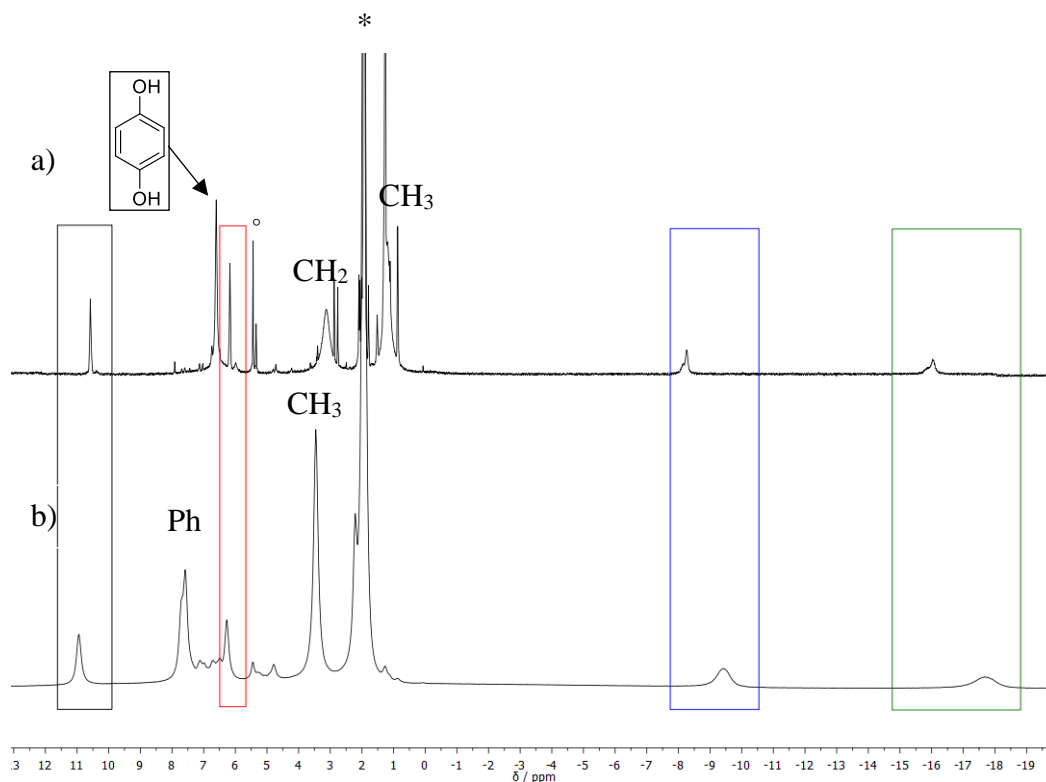


Figure 5.12. Comparison of the ^1H NMR spectra of a) $(\text{Et}_4\text{N})_2\mathbf{38} + 3$ *p*-benzoquinone and b) $(\text{Me}_3\text{PhN})_2\mathbf{38} +$ dioxygen. Little deviation in the chemical shift of the signals can be attributed to measuring at slightly different room temperature. (°) denotes DCM. (*) denotes residual solvent. A spectrum of the reaction in acetone- d_6 and Curie behavior thereof can be found in the appendix (Figure 8.8).

In summary, 38^{2-} reacts with approximately 1.5 equivalents of dioxygen or 3 equivalents of *p*-benzoquinone. Both oxidants yield 38^{ox} as reaction product according to UV-vis, Mössbauer, and ^1H NMR spectroscopy. The number of equivalents was determined by a Clark electrode or UV-vis spectroscopy, respectively. The result would imply that in both cases 6 electrons and 6 protons are abstracted from the cluster according to Scheme 5.1 and Scheme 5.2. However, these numbers should be treated with caution for three reasons. Firstly, dioxygen can be reduced to either H_2O_2 or H_2O and the reaction mechanism is not fully elucidated yet. Secondly, a side product is detected in the Mössbauer spectrum after the reaction of 38^{2-} with *p*-benzoquinone. Apparently, a surplus of oxidant causes the degradation of 38^{ox} and an increase of the amount of side product. Thirdly, abstraction of 6 H atoms is contradicted by the ESI-MS spectrum of 38^{ox} (Figure 5.3) in which the molecular ion peak has a mass of $[\mathbf{38}-4\text{H}]$.

5.4 Conclusion

Oxidation of **38**²⁻ with dioxygen or *p*-benzoquinone afforded a UV-vis spectrum with a prominent band at 550 nm ($\epsilon = 9\,600\text{ cm}^{-1}\text{M}^{-1}$). This bathochromic shift from 484 nm ($\epsilon = 7700$) is typical for oxidation of [4Fe-4S] clusters. The oxidation product was stable under air for a few hours. The oxidation could be reversed with CoCp^*_2 , however, subsequent exposure to air only retrieved the band at 550 nm with less intensity in the UV-vis spectrum.

ESI-MS of **38**^{ox} suggested that the cluster core was still intact but indicated the loss of four hydrogen atoms. Mössbauer spectroscopy showed only one doublet with an isomer shift of 0.19 mm s^{-1} and a quadrupole splitting of 1.79 mm s^{-1} . According to this data, all four iron ions are in the oxidation state +3 and they are bidentally bound by the amine and the thiolate of 2-aminothiophenolate. Mössbauer data of the only reported all-ferric [4Fe-4S]⁴⁺ cluster **11** compare well to **38**^{ox} with an isomer shift of 0.26 mm s^{-1} and a quadrupole splitting of 1.67 mm s^{-1} . [4Fe-4S]³⁺ clusters, on the other hand, have a significantly higher isomer shift of $0.32\text{--}0.40\text{ mm s}^{-1}$ and smaller quadrupole splitting of $0.73\text{--}1.35\text{ mm s}^{-1}$.

All-ferric [4Fe-4S]⁴⁺ clusters are EPR-silent. However, a spin of $S = \frac{1}{2}$ was detected on **38**^{ox} with EPR spectroscopy and SQUID magnetometry. NMR-spectroscopy confirmed Curie-behavior of the paramagnetic compound.

The number of equivalents of oxidant was quantified with a Clark electrode (O₂) and UV-vis spectroscopy titration (*p*-benzoquinone). Results point towards a mechanism involving 6 electrons/6 protons. However, Mössbauer spectroscopy identified a Fe-containing side product insinuating that a surplus of oxidant leads to degradation of **38**^{ox}.

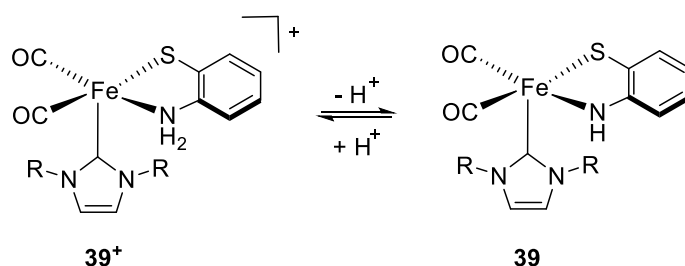


Figure 5.13. Iron complex with similar binding motif as **38**²⁻ (R = Mes).

In conclusion, further investigations are necessary to elucidate the structure of **38**^{ox}. A pentacoordinate iron complex with the same ligand was published in 2016. Jiang *et al.* synthesized the mononuclear 1s-Fe^{II} complex **39** with a similar binding motif as is proposed for **38**^{ox} (Figure 5.13).²¹² A proton can be removed from **39**⁺ with *t*-BuOK and then again

added with HBF₄. This example points towards an easy proton abstraction from the amine and a preferred pentacoordination of the iron ion. However, **38**^{ox} only reacted under simultaneous abstraction of electrons and protons in contrast to **39**⁺. Also, the strong-field ligands of **39** impose a 1s spin state. It is probably due to their different oxidation and spin state that the two complexes exhibit ultimately different reaction behavior.

6 Protonation of 5,6-Dithia-1,10-phenanthroline, its application as disulfide/dithiol switch, and as ligand for [2Fe–2S] clusters

6.1 Introduction and objective

2,2'-bipyridines are important ligands for complexation of metal ions and they are widely used as parts of “photosensitizer”, especially with ruthenium as central atom ($[\text{Ru}(\text{bpy})_3]^{2+}$).^{213,214} The complex absorbs light via metal to ligand charge transfer (MLCT) at 452 nm, ligand centered transition (285 nm) and metal centered transition (350 nm). The resulting MLCT excited state $[\text{Ru}(\text{bpy})_3]^{2+*}$ has a comparatively long lifetime (0.9 μs in MeCN) due to a forbidden singlet-triplet transition. The triplet excited state has both oxidizing and reducing properties. Exchange of one pyridine ring with imidazole allows for proton coupled electron transfer (PCET).²¹⁵ Extensive literature is dedicated to modification and functionalization of bipyridines with altered electronic and steric properties.^{216,217}

Light-driven reduction of Fe_2S_2 complexes and related systems has been an active topic of research in recent years.^{218–221} Not yet reported complex **40** combines two active sites: a chromophore ($\text{Ru}(\text{bpy})_3$) and an electron storage moiety (Fe-S cluster). Due to the covalent linkage, the electronic communication between the two sites would be more effective than in multicomponent systems like the triad system in Figure 6.1, b.²²² Here, photoinduced electron transfer results ultimately in the reduction of the Fe-Fe complex mimicking the iron-only hydrogenase.

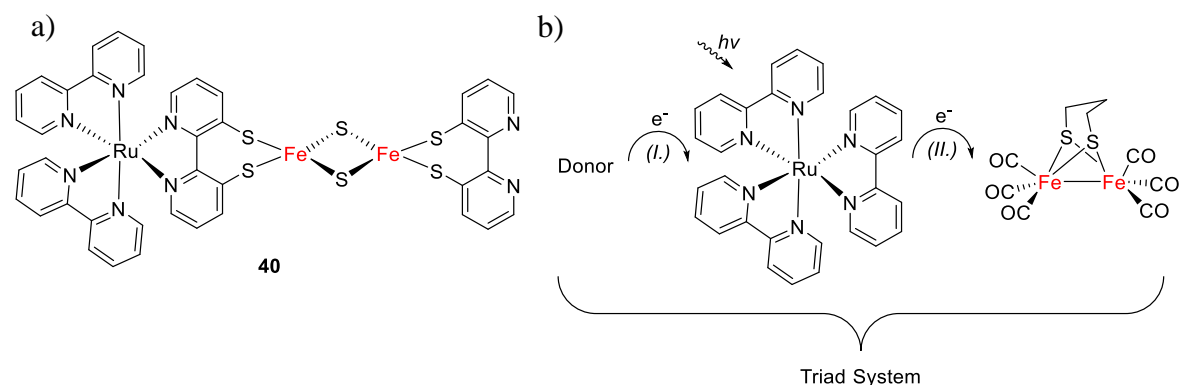


Figure 6.1. a) Target compound **40**, a coupled $\text{Ru}(\text{bpy})_3$ -[2Fe–2S] molecule, b) bioinspired triad system for photoinduced electron transfer, (I.) reductive quenching, (II.) intermolecular electron transfer.²²²

6 Protonation of 5,6-Dithia-1,10-phenanthroline, its application as disulfide/dithiol switch, and as ligand for [2Fe–2S] clusters

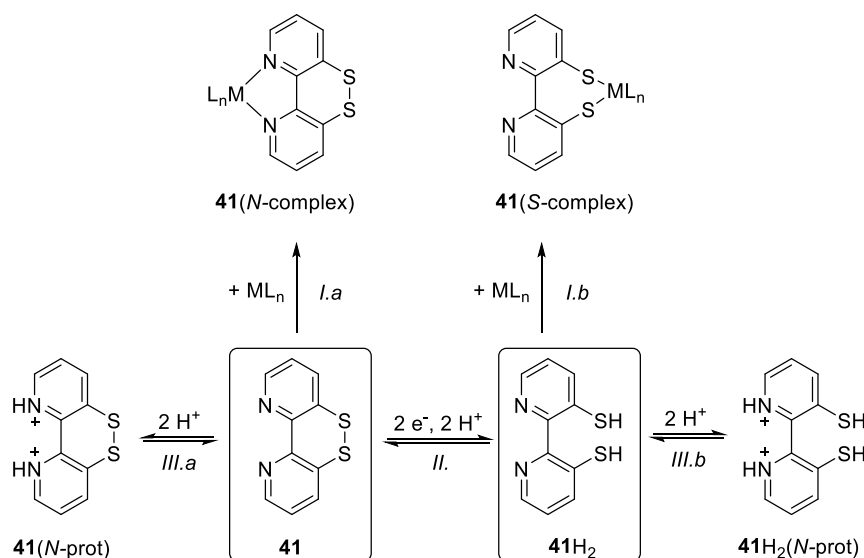


Figure 6.2. Compound **41** and its reactivity: *I.a*) *N*-coordination to metal, *I.b*) *S*-coordination to metal, *II*) disulfide/dithiol switch, *I.a*) and *b*) protonation at the pyridine-*N*.

The first step towards target molecule **40** is the synthesis of the linking bipyridine ligand. Cattaneo developed the synthesis of 5,6-dithia-1,10-phenanthroline (**41**) in our group.²²³ Patents for **41** have been filed, but they do not give any details on the synthesis.^{224,225} **41** is versatile in terms of its application due to two functional sites (Figure 6.2): the bipyridine-*N* atoms on one hand and the disulfide/dithiol on the other. The coordination to a metal ion can take place via the *N*-atoms (*I.a*) or the *S*-atoms (*I.b*), if the disulfide bridge is cleaved. Route *I.a* is preferred for Ru-complexes. In this thesis, route *I.b* will be explored as Fe–S clusters are prone to binding to thiols. Preliminary results on [2Fe–2S] cluster **42²⁻** (Figure 6.3) will be presented. Here, the pyridine-*N* can serve as coordination site for protons, Lewis acids or, as desired, for metals/complexes.

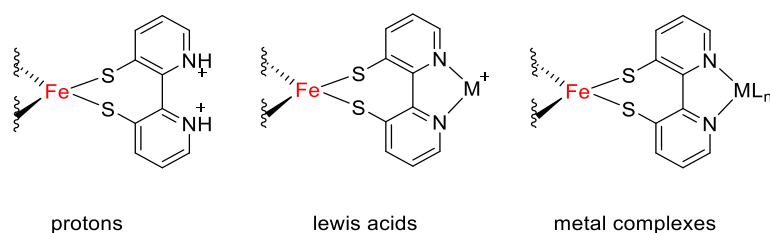


Figure 6.3. [2Fe–2S] cluster with **41** as ligand (**42²⁻**, top) and possible further reactivity of cluster **42²⁻** (bottom).

The redox properties of **41** were investigated thoroughly as part of this thesis. The disulfide bond can be opened reversibly via a two-electron two-proton reaction (Figure 6.2, step *II*). These disulfide/dithiol switches are important in redox control and charge storage in biochemical systems and offer the opportunity for multiple electron storage.^{226,227}

Reactivity of **41** towards acid is also of interest as protonation can occur on the bipyridine-*N* site (*III.a* and *b*) and will be presented in the subchapter 6.3.

6.2 Synthesis of the ligand

Some parts of this chapter have been adapted from a submitted manuscript.²²³

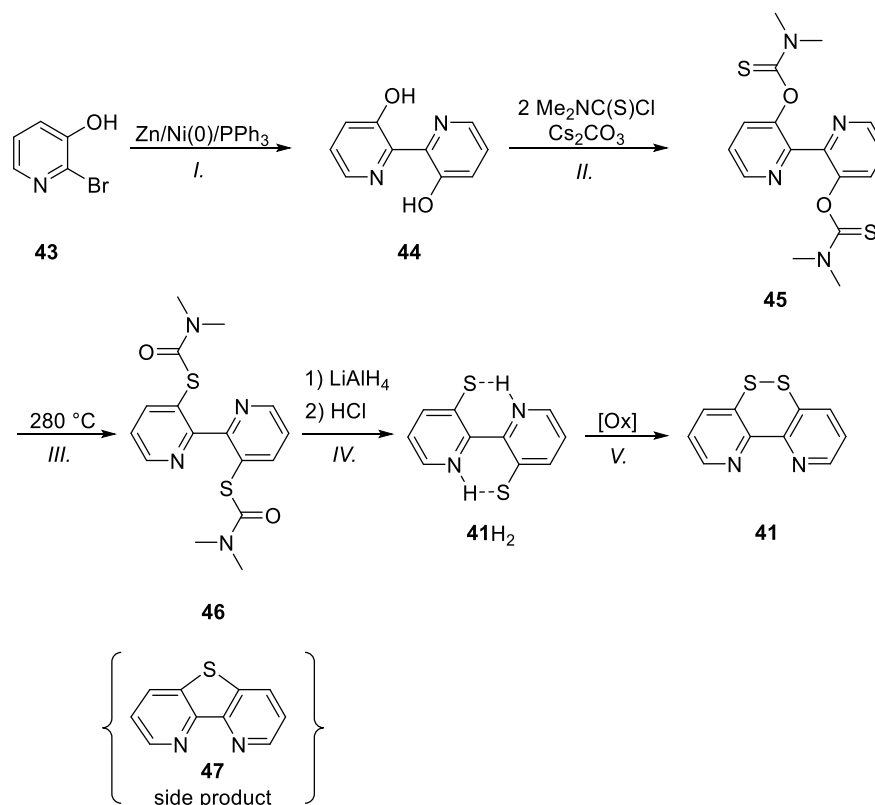


Figure 6.4. Synthesis of [1,2]dithiino[4,3-b:5,6-b']dipyridine **41**. *I.* DMF, 50 °C, 24 h, *II.* acetone, reflux, 24 h, *III.* powder, 7 min, *IV.* THF, 50 °C, 3 h, *V.* O₂, DCM.

[1,2]dithiino[4,3-b:5,6-b']dipyridine **41** was obtained by a multistep synthesis initially developed by Cattaneo (Figure 6.4).²²³ For this thesis, the reaction conditions in step *II* were modified in order to improve the yield of **45**. Caesium carbonate was used instead of sodium hydride as base and the reaction time was increased. Generally, Newman-Kwart rearrangement reactions as in step *III* require high temperature and a reaction time of 1–2 hours in order to ensure quantitative yields. However, careful optimization of the reaction condition was necessary in order to minimize the amount of side products, for instance, thieno[3,2-b:4,5-b']bipyridine (**47**). Experiments with microwave instead of thermal energy to avoid the formation of **47** were unsuccessful. HPLC was not able to properly separate the not-rearranged (**45**), once-rearranged, twice rearranged (**46**), and the mono-sulfur compound (**47**). Therefore, the procedure developed by Cattaneo was applied for

step III–V. After reduction with LiAlH₄ (step IV) the product oxidizes to **41** when handled under air. It is obtained as a pale yellow oil. Work-up of **46** under argon atmosphere and with degassed water results in isolation of the new compound **41H₂**. Recrystallization from toluene yields red crystals suitable for X-ray crystallography (Figure 6.5). **41H₂** crystallizes in the space group monoclinic *P2₁/c*. The pyridine units are in *anti* orientation. The zwitterionic form is preferred for the hydrogen bonding between thiols and pyridinic-nitrogen atoms. Hydrogen atom positions have been refined freely giving bond distances to the bridging hydrogen of $d(\text{S1}\cdots\text{H1}) = 2.02(2)$ Å and $d(\text{N1}-\text{H1}) = 0.92(2)$ Å, respectively, and an angle $\angle(\text{N1}-\text{H1}\cdots\text{S1})$ of $1.58(2)^\circ$.

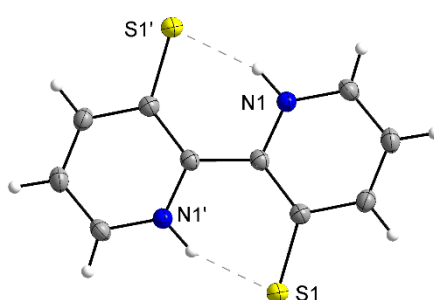


Figure 6.5. Molecular structure of **41H₂** determined by X-ray crystallography. The thermal displacement ellipsoids are shown at 50% probability. Selected bond lengths [Å] and angles [°]: S(1)–C(2) 1.7318(16), N(1)–C(5) 1.337(2), N(1)–C(1) 1.357(2), C(5)–N(1)–C(1) 125.46(15). Hydrogen bonds for **40H₂** [Å and °] N(1)–H(1) 0.92(2), S(1)⋯H(1) 2.02(2), N(1)–H(1)⋯S(1) 1.58(2). Symmetry transformation used to generate equivalent atoms: (') 1–x, 1–y, 1–z.

6.3 UV-vis titration of **41** with PhCOOH, TFA and TfOH in MeCN

Some parts of this chapter have been adapted from a submitted manuscript.²²³

Cattaneo measured UV-vis spectra of pale yellow **41** in buffered, neutral water and reported bands at 270 and 305 nm ($\pi-\pi^*$) and a weaker, broad absorption at 380 nm ($n-\pi^*$). He observed that protonation of **41** causes a bathochromic shift of all bands to 279, 322, and 423 nm with isosbestic points indicating clean interconversion between **41** and its protonated form. He derived a pK_a value of 2.88(1) from pH dependent UV-vis titrations. The pK_a value of **41** is substantially lower than that of parent 2,2'-bipyridine ($pK_a = 4.45$)²²⁸ or phenanthroline ($pK_a = 4.84$).²²⁹ NMR spectroscopy confirmed the bipyridine-N as the protonation site.

Cattaneo conducted his protonation experiments in buffered water. However, a change of the solvent to MeCN was needed in order to prove that it is appropriate for the CV experiments presented in chapter 6.4. The band at 270 and 305 nm of **41** were badly resolved because

the window for UV spectra closes around 300 nm for the solvent MeCN. On grounds of the previous results by Cattaneo, UV-vis titrations were conducted with three different acids, namely, benzoic acid (PhCOOH, $pK_{a,MeCN} = 21.51$),²³⁰ trifluoroacetic acid (TFA, $pK_{a,MeCN} = 12.65$)²³¹ and trifluoromethanesulfonic acid (TfOH, $pK_{a,MeCN} = 2.60$).²³¹

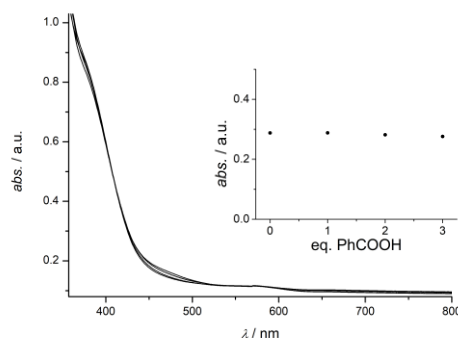


Figure 6.6. Titration of **41** with benzoic acid (PhCOOH) in MeCN. The insert shows that no change in absorbance is observed at 423 nm.

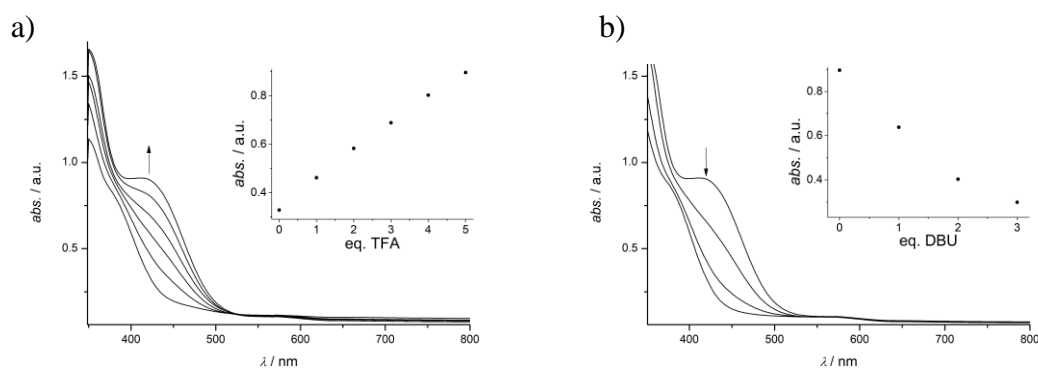


Figure 6.7. a) Titration of **41** with trifluoroacetic acid (TFA) in MeCN, b) backtitration with 1,8-diazabicyclo(5.4.0)undec-7-ene (DBU) in MeCN. Inserts show absorbance vs equivalents of TFA or DBU at 423 nm.

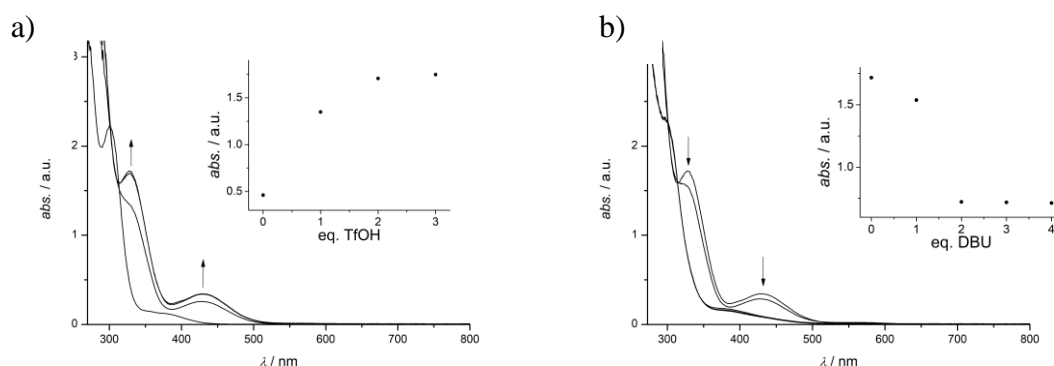


Figure 6.8. a) Titration of **41** with trifluoromethanesulfonic acid (TfOH) in MeCN, b) backtitration with 1,8-diazabicyclo(5.4.0)undec-7-ene (DBU) in MeCN. Inserts show absorbance vs equivalents of TfOH or DBU at 329 nm.

Addition of PhCOOH does not cause a change in the UV-vis spectrum (Figure 6.6) while addition of TFA affects a rise of bands assigned to the protonation product (Figure 6.7, a). Full protonation of **41** is achieved after addition of 2 equivalents of TfOH (Figure 6.8, a). The same bands are observed as reported for the protonation of **41** in buffered water by Cattaneo. Backtitration to the original spectrum was possible by addition of DBU (Figure 6.7 and 6.8, b).

Based on these observations, PhCOOH is too weak to protonate **41** in MeCN, but with TFA the spectrum of the protonated species is replicated. Therefore, the pK_a for the first protonation of **40** must be between 21.51 and 12.65 in MeCN. As 2 equivalents of the strong acid TfOH are needed, it is reasonable to aver that with each equivalent one pyridine-N atom is protonated yielding the proposed structures for the protonated species in Figure 6.9.

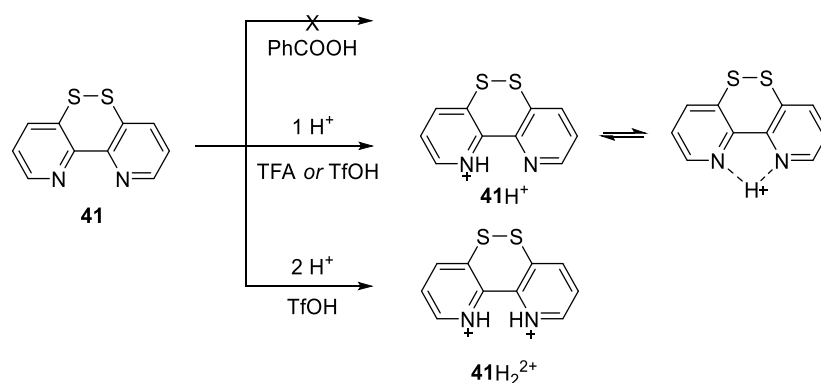


Figure 6.9. Proposed protonation of **40** with PhCOOH, TFA, and 1 or 2 equivalents of TfOH.

6.4 S–S bond cleavage mechanism: the disulfide/dithiol switch

Some parts of this chapter have been adapted from a submitted manuscript.²²³

Cyclic voltammetry and DFT calculations were conducted in order to decipher the mechanism of the reductive S–S bond cleavage of compound **41**. The voltammogram of **41** in MeCN (0.1 M Bu₄NPF₆) exhibits one reduction with a peak potential of –1.76 V and a re-oxidation at –0.74 V vs. ferrocene at a scan rate of 100 mV s^{–1} (Figure 6.10, a). The absolute value of the peak current $I_{p,c}$ of the reduction wave increased linearly with the square root of the scan rate (0.1 – 10 Vs^{–1}), which is characteristic for diffusion controlled processes (Figure 6.10, b). The cathodic and anodic wave are separated by approximately 1000 mV. This large separation and the linear shift of the cathodic peak potential $E_{p,c}$ per

$\log(\nu)$ (Figure 6.10, c) is indicative for either an irreversible electron transfer process or (ir)reversible electron transfer processes followed by a fast chemical reaction. The second would be the case for reductive S–S bond cleavage.

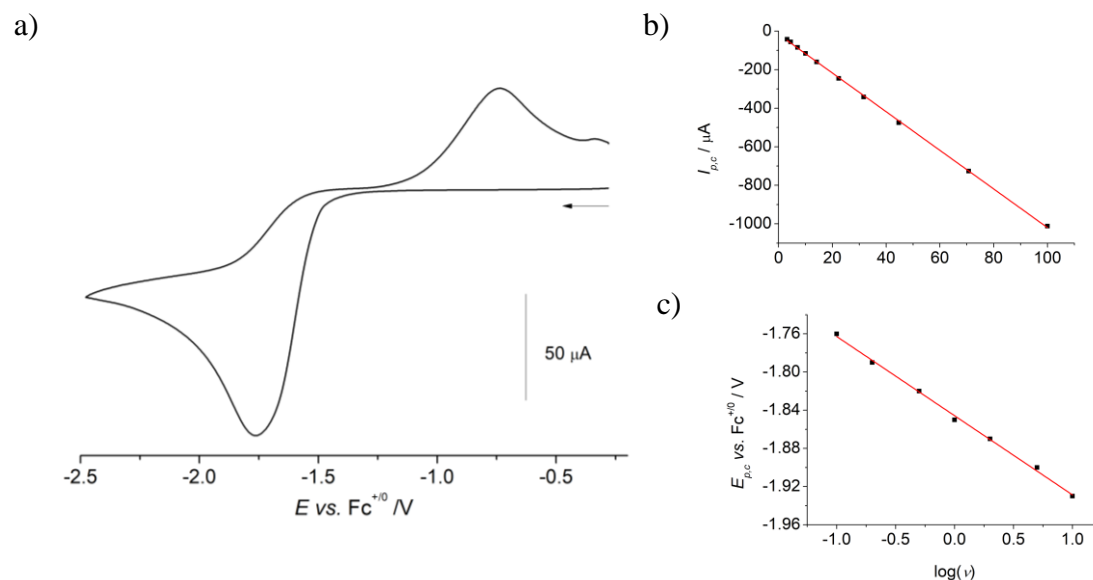


Figure 6.10. a) Cyclic voltammogram of **41** in MeCN at rt (0.1 M Bu_4NPF_6 , $c(\mathbf{41}) = 3.1$ mM), $\nu = 100$ mVs^{-1} , b) peak current $I_{p,c}$ vs. $\nu^{1/2}$, c) cathodic peak potential $E_{p,c}$ vs. $\log(\nu)$.

Similar voltammograms have been reported for compounds **48–50** (Figure 6.11). The S–S bond cleavage mechanism has been thoroughly investigated for 8-diiodo-dibenzo[1,2]dithiine (**48**),²³² 4,4'-bipyridyl-3,3'-disulfid (**49**),²³³ and disulfide-strapped N,N-alkylated bipyridinium cation (viologen, **50**).²³⁴ The respective authors conclude a EEC mechanism for **48** and EE mechanism for **49** and **50**. In other accounts, a ECE mechanism is described for S–S bond cleavage in diaryl disulphides.²³⁵

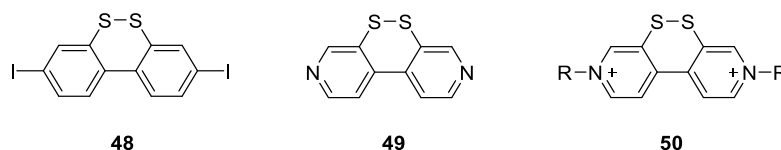


Figure 6.11. Well-investigated molecules with disulfide/dithiol switch.^{232–234}

In order to elucidate the details of the reduction mechanism of **41**, DFT studies were performed by Dr. Dechert in our group; computational details can be found in the respective publication.²²³ It was found that the LUMO of **41** has antibonding character with respect to the S–S bond provoking a significant elongation of the S–S bond from 2.076 to 2.747 Å upon the first reduction (Figure 6.12). The SOMO of **41**[–] has σ^* S–S antibonding character (Figure 6.12, b). Further reduction of **41**[–] results in twisting of the pyridine rings and S–S

bond cleavage according to DFT calculations. The two-electron reduced product, **41**²⁻, exhibits a C–S⋯S–C torsion of $\varphi = 94^\circ$ and a long S⋯S separation of 4.398 Å, thus any bonding interactions are no longer present (Figure 6.12, c). The close to orthogonal orientation of the pyridine rings in **41**²⁻ results as a compromise between electrostatic repulsion of the two thiolates and repulsive interactions between the thiolate and pyridine-N lone pairs. In conclusion, the DFT calculations suggest an EEC mechanism for the reduction of **41**. After the first reduction the S–S bond is elongated, but not cleaved. S–S bond breakage occurs only after a second electron is added.

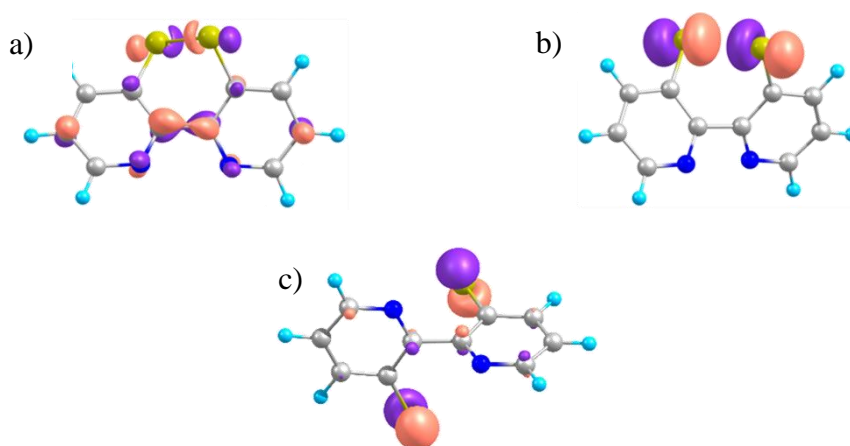


Figure 6.12. a) LUMO of **41** (contour value: 0.08), torsion angle $\varphi(\text{C-S-S-C}) = 49.1^\circ$, $d(\text{S-S}) = 2.076 \text{ \AA}$; b) SOMO of **41**⁻ (contour value: 0.08), c) HOMO of **41**²⁻ (at global minimum with $\varphi = 94.1^\circ$; contour value: 0.08), torsion angle $\varphi(\text{C-S}\cdots\text{S-C}) = 94^\circ$, $d(\text{S}\cdots\text{S}) = 4.398 \text{ \AA}$.

The experimental CV data, which were recorded as part of this thesis, were then simulated by Prof. Dr. Siewert with the software *DigiElch* to experimentally substantiate the proposed EEC mechanism. Simulations were carried out for sweep rates of 0.1 to 10 Vs⁻¹, and the entire curves were simulated (Figure 6.13). Good simulations could be achieved using reasonable values for the various parameters over the entire sweep rate range. The initial reduction of **41** to give **41**⁻ exhibits a potential of -1.20 V at a rather small electron transfer rate $k_{s,1}$ of $1 \times 10^{-5} \text{ cm s}^{-1}$, likely due to the significant structural change accompanying the reduction. The second reduction to give **41**²⁻ occurs at a slightly lower potential of -1.38 V ($k_{s,2} = 1 \times 10^{-4} \text{ cm s}^{-1}$) and is followed by a fast chemical reaction with a rate constant $k_{c,1} \geq 50 \text{ s}^{-1}$ leading to **41**²⁻(*open*). The second reduction hence occurs at a more negative potential than the first reduction, in contrast to what has been proposed previously for related dithiins **48** and **49**. Fast chemical reaction upon twofold reduction is consistent with S–S bond breaking and twisting of the pyridine units against each other.

The anodic feature can be modelled by re-oxidation of $\mathbf{41}^-$ (*open*) at a potential of E_3 of -1.15 V ($k_{s,3} = 1 \times 10^{-4}$ cm $^{-1}$) and subsequent very fast chemical reaction forming $\mathbf{41}^-$ ($k_{c,2} \geq 100$ s $^{-1}$). A further unproductive pseudo first order chemical side reaction has to be considered to successfully model the data ($k_{c,3}$ in Figure 6.13), which likely reflects the partial protonation of $\mathbf{41}^{2-}$ (*open*) forming $\mathbf{41H}_2$ due to traces of water in the solvent MeCN.

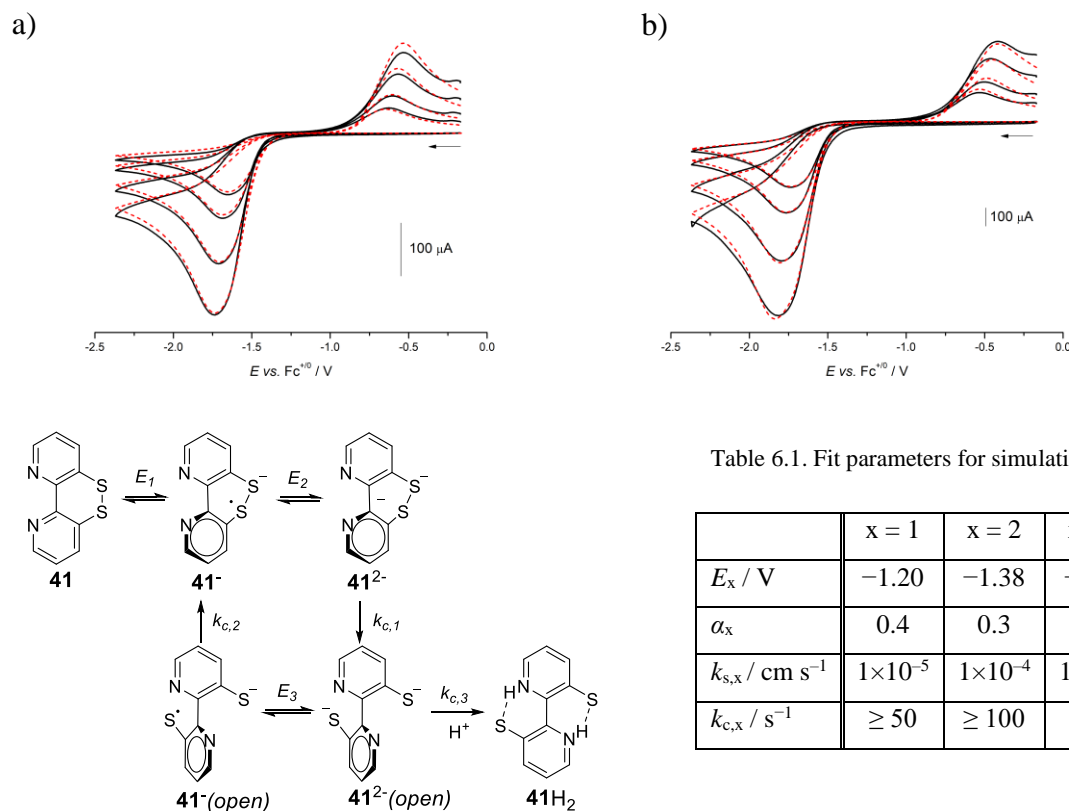


Table 6.1. Fit parameters for simulation.

	x = 1	x = 2	x = 3
E_x / V	-1.20	-1.38	-1.15
α_x	0.4	0.3	0.7
$k_{s,x} / \text{cm s}^{-1}$	1×10^{-5}	1×10^{-4}	1×10^{-4}
$k_{c,x} / \text{s}^{-1}$	≥ 50	≥ 100	0.02

Figure 6.13. Cyclic voltammograms of 0.31 mM $\mathbf{41}$ in MeCN (0.1 M Bu $_4$ NPF $_6$) at rt with the scan rates a) 100–1000 mV/s and b) 1000–10000 mV/s. Black lines correspond to experimental data and red dashed lines to simulation according to the mechanism depicted for reductive S–S bond cleavage reaction of $\mathbf{41}$ and re-oxidation.

Water strongly influences the redox properties of $\mathbf{41}$ as revealed by electrochemical measurements conducted in the presence of water (Figure 6.14). Upon adding 10 eq. of water, the cathodic peak gets much sharper and shifts anodically. This is even more pronounced in the presence of 100 eq. of water. The peak current $I_{p,c}$ of the reduction wave increased linearly with the square root of the scan rate (0.1 – 10 Vs $^{-1}$) indicating a diffusion controlled process (Figure 8.9, a in appendix). The cathodic and anodic waves are largely separated while a linear shift of $E_{p,c}$ with log(ν) is still observed, which points to a fast chemical reaction following the reduction (Figure 8.9, b in the appendix). Initial inspection of the CV data in the presence of 10 and 100 eq. of water suggested an ECE mechanism, the chemical reaction being first order with regard to water. The steep slope of the reduction

6 Protonation of 5,6-Dithia-1,10-phenanthroline, its application as disulfide/dithiol switch, and as ligand for [2Fe-2S] clusters

wave indicates potential inversion of the first and second reduction process. Protonation and bond breaking following the initial reduction was previously reported for **48** and seemed also reasonable for **41**.

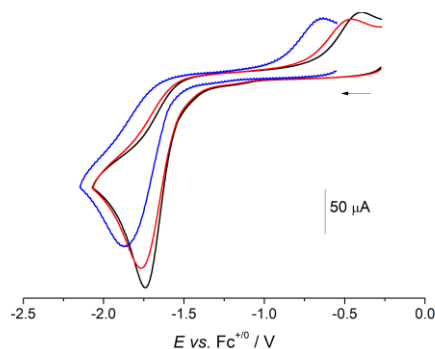


Figure 6.14. Cyclic voltammograms of **41** (blue) with 10 eq. water (red) and 100 eq. water (black) in MeCN (0.1 M Bu_4NPF_6 , 100 mV s^{-1} , rt).

However, **41**⁻ possesses a basic N atom of the pyridine unit in contrast to **48** which naturally impacts the reaction with water greatly. DFT studies of the protonated reduced form **41H**⁻ revealed a global minimum energy structure in the closed form. The S–S distance of ground state **41H**⁻ is much shorter than in **41**⁻ ($d(\text{S}–\text{S}) = 2.11$ vs. 2.75 \AA) and similar to the S–S bond length in **41**, and the tilting of the two pyridine rings is less pronounced (C–S–S–C torsion angle $\varphi = 27.0^\circ$). In fact, the SOMO of **41H**⁻ has no σ^* S–S antibonding character as in **41**⁻, but it of π^* orbital type and is localized at the bipyridine unit (Figure 6.15). Protonation hence changes drastically the electronic structure of the radical **41**⁻, but does not induce S–S bond rupture.

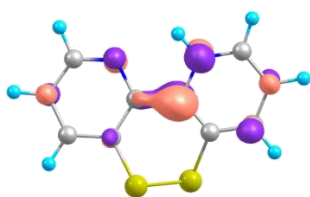


Figure 6.15. SOMO of protonated **41H**⁻ (contour value: 0.08).

Since protonation of **41**⁻ does not result in any bond cleavage, the CV data of **41** in the presence of water was simulated by adding to the original model an equilibrium reaction involving **41**⁻ and water, as depicted in Figure 6.16.

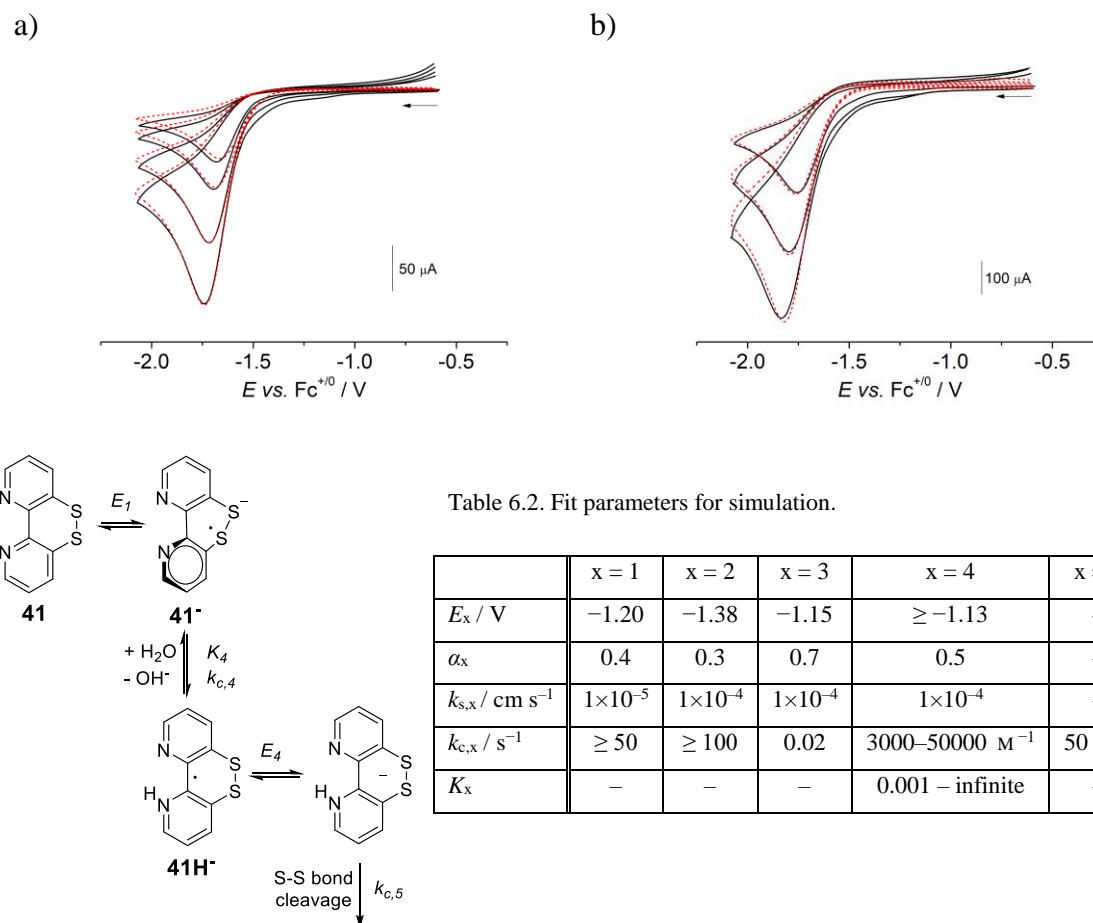


Figure 6.16. Cyclic voltammograms of 1.8 mM **41** and 0.21 M water in MeCN (0.1 M Bu₄NPF₆) at rt with scan rates of a) 100–1000 mV and b) 2000–10000 mV. Black lines correspond to experimental data and red dashed lines to simulation according to mechanism depicted above with the parameter from Table 6.2.

By simulating the data, it became apparent that the equilibrium constant K_4 and the reaction rate $k_{c,4}$ are interdependent parameters, i. e. a small equilibrium constant K_4 can be compensated by a faster reaction rate $k_{c,4}$ and vice versa. Therefore, only ranges of the two values are given. Reasonable fits could be obtained by using rather large second order reaction rate constants ($k_{c,4} \geq 3000 \text{ M}^{-1}\text{s}^{-1}$) and equilibrium constants between 0.001 and infinite, the latter describing an irreversible reaction. Interestingly, the generated **41H**^{•-} species exhibits a further reduction potential of $\geq -1.13 \text{ V}$, hence it is easier to reduce than **41** and non-protonated **41**^{•-}. The potential of **41H**^{•-} is shifted by $\geq +250 \text{ mV}$ with regard to **41**^{•-} due to the charge compensation by protonation. Subsequently, the S–S bond in **41H**²⁻ breaks with a rate constant $k_{c,5} \geq 50 \text{ s}^{-1}$.

In conclusion, **41** exhibits two chemically reversible reduction processes. The potential of the second reduction event can be tuned via protonation of **41**^{•-} by a weak acid such as

6 Protonation of 5,6-Dithia-1,10-phenanthroline, its application as disulfide/dithiol switch, and as ligand for [2Fe–2S] clusters

water. Protonation triggers potential inversion which means that the second reduction becomes easier than the first one.

6.5 Preliminary application as a chelate ligand for [2Fe–2S] clusters

46 was reacted with of KH to yield **41K₂** in THF. The solution was cooled to $-35\text{ }^{\circ}\text{C}$ and slowly added to $(\text{Me}_3\text{PhN})_2$ **51** in MeCN. The reaction mixture was stirred for 3 hours and slowly warmed to room temperature. Removal of the solvent under reduced pressure afforded $(\text{Me}_3\text{PhN})_2$ **42** (Figure 6.17). Unfortunately, attempts to obtain crystals suitable for X-ray crystallography failed. Therefore, characterization of $(\text{Me}_3\text{PhN})_2$ **42** was pursued with polycrystalline material.

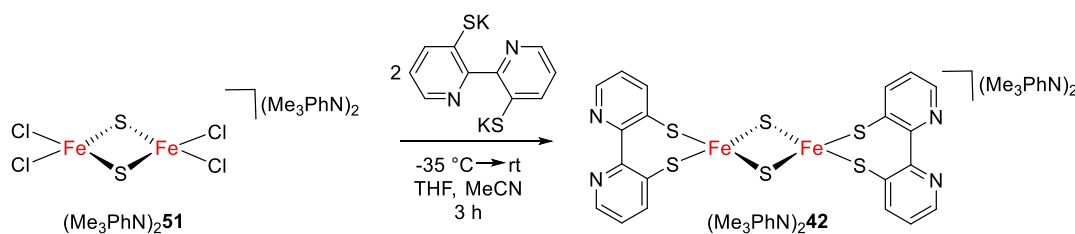


Figure 6.17. Synthesis of $(\text{Me}_3\text{PhN})_2$ **42**.

First evidence on the formation of $(\text{Me}_3\text{PhN})_2$ **42** is found in ESI(–)MS (Figure 6.18, a) and ESI(+)MS (Figure 8.10, in appendix). The main peaks at high m/z can be assigned to adducts of **42**^{2–}. A UV-vis spectrum of a recrystallized sample was recorded in DMF (Figure 6.18, b). The bands that are detected compare well to related thiophenyl clusters **52**^{2–}–**54**^{2–} (Figure 6.19, Table 6.3); only the extinction coefficient is smaller.

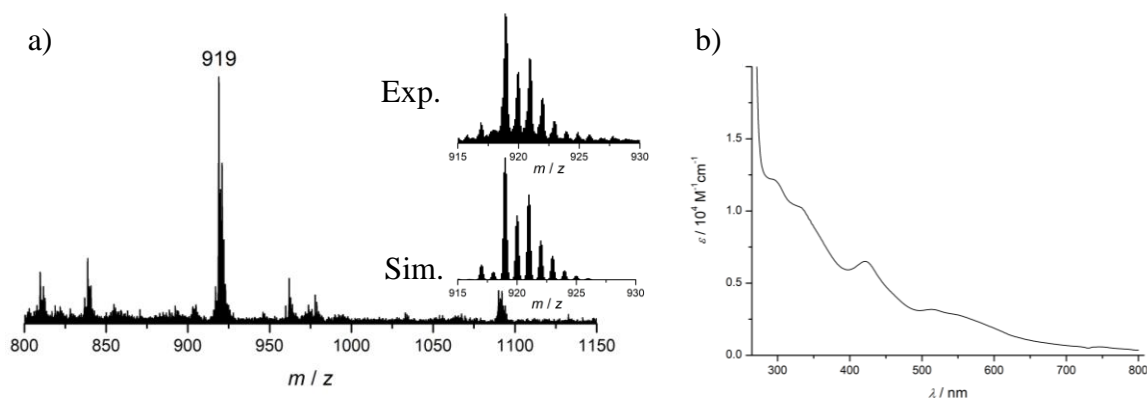


Figure 6.18. a) m/z 800–1150 range of ESI(–)MS spectrum of cluster $(\text{Me}_3\text{PhN})_2$ **42**. The inserted graphs depict an excerpt from the spectrum and the simulation with $[\mathbf{42}+2(\text{Me}_3\text{PhN})+\text{Cl}]^-$. b) UV-vis spectrum of cluster $(\text{Me}_3\text{PhN})_2$ **42** in DMF.

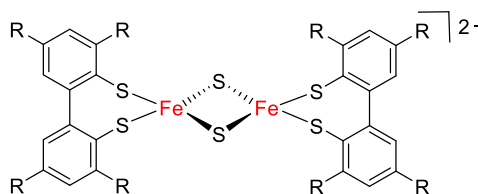


Figure 6.19. [2Fe–2S] clusters with 2,2'-dithiobiphenyl chelate ligands with three different back-bone substituents (R = Cl (**52**²⁻), H (**53**²⁻), ^tBu (**54**²⁻)).

Table 6.3. Electronic absorption data of [2Fe–2S] clusters with dithiobipyridin and dithiobiphenyl ligation.

	λ [nm] (ϵ [$M^{-1}cm^{-1}$])	<i>ref.</i>
42 ²⁻	291 (11700), 339 (9500), 421 (6250), 512 (3050) 559 (2500)	this work
52 ²⁻	260 (44000), 350 (37000), 424 (30000), 523 (12500)	236
53 ²⁻	257 (47500), 336 (33400), 425 (29500), 520 (13250), 547 (13500)	236
54 ²⁻	260 (45000), 345 (26500), 383 (23600), 443 (22000), 550 (12000)	236

These preliminary results attest that **41** is suitable as ligand for Fe–S clusters. It is impossible to infer from ESI-MS or UV-vis spectroscopy whether the iron ions are coordinated by the pyridine-N atoms or the thiolate. However, the proposed structure (Me₃PhN)₂**42** seems most probable given the high preference for sulfur-ligands by Fe–S clusters.

6.6 Conclusion and Outlook

The synthesis of **41** was optimized prior to investigation of its properties and reactivity. The molecular structure of **41**H₂ in crystal was elucidated by X-ray crystallography. It was shown that the protonation of **41** proceeds in MeCN in the same manner as in water. Full protonation of the pyridine-N atoms is only achieved by addition of the strong acid TfOH.

The disulfide/dithiole switch of **41** was studied thoroughly with cyclic voltammetry and DFT calculations. An EEC mechanism was found for the reductive S–S bond cleavage. The mechanism changes to ECEC in the presence of a weak acid like water: After the first reduction a protonation takes place followed by the second reduction. The breakage of the S–S bond is the final step.

Finally, preliminary results on the formation of [2Fe-2S] complexes with **41** as ligand open the field for further investigations towards a directly coupled Ru(bpy)₃-[2Fe-2S] system **40** (Figure 6.1, a).

7 Experimental Section

7.1 Author contributions

Prof. Dr. Inke Siewert simulated the electrochemical data and Dr. Sebastian Dechert carried out the theoretical calculations in chapter 6.4. Dr. Sebastian Dechert and Dr. Nicole Kindermann performed X-ray analysis of all compounds. Dr. Serhiy Demeschko measured and fitted the SQUID data. Dr. Marie Bergner measured and simulated all EPR spectra.

7.2 Materials and methods

All manipulations of air- and moisture-sensitive materials were carried out under an anaerobic and anhydrous atmosphere of dry dinitrogen or argon gas by standard Schlenk techniques or in a MBraun glovebox. Glassware was dried prior to use at 120 °C overnight in a heating oven. Diethyl ether and pentane were dried over sodium benzophenone ketyl, THF over Na/K alloy and hexane over potassium benzophenone ketyl, MeCN over CaH₂, acetone over P₂O₅ MeOH over Mg, and distilled prior to use. Deuterated solvents were dried and distilled according to the undeuterated analogues. For reactions involving NO, care was taken to prevent light exposure by covering reaction glassware in aluminum foil or by performing experiments in a darkened glovebox. Nitric oxide (Linde, 2.5) was purified by passing the NO gas stream through an Ascarite column (NaOH fused on silica gel) and a cooling trap with glass spikes at -78 °C. If not mentioned otherwise all chemicals were acquired from commercial sources (*Acros, Sigma Aldrich, abcr, Deutero, Merck*) and used without further purification.

¹H NMR spectra were recorded on an Avance III 300, HD 400 or HD 500 spectrometer from Bruker. Chemical shifts are reported in ppm relative to residual proton signals of CDCl₃ (7.26 ppm for ¹H NMR experiments, 77.2 ppm for ¹³C NMR experiments), MeCN-d₃ (1.94 ppm for ¹H NMR experiments, 118.3 ppm for ¹³C NMR experiments) and DMF-d₇ (8.03 ppm for ¹H NMR experiments) at 298 K unless stated otherwise.²³⁷ The following abbreviations were used for the multiplicity of the NMR signals: s (singlet), d (doublet), t (triplet), q (quartet), m (multiplet).

Elemental analyses were submitted to the analytical laboratory of the department of inorganic chemistry at the Georg-August-Universität Göttingen and performed on an Elementar Vario EL III.

UV-vis spectra were recorded with a Cary5000 Bio Spectrophotometer, using Schlenk quartz cuvettes. Spectra were analyzed by Cary Win UV software.

IR spectra were measured on an Agilent Technologies Cary 630 FTIR. Intensities of the observed bands in the spectra are abbreviated as follows: s (strong), m (medium), w (weak).

ESI mass spectra were measured on a Thermo Finnigan Trace LCQ spectrometer.

Mössbauer spectra were recorded with a ^{57}Co source in a Rh matrix using an alternating constant acceleration Wissel Mössbauer spectrometer operated in the transmission mode and equipped with a Janis closed-cycle helium cryostat. Isomer shifts are given relative to iron metal at ambient temperature. Simulation of the experimental data was performed with the Mfit program using Lorentzian line doublets: E. Bill, Max-Planck Institute for Chemical Energy Conversion, Mülheim/Ruhr, Germany.

EPR spectra were measured with a Bruker E500 ELEXSYS X-band spectrometer equipped with a standard cavity (ER4102ST, 9.45 GHz). The sample temperature was maintained constant with an Oxford instrument Helium flow cryostat (ESP910) and an Oxford temperature controller (ITC-4). The microwave frequency was measured with the built-in frequency counter and the magnetic field was calibrated by using a NMR field probe (Bruker ER035M). The spectra were simulated with *easy spin*.

Cyclic voltammetry experiments were carried out in CH_3CN with a *Gamry* Reference 600. A silver wire as (pseudo)reference electrode was used with ferrocene as internal standard, a glassy carbon disk electrode as working electrode (*IJ Cambria*, $A = 0.707 \text{ cm}^2$), a Pt wire as auxiliary electrode, and $0.1 \text{ M } n\text{-Bu}_4\text{NPF}_6$ as supporting electrolyte. All electrochemical measurements were conducted in a glove box, those in the presence of water in a home-made tight CV cell. iR compensation was applied by the positive feedback method, which is implemented in the PHE200 software of *Gamry*. CV data was simulated with DigiElch 8 FD purchased from *Gamry*.

X-ray data for all compounds were collected on a STOE IPDS II diffractometer (graphite monochromated $\text{Mo-K}\alpha$ radiation, $\lambda = 0.71073 \text{ \AA}$) by use of ω scans at 133 K. The structures were solved by direct methods with SHELXS and refined on F^2 using all

reflections with SHELXL.²³⁸ Most non-hydrogen atoms were refined anisotropically. Hydrogen atoms were placed in calculated positions and assigned to an isotropic displacement parameter of 1.2 / 1.5 $U_{eq}(C)$. Face-indexed absorption corrections were performed numerically with the program X-RED.²³⁹

7.3 Synthesis

7.3.1 Fe–S clusters

29²⁻, **29³⁻**, **29H₂**, **30²⁻**, **30³⁻**, **30H₂** and (Et₄N)[FeCl₂(NO)₂] were prepared according to reported methods.^{90,163,168} The synthesis of (Et₄N)₂**38** is already published, but the authors followed a different protocol, namely, ligand substitution reaction of [Fe₄S₄(S-^{tert}Bu)₄]²⁻.¹⁹⁵

Bis(tetraethylammonium)-tetrakis[(2-aminothiophenolato)(μ^3 -sulfido)-ferrate(II,III)] [(Et₄N)₂38**] and Bis(trimethylphenylammonium) tetrakis[(2-aminothiophenolato)(μ^3 -sulfido)-ferrate(II,III)] [(Me₃PhN)₂**38**]**

Sodium methoxide (0.25 g, 4.50 mmol) and 2-aminothiophenol (0.48 mL, 4.50 mmol) were mixed in MeOH (10 mL). Iron(III)chloride (0.244 g, 1.50 mmol) in MeOH (6 mL) was added dropwise to the solution which turned into a black suspension. Dilithiumsulfide (0.070 g, 1.5 mmol) was added in one portion and the suspension was stirred overnight.

The halide salt of the counterion in MeOH (5 mL) was added: trimethylphenylammonium chloride (0.216 g, 1.25 mmol) or tetraethylammonium chloride (0.208 g, 1.25 mmol), respectively. The black precipitate was filtered off and washed with MeOH (3 × 10 mL). The product was extracted with MeCN (5 × 5 mL). Crystals suitable for X-ray crystallography were obtained from slow diffusion of diethyl ether into a MeCN solution of the product. The yield was not determined.

Analytical data of (Et₄N)₂**38**:

¹H NMR (400 MHz, MeCN-d₆, 298 K): δ [ppm] = 1.18 (s_{br}, 24 H, 8 CH₃), 3.12 (s_{br}, 16 H, 8 CH₂), 4.59 (s_{br}, 8 H, NH₂), 5.50 (s_{br}, 4 H, *p*-H), 6.10 (s_{br}, 4 H, *o*-H), 7.63 (s_{br}, 4 H, *m*-H), 7.75 (s_{br}, 4 H, *m*-H). **UV-vis** (MeCN): λ [nm] (ϵ_{rel} [M⁻¹cm⁻¹]) = 484 (7700), 350 (sh), 303 (14000). **EA** calculated (%) for C₄₀H₆₄Fe₄N₆S₈ (no solvent molecule in crystal structure): C 43.33, H 5.82, N 7.58, S 23.13; found: C 43.06, H 5.72, N 7.47, S 22.77.

Analytical data of (Me₃PhN)₂**38**:

¹H NMR (500 MHz, MeCN-d₆): δ [ppm] = 3.46 (sbr, 18 H, 6 CH₃), 4.62 (sbr, 8 H, NH₂), 5.65 (sbr, 4 H, ar-H), 6.18 (sbr, 4 H, ar-H), 7.46 (sbr, 4 H, ar-H), 7.53–7.64 (m, 10 H, 2 Ph), 7.73 (d, J = 7.3 Hz, 4 H, ar-H). **UV-vis** (MeCN): λ [nm] (ϵ_{rel} [M⁻¹cm⁻¹]) = 484 (7700), 350 (sh), 303 (14000). **EA** calculated (%) for C₄₄H₅₅Fe₄N₇S₈ (complex + one MeCN molecule which cocrystallizes in the unit cell): C 45.49, H 4.77, N 8.44, S 22.08; found: C 45.44, H 4.72, N 8.22, S 22.41. **ATR-IR** [cm⁻¹] = 3457, 3346, 3058, 2930, 1600 (s), 1498, 1475 (s), 1442, 1370, 1291, 1247, 1156, 1078, 1027, 947, 845, 768, 746 (s), 690, 670.

Oxidation of **38²⁻:**

(Et₄N)₂**38** (20.0 mg, 18.0 μ mol) or (Me₃PhN)₂**38** (22.2mg, 18.0 μ mol) was dissolved in MeCN (20 mL) and exposed to dioxygen, or *p*-benzoquinone (5.84 mg, 54.0 μ mol) was added to the solution. The solvent was removed under reduced pressure after stirring for 30 min at rt. The dark blue solid was washed with Et₂O and pentane. The yield was not determined.

UV-vis (MeCN): λ [nm] (ϵ_{rel} [M⁻¹cm⁻¹]) = 550 (9 600). **ATR-IR** [cm⁻¹] = 1618, 1561, 1539, 1497, 1487, 1448, 1435, 1329, 1313 (s), 1251 (s), 1152, 1123, 1053 (s), 1020, 947, 852, 750, 724, 689. **ESI(-)MS** (MeCN) m/z (%) = 1113 (100) [**38** - 4 H]⁻.

Bis(trimethylphenylammonium)-bis-[(2,2'-bipyridine-3,3'-dithiolato)-(μ -sulfido)-ferrate(III)] [(Me₃PhN)₂42**]**

45 (50.0 mg, 0.139 mmol) was dissolved in THF (20 mL) and K (11.0 mg, 0.278 mmol) was added. (Me₃PhN)₂**50** (40.9 mg, 69.3 μ mol) was dissolved in MeCN (20 mL). Both solutions were cooled to -35 °C and then slowly combined. The solvent was removed under reduced pressure yielding (Me₃PhN)₂**41** as brown precipitate. The yield was not determined.

UV-vis (DMF): λ [nm] (ϵ_{rel} [M⁻¹cm⁻¹]) = 290 (1200), 340 (950), 420 (625), 515 (305), 560 (250), 750 (55). **ESI(-)MS** (MeCN) m/z (%) = 919.0 (6) [**41**+2(Me₃PhN)+Cl]⁻. **ESI(+)**MS (MeCN) m/z (%) = 1020.2 (4) [**41**+Me₃PhN]⁺, 1191.3 (1) [**41**+2NMe₃Ph+Cl]⁺. **¹H NMR** (400 MHz, MeCN-d₃): δ [ppm] = 4.24 (d, J = 48 Hz, 2 H), 4.62 (sbr, 2 H), 8.89 (d, J = 28 Hz, 2 H).

7.3.2 DNICS

[Fe(NN)(NO)₂]⁻ (33⁻) and [Fe(SN)(NO)₂]⁻ (34⁻)

Route 1: **29²⁻** or **30²⁻** (0.231 mmol) was dissolved in MeCN (40 mL) and NO (22.7 mL, 0.924 mmol) was added into the headspace of the flask. After stirring the reaction mixture for three hours the solvent was removed under reduced pressure and the remaining solid was washed with Et₂O (3 × 5 mL). **33⁻** or **34⁻** was taken up in THF (10 mL) and dried *in vacuo* to afford the DNIC as a brown powder. Layering of a saturated THF solution with MTBE or hexane afforded dark crystals suitable for X-ray crystallography in the case of **33⁻**. **34⁻** was crystallized from slow diffusion of Et₂O in a MeCN solution of the complex after repetitive recrystallization. The yield was not determined.

Route 2 was partially adapted from literature.¹⁶⁸ It offers a convenient path to introduce two different ligands, Phenylbis(benzimidazol-2-yl)methane **NN** and Benzimidazolthiophenol **SN**, to the scaffold. KH (0.030 g, 0.758 mmol) was added to a solution of **NN** (0.123 g, 0.379 mmol) or **SN** in THF (5 mL) and stirred at rt overnight. A flask was charged with (Et₄N)[FeCl₂(NO)₂] (0.120 g, 0.379 mmol) in THF (10 mL) and both solutions were cooled to -35°C before mixing. The mixture was allowed to stir at ambient temperature for 2 h. Then the solvent was removed under reduced pressure affording the corresponding DNIC as brown powder. The yield was not determined.

Analytics 33⁻: **UV-vis** (THF): λ [nm] (ε_{rel} [M⁻¹cm⁻¹]) = 430 (1480), 705 (300). **DialPath-IR** ν_{NO} [cm⁻¹] = 1780, 1714 (MeCN); 1773, 1705 (THF).

Analytics 34⁻: **UV-vis** (THF): λ [nm] (ε_{rel} [M⁻¹cm⁻¹]) = 470 (340), 545 (260), 685 (200). **DialPath-IR** ν_{NO} [cm⁻¹] = 1751, 1700 (MeCN); 1744, 1695 (THF).

7.3.3 3,3'-Disulfur-2,2'-bipyridine

The synthesis of **45**, **46**, and **41** was adapted from unpublished results by Mauricio Cattaneo.²²³

3,3'-dihydroxy-dimethylthiocarbamoyl-2,2'-bipyridine (45)

3,3'-dihydroxy-2,2'-bipyridine (1.3 g, 6.9 mmol) was dissolved in anhydrous and degassed acetone (130 ml) under inert conditions. Dimethylthiocarbamoyl chloride (2.56 g, 20.7 mmol) and CsCO₃ (6.75 g, 20.7 mmol) was then added and the reaction mixture was stirred for 24 hours at 65 °C. The solution was allowed to cool to rt and the solvent was removed under reduced pressure. The solid was dissolved in demineralized water and neutralized

with HCl (0.1 M). The aqueous solution was extracted with DCM (3×100 ml). The combined organic phases were evaporated to dryness under reduced pressure. Column chromatography (silica gel, R_f (ethyl acetate) = 0.06) of the resulting brown oil afforded a yellow solid (yield 60 %). **EA** for $C_{16}H_{18}N_4O_2S_2$ (%): C 53.02, H 5.00, N 15.46, S 17.69. Found: C 53.05, H 4.93, N 15.65, S 17.85. **IR** (KBr pellets) [cm^{-1}]: 3065 (w), 2940 (w), 2880 (w), 1627 (w), 1537 (s), 1454 (w), 1441 (w), 1419 (s), 1394 (s), 1289 (s), 1240 (s), 1202 (s), 1178 (m), 1126 (s), 1106 (m), 1060 (w), 1039 (m), 819 (w), 791 (w), 756 (w), 687 (w), 619 (w). **1H NMR** (300 MHz, $CDCl_3$): δ [ppm] = 8.52 (2, dd, 2H, $^{2-3}J = 4.6$ Hz, $^{2-4}J = 1.4$ Hz), 7.76 (4, dd, 2H, $^{4-3}J = 8.2$ Hz, $^{4-2}J = 1.4$ Hz), 7.38 (3, dd, 2H, $^{3-4}J = 8.3$ Hz, $^{3-2}J = 4.7$ Hz), 3.29 (11, s, 6H), 3.03 (12, s, 6H). **^{13}C NMR** (75 MHz, $CDCl_3$) δ [ppm] = 185.99, 148.74, 148.63, 146.09, 133.03, 123.47, 43.35, 38.97. **^{15}N NMR** (30 MHz, $CDCl_3$): δ [ppm] = -62.8, -262.2. **ESI(+)**MS (MeCN) m/z (%): $[M+H]^+$ 363.1 (100). **UV-vis** (CH_3CN): λ_{max} [nm] (ϵ_{rel} [$M^{-1}cm^{-1}$]) = 251 (34600).

3,3'-dithio-dimethylcarbamoyl-2,2'-bipyridine (46) and 3,3'-thiocyclo-2,2'-bipyridine (47)

After extensive optimization of the reaction conditions, best results were obtained by heating neat **45** (100 mg) to 280 °C under argon atmosphere for 7 min. 1H NMR spectroscopy suggested the black product mixture to contain **47** (~36%), **45** with only one rearranged arm (~26%) and **46** (~16%) besides some remaining **45** and other unidentified side products. The compounds were separated by column chromatography (silica gel, hexanes/diethyl acetate 1:1).

The first fraction is **47** (R_f in ethyl acetate (3×TLC) ~0.71). **EA** $C_{10}H_6N_2S$ (%): C 64.29, H 3.60, N 14.37, S 16.40. Found: C 64.12, H 3.82, N 14.07, S 16.18. **IR** (KBr pellets) [cm^{-1}]: 3046 (w), 2925 (w), 2956 (w), 1541 (s), 1462 (w), 1395 (s), 1335 (w), 1288 (m), 1225 (w), 1196 (m), 1146 (m), 1067 (s), 1040 (w), 1031 (w), 986 (w), 967 (w), 814 (w), 801 (m), 789 (s), 733 (s), 696 (m), 621 (m). **1H NMR** (300 MHz, $CDCl_3$): δ [ppm] = 8.91 (2, dd, 2H, $^{2-3}J = 4.6$ Hz, $^{2-4}J = 1.4$ Hz), 8.23 (4, dd, 2H, $^{4-3}J = 8.2$ Hz, $^{4-2}J = 1.4$ Hz), 7.48 (3, dd, 2H, $^{3-4}J = 8.2$ Hz, $^{3-2}J = 4.5$ Hz). **^{13}C NMR** (75 MHz, $CDCl_3$): δ [ppm] = 150.54, 148.08, 134.63, 131.09, 120.40. **^{15}N NMR** (30 MHz, $CDCl_3$): δ [ppm] = -78. **ESI-MS** (MeCN) m/z (%): $[M+H]^+$ 187.03 (100). **UV-vis** (CH_3CN): λ_{max} [nm] (ϵ_{rel} [$M^{-1}cm^{-1}$]) = 298 (14300), 290 (sh), 257 (10700), 228 (38200), 210 (15800).

The second fraction is the starting material **45** (R_f in ethyl acetate (3×TLC) ~0.58).

The third fraction is the singly rearranged product **45** (R_f in ethyl acetate (3×TLC) ~0.26). **EA** C₁₆H₁₈N₄O₂S₂ (%): C 53.02, H 5.00, N 15.46. Found: C 53.25, H 5.10, N 15.17. **IR** (KBr pellets) [cm⁻¹]: 3055 (w), 3014 (w), 2956 (w), 2918 (w), 2856 (w), 1635 (m), 1594 (s), 1552 (s), 1458 (m), 1432 (m), 1371 (s), 1327 (m), 1277 (w), 1218 (w), 1156 (w), 1106 (w), 1066 (w), 988 (w), 970 (w), 903 (w), 826 (s), 748 (w), 684 (m), 669 (w), 530 (m), 414 (w). **¹H NMR** (300 MHz, CDCl₃): δ [ppm] = 8.61 (2, dd, 1H, ²⁻³ J = 4.6 Hz, ²⁻⁴ J = 1.7 Hz), 8.52 (2', dd, 1H, ²⁻³ J = 4.7 Hz, ²⁻⁴ J = 1.4 Hz), 7.97 (4, dd, 1H, ³⁻⁴ J = 8.0 Hz, ²⁻⁴ J = 1.7 Hz), 7.77 (4', dd, 1H, ³⁻⁴ J = 8.3 Hz, ²⁻⁴ J = 1.4 Hz), 7.37 (3', dd, 1H, ³⁻² J = 4.7 Hz, ³⁻⁴ J = 8.3 Hz), 7.35 (3, dd, 1H, ³⁻² J = 4.7 Hz, ³⁻⁴ J = 8.0 Hz), 3.21 (11', s, 3H), 2.89 (11-12, s, 6H), 2.86 (12', s, 3H). **¹³C NMR** (200 MHz, CDCl₃): δ [ppm] = 185.12, 164.88, 157.52, 150.44, 148.55, 147.78, 145.77, 145.69, 132.69, 127.01, 123.27, 123.23, 42.93, 38.37, 36.88. **¹⁵N NMR** (30 MHz, CDCl₃): δ [ppm] = -63.2, -65.7, -262.5. **ESI-MS** (MeCN) m/z (%): [M+H]⁺ 363.09 (100).

The last fraction is **46** (R_f in ethyl acetate (3×TLC) ~0.17). **EA** C₁₆H₁₈N₄O₂S₂ (%): C 53.02, H 5.00, N 15.46, S 17.69. Found: C 53.67, H 4.97, N 15.34, S 17.60. **IR** (KBr pellets) [cm⁻¹]: 3056 (w), 3017 (w), 2916 (w), 1626 (s), 1553 (m), 1477 (w), 1459 (w), 1434 (m), 1400 (s), 1369 (s), 1257 (m), 1099 (m), 1072 (w), 1043 (m), 1037 (w), 906 (w), 813 (w), 801 (m), 786 (w), 774 (w), 685 (s), 648 (w), 623 (w), 525 (w). **¹H NMR** (300 MHz, CDCl₃): δ [ppm] = 8.65 (2, dd, 2H, ²⁻³ J = 4.8 Hz, ²⁻⁴ J = 1.6 Hz), 8.01 (4, dd, 2H, ⁴⁻³ J = 8.0 Hz, ⁴⁻² J = 1.6 Hz), 7.39 (3, dd, 2H, ³⁻⁴ J = 8.0 Hz, ³⁻² J = 4.8 Hz), 2.91 (11, s, 12H). **¹³C NMR** (75 MHz, CDCl₃): δ [ppm] = 165.15, 159.80, 148.88, 145.33, 126.52, 123.42, 37.04. **¹⁵N NMR** (30 MHz, CDCl₃): δ [ppm] = -66.0, -285.5. **ESI-MS** (MeCN) m/z (%): [M+H]⁺ 368.09 (100).

[1,2]dithiino[4,3-b:5,6-b']dipyridine (**41**)

To a solution of LiAlH₄ (190 mg, 5 mmol) in dry THF under argon atmosphere was added **46** (234 mg, 0.645 mmol) dissolved in dry THF (15 ml). The reaction mixture was stirred under argon atmosphere for 30 min and then heated to 50 °C for 3 h. After cooling down to 0 °C, 0.1 M aqueous HCl (10 ml) was added slowly until the solution turned to intense red. The product was extracted with DCM (4 × 50 ml) and the combined organic phases were exposed to air, causing the color of the solution to turn yellow. The solution was concentrated in vacuo and the yellow oil was chromatographed on silica gel with ethyl acetate. **41** was isolated as a yellow oil (R_f in ethyl acetate ~0.1). **¹H NMR** (300 MHz,

CDCl_3): δ [ppm] = 8.68 (2, dd, 2H, $^{2-3}J = 4.6$ Hz, $^{2-4}J = 1.6$ Hz), 7.72 (4, dd, 2H, $^{4-3}J = 7.9$ Hz, $^{4-2}J = 1.6$ Hz), 7.22 (3, dd, 2H, $^{3-4}J = 7.9$ Hz, $^{3-2}J = 4.7$ Hz). $^{13}\text{C NMR}$ (75 MHz, CDCl_3): δ [ppm] = 153.08, 149.44, 136.01, 133.94, 123.67. $^{15}\text{N NMR}$ (30 MHz, CDCl_3): δ [ppm] = -70.6. **ESI-MS** (MeCN) m/z (%): $[\text{M}+\text{H}]^+$ 219.00 (100%), $[\text{M}+\text{Na}]^+$ 240.99 (30%). **UV-vis** (CH_3CN): λ_{max} [nm] (ϵ_{rel} [$\text{M}^{-1}\text{cm}^{-1}$]) = 360 (360), 302 (5900), 265 (9400).

3,3'-dithiol-2,2'-bipyridine (41H₂)

41H₂ was synthesized following the procedure for **41**, but the reaction mixture was kept under inert conditions throughout. LiAlH_4 (200 μL of a 1.0 M solution in THF, 200 μmol) was added to **46** (8.0 mg, 22 μmol) under an atmosphere of dry Ar and the reaction mixture stirred for 5 min, then heated to 50 °C for 3 h. After cooling to 0 °C, 0.1 M aqueous HCl (3 ml) were added slowly. The aqueous phase was further diluted with 0.1 M aqueous HCl (50 ml) and the solution turned intense red. **41H₂** was extracted with DCM (6 x 5 ml) under argon atmosphere. The solvent was then removed under reduced pressure and the remaining red solid was recrystallized from DCM/toluene. $^1\text{H NMR}$ (300 MHz, CDCl_3) δ [ppm] = 8.39 (2, dd, 2H, $^{2-3}J = 8.3$ Hz, $^{2-4}J = 1.6$ Hz), 8.01 (4, dd, 2H, $^{4-3}J = 5.1$ Hz, $^{4-2}J = 1.6$ Hz), 7.31 (3, dd, 2H, $^{3-4}J = 5.1$ Hz, $^{3-2}J = 8.3$ Hz).

7.4 DFT calculations

All computations were carried out with the ORCA program package.²⁴⁰ X-ray data of the DNIC anions were employed as starting coordinates for the geometry optimization. For the protonated species H-atoms were added to the structure with the program *Chemcraft* and the charge was changed to zero. The spin-unrestricted Kohn-Sham approach was used in all cases to account for the unpaired spin of the $S = 1/2$ system. Geometry optimizations and frequency calculations were performed with the BP86,^{241–243} TPSS,^{244,245} B3LYP^{246,247} and TPSSh²⁴⁸ density functionals. The def2-TZVP basis set was applied in combination with the auxiliary basis set def2-TZV/J.^{249–251} The RI approximation was used to accelerate the calculations. The Mössbauer spectroscopic parameters were computed using the CP(PPP) basis set for Fe and def2-TZVP for the other atoms.¹⁸⁶ Counterions or crystal inclusions were omitted since Lippard and Zhang showed before that counterions and cocrystallized neutral molecules have only a marginal influence on Mössbauer parameters of iron complexes.^{252,253} The COSMO package included in ORCA was employed to mimic MeCN or THF as solvent in form of an infinite dielectric field.

Isomer shifts δ_{IS} were calculated from the electron densities at the Fe nucleus ρ_0 employing the linear regression formula: $\delta_{IS} = \alpha(\rho_0 - C) + \beta$. Here, α , β and C are the fit parameters. Neese and coworkers published their values for different combinations of the functionals and basis sets.¹⁸⁴ Quadrupole splittings ΔE_Q were obtained from electric field gradients V_i ($i = x, y, z$; V_i are the eigenvalues of the electric field gradient tensor) employing a nuclear quadrupole moment $Q(^{57}\text{Fe}) = 0.16$ barn: $\Delta E_Q = 1/2 e Q V_z (1 + 1/2 \eta^2)^{1/2}$. Here, $\eta = (V_x - V_y)/V_z$ is the asymmetry parameter.

8 Appendix

8.1 Benchmark substances for X-ray spectroscopy of iron-sulfur clusters

Samples of (NEt₄)₂**29** and (NEt₄)₃**29** were prepared and sent to the group of Prof. Serena DeBeer at the Max-Planck Institute for Chemical Energy Conversion in Mülheim for iron and sulfur K-edge X-ray absorption (XAS), iron K β and valence-to-core X-ray emission (XES) and X-ray magnetic circular dichroism (XMCD) measurements of iron complexes in different redox states. The results allowed quantitative assessment of the electronic structure of iron-sulfur clusters and were published in the Journal *Inorganic Chemistry* in 2016 and 2017.^{254,255}

More precisely, Fe K edge XAS in combination with DFT calculations allowed for a distinction between localized valence and delocalized valence species on basis of pre-edge and K-edge energies. Fe K β XES mainlines, on the other hand, were found not suitable for the elucidation of oxidation states of iron-sulfur clusters as isolated method because of cancelling effects of covalency and spin state. XMCD proved to be an effective tool for the elucidation of oxidation states as distinct features appear at the L₃ and L₂ edges. The signal's intensity correlates to the molecule's covalency. With knowledge obtained from the test molecules, spectra of [MoFe₃S₄]³⁺ and [VFe₃S₄]²⁺ as models for FeMoCo and FeVCo of nitrogenase were analyzed. XMCD delivers more precise information on the oxidation state distribution than XAS alone. To summarize, most information can be obtained in the order XMCD > XAS > XES. Well characterized molecules in different oxidation states like (NEt₄)₂**29** and (NEt₄)₃**29** served as benchmark in order to understand the effect of oxidation state and covalency on the three methods. The elucidation of the electronic structure of iron-sulfur clusters in proteins can be supported by them in the future.

8.2 Supplementary spectra and information

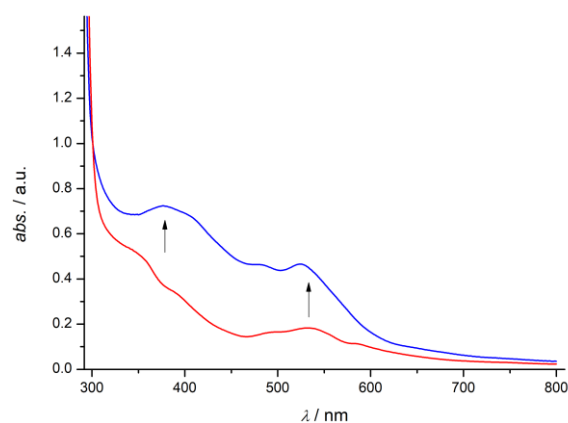


Figure 8.1. UV-vis of starting material 29^{3-} in DMF (red) and reaction mixture after 35 min in MeCN (blue).

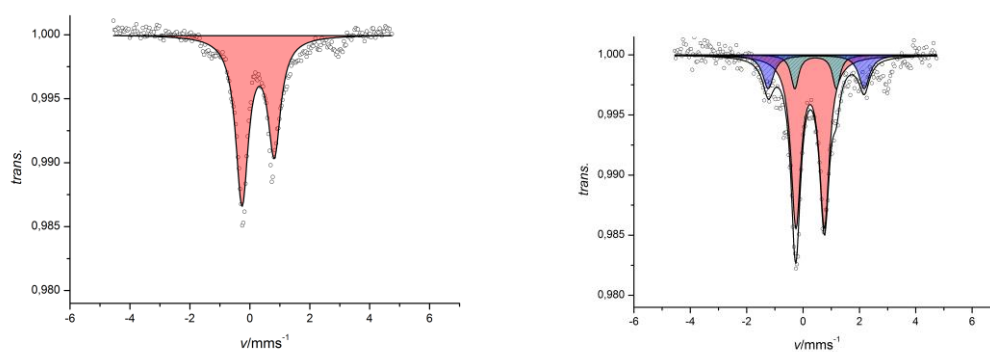


Figure 8.2. Zero-field Mössbauer spectrum of intermediate 1 at 80 K (left) and 6 K (right).

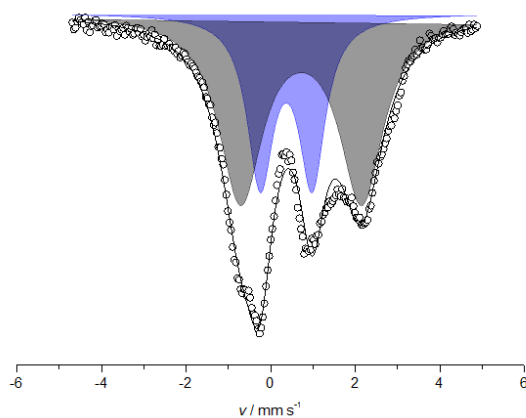


Figure 8.3. Mössbauer spectrum of 33% ^{57}Fe enriched 29^{3-} .

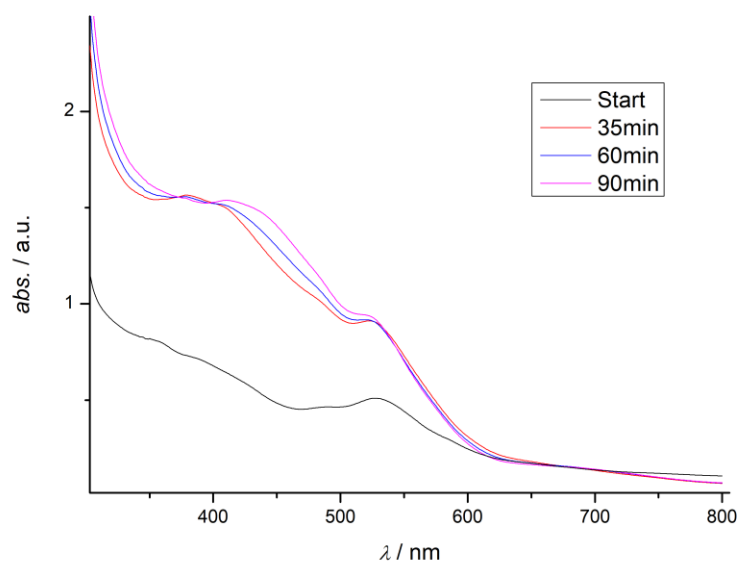


Figure 8.4. UV-vis spectra of the ^{57}Fe enriched 29^3- in DMF (black) and after 35 (red), 60 (blue), and 90 min (magenta) after addition of NO.

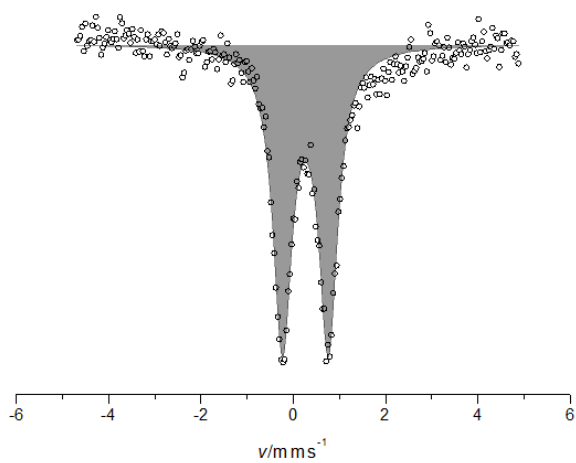


Figure 8.5. Mössbauer spectrum of intermediate 2 in frozen MeCN solution.

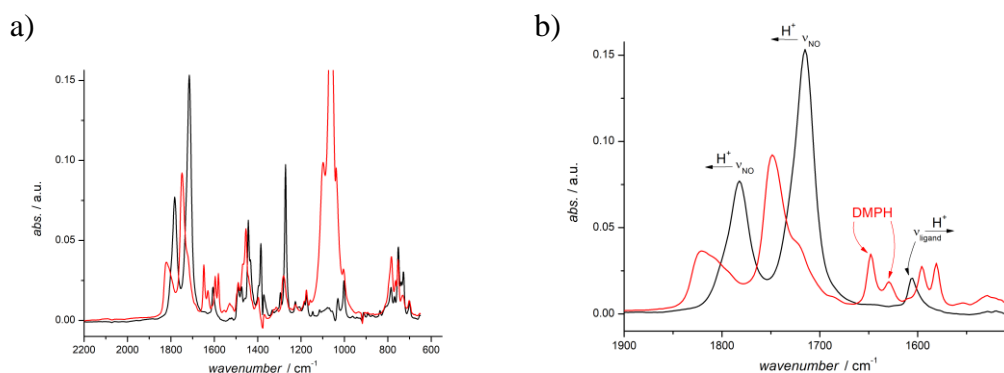


Figure 8.6 (a) IR spectra of **33⁻** (black) after addition of 1 eq. DMPH (red), (b) excerpt of ν_{NO} region of IR spectrum. Upon protonation ν_{NO} shift to higher wavenumbers while ν_{ligand} splits in two signals and shifts to lower wavenumbers.

Table 8.1. Experimental and calculated infrared spectroscopic parameters for ν_{NO} of **33⁻** and **34⁻** in MeCN and THF.

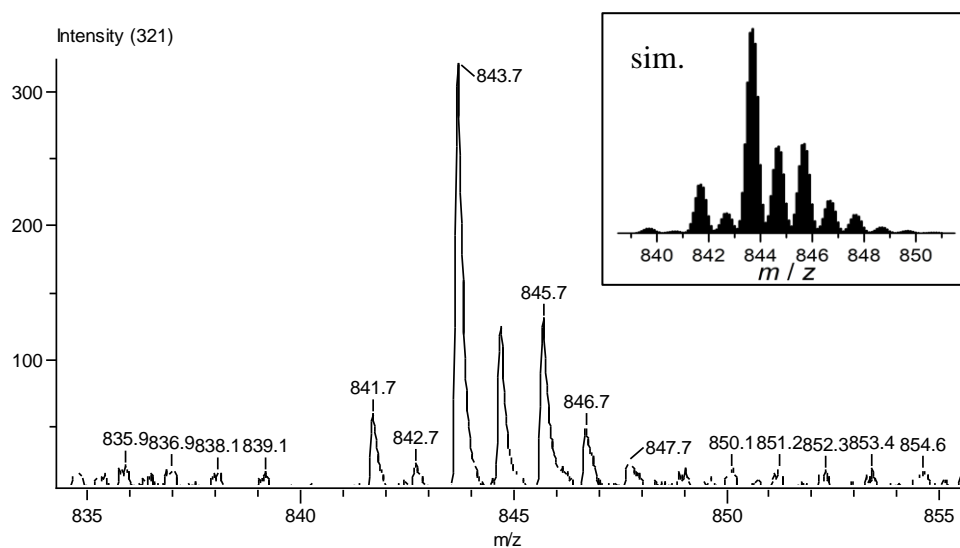
	solvent	functional	IR $\nu_{\text{NO}}/\text{cm}^{-1}$	$\Delta(\nu_{\text{NO,exp}}-\nu_{\text{NO,calc}})/\text{cm}^{-1}$	Figure 3.5
33 exp	MeCN	—	1714, 1780	—	—
33 calc	MeCN	BP86	1673, 1749	41, 31	a)
	MeCN	TPSS	1671, 1752	43, 28	—
34 exp	MeCN	—	1700, 1751	—	—
34 calc	MeCN	BP86	1643, 1709	57, 42	b)
33 exp	THF	—	1705, 1773	—	—
33 calc	THF	BP86	1681, 1752	24, 21	c)
34 exp	THF	—	1694, 1744	—	—
34 calc	THF	BP86	1657, 1716	37, 28	d)

Table 8.2. Experimental and calculated infrared spectroscopic parameters for ν_{NO} of **33H** and **34H** in MeCN and THF.

		functional	solvent	$\nu_{\text{NO}}/\text{cm}^{-1}$	$\Delta(\nu_{\text{NO,exp}}-\nu_{\text{NO,calc}})/\text{cm}^{-1}$
33H	exp	—	THF	1743, 1820	—
33H-rearranged	calc	BP86	MeCN	1648, 1680	95, 140
33H	calc	BP86	MeCN	1697, 1775	46, 45
34H	exp	—	THF	1722, 1775	—
34H	calc	BP86	MeCN	1667, 1735	55, 40

Table 8.3 Calculated Mössbauer parameters.

	functional	33	34	33H	34H
$\delta_{\text{IS}} / \text{mm s}^{-1}$	B3LYP	0.0513	0.0043	0.1005	0.0511
	TPSS	0.1062	0.0631	—	—
	TPSSH	0.0405	-0.0049	—	—
$\Delta E_{\text{Q}} / \text{mm s}^{-1}$	B3LYP	1.0730	0.981	1.326	1.163
	TPSS	0.7530	-0.668	—	—
	TPSSH	0.9170	0.832	—	—

Figure 8.7. Excerpt from LIFDI spectrum of **38^{ox}** in THF. The insert depicts the simulation of the isotopic pattern.

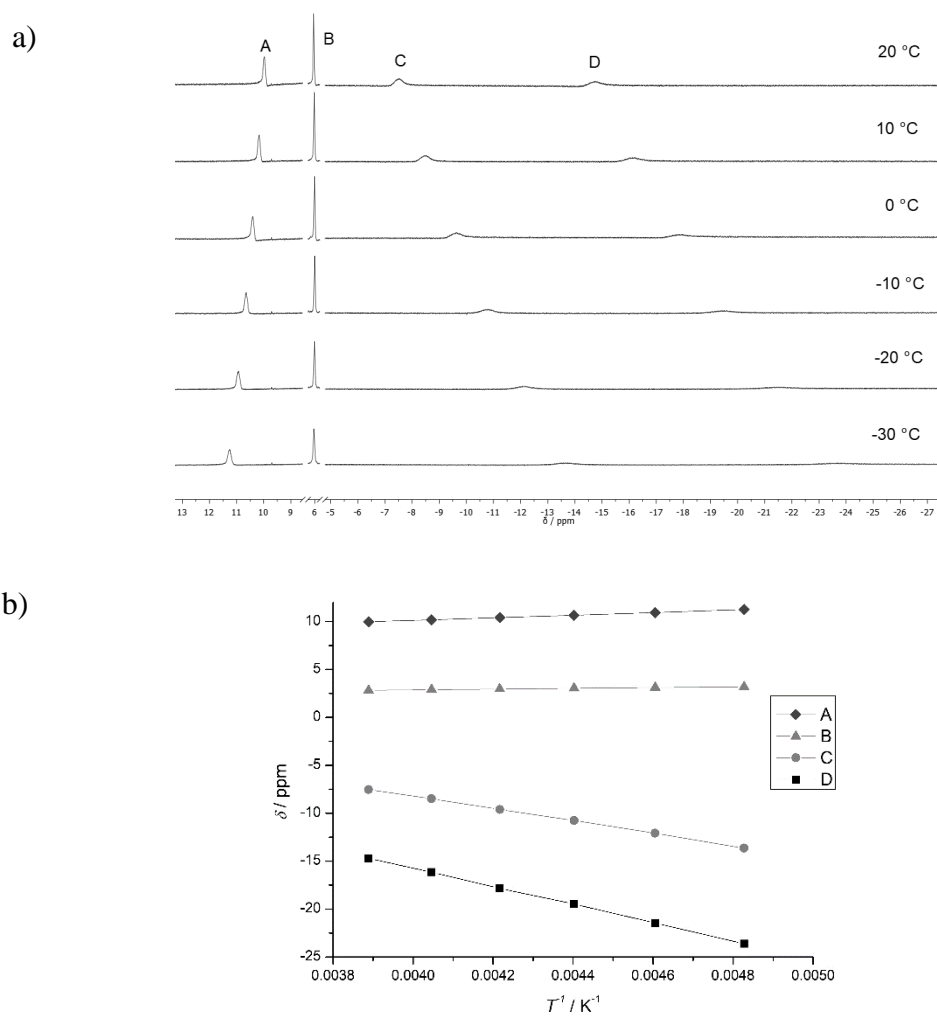


Figure 8.8. a) Paramagnetic signals of the oxidation product in acetone- d_6 at various temperatures. b) Curie behavior of the signals.

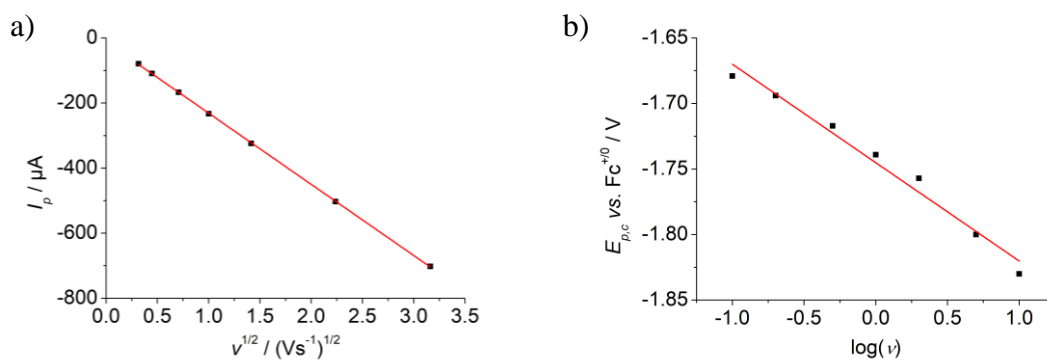
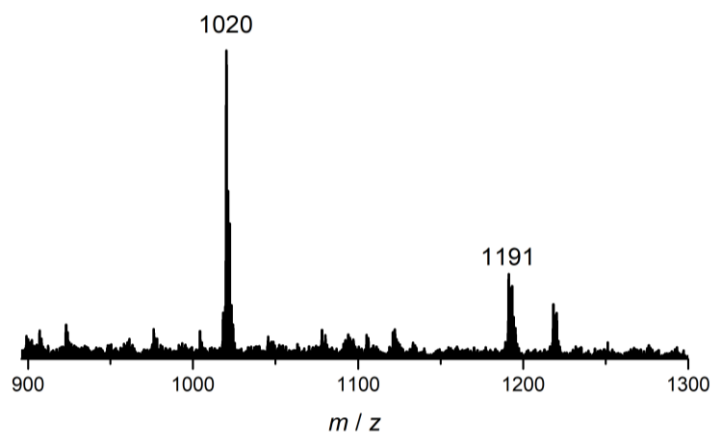
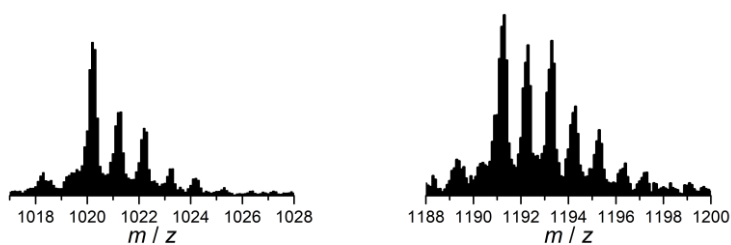


Figure 8.9. a) Plot of the peak current $I_{p,c}$ vs. the square root of the scan rate (0.1 M Bu_4NPF_6 , $c(\mathbf{41}) = 1.8$ mM, $c(\text{H}_2\text{O}) \sim 0.21$ M), b) plot of the peak potential of the reduction wave at different scan rates vs. the logarithm of the scan rate (0.1 M Bu_4NPF_6 , $c(\mathbf{41}) = 1.8$ mM).



Excerpt from spectrum:



Simulation:

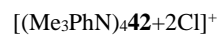
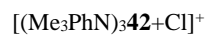
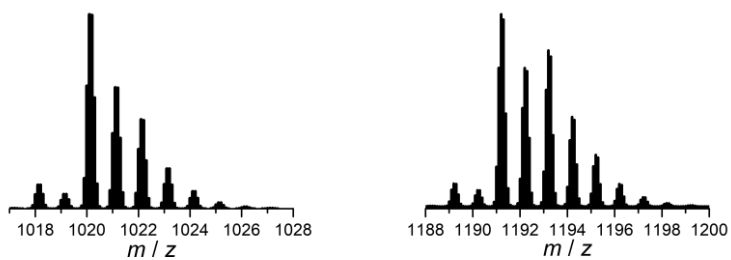


Figure 8.10. ESI(+)-MS of $(\text{Me}_3\text{PhN})_3\mathbf{42}$. Excerpt of spectrum and simulation.

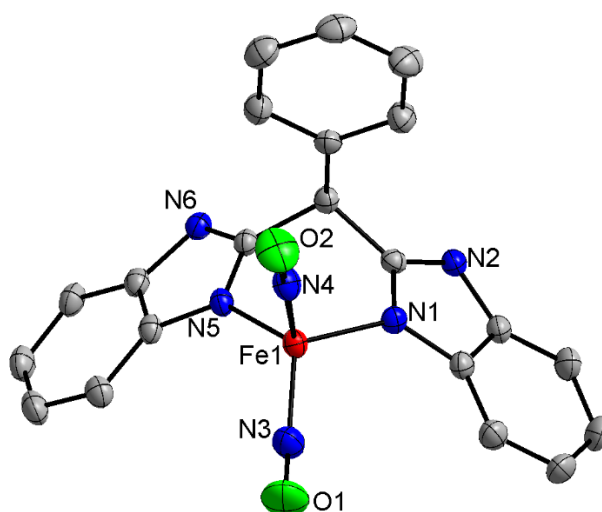


Figure 8.11. Plot (50% probability thermal ellipsoids) of the anion of (PPN)**33** (hydrogen atoms and counter ions omitted for clarity). Selected bond lengths [\AA] and angles [$^\circ$]: Fe1–N4 1.683(2), Fe1–N3 1.701(3), Fe1–N1 1.979(2), Fe1–N5 1.996(2); N1–Fe1–N5 93.75(9), N4–Fe1–N5 108.80(11), N4–Fe1–N3 111.52(13), N4–Fe1–N1 111.77(10), N3–Fe1–N1 111.90(11), N3–Fe1–N5 117.92(10), C2–N1–Fe1 120.08(16), C9–N5–Fe1 120.27(14), C3–N1–Fe1 132.69(18), C10–N5–Fe1 134.83(18), O1–N3–Fe1 157.3(3), O2–N4–Fe1 171.3(3).

Table 8.4 Crystal data and refinement details for (PPN)**33**.

compound	(PPN) 33
empirical formula	$\text{C}_{57}\text{H}_{44}\text{FeN}_7\text{O}_2\text{P}_2$
formula weight	976.78
T [K]	133(2)
crystal size [mm^3]	0.530 x 0.230 x 0.150
crystal system	monoclinic
space group	$P2_1$ (No. 4)
a [\AA]	10.635(2)
b [\AA]	22.009(4)
c [\AA]	10.688(2)
α [$^\circ$]	90
β [$^\circ$]	104.51(3)
γ [$^\circ$]	90
V [\AA^3]	2421.8(9)
Z	2
ρ [$\text{g}\cdot\text{cm}^{-3}$]	1.339
$F(000)$	1014
μ [mm^{-1}]	0.429
θ -range [$^\circ$]	1.851 - 26.723
hkl -range	$\pm 13, \pm 27, \pm 13$
measured refl.	18082
unique refl. [R_{int}]	9407 [0.0415]
observed refl. ($I > 2\sigma(I)$)	8975
data / restr. / param.	9407 / 1 / 622
goodness-of-fit (F^2)	0.922
$R1, wR2$ ($I > 2\sigma(I)$)	0.0284 / 0.0730
$R1, wR2$ (all data)	0.0300 / 0.0739
res. el. dens. [$\text{e}\cdot\text{\AA}^{-3}$]	-0.333 / 0.432

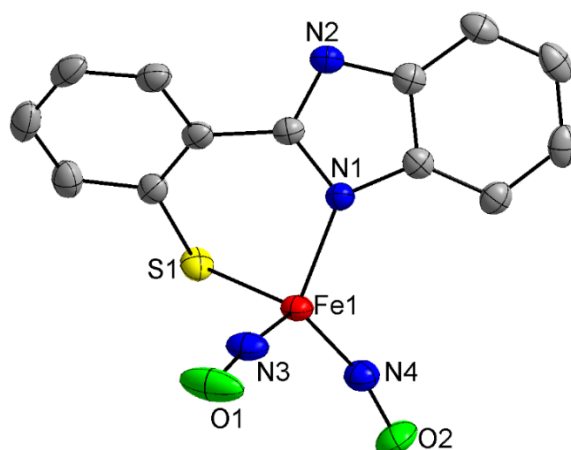


Figure 8.12. Plot (50% probability thermal ellipsoids) of the anion of (PPN)**34** (hydrogen atoms and counter ions omitted for clarity). Selected bond lengths [\AA] and angles [$^\circ$]: Fe(1)–N(3) 1.676(2), Fe(1)–N(4) 1.681(2), Fe(1)–N(1) 1.970(2), Fe(1)–S(1) 2.2544(8), O(1)–N(3) 1.171(3), O(2)–N(4) 1.185(3); N(3)–Fe(1)–N(4) 113.70(12), N(3)–Fe(1)–N(1) 111.34(10), N(4)–Fe(1)–N(1) 117.04(10), N(3)–Fe(1)–S(1) 105.36(10), N(4)–Fe(1)–S(1) 112.76(8), N(1)–Fe(1)–S(1) 94.51(6), O(1)–N(3)–Fe(1) 169.1(2), O(2)–N(4)–Fe(1) 160.5(2).

Table 8.5. Crystal data and refinement details for (PPN)**34**.

compound	(PPN) 34
empirical formula	$\text{C}_{49}\text{H}_{38}\text{FeN}_5\text{O}_2\text{P}_2\text{S}$
formula weight	878.69
T [K]	133(2)
crystal size [mm^3]	0.340 x 0.140 x 0.100
crystal system	monoclinic
space group	$P2_1/n$ (No. 14)
a [\AA]	10.62000(10)
b [\AA]	30.8737(6)
c [\AA]	12.9499(2)
α [$^\circ$]	90
β [$^\circ$]	95.1970(10)
γ [$^\circ$]	90
V [\AA^3]	4228.54(11)
Z	4
ρ [$\text{g}\cdot\text{cm}^{-3}$]	1.380
$F(000)$	1820
μ [mm^{-1}]	0.529
$T_{\text{min}} / T_{\text{max}}$	0.8854 / 0.9672
θ -range [$^\circ$]	1.711 - 25.660
hkl -range	$\pm 12, \pm 37, -14$ to 15
measured refl.	42573
unique refl. [R_{int}]	7958 [0.0504]
observed refl. ($I > 2\sigma(I)$)	6398
data / restr. / param.	7958 / 0 / 541
goodness-of-fit (F^2)	1.126
$R1, wR2$ ($I > 2\sigma(I)$)	0.0420 / 0.0934
$R1, wR2$ (all data)	0.0605 / 0.1049
res. el. dens. [$\text{e}\cdot\text{\AA}^{-3}$]	-0.330 / 0.606

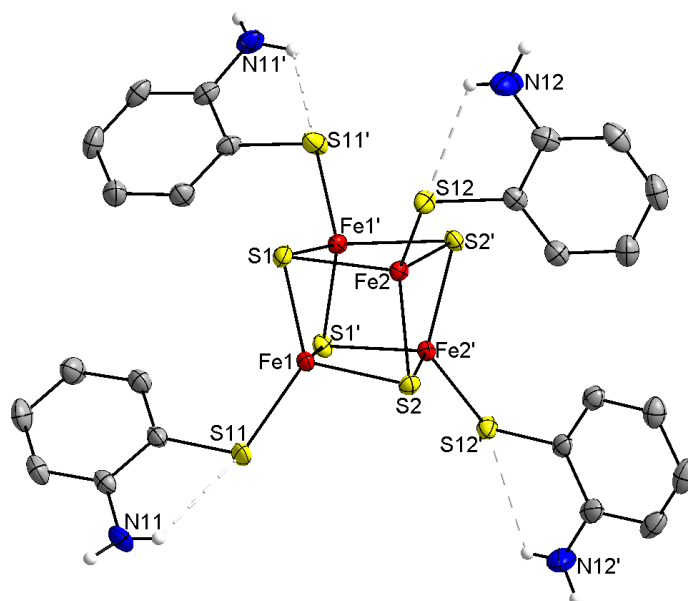


Figure 8.13. Plot (50% probability thermal ellipsoids) of the anion of $(\text{Et}_4\text{N})_2\mathbf{38}$ (hydrogen atoms bound to carbons and counter ions omitted for clarity). Selected bond lengths [\AA] and angles [$^\circ$]: Fe(1)–S(1) 2.2666(6), Fe(2)–S(12) 2.2725(6), Fe(1)–S(1) 2.2315(6), Fe(1)–S(2) 2.3154(6), Fe(2)–S(2) 2.2418(6), Fe(2)–S(1) 2.3145(6), S(1)–Fe(1)–S(11) 124.19(3), S(1)–Fe(1)–S(2) 102.86(2), S(11)–Fe(1)–S(2) 103.86(2), S(2)–Fe(2)–S(1) 102.57(2), S(12)–Fe(2)–S(1) 103.59(2), S(2)–Fe(2)–S(12) 124.42(2).

Table 8.6. Crystal data and refinement details for $(\text{Et}_4\text{N})_2\mathbf{38}$.

compound	$(\text{Et}_4\text{N})_2\mathbf{38}$
empirical formula	$\text{C}_{40}\text{H}_{64}\text{Fe}_4\text{N}_6\text{S}_8$
formula weight	1108.85
T [K]	133(2)
crystal size [mm^3]	0.500 x 0.470 x 0.410
crystal system	orthorhombic
space group	$Aba2$ (No. 41)
a [\AA]	19.1273(6)
b [\AA]	17.6918(5)
c [\AA]	14.4661(5)
α [$^\circ$]	90
β [$^\circ$]	90
γ [$^\circ$]	90
V [\AA^3]	4895.3(3)
Z	4
ρ [$\text{g}\cdot\text{cm}^{-3}$]	1.505
$F(000)$	2312
μ [mm^{-1}]	1.539
$T_{\text{min}} / T_{\text{max}}$	0.4823 / 0.7049
θ -range [$^\circ$]	2.107 - 26.706
hkl -range	$\pm 24, \pm 22, \pm 18$
measured refl.	33515
unique refl. [R_{int}]	5182 [0.0623]
observed refl. ($I > 2\sigma(I)$)	5166
data / restr. / param.	5182 / 1 / 282
goodness-of-fit (F^2)	1.099
$R1, wR2$ ($I > 2\sigma(I)$)	0.0192 / 0.0494
$R1, wR2$ (all data)	0.0193 / 0.0494
res. el. dens. [$\text{e}\cdot\text{\AA}^{-3}$]	-0.409 / 0.453

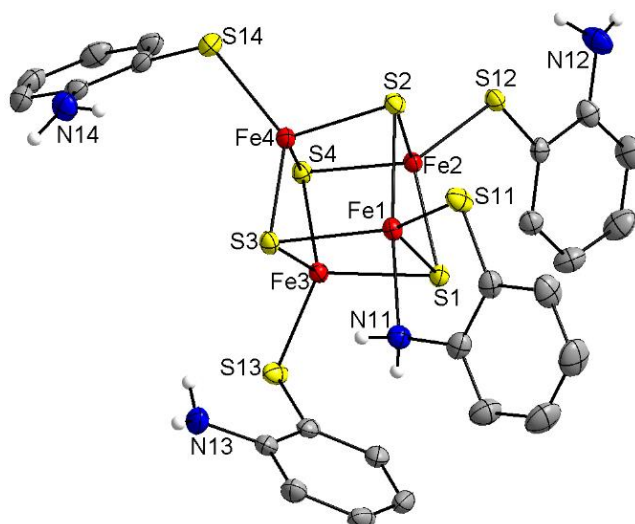


Figure 8.14. Plot (50% probability thermal ellipsoids) of the anion of $(\text{Me}_3\text{PhN})_2\mathbf{38}$ (hydrogen atoms bound to carbons, counter ions and solvent molecules omitted for clarity). Selected bond lengths [\AA] and angles [$^\circ$]: Fe(1)–N(11) 2.2770(13), Fe(1)–S(1) 2.2790(4), Fe(1)–S(11) 2.3318(4), Fe(1)–S(3) 2.3462(4), Fe(1)–S(2) 2.4500(4), Fe(2)–S(2) 2.2168(4), Fe(2)–S(12) 2.2707(4), Fe(2)–S(1) 2.2818(4), Fe(2)–S(4) 2.3073(4), Fe(3)–S(3) 2.2562(4), Fe(3)–S(13) 2.2711(4), Fe(3)–S(1) 2.2905(4), Fe(3)–S(4) 2.3075(4), Fe(4)–S(4) 2.2486(4), Fe(4)–S(2) 2.2740(4), Fe(4)–S(14) 2.2756(4), Fe(4)–S(3) 2.2928(4), N(11)–Fe(1)–S(1) 90.40(4), N(11)–Fe(1)–S(11) 79.64(4), S(1)–Fe(1)–S(11) 124.115(17), N(11)–Fe(1)–S(3) 89.96(4).

Table 8.7. Crystal data and refinement details for $(\text{Me}_3\text{PhN})_2\mathbf{38}$.

compound	$(\text{Me}_3\text{PhN})_2\mathbf{38}$
empirical formula	$\text{C}_{40}\text{H}_{64}\text{Fe}_4\text{N}_6\text{S}_8$
formula weight	1108.85
T [K]	133(2)
crystal size [mm^3]	0.500 x 0.470 x 0.410
crystal system	orthorhombic
space group	$Aba2$ (No. 41)
a [\AA]	19.1273(6)
b [\AA]	17.6918(5)
c [\AA]	14.4661(5)
α [$^\circ$]	90
β [$^\circ$]	90
γ [$^\circ$]	90
V [\AA^3]	4895.3(3)
Z	4
ρ [$\text{g}\cdot\text{cm}^{-3}$]	1.505
$F(000)$	2312
μ [mm^{-1}]	1.539
$T_{\text{min}} / T_{\text{max}}$	0.4823 / 0.7049
θ -range [$^\circ$]	2.107 - 26.706
hkl -range	$\pm 24, \pm 22, \pm 18$
measured refl.	33515
unique refl. [R_{int}]	5182 [0.0623]
observed refl. ($I > 2\sigma(I)$)	5166
data / restr. / param.	5182 / 1 / 282
goodness-of-fit (F^2)	1.099
$R1, wR2$ ($I > 2\sigma(I)$)	0.0192 / 0.0494
$R1, wR2$ (all data)	0.0193 / 0.0494
res. el. dens. [$\text{e}\cdot\text{\AA}^{-3}$]	-0.409 / 0.453

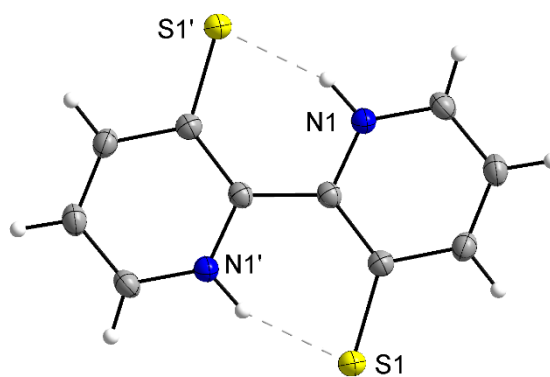


Figure 8.15. Plot (50% probability thermal ellipsoids) of the anion of **41H₂** (hydrogen atoms bound to carbons, counter ions and solvent molecules omitted for clarity). Selected bond lengths [Å] and angles [°]: S(1)–C(2) 1.7318(16), N(1)–C(5) 1.337(2), N(1)–C(1) 1.357(2), C(5)–N(1)–C(1) 125.46(15).

Table 8.8. Crystal data and refinement details for **41H₂**.

compound	41H₂
empirical formula	C ₁₀ H ₈ N ₂ S ₂
formula weight	220.30
<i>T</i> [K]	133(2)
crystal size [mm ³]	0.310 x 0.230 x 0.120
crystal system	monoclinic
space group	<i>P</i> 2 ₁ / <i>c</i> (No. 14)
<i>a</i> [Å]	4.1146(3)
<i>b</i> [Å]	10.8240(11)
<i>c</i> [Å]	10.4628(9)
α [°]	90
β [°]	90.143(7)
γ [°]	90
<i>V</i> [Å ³]	465.97(7)
<i>Z</i>	2
ρ [g·cm ⁻³]	1.570
<i>F</i> (000)	228
μ [mm ⁻¹]	0.525
<i>T</i> _{min} / <i>T</i> _{max}	0.8526 / 0.9390
θ -range [°]	2.708 - 26.796
<i>hkl</i> -range	±5, ±13, ±13
measured refl.	5273
unique refl. [<i>R</i> _{int}]	991 [0.0214]
observed refl. (<i>I</i> > 2σ(<i>I</i>))	889
data / restr. / param.	991 / 0 / 80
goodness-of-fit (<i>F</i> ²)	1.087
<i>R</i> 1, <i>wR</i> 2 (<i>I</i> > 2σ(<i>I</i>))	0.0296 / 0.0786
<i>R</i> 1, <i>wR</i> 2 (all data)	0.0344 / 0.0819
res. el. dens. [e·Å ⁻³]	-0.172 / 0.357

Table 8.9 Hydrogen bonds for **41H₂** [Å and °].

D–H...A	d(D–H)	d(H...A)	d(D...A)	<(DHA)
N(1)–H(1)...S(1)#1	0.92(2)	2.02(2)	2.8844(15)	158(2)

Symmetry transformations used to generate equivalent atoms:
 #1 $-x+1, -y+1, -z+1$

9 Literature

- (1) Beinert, H.; Holm, R. H.; Münck, E. *Science* **1997**, *277*, 653.
- (2) Wächtershäuser, G. *Prog. Biophys. molec. Biol.* **1992**, *58*, 85.
- (3) Wächtershäuser, G. *Chem. Biodivers.* **2007**, *4*, 584.
- (4) Huber, C.; Wächtershäuser, G. *Science* **1997**, *276*, 245.
- (5) Daniel, R. M.; Danson, M. J. *J. Mol. Evol.* **1995**, *40*, 559.
- (6) Bonfio, C.; Valer, L.; Scintilla, S.; Shah, S.; Evans, D. J.; Jin, L.; Szostak, J. W.; Sasselov, D. D.; Sutherland, J. D.; Mansy, S. S. *Nat. Chem.* **2017**, *9*, 1229.
- (7) Hagen, W. R. *Adv. Inorg. Chem.* **1992**, *38*, 165.
- (8) Beinert, H.; Sands, R. H. *Biochem. Biophys. Res. Commun.* **1960**, *3*, 41.
- (9) Gibson, J. F.; Hall, D. O.; Thornley, J. H. M.; Whatley, F. R. *Proc. Natl. Acad. Sci.* **1966**, *56*, 987.
- (10) Rao, P. V.; Holm, R. H. *Chem. Rev.* **2004**, *104*, 527.
- (11) Lee, S. C.; Lo, W.; Holm, R. H. *Chem. Rev.* **2014**, *114*, 3579.
- (12) Yao, W.; Gurubasavaraj, P. M.; Holland, P. L. In *Molecular Design in Inorganic Biochemistry*; Rabinovich, D., Ed.; Springer: Berlin, 2014; pp 1–36.
- (13) Kennedy, M. C.; Kent, T. A.; Emptage, M.; Merkle, H.; Beinert, H. *J. Biol. Chem.* **1984**, *259*, 14463.
- (14) Khoroshilova, N.; Popescu, C.; Münck, E.; Beinert, H.; Kiley, P. J. *Proc. Natl. Acad. Sci.* **1997**, *94*, 6087.
- (15) Rees, D. C.; Howard, J. B. *Science* **2003**, *300* (May), 929.
- (16) Bak, D. W.; Elliott, S. J. *Curr. Opin. Chem. Biol.* **2014**, *19*, 50.
- (17) Link, T. A. *Adv. Inorg. Chem.* **1999**, *47*, 83.
- (18) Calzolari, L.; Zhou, Z. H.; Adams, M. W. W.; La Mar, G. N. *J. Am. Chem. Soc.* **1996**, *118*, 2513.
- (19) Hunsicker-Wang, L. M.; Heine, A.; Chen, Y.; Luna, E. P.; Todaro, T.; Zhang, Y. M.; Williams, P. A.; McRee, D. E.; Hirst, O. J.; Stout, C. D.; Fee, J. A. *Biochemistry* **2003**, *42*, 7303.
- (20) Konkle, M. E.; Muellner, S. K.; Schwander, A. L.; Dicus, M. M.; Pokhrel, R.; Britt, R. D.; Taylor, A. B.; Hunsicker-Wang, L. M. *Biochemistry* **2009**, *48*, 9848.
- (21) Lill, R. *Nature* **2009**, *460*, 831.
- (22) Malkin, R.; Rabinowitz, J. C. *Biochem. Biophys. Res. Commun.* **1966**, *23*, 822.
- (23) Py, B.; Barras, F. *Nat. Rev. Microbiol.* **2010**, *8*, 436.
- (24) Roche, B.; Aussel, L.; Ezraty, B.; Mandin, P.; Py, B.; Barras, F. *Biochim. Biophys. Acta* **2013**, *1827*, 455.

- (25) Takahashi, Y.; Tokumoto, U. *J. Biol. Chem.* **2002**, *277*, 28380.
- (26) Fontecave, M.; Choudens, S. O. De; Py, B.; Barras, F. *J. Biol. Inorg. Chem.* **2005**, *10*, 713.
- (27) Lill, R.; Dutkiewicz, R.; Freibert, S. A.; Heidenreich, T.; Mascarenhas, J.; Netz, D. J.; Paul, V. D.; Pierik, A. J.; Richter, N.; Stümpfig, M.; Srinivasan, V.; Stehling, O.; Mühlenhoff, U. *Eur. J. Cell Biol.* **2015**, *94*, 280.
- (28) Braymer, J. J.; Lill, R. *J. Biol. Chem.* **2017**, *292*, 12754.
- (29) Maio, N.; Rouault, T. A. *Biochim. Biophys. Acta* **2015**, *1853*, 1493.
- (30) Netz, D. J. A.; Mascarenhas, J.; Stehling, O.; Pierik, A. J.; Lill, R. *Trends Cell Biol.* **2014**, *24*, 303.
- (31) Freibert, S.-A.; Goldberg, A. V.; Hacker, C.; Molik, S.; Dean, P.; Williams, T. A.; Nakjang, S.; Long, S.; Sendra, K.; Bill, E.; Heinz, E.; Hirt, R. P.; Lucocq, J. M.; Embley, T. M.; Lill, R. *Nat. Commun.* **2017**, *8*, 13932.
- (32) Tanaka, N.; Kanazawa, M.; Tonosaki, K.; Yokoyama, N.; Kuzuyama, T.; Takahashi, Y. *Mol. Microbiol.* **2016**, *99*, 835.
- (33) Vaccaro, B. J.; Clarkson, S. M.; Holden, J. F.; Lee, D.; Wu, C.; Poole II, F. L.; Cotelesage, J. J. H.; Hackett, M. J.; Mohebbi, S.; Sun, J.; Li, H.; Johnson, M. K.; George, G. N.; Adams, M. W. W. *Nat. Commun.* **2017**, *8*, 16110.
- (34) Campuzano, V.; Montermini, L.; Molto, M. D.; Pianese, L.; Cossee, M.; Cavalcanti, F.; Monros, E.; Rodius, F.; Duclos, F.; Monticelli, A.; Zara, F.; Canizares, J.; Koutnikova, H.; Bidichandani, S.; Gellera, C.; Brice, A.; Trouillas, P.; Michele, G. De; Filla, A.; Frutos, R. De; Patel, P.; Donato, S. Di; Mandel, J.; Coccozza, S.; Koenig, M.; Pandolfoll, M. *Science* **1996**, *271*, 1423.
- (35) Colin, F.; Martelli, A.; Clémancey, M.; Latour, J.-M.; Gambarelli, S.; Zeppieri, L.; Birck, C.; Page, A.; Puccio, H.; Ollagnier de Choudens, S. *J. Am. Chem. Soc.* **2013**, *135*, 733.
- (36) Johnson, D. C.; Dean, D. R.; Smith, A. D.; Johnson, M. K. *Annu. Rev. Biochem.* **2005**, *74*, 247.
- (37) Capozzi, F.; Ciurli, S.; Luchinat, C. In *Structure and Bonding*; 1998; Vol. 90, pp 127–160.
- (38) Noodleman, L.; Lovell, T.; Liu, T.; Himo, F.; Torres, R. A. *Curr. Opin. Chem. Biol.* **2002**, *6*, 259.
- (39) Peters, J. W.; Stowell, M. H. B.; Soltis, S. M.; Finnegan, M. G.; Johnson, M. K.; Rees, D. C. *Biochemistry* **1997**, *36*, 1181.
- (40) Crouse, B. R.; Meyer, J.; Johnson, M. K. *J. Am. Chem. Soc.* **1995**, *117*, 9612.
- (41) Yoo, S. J.; Angove, H. C.; Burgess, B. K.; Hendrich, M. P.; Münck, E. *J. Am. Chem. Soc.* **1999**, *121*, 2534.
- (42) Hans, M.; Buckel, W.; Bill, E. *J. Biol. Inorg. Chem.* **2008**, *13*, 563.
- (43) Takeda, K.; Miki, K. *FEBS J.* **2017**, *284*, 2163.

- (44) Banci, L.; Bertini, I.; Ciurli, S.; Ferretti, S.; Luchinat, C.; Piccioliti, M. *Biochemistry* **1993**, *32*, 9387.
- (45) Meyer, J. J. *Biol. Chem.* **2008**, *13*, 157.
- (46) Bartsch, R. *Methods Enzymol.* **1978**, *53*, 329.
- (47) Ohta, S.; Ohki, Y. *Coord. Chem. Rev.* **2017**, *338*, 207.
- (48) Colbert, C. L.; Couture, M. M.; Eltis, L. D.; Bolin, J. T.; Lafayette, W. *Structure* **2000**, *8*, 1267.
- (49) Link, T. A. *Biochim. Biophys. Acta* **1994**, *1185*, 81.
- (50) Hsueh, K.-L.; Westler, W. M.; Markley, J. L. *J. Am. Chem. Soc.* **2010**, *132*, 7908.
- (51) Zu, Y.; Couture, M. M.; Kolling, D. R. J.; Crofts, A. R.; Eltis, L. D.; Fee, J. A.; Hirst, J. *Biochemistry* **2003**, *42*, 12400.
- (52) Paddock, M. L.; Wiley, S. E.; Axelrod, H. L.; Cohen, A. E.; Roy, M.; Abresch, E. C.; Capraro, D.; Murphy, A. N.; Nechushtai, R.; Dixon, J. E.; Jennings, P. A. *Proc. Natl. Acad. Sci.* **2007**, *104*, 14342.
- (53) Lin, J.; Zhang, L.; Lai, S.; Ye, K. *PLoS One* **2011**, *6*, 24790.
- (54) Bak, D. W.; Elliott, S. J. *Biochemistry* **2013**, *52*, 4687.
- (55) Fontecilla-Camps, J. C.; Volbeda, A.; Cavazza, C.; Nicolet, Y. *Chem. Rev.* **2007**, *107*, 4273.
- (56) Kiley, P. J.; Beinert, H. *Curr. Opin. Microbiol.* **2003**, *6*, 181.
- (57) Mettert, E. L.; Kiley, P. J. *Biochim. Biophys. Acta* **2015**, *1853*, 1284.
- (58) Miller, H. K.; Auerbuch, V. *Metallomics* **2015**, *7*, 943.
- (59) Kobayashi, K. *Acc. Chem. Res.* **2017**, *50*, 1672.
- (60) Gu, M.; Imlay, J. A. *Mol. Microbiol.* **2011**, *79*, 1136.
- (61) Rouault, T. A.; Klausner, R. D. *Trends Biochem. Sci.* **1996**, *21*, 174.
- (62) Crack, J. C.; Thomson, A. J.; LeBrun, N. E. *Proc. Natl. Acad. Sci.* **2017**, *114*, 3215.
- (63) Tucker, N. P.; Brun, N. E. Le; Dixon, R.; Hutchings, M. I. *Trends Microbiol.* **2010**, *18*, 149.
- (64) Volbeda, A.; Dodd, E. L.; Darnault, C.; Crack, J. C.; Renoux, O.; Hutchings, M. I.; Brun, N. E. Le; Fontecilla-camps, J. C. *Nat. Commun.* **2017**, *8*, 15052.
- (65) Anderson, C. P.; Shen, M.; Eisenstein, R. S.; Leibold, E. A. *Biochim. Biophys. Acta* **2012**, *1823*, 1468.
- (66) Spatzal, T.; Aksoyoglu, M.; Zhang, L.; Andrade, S. L. A.; Schleicher, E.; Weber, S.; Rees, D. C.; Einsle, O. *Science* **2011**, *334*, 940.
- (67) Lancaster, K. M.; Roemelt, M.; Ettenhuber, P.; Hu, Y.; Ribbe, M. W.; Neese, F.; Bergmann, U.; DeBeer, S. *Science* **2011**, *334*, 974.
- (68) Grunenberg, J. *Angew. Chem.* **2017**, *56*, 7288.

- (69) Eady, R. R. *Chem. Rev* **1996**, 962, 3013.
- (70) Lee, C. C.; Hu, Y.; Ribbe, M. W. *Science* **2010**, 329, 642.
- (71) Vincent, K. A.; Parkin, A.; Armstrong, F. A. *Chem. Rev.* **2007**, 107, 4366.
- (72) Beinert, H.; Kennedy, M. C.; Stout, C. D. *Chem. Rev.* **1996**, 96, 2335.
- (73) Kennedy, M. C.; Werst, M.; Telser, J.; Emptage, M. H.; Beinert, H.; Hoffman, B. M. *Proc. Natl. Acad. Sci.* **1987**, 84, 8854.
- (74) Frey, P. A.; Hegeman, A. D.; Ruzicka, F. J.; Frey, P. A.; Hegeman, A. D.; Ruzicka, F. J.; Radical, T.; Frey, P. A.; Hegeman, A. D.; Ruzicka, F. J. *Crit. Rev. Biochem. Mol. Biol.* **2017**, 43, 63.
- (75) Walsby, C. J.; Ortillo, D.; Broderick, W. E.; Broderick, J. B.; Hoffman, B. M. *J. Am. Chem. Soc.* **2002**, 124, 11270.
- (76) Hiscox, M. J.; Driesener, R. C.; Roach, P. L. *Biochim. Biophys. Acta* **2012**, 1824, 1165.
- (77) Lanz, N. D.; Booker, S. J. *Biochim. Biophys. Acta* **2012**, 1824, 1196.
- (78) Hutcheson, R. U.; Broderick, J. B. *Metallomics* **2012**, 4, 1149.
- (79) Shisler, K. A.; Broderick, J. B. *Curr. Opin. Struct. Biol.* **2012**, 22, 701.
- (80) Broach, R. B.; Jarrett, J. T. *Biochemistry* **2006**, 45, 14166.
- (81) Jarrett, J. T. *Arch. Biochem. Biophys.* **2005**, 433, 312.
- (82) Harmer, J.; Hiscox, M. J.; Dinis, P. C.; Fox, S. J.; Iliopoulos, A.; Hussey, J. E.; Sandy, J.; Van Beek, F. T.; Essex, J. W.; Roach, P. L. *Biochem. J.* **2014**, 464, 123.
- (83) Que, L.; Holm, R. H. *J. Am. Chem. Soc.* **1975**, 97, 463.
- (84) Herskovitz, T.; Averill, B. A.; Holm, R. H.; Ibers, J. A.; Phillips, W. D.; Weiher, J. F. *Proc. Natl. Acad. Sci.* **1972**, 69, 2437.
- (85) Mayerle, J. J.; Frankel, R. B.; Holm, R. H.; Ibers, J. A.; Phillips, W. D.; Weiher, J. F. *Proc. Natl. Acad. Sci.* **1973**, 70, 2429.
- (86) Lane, R. W. *Proc. Natl. Acad. Sci.* **1975**, 72, 2868.
- (87) Hagen, K. S.; Watson, A. D.; Holm, R. H. *J. Am. Chem. Soc.* **1983**, 105, 3905.
- (88) Zhou, J.; Holm, R. H. *J. Am. Chem. Soc.* **1995**, 117, 11353.
- (89) Beardwood, P.; Gibson, J. F. *J. Chem. Soc. Chem. Commun.* **1986**, 490.
- (90) Beardwood, P.; Gibson, J. F. *J. Chem. Soc. Dalton Trans.* **1992**, 2457.
- (91) Ohki, Y.; Sunada, Y.; Tatsumi, K. *Chem. Lett.* **2005**, 34, 172.
- (92) Ballmann, J.; Albers, A.; Demeschko, S.; Dechert, S.; Bill, E.; Bothe, E.; Ryde, U.; Meyer, F. *Angew. Chem.* **2008**, 47, 9537.
- (93) Qi, W.; Li, J.; Chain, C. Y.; Pasquevich, G. A.; Pasquevich, A. F.; Cowan, J. A. *Chem. Commun.* **2013**, 49, 6313.
- (94) Sharp, C. R.; Duncan, J. S.; Lee, S. C. *Inorg. Chem.* **2010**, 49, 6697.

- (95) Sullivan, T. O.; Millar, M. M. *J. Am. Chem. Soc.* **1985**, *107*, 4096.
- (96) Papaefthymiou, V.; Millar, M. M.; Münck, E. *Inorg. Chem.* **1986**, *25*, 3010.
- (97) Job, R. C.; Bruice, T. C. *Proc. Natl. Acad. Sci.* **1975**, *72*, 2478.
- (98) Carrell, H. L.; Glusker, J. P.; Bruice, T. C.; Job, R. *J. Am. Chem. Soc.* **1977**, *99*, 3683.
- (99) Deng, L.; Holm, R. H. *J. Am. Chem. Soc.* **2008**, *130*, 9878.
- (100) Ohki, Y.; Tanifuji, K.; Yamada, N.; Imada, M.; Tajima, T.; Tatsumi, K. *Proc. Natl. Acad. Sci.* **2011**, *108*, 12635.
- (101) Stack, T. D. . P.; Holm, R. H. *J. Am. Chem. Soc.* **1988**, *110*, 2484.
- (102) Ciurli, S.; Carney, J.; Weigel, J. A.; Carney, M. J.; Stack, T. D. P.; Papaefthymiou, G. C.; Holm, R. H. *J. Am. Chem. Soc.* **1990**, *112*, 2654.
- (103) Holm, R. H. *Adv. Inorg. Chem.* **1992**, *38*, 1.
- (104) Johnson, M. K.; Duderstadt, R. E. *Adv. Inorg. Chem.* **1999**, *47*, 1.
- (105) Corlic, I.; Mercado, B. Q.; Bill, E.; Vinyard, D. J.; Holland, P. L. *Nature* **2015**, *526*, 96.
- (106) Ilija, C.; Holland, P. L. *J. Am. Chem. Soc.* **2016**, *138*, 7200.
- (107) Stamler, J.; Singel, D.; Loscalzo, J. *Science* **1992**, *258*, 1898.
- (108) Murad, F. *Angew. Chem.* **1999**, *38*, 1856.
- (109) Brown, G. C. *Front. Biosci.* **2007**, *12*, 1024.
- (110) Watmough, N. J.; Butland, G.; Cheesman, M. R.; Moir, J. W.; Richardson, D. J.; Spiro, S. *Biochim. Biophys. Acta* **1999**, *1411*, 456.
- (111) Derbyshire, E. R.; Marletta, M. A. In *Handbook of Experimental Pharmacology*; Schmidt, H., Hofmann, F., Stasch, J.-P., Eds.; Springer-Verlag: Berlin, Heidelberg, 2009; pp 17–31.
- (112) Ibrahim, M.; Derbyshire, E. R.; Soldatova, A. V; Marletta, M. A.; Spiro, T. G. *Biochemistry* **2010**, *49*, 4864.
- (113) Furchgott, R. F. *Angew. Chem.* **1999**, *38*, 1870.
- (114) Ignarro, L. J. *Angew. Chem.* **1999**, *38*, 1882.
- (115) Prast, H.; Philippu, A. *Prog. Neurobiol.* **2001**, *64*, 51.
- (116) Bogdan, C. *Nat. Immunol.* **2001**, *2*, 907.
- (117) Bronte, V.; Zanollo, P. *Nat. Rev. Immunol.* **2005**, *5*, 641.
- (118) Calabrese, V.; Mancuso, C.; Calvani, M.; Rizzarelli, E.; Butterfield, D. A.; Stella, A. M. G. *Nat. Rev. Neurosci.* **2007**, *8*, 766.
- (119) Richardson, D. R.; Lok, H. C. *Biochim. Biophys. Acta* **2008**, *1780*, 638.
- (120) Enemark, J. H.; Feltham, R. D. *Coord. Chem. Rev.* **1974**, *13*, 339.

- (121) Roussin, M. L. *Ann. Chim. Phys.* **1858**, 52, 285.
- (122) Butler, A. R.; Megson, I. L. *Chem. Rev.* **2002**, 102, 1155.
- (123) Lu, T.-T.; Tsou, C. C.; Huang, H. W.; Hsu, I. J.; Chen, J. M.; Kuo, T. S.; Wang, Y.; Liaw, W. F. *Inorg. Chem.* **2008**, 47, 6040.
- (124) Seto, M.; Yoda, Y.; Kikuta, S.; Zhang, X. W.; Ando, M. *Phys. Rev. Lett.* **1995**, 74, 3828.
- (125) Wang, H.; Alp, E.; Yoda, Y.; Cramer, S. P. *Methods Mol. Biol.* **2014**, 1122, 125.
- (126) Tonzetich, Z. J.; Wang, H.; Mitra, D.; Tinberg, C. E.; Do, L. H.; Jenney, F. E.; Adams, M. W. W.; Cramer, S. P.; Lippard, S. J. *J. Am. Chem. Soc.* **2010**, 132, 6914.
- (127) Tinberg, C. E.; Tonzetich, Z. J.; Wang, H.; Do, L. H.; Yoda, Y.; Cramer, S. P.; Lippard, S. J. *J. Am. Chem. Soc.* **2010**, 132, 18168.
- (128) Serrano, P. N.; Wang, H.; Crack, J. C.; Prior, C.; Hutchings, M. I.; Thomson, A. J.; Kamali, S.; Yoda, Y.; Zhao, J.; Hu, M. Y.; Alp, E. E.; Oganessian, V. S.; Brun, N. E. Le; Cramer, S. P. *Angew. Chem.* **2016**, 55, 14575.
- (129) Xiao, Y.; Wang, H.; George, S. J.; Smith, M. C.; Adams, M. W. W.; Jenney, F. E.; Sturhahn, W.; Alp, E. E.; Zhao, J.; Yoda, Y.; Dey, A.; Solomon, E. I.; Cramer, S. P. *J. Am. Chem. Soc.* **2005**, 127, 14596.
- (130) Lauterbach, L.; Wang, H.; Horch, M.; Gee, L. B.; Yoda, Y.; Tanaka, Y.; Zebger, I.; Lenz, O.; Cramer, S. P. *Chem. Sci.* **2015**, 6, 1055.
- (131) Kamali, S.; Wang, H.; Mitra, D.; Ogata, H.; Lubitz, W.; Manor, B. C.; Rauchfuss, T. B.; Byrne, D.; Bonnefoy, V.; Jenney, F. E.; Adams, M. W. W.; Yoda, Y.; Alp, E.; Zhao, J.; Cramer, S. P. *Angew. Chem.* **2013**, 52, 724.
- (132) Mitra, D.; Pelmeshnikov, V.; Guo, Y.; Case, D. A.; Wang, H.; Dong, W.; Tan, M.; Ichiye, T.; Jenney, F. E.; Adams, M. W. W.; Yoda, Y.; Zhao, J.; Cramer, S. P. *Biochemistry* **2011**, 50, 5220.
- (133) Ogata, H.; Krämer, T.; Wang, H.; Schilter, D.; Pelmeshnikov, V.; van Gastel, M.; Neese, F.; Rauchfuss, T. B.; Gee, L. B.; Scott, A. D.; Yoda, Y.; Tanaka, Y.; Lubitz, W.; Cramer, S. P. *Nat. Commun.* **2015**, 6, 7890.
- (134) Tsai, M.-L.; Tsou, C.-C.; Liaw, W.-F. *Acc. Chem. Res.* **2015**, 48, 1184.
- (135) Fitzpatrick, J.; Kalyvas, H.; Shearer, J.; Kim, E. *Chem. Commun.* **2013**, 49, 5550.
- (136) Drapier, J. C. *Methods* **1997**, 11, 319.
- (137) Lu, T.-T.; Huang, H.-W.; Liaw, W.-F. *Inorg. Chem.* **2009**, 48, 9027.
- (138) Yang, W.; Rogers, P. A.; Ding, H. *J. Biol. Chem.* **2002**, 277, 12868.
- (139) Rogers, P. A.; Ding, H. *J. Biol. Chem.* **2001**, 276, 30980.
- (140) Kennedy, M. C.; Antholine, W. E.; Beinert, H. *J. Biol. Chem.* **1997**, 272, 20340.
- (141) Foster, M. W.; Cowan, J. A. *J. Am. Chem. Soc.* **1999**, 121, 4093.
- (142) D'Autréaux, B.; Horner, O.; Oddou, J.; Jeandey, C.; Gambarelli, S.; Berthomieu, C.; Latour, J.; Michaud-Soret, I. *J. Am. Chem. Soc.* **2004**, 126, 6005.

- (143) D'Autréaux, B.; Tucker, N. P.; Dixon, R.; Spiro, S. *Nature* **2005**, *437*, 769.
- (144) Strube, K.; de Vries, S.; Cramm, R. *J. Biol. Chem.* **2007**, *282*, 20292.
- (145) Landry, A. P.; Duan, X.; Huang, H.; Ding, H. *Free Radic. Biol. Med.* **2011**, *50*, 1582.
- (146) Yukl, E.; Elbaz, M.; Nakano, M.; Moënné-Loccoz, P. *Biochemistry* **2008**, *47*, 13084.
- (147) Cruz-Ramos, H.; Crack, J.; Wu, G.; Hughes, M. N.; Scott, C.; Thomson, A. J.; Green, J.; Poole, R. K. *EMBO J.* **2002**, *21*, 3235.
- (148) Crack, J. C.; Svistunenko, D. A.; Munnoch, J.; Thomson, A. J.; Hutchings, M. I.; Brun, N. E. *J. Biol. Chem.* **2016**, *291*, 8663.
- (149) Crack, J. C.; Smith, L. J.; Stapleton, M. R.; Peck, J.; Watmough, N. J.; Buttner, M. J.; Buxton, R. S.; Green, J.; Oganessian, V. S.; Thomson, A. J.; Le Brun, N. E. *J. Am. Chem. Soc.* **2011**, *133*, 1112.
- (150) Crack, J. C.; Stapleton, M. R.; Green, J.; Thomson, A. J.; Le Brun, N. E. *J. Biol. Chem.* **2013**, *288*, 11492.
- (151) Ding, H.; Demple, B. *Proc. Natl. Acad. Sci.* **2000**, *97*, 5146.
- (152) Lo, F. C.; Lee, J. F.; Liaw, W. F.; Hsu, I. J.; Tsai, Y. F.; Chan, S. I.; Yu, S. S. F. *Chem. Eur. J.* **2012**, *18*, 2565.
- (153) Fujikawa, M.; Kobayashi, K.; Kozawa, T. *J. Biochem.* **2014**, *156*, 163.
- (154) Grabarczyk, D. B.; Ash, P. A.; Vincent, K. A. *J. Am. Chem. Soc.* **2014**, *136*, 11236.
- (155) Cheng, Z.; Landry, A. P.; Wang, Y.; Ding, X. H. *J. Biol. Chem.* **2017**, *292*, 3146.
- (156) Lin, Z.; Lo, F.; Li, C.; Chen, C.; Huang, W.; Hsu, I.; Lee, J.; Horng, J.; Liaw, W. *Inorg. Chem.* **2011**, *50*, 10417.
- (157) Tsai, M.-C.; Tsai, F.-T.; Lu, T.-T.; Tsai, M.-L.; Wei, Y.-C.; Hsu, I.-J.; Lee, J.-F.; Liaw, W.-F. *Inorg. Chem.* **2009**, *48*, 9579.
- (158) Harrop, T. C.; Tonzetich, Z. J.; Reisner, E.; Lippard, S. J. *J. Am. Chem. Soc.* **2008**, *130*, 15602.
- (159) Butler, A. R.; Glidewell, C.; Hyde, A. R.; Walton, J. C. *Inorg. Chim. Acta* **1985**, *106*, L7.
- (160) Tonzetich, Z. J.; McQuade, L. E.; Lippard, S. J. *Inorg. Chem.* **2010**, *49*, 6338.
- (161) Tran, C. T.; Williard, P. G.; Kim, E. *J. Am. Chem. Soc.* **2014**, *136*, 11874.
- (162) Victor, E.; Lippard, S. J. *Inorg. Chem.* **2014**, *53*, 5311.
- (163) Albers, A.; Bayer, T.; Demeshko, S.; Dechert, S.; Meyer, F. *Chem. Eur. J.* **2013**, *19*, 10101.
- (164) Albers, A.; Demeshko, S.; Dechert, S.; Saouma, C. T.; Mayer, J. M.; Meyer, F. *J. Am. Chem. Soc.* **2014**, *136*, 3946.
- (165) Albers, A.; Demeshko, S.; Dechert, S.; Bill, E.; Bothe, E.; Meyer, F. *Angew. Chem.* **2011**, *50*, 9191.
- (166) Bergner, M.; Dechert, S.; Demeshko, S.; Kupper, C.; Mayer, J. M.; Meyer, F. *J. Am.*

- Chem. Soc.* **2017**, *139*, 701.
- (167) Bergner, M.; Roy, L.; Dechert, S.; Neese, F.; Ye, S.; Meyer, F. *Angew. Chem.* **2017**, *56*, 4882.
- (168) Tonzetich, Z. J.; Do, L. H.; Lippard, S. J. *J. Am. Chem. Soc.* **2009**, *131*, 7964.
- (169) Schiewer, C. E. Master Thesis: Reactions of Biomimetic Iron-Sulfur Clusters, Georg-August-Universität Göttingen, 2013.
- (170) Hung, M.; Tsai, M.; Lee, G.; Liaw, W. *Inorg. Chem.* **2006**, *45*, 6041.
- (171) Pulukkody, R.; Darensbourg, M. Y. *Acc. Chem. Res.* **2015**, *48*, 2049.
- (172) Tran, C. T.; Skodje, K. M.; Kim, E. In *Progress in Inorganic Chemistry*; Karlin, K. D., Ed.; John Wiley & Sons, 2014; Vol. 59, pp 339–379.
- (173) Shih, W. C.; Lu, T. Te; Yang, L. B.; Tsai, F. Te; Chiang, M. H.; Lee, J. F.; Chiang, Y. W.; Liaw, W. F. *J. Inorg. Biochem.* **2012**, *113*, 83.
- (174) Tsou, C.; Tsai, F.; Chen, H.; Hsu, I.; Liaw, W. *Inorg. Chem.* **2013**, *52*, 1631.
- (175) Vanin, A. F. *Nitric Oxide* **2016**, *54*, 15.
- (176) Vanin, A. F. *Biophysics* **2017**, *62*, 509.
- (177) Fitzpatrick, J.; Kim, E. *Acc. Chem. Res.* **2015**, *48*, 2453.
- (178) Yuan, S.; Liaw, W.; Wang, Y. *Inorg. Chem.* **2016**, *55*, 9383.
- (179) Li, M.; Bonnet, D.; Bill, E.; Neese, F.; Weyhermüller, T.; Blum, N.; Sellmann, D.; Wieghardt, K. *Inorg. Chem.* **2002**, *41*, 3444.
- (180) Kupper, C.; Rees, J. A.; Dechert, S.; Debeer, S.; Meyer, F. *J. Am. Chem. Soc.* **2016**, *138*, 7888.
- (181) Speelman, A. L.; Zhang, B.; Silakov, A.; Skodje, K. M.; Alp, E. E.; Zhao, J.; Hu, M. Y.; Kim, E.; Krebs, C.; Lehnert, N. *Inorg. Chem.* **2016**, *55*, 5485.
- (182) Ye, S.; Neese, F. *J. Am. Chem. Soc.* **2010**, *132*, 3646.
- (183) Neese, F. *Wiley Interdiscip. Rev. - Comput. Mol. Sci.* **2012**, *2*, 73.
- (184) Römel, M.; Ye, S.; Neese, F. *Inorg. Chem.* **2009**, *48*, 784.
- (185) Sinnecker, S.; Slep, L. D.; Bill, E.; Neese, F. *Inorg. Chem.* **2005**, *44*, 2245.
- (186) Neese, F. *Inorg. Chim. Acta* **2002**, *337*, 181.
- (187) Berkovitch, F.; Nicolet, Y.; Wan, J. T.; Jarrett, J. T.; Drennan, C. L. *Science* **2004**, *303*, 76.
- (188) Costanzo, L. Di; Flores Jr., L. V.; Christianson, D. W. *Proteins* **2006**, *65*, 637.
- (189) Ballmann, J.; Dechert, S.; Bill, E.; Ryde, U.; Meyer, F. *Inorg. Chem.* **2008**, *47*, 1586.
- (190) Fuchs, M. G. G.; Dechert, S.; Demeshko, S.; Ryde, U.; Meyer, F. *Inorg. Chem.* **2010**, *49*, 5853.
- (191) Werst, M. M.; Kennedy, I. M. C.; Houseman, A. L. P.; Beinert, H.; Hoffman, B. M. *Biochemistry* **1990**, *29*, 10533.

- (192) Armstrong, F. A.; George, S. J.; Cammack, R.; Hatchikian, E. C.; Thomson, A. J. *Biochem. J.* **1989**, *264*, 265.
- (193) George, S. J.; Armstrong, F. A.; Hatchikian, E. C.; Thomson, A. J. *Biochem. J.* **1989**, *264*, 275.
- (194) Conover, R. C.; Kowal, A. T.; Fu, W.; Park, J. B.; Aono, S.; Adams, M. W. W.; Johnson, M. K. *J. Biol. Chem.* **1990**, *265*, 8533.
- (195) Johnson, R. E.; Papaefthymiou, G. C.; Frankel, R. B.; Holm, R. H. *J. Am. Chem. Soc.* **1983**, *105*, 7280.
- (196) Pape, L. Le; Lamotte, B.; Mouesca, J. *J. Am. Chem. Soc.* **1997**, *119*, 9757.
- (197) Pape, L. Le; Lamotte, B.; Mouesca, J. *J. Am. Chem. Soc.* **1997**, *119*, 9771.
- (198) Dey, A.; Jenney, F. E.; Adams, M. W. W.; Babini, E.; Takahashi, Y.; Fukuyama, K.; Hodgson, K. O.; Hedman, B.; Solomon, E. I. *Science* **2007**, *318*, 1464.
- (199) Pandelia, M.-E.; Nitschke, W.; Infossi, P.; Giudici-Ortoni, M.-T.; Bill, E.; Lubitz, W. *Proc. Natl. Acad. Sci.* **2011**, *108*, 6097.
- (200) Rius, G.; Lamotte, B. *J. Am. Chem. Soc.* **1989**, *111*, 2464.
- (201) Mouesca, J.-M.; Rills, G.; Lamotte, B. *J. Am. Chem. Soc.* **1993**, *115*, 4714.
- (202) Brien, E. O.; Holt, M. E.; Thompson, M. K.; Salay, L. E.; Ehlinger, A. C.; Chazin, W. J.; Barton, J. K. *Science* **2017**, *355*, 813.
- (203) Tse, E. C. M.; Zwang, T. J.; Barton, J. K. *J. Am. Chem. Soc.* **2017**, *139*, 12784.
- (204) Boon, E. M.; Livingston, A. L.; Chmiel, N. H.; David, S. S.; Barton, J. K. *Proc. Natl. Acad. Sci.* **2003**, *100*, 12543.
- (205) Bartels, P. L.; Zhou, A.; Arnold, A. R.; Nun, N. N.; Crespilho, F. N.; David, S. S.; Barton, J. K. *Langmuir* **2017**, *33*, 2523.
- (206) Dus, K.; De Klerk, H.; Sletten, K.; Bartsch, R. G. *Biochim. Biophys. Acta* **1967**, *140*, 291.
- (207) Middleton, P.; Dickson, D. P. E.; Johnson, C. E.; Rush, J. D. *Eur. J. Biochem.* **1980**, *104*, 289.
- (208) Gloux, J.; Gloux, P.; Lamotte, B.; Mouesca, J.-M.; Rius, G. *J. Am. Chem. Soc.* **1994**, *116*, 1953.
- (209) Gloux, J.; Gloux, P.; Lamotte, B.; Rius, G. *Phys. Rev. Lett.* **1985**, *54*, 599.
- (210) Gloux, J.; Gloux, P.; Hendriks, H.; Rius, G. *J. Am. Chem. Soc.* **1987**, *109*, 3220.
- (211) Priem, A. H.; Klaassen, A. A. K.; Reijerse, E. J.; Meyer, T. E.; Luchinat, C.; Capozzi, F.; Dunham, W. R.; Hagen, W. R. *J. Biol. Inorg. Chem.* **2005**, *10*, 417.
- (212) Jiang, S.; Zhang, T.; Zhang, X.; Zhang, G.; Hai, L.; Li, B. *RSC Adv.* **2016**, *6*, 84139.
- (213) Thompson, D. W.; Ito, A.; Meyer, T. J. *Pure Appl. Chem.* **2013**, *85*, 1257.
- (214) Dongare, P.; Myron, B. D. B.; Wang, L.; Thompson, D. W.; Meyer, T. J. *Coord. Chem. Rev.* **2017**, *345*, 86.

- (215) Pannwitz, A.; Prescimone, A.; Wenger, O. S. *Eur. J. Inorg. Chem.* **2017**, 609.
- (216) Kaes, C.; Katz, A.; Hosseini, M. W. *Chem. Rev.* **2000**, *100*, 3553.
- (217) Newkome, G. R.; Patri, A. K.; Holder, E.; Schubert, U. S. *Eur. J. Org. Chem.* **2004**, 235.
- (218) Wang, M.; Chen, L.; Li, X.; Sun, L. *Dalt. Trans.* **2011**, *40*, 12793.
- (219) Lomoth, R.; Ott, S. *Dalt. Trans.* **2009**, 9952.
- (220) Summers, P. A.; Calladine, J. A.; Ghiotto, F.; Dawson, J.; Sun, X. Z.; Hamilton, M. L.; Towrie, M.; Davies, E. S.; McMaster, J.; George, M. W.; Schröder, M. *Inorg. Chem.* **2016**, *55*, 527.
- (221) Li, P.; Amirjalayer, S.; Hartl, F.; Lutz, M.; Bruin, B. De; Becker, R.; Woutersen, S.; Reek, J. N. H. *Inorg. Chem.* **2014**, *53*, 5373.
- (222) Na, Y.; Pan, J.; Wang, M.; Sun, L. *Inorg. Chem.* **2007**, *46*, 3813.
- (223) Cattaneo, M.; Schiewer, C. E.; Schober, A.; Dechert, S.; Siewert, I.; Meyer, F. manuscript submitted.
- (224) Lu, Y. Patent. US 20150336884 A1 20151126, 2015.
- (225) Baek, J. Y.; Lee, S. H.; Lee, J. U.; Lee, D. W.; Kim, S. H. Patent. KR 2014121991 A 20141017, 2014.
- (226) Sevier, C. S.; Kaiser, C. A. *Nat. Rev. Mol. Cell Biol.* **2002**, *3*, 836.
- (227) Ragsdale, S. W.; Yi, L. *Antioxid. Redox Signal.* **2011**, *14*, 1039.
- (228) Babic, S.; Horvat, A. J. M.; Pavlovic, D. M.; Kastelan-Macan, M. *Trends Anal. Chem.* **2007**, *26*, 1043.
- (229) In *CRC Handb. Chem. Physics*; Lide, D. R., Ed.; 2005; pp 42–51.
- (230) Kütt, A.; Leito, I.; Kaljurand, I.; Sooväli, L.; Vlasov, V. M.; Yagupolskii, L. M.; Koppel, I. A. *J. Org. Chem.* **2006**, *71*, 2829.
- (231) Muckerman, J. T.; Skone, J. H.; Ning, M.; Wasada-Tsutsui, Y. *Biochim. Biophys. Acta* **2013**, *1827*, 882.
- (232) Benniston, A. C.; Allen, B. D.; Harriman, A.; Llarena, I.; Rostron, J. P.; Stewart, B. *New J. Chem.* **2009**, *33*, 417.
- (233) Hall, G. B.; Kottani, R.; Felton, G. a N.; Yamamoto, T.; Evans, D. H.; Glass, R. S.; Lichtenberger, D. L. *J. Am. Chem. Soc.* **2014**, *136*, 4012.
- (234) Benniston, A. C.; Hagon, J.; He, X.; Yang, S.; Harrington, R. W. *Org. Lett.* **2012**, *14*, 506.
- (235) Maran, F.; Wayner, D. D. M.; Workentin, M. S. *Adv. Phys. Org. Chem.* **2001**, *36*, 85.
- (236) Ballmann, J.; Dechert, S.; Demeshko, S.; Meyer, F. *Eur. J. Inorg. Chem.* **2009**, 3219.
- (237) Fulmer, G. R.; Miller, A. J. M.; Sherden, N. H.; Gottlieb, H. E.; Nudelman, A.; Stoltz, B. M.; Bercaw, J. E.; Goldberg, K. I. *Organometallics* **2010**, *29*, 2176.

-
- (238) Sheldrick, G. M. *Acta Crystallogr. Sect. A. Found. Crystallogr.* **2008**, *64*, 112.
- (239) X-Red. STOE & CIE GmbH, Darmstadt, Germany, 2002.
- (240) Neese, F. *WIREs Comput. Mol. Sci.* **2012**, *2*, 73.
- (241) Becke, A. *Phys. Rev. A* **1988**, *38*, 3098.
- (242) Perdew, J. P. *Phys. Rev. B* **1986**, *33*, 8822.
- (243) Perdew, J. P. *Phys. Rev. B* **1986**, *34*, 7406.
- (244) Tao, J.; Perdew, J. P.; Staroverov, V. N.; Scuseria, G. E. *Phys. Rev. Lett.* **2003**, *91*, 146401.
- (245) Perdew, J. P.; Tao, J.; Staroverov, V. N.; Scuseria, G. E. *J. Chem. Phys.* **2004**, *120*, 6898.
- (246) Becke, A. D. *J. Chem. Phys.* **1993**, *98*, 1372.
- (247) Lee, C.; Yang, W.; Parr, R. G. *Phys. Rev. B* **1988**, *37*, 785.
- (248) Staroverov, V. N.; Scuseria, G. E.; Tao, J.; Perdew, J. P. *Chem. Phys.* **2003**, *119*, 12129.
- (249) Schafer, A.; Horn, H.; Ahlrichs, R. *J. Chem. Phys.* **1992**, *97*, 2571.
- (250) Schäfer, A.; Huber, C.; Ahlrichs, R. *J. Chem. Phys.* **1994**, *100*, 5829.
- (251) Weigend, F.; Ahlrichs, R. *Phys. Chem. Chem. Phys.* **2005**, *7*, 3297.
- (252) Bochevarov, A. D.; Friesner, R. a; Lippard, S. J. *J. Chem. Theory Comput.* **2010**, *6*, 3735.
- (253) Zhang, Y.; Oldfield, E. *J. Phys. Chem. B* **2003**, *107*, 7180.
- (254) Kowalska, J. K.; Hahn, A. W.; Albers, A.; Schiewer, C. E.; Bjornsson, R.; Lima, F. A.; Meyer, F.; DeBeer, S. *Inorg. Chem.* **2016**, *55*, 4485.
- (255) Kowalska, J. K.; Nayyar, B.; Rees, J. A.; Schiewer, C. E.; Lee, S. C.; Kovacs, J. A.; Meyer, F.; Weyhermüller, T.; Otero, E.; DeBeer, S. *Inorg. Chem.* **2017**, *56*, 8147.

Abbreviations

α	Charge transfer coefficient from Butler-Volmer equation
Arg	Arginine
Bn	Benzyl
Bpy	2,2'-Bipyridine
br	Broad
Bu	Butyl
Cp	Cyclopentadiene
Cp*	Pentamethylcyclopentadiene
Cys	Cysteine
d	Doublet
DBU	1,8-Diazabicyclo(5.4.0)undec-7-ene
DCM	Dichloromethane
DDQ	2,3-Dichloro-5,6-dicyano-1,4-benzoquinone
DMF	Dimethylformamide
DMPH	2,6-Dimethylpyridinium tetrafluoroborate
DNA	Deoxyribonucleic acid
DNIC	Dinitrosyl Iron Complex
EDTA	Ethylenediaminetetraacetic acid
EFG	Electric Field Gradient
EPR	Electron Paramagnetic Resonance
eq	Equivalent
ESI	Electrospray Ionization
Et	Ethyl
Et ₂ O	Diethylether
EtCN	Propionitrile
Fc	Ferrocene
FeMoCo	Iron-Molybdenum Cofactor
FNR	Transcriptional Activator of Fumarate and Nitrate Redcutase
fwhm	Full width half maximum
<i>g</i>	Landé factor

HiPIP	High Potential Iron-Sulfur Protein
His	Histidine
hs	High spin
HSDmp	2,6-(2,4,6-Me ₃ C ₆ H ₂) ₂ C ₆ H ₃
int.	intermediate
ISC	Iron Sulfur Cluster Formation System
IscR	Iron Sulfur Cluster Regulator
IscU	Scaffold Protein in ISC System
IUPAC	International Union of Pure and Applied Chemistry
k_c	Rate of chemical reaction
k_s	Rate constant for electron transfer
LIFDI	Liquid Injection Field Desorption Ionization
LMCT	Ligand to Metal Charge Transfer
Lys	Lysine
m	Multiplett
Me	Methyl
MeCN	Acetonitrile
MS	Mass Spectrometry
NMR	Nuclear Magnetic Resonance
obs	Observed
OTf	Triflate (CF ₃ SO ₃) ⁻
PCET	Proton Coupled Electron Transfer
Ph	Phenyl
ppm	Parts per million
PPN	Bis(triphenylphosphine)iminium
Pr	Propyl
q	Quartet
RBS	Roussin's Black Salt [Fe ₄ S ₃ (NO) ₇] ⁻
RNA	Ribonucleic Acid
RRE	Roussin's Red Ester [Fe ₂ (SR) ₂ (NO) ₄]
RRS	Roussin's Red Salt [Fe ₂ S ₂ (NO) ₄] ²⁻
rt	Room temperature

Abbreviations

Ser	Serine
sh	Shoulder
SHE	Standard Hydrogen Electrode
SQUID	Superconducting Quantum Interference Device
SUF	Sulfur Formation System
TEMPO	2,2,6,6-Tetramethylpiperidinyloxy
tert	Tertiary
THF	Tetrahydrofuran
TIP	Temperature-Independent Paramagnetism
tRNA	Transfer Ribonucleic Acid
TS	Transition State
UV-vis	Ultraviolet and visible

Curriculum Vitae

Christine Elisabeth Schiewer

Date and Place of Birth: 10/10/1988 in Menden (Sauerland)

Education

PhD Thesis	PhD student in the group of Prof. Dr. Franc Meyer, Department of Inorganic Chemistry, Georg-August University Göttingen, Germany. Thesis: <i>“Nitric Oxide Reactivity and Unusual Redox Properties of Biomimetic Iron-Sulfur Clusters with Alternative Cluster Ligands”</i>	12/2013 – present
Research Stays Abroad	Visiting research scientist in the group of Prof. Dr. Ulf Ryde, Lund University, Sweden.	09/2015 – 10/2015
	Research student in the group of Prof. Dr. Martina Lahmann, Bangor University, UK.	10/2012 – 01/2013
M. Sc. Studies	in Chemistry at Georg-August University Göttingen, Germany; cumulative grade: 1.4 (with distinction). Master thesis in the group of Prof. Dr. Franc Meyer, Department of Inorganic Chemistry. Thesis: <i>“Biomimetic Iron-Sulfur Clusters”</i> (grade 1.0)	10/2011 – 11/2013
B. Sc. Studies	in Chemistry at Georg-August University Göttingen, Germany; cumulative grade: 1.7. Master Thesis in the group of Prof. Dr. Franc Meyer, Department of Inorganic Chemistry. Thesis: <i>“Biomimetic Iron-Sulfur Clusters”</i> (grade 1.0)	10/2008 – 06/2011
Secondary School	Abitur (university-entrance diploma) at Pestalozzi-Gymnasium Unna, Germany: Cumulative grade: 1.5	09/1999 06/2008
	High School Diploma (cum laude) at MacArthur High School, San Antonio, USA.	06/2006

Method Courses

03/2015	Advanced Electrochemistry (Prof. M. Robert)
02/2015	Introduction to Electrochemistry (Prof. C. Jooß, Prof. S. Schneider)
12/2014	X-Ray Absorption Spectroscopy (Prof. S. De Beer)
WiSe 14	Practical NMR Spectroscopy (Dr. M. John)
09/2013	Summer School on Methods in Molecular Energy Research (organized by Max Planck Institute for Chemical Energy Conversion Mühlheim)

Teaching Experience

- Supervision of a bachelor thesis
- Seminars in *Advanced Analytical Methods in Inorganic Chemistry, Coordination Chemistry,*
- Supervision of *Inorganic Chemistry Practical Courses* and *Advanced Analytical Methods Practical Course* (EPR- and Mössbauer spectroscopy, Cyclic Voltammetry, and SQUID magnetometry)

Soft Skill Courses

- Good Scientific Practice
- Project Management
- Leadership
- Intercultural Competence
- Academic Writing

IT

- Origin, MestReNova, MS Office, DFT calculations with ORCA

Languages

- German (native speaker)
- English (fluent)
- French (A2 of European Reference Framework)

Scientific Contributions

Publications

M. Cattaneo,[§] C. E. Schiewer,[§] A. Schober, S. Dechert, I. Siewert, F. Meyer, *2,2'-Bipyridine Equipped with a Disulfide/Dithiol Switch for Coupled Two Electron and Proton Transfer*, submitted. [§] These authors contributed equally to the work.

J. K. Kowalska, B. Nayyar, J. A. Rees, C. E. Schiewer, S. C. Lee, J. A. Kovacs, F. Meyer, T. Weyhermüller, E. Otero, S. DeBeer *Inorg. Chem.* **2017**, *56*, 8147–8158. '*Iron L_{2,3}-Edge X-ray Absorption and X-ray Magnetic Circular Dichroism Studies of Molecular Iron Complexes with Relevance to the FeMoco and FeVco Active Sites of Nitrogenase*'.

J. K. Kowalska, A. W. Hahn, A. Albers, C. E. Schiewer, R. Bjornsson, F. A. Lima, F. Meyer, S. DeBeer *Inorg. Chem.* **2016**, *55*, 4485–4497. *X-ray Absorption and Emission Spectroscopic Studies of [L₂Fe₂S₂]ⁿ⁻ Model Complexes: Implications for the Experimental Evaluation of Redox States in Iron–Sulfur Clusters.*

Presentations at International Conferences and Workshops

AGIChem, Göttingen, Germany, August 2017 (Poster).

42nd ICCG, Brest, France, July 2016 (Poster).

6th IMBG Meeting, Grenoble, France, September 2015 (Poster).

Final Symposium of the IRTG 1422, Göttingen, Germany, August 2015 (Poster).

Workshop of the IRTG 1422, Katlenburg, Germany, May 2015 (Oral contribution & poster).

Trends in Inorganic Chemistry (TINC), Lund, Sweden, May 2014 (Poster).

Acknowledgements

Ich möchte mich herzlich bei meinem Doktorvater Prof. Dr. Franc Meyer dafür bedanken, dass ich in seinem Arbeitskreis promovieren durfte. Ich danke ihm für die freundliche Betreuung und die Vermittlung diverser Kooperationen.

Prof. Dr. Kai Tittmann danke ich für die Übernahme des Koreferats. Ich freue mich, dass es ihm nach schwerer Krankheit wieder besser geht und er weiterhin bereit ist, mein Zweitbetreuer zu sein.

Prof. Dr. Ebbe Nordländer danke ich für die Übernahme der Aufgabe des dritten Betreuers; auch wenn wir uns wegen der räumlichen Distanz nur auf Workshops und dem Abschluss Symposium des IRTGs treffen konnten.

Dr. Serhiy Demeschko danke ich für die Einweisung in die Mössbauerspektroskopie und das Anlernen der Bedienung des Gerätes. Mössbauerspektroskopie hat mich schon als Student fasziniert und ich bin froh, dass ich während meiner Doktorarbeit meine Kenntnisse auf diesem Gebiet erweitern konnte. Zudem danke ich Serhiy für Ausführung und Auswertung magnetischer Messungen.

Prof. Dr. Ulf Ryde danke ich für die Betreuung in Lund und die Einweisung in DFT-Rechnungen. Die IT-Kenntnisse, die ich in Lund gelernt habe, konnte ich in Göttingen einfach auf ORCA übertragen, womit ich dann die Rechnungen in dieser Arbeit durchgeführt habe.

Prof. Dr. Inke Siewert danke ich für ihre ansteckende Begeisterung für das Bipyridin-Projekt. Ich danke ihr für die Beratung bei der Messung von CVs und die Simulation der entstandenen Voltammogramme.

Dr. Sebastian Dechert danke ich für die Beratung bei Fragen zu ORCA und anderen IT-Problemen. Zudem danke ich ihm dafür, dass ich seine DFT-Berechnung zum Bipyridin-Thema in meine Arbeit einfließen lassen durfte. Schließlich danke ich ihm und Nicole Kindermann für das Messen und Auswerten von Kristallstrukturen.

Desweiteren möchte ich mich bei meinen Kooperationspartnern bedanken: Christina Müller und Prof. Volker Schünemann für die NIS-Messung an deprotonierten und protonierten DNICs.

Marie Bergner danke ich für das Messen und Simulieren von ESR-Spektren. Als Laborkolleginnen, die beide an Eisen-Schwefel Clustern arbeiteten, sind wir auf den meisten Konferenzen zusammen gewesen und hatten viel Spaß. Neben Marie danke ich noch Mattia Veronelli für die tolle Zeit im Labor.

Ich danke meiner Vorgängerin Antonia Albers für das Anlernen im Labor. Durch sie bin ich auf die Idee gekommen meine Bachelorarbeit über Eisen-Schwefel Cluster zu schreiben. Diese zufällige Begegnung im AC-Synthese Praktikum hatte nun letztendlich einen entscheidenden Einfluss auf meinen Lebenslauf genommen, für den ich ihr sehr dankbar bin.

Ich danke der Analytikabteilung und den Werkstätten, ohne deren Hilfe eine solche Doktorarbeit nicht möglich gewesen wäre. Insbesondere herausstellen möchte ich Andreas Schwarz und Jörg Teichgräber, die mir bei praktischen Problemen mir mit Rat und Tat zur Seite standen. Frau Dr. Claudia Stückl, Britta Müller, Petra Unger und Petra Gaugel danke ich für die Unterstützung in administrativen Dingen. Ich bedanke mich bei meiner Bachelorstudentin Julia Struwe und bei meinem Hiwi Svenja Neumann für ihre tatkräftige Unterstützung.

Dem IRTG 1422 danke ich für finanzielle Unterstützung und für die Möglichkeit an zahlreichen Seminaren, Workshops und Konferenzen teilnehmen zu können.

Ich möchte mich bei Arne Glüer, Marie Bergner, Claudia Schremmer, Sebastian Neske und Fabian Rabe von Pappenheim für das Korrekturlesen meiner Arbeit danken.

Schließlich danke ich allen Mitgliedern des Arbeitskreises, meinen Freunden und meiner Familie, die mich während der Doktorarbeit begleitet und stets unterstützt haben.

Vielen Dank, Arne, dass du an meiner Seite stehst und immer für mich da bist.